# Theoretical description of quarkonium dynamics in the quark gluon plasma with a quantum master equation approach

Stéphane Delorme

DOCTORAT MATIERE BRETAGNE MOLECULES LOIRE ET MATERIAUX

IMT Atlantique
Bretagne-Pays de la Loire
École Mines-Télécom

# THÈSE DE DOCTORAT DE

L'ÉCOLE NATIONALE SUPÉRIEURE MINES-TÉLÉCOM ATLANTIQUE
BRETAGNE PAYS DE LA LOIRE - IMT ATLANTIQUE

ÉCOLE DOCTORALE N° 596
*Matière, Molécules, Matériaux*
Spécialité : *Physique Subatomique et Instrumentation Nucléaire*

Par
**Stéphane DELORME**

## Theoretical description of quarkonia dynamics in the Quark Gluon Plasma with a quantum master equation approach

**Thèse présentée et soutenue à Nantes, le 01/10/2021**
**Unité de recherche : Laboratoire SUBATECH, UMR 6457**
**Thèse N° : 2021IMTA0264**

**Rapporteurs avant soutenance :**

| | |
|---|---|
| Nora BRAMBILLA | Professeur, Technical University Munich |
| Elena GONZALES FERREIRO | Professeur, Universidad de Santiago de Compostella |

**Composition du Jury :**

| | | |
|---|---|---|
| Président : | Jean-Paul BLAIZOT | Professeur émerite, CEA Saclay |
| Examinateurs : | Nora BRAMBILLA | Professeur, Technical University Munich |
| | Elena GONZALES FERREIRO | Professeur, Universidad de Santiago de Compostella |
| | Alexander ROTHKOPF | Associate Professor, University of Stavanger |
| Dir. de thèse : | Pol-Bernard GOSSIAUX | Professeur, IMT Atlantique |
| Co-dir. de thèse : | Thierry GOUSSET | Professeur, Université de Nantes |

**Invité(s) :**

| | |
|---|---|
| Roland KATZ | Docteur, CNRS/SUBATECH |

# *Remerciements*

Après exactement trois ans (la précision suisse sans doute...), mon aventure doctorale arrive à son terme, et j'aimerais remercier "quelques" personnes. Tout d'abord, les membres de mon jury de thèse Elena Gonzales Ferreiro, Nora Brambilla, Alexander Rothkopf et Jean-Paul Blaizot pour avoir accepté de participer à ma soutenance. Merci à Elena et Nora pour leur travail de rapporteuse et leur corrections. Merci à Alexander pour les nombreux échanges que nous avons eu pendant la rédaction du projet pour la Marie-Curie. Merci à Jean-Paul pour son rôle de président du jury, de membre de mon CSI, ainsi que pour les discussions que nous avons eu pendant ma thèse, qui ont toujours été très intéressantes et utiles. Je remercie également Philippe Pillot pour son rôle de membre de mon CSI.

Une thèse ne se fait pas seulement avec un thésard, donc j'aimerais remercier mes deux directeurs de thèse Pol-Bernard Gossiaux et Thierry Gousset. D'abord Thierry, merci pour toutes les discussions informelles (ou formelles) que nous avons pu avoir, notamment au moment de dériver ces fichus termes supplémentaires ou sur la manière de jouer avec les facteurs de couleur. Merci pour tes conseils et ton encadrement. Pol, merci beaucoup pour tout ce que tu as fait pendant ma thèse, à chaque fois que j'avais un problème (et on peut dire qu'il y en a eu un sacré paquet), tu proposais une piste (ou plusieurs !) pour essayer de mieux comprendre ce qu'il se passait et corriger les pépins. Merci d'avoir toujours dégagé du temps pour moi, alors même que tu croulais sous toutes tes autres responsabilités. Merci également pour tes conseils. On se souviendra de cette fameuse soirée de janvier à galérer dans Paris en rentrant de Quarkonia as Tools !

Puisqu'on parle d'encadrants, j'en profite pour remercier mon "presque-encadrant" Roland Katz. C'était un plaisir d'avoir bossé avec toi (et un plaisir qui va continuer encore !), merci pour tous tes conseils, tes encouragements, ton aide...ça serait sans doute plus simple de faire la liste de ce pourquoi je ne te remercie pas ! Ah si, merci aussi de m'avoir supporté dans le bureau à chaque fois que je trouvais une erreur et que j'employais un langage fleuri à mon égard !

Je ne vais pas tous les citer car je risquerais d'oublier des gens mais j'aimerais remercier tous les membres du labo avec qui j'ai pu interagir, notamment le service communication et le service administratif (en particulier Farah, Isabelle, Tanja, Stéphanie, les deux Sophie et Séverine) pour toute l'aide qu'ils m'ont apporté pendant ma thèse. Merci également aux membres du groupe théorie avec qui j'ai pu interagir

pendant ces trois ans.

Qui dit un thésard, dit bien souvent plusieurs thésards (et ex-thésards !), et je les remercie pour toute la bonne humeur et les discussions qu'on a pu avoir. Merci à Florian, Anthony, Erwann, David Henaff, Manu, Chloé, Maria, Yajing, Yuwei, Flavien, Victor, Maxime, Thomas, Emeline, Etienne, Claudia, Mahbobbeh, Denys, Michael pour son aide informatique, Johannes alias le spécialiste pour toutes les discussions plus ou moins intelligentes à base de vieux monsieur et de roscasse, Gabriel pour m'avoir lancé dans une aventure à base de tickets et de clochettes (ou peut-être que je te remercie pas pour ça, je sais pas trop en fait…), Rita pour ta bonne humeur constante avec ou sans boules de papier et ce depuis Grenoble, Ophélie et Quentin pour toutes nos discussions autour d'un café ou thé, à base de pandas ou encore de fables géométriques (au passage, j'ai perdu !), courage Ophélie c'est bientôt terminé ! Une pensée pour les petits nouveaux aussi, courage à vous !

Je garde le bureau H221 pour la fin, dans ses deux incarnations pré-Covid et post-Covid (qu'on ne remercie pas d'ailleurs). Merci à David Fuseau et Grégoire pour tous les délires plus absurdes les uns que les autres avec Roland, toujours présent (enfin après 14h…) pour en rajouter une couche et pour la génèse de grandes légendes telles que la delormalisation (toujours à définir) et Steph-Chan. Vivement que je puisse voir David aux Oscars, il paraît que c'est bien parti ! Merci à Nathan, qui a eu la lourde tâche de remplacer David comme partenaire de choc de Grégoire, tu as l'air de très bien t'en tirer !

Un grand merci à la "délégation franc-comtoise" Coraline et Clément, qui s'est déplacée pour assister à ma soutenance, mais aussi pour tous les bons souvenirs de Licence (il y en a trop pour les citer). Merci en particulier à Clément pour toutes ces soirées à casser des cubes dans un jeu cubique, ou à s'énerver à taper sur des notes de façon plus ou moins rapide et précise (un jour on fera des 8*, enfin je crois), courage pour la fin de thèse, on se revoit cet été !

Enfin, un grand merci à ma famille et mes parents pour leur soutien pendant la thèse (et avant !). En particulier, merci à mon père pour m'avoir supporté pendant les phases de bien et de moins bien, pendant toutes mes envolées lyriques quand je m'énervais sur des choses plus ou moins futiles, et pour m'avoir toujours soutenu. Enfin, une pensée émue à ma mère, qui n'a pas pu assister à tout ça, merci pour tout, où que tu sois, on se reverra un jour.

# Contents

**Remerciements** **i**

**Introduction** **1**

**1 The Standard Model and the Quark-Gluon Plasma** **3**
1.1 The Standard Model of particle physics . . . . . 3
1.1.1 The Standard Model . . . . . 3
1.1.2 Quantum Chromodynamics . . . . . 5
1.1.3 Quarkonia . . . . . 11
1.2 The Quark-Gluon Plasma . . . . . 14
1.2.1 Phase diagram of the nuclear matter . . . . . 14
1.2.2 Heavy ion collisions . . . . . 16
1.2.3 Probes of the QGP . . . . . 19
1.3 Summary . . . . . 24

**2 Phenomenology of quarkonia suppression** **25**
2.1 Quarkonia suppression and recombination . . . . . 25
2.1.1 Cold nuclear effects on suppression . . . . . 25
2.1.2 QGP effects on suppression . . . . . 28
2.1.3 Recombination . . . . . 30
2.1.4 Experimental measurements at RHIC and LHC . . . . . 31
2.2 Theoretical models of quarkonia suppression . . . . . 38
2.2.1 Sequential suppression . . . . . 38
2.2.2 Co-movers . . . . . 40
2.2.3 Statistical hadronization . . . . . 41
2.2.4 Transport models . . . . . 43
2.3 Summary . . . . . 45

**3 Open Quantum Systems** **47**
3.1 Density operator and quantum master equations . . . 47
3.2 Dynamics of open quantum systems . . . 49
3.3 The Linblad equation . . . 51
3.4 Weak coupling limit and Born-Markov approximation . . . 53
3.5 The quantum optical limit . . . 55
3.6 The quantum brownian motion . . . 56
3.7 Quarkonia as open quantum systems . . . 59
3.7.1 Early phenomenological approaches . . . 59
3.7.2 Katz and Gossiaux . . . 61
3.7.3 Akamatsu et al.: Quarkonium quantum master equation in the Lindblad form . . . 62
3.7.4 Brambilla et al.: A pNRQCD based quantum master equation approach . . . 63
3.7.5 Yao et al.: Boltzmann equation derived from pNRQCD effective theory . . . 64
3.7.6 Blaizot et al.: Quantum dynamics of heavy quarks in the QGP 66
3.8 Quantum dynamics of heavy quarks in the QGP and semi-classical approximation . . . 67

**4 Extension of the Blaizot-Escobedo equations and restoration of positivity** **75**
4.1 Alternative time discretization . . . 75
4.1.1 Derivation of the $\mathcal{L}_3'$ terms . . . 76
4.1.2 Derivation of the $\mathcal{L}_4$ terms . . . 79
4.1.3 Derivation for QCD . . . 83
4.2 Reduction of the center of mass degrees of freedom . . . 84
4.2.1 Reduction of the $\mathcal{L}_0$ terms . . . 85
4.2.2 Reduction of the $\mathcal{L}_1$ terms . . . 86
4.2.3 Reduction of the $\mathcal{L}_2$ terms . . . 87
4.2.4 Reduction of the $\mathcal{L}_3'$ terms . . . 88
4.2.5 Reduction of the $\mathcal{L}_4$ terms . . . 90
4.3 Conservation of the trace . . . 94
4.3.1 Trace at the $\mathcal{L}_2$ level . . . 95
4.3.2 Trace at the $\mathcal{L}_3'$ level . . . 97
4.3.3 Trace at the $\mathcal{L}_4$ level . . . 99

4.4 Positivity . . . 101
4.4.1 Positivity at the $\mathcal{L}_2$ level . . . 102
4.4.2 Positivity at the $\mathcal{L}'_3$ level . . . 105
4.4.3 Positivity at the $\mathcal{L}_4$ level . . . 108
4.4.4 Full QCD case . . . 112
$\mathcal{L}_2$ level: . . . 112
$\mathcal{L}'_3$ level: . . . 113
$\mathcal{L}_4$ level: . . . 114
4.5 UV divergences and minimal set . . . 115
4.6 Conclusion . . . 116

**5 Numerical implementation** **117**
5.1 One-dimensionnal equations . . . 117
5.2 One dimensional potential for quarkonia in the Quark-Gluon Plasma 120
5.2.1 Generalized Gauss law model . . . 120
5.2.2 Real part of the one dimensional potential . . . 122
5.2.3 Imaginary part of the one dimensional potential . . . 125
5.2.4 Spectral decomposition . . . 126
5.3 Numerical method . . . 127
5.4 Trace conservation and determination of numerical parameters . . . 131
5.5 Positivity conservation . . . 137
5.6 Conclusion . . . 139

**6 Quarkonium dynamics in the Quark-Gluon Plasma** **141**
6.1 Quarkonium dynamics at fixed temperature . . . 141
6.1.1 Color dynamics . . . 142
6.1.2 Dynamics of a $c\bar{c}$ pair . . . 145
6.1.3 Projections on vacuum states . . . 155
6.2 Quarkonium dynamics in an evolving medium . . . 160
6.2.1 Projections on vacuum states . . . 161
6.2.2 $c\bar{c}$ dynamics . . . 162
6.3 Summary and conclusion . . . 164

**Conclusion** **167**

**A Derivation of QCD terms** **169**
A.1 Derivation procedure . . . . . 169
A.2 QCD color factors and QCD equations . . . . . 171

**B Résumé en français** **177**

**Bibliography** **191**

# List of Figures


1.1 Table of particles in the Standard Model. [7] . . . . . 4
1.2 *Left panel:* Gluon splitting into a virtual pair of quarks leading to screening. *Right panel:* Gluon self-interaction leading to antiscreening. [19] . . . . . 7
1.3 QCD coupling constant as a function of the transfered energy Q between two color charges [20] . . . . . 8
1.4 Illustration of the gluon string breaking, leading to two new composite systems. [22] . . . . . 9
1.5 Representation of the lattice used to discretize space-time in Lattice QCD. [7] . . . . . 10
1.6 *Left panel:* Mass spectrum of charmonia states. *Right panel:* Same for bottomonia states. [25] . . . . . 11
1.7 *Left panels:* Sources of prompt $J/\Psi$. *Right panels:* Sources of prompt Y(1S). [33] . . . . . 14
1.8 Schematic view of the phase diagram of QCD as function of temperature and baryon chemical potential [19] . . . . . 15
1.9 Schematization of the whole evolution [19] . . . . . 16
1.10 Representation of the initial heavy-ion collision [7] . . . . . 17
1.11 Representation of the Björken scenario with and without a QGP phase [46] . . . . . 18
1.12 Normalized production rates of hyperons and antihyperons in Pb-Pb collisions at $\sqrt{s_{NN}}$ = 17.3 GeV with respect to production rates in p-Be collisions measured by the NA57 experiment at the SPS [50] . . . . . 20
1.13 Schematic view of a peripheral heavy ion collision. [7] . . . . . 21
1.14 Schematic view of the reaction plane. [7] . . . . . 21
1.15 $v_2$ coefficient measured by the PHENIX and STAR experiments in Au-Au collisions at $\sqrt{s_{NN}}$ = 200 GeV. [55] . . . . . 22

1.16 Nuclear modification factor $R_{AA}$ as function of the jet transverse momentum for different centrality classes and isolation cone radius measured by CMS in Pb-Pb collisions at $\sqrt{s_{NN}}$ = 5.02 TeV [56]. . . . . 23

2.1 Nuclear modification factor $R_{AA}$ for $J/\Psi$ (upper panels) and Y (lower panels) using the EPS09 nPDFs as function of rapidity (left panels) and transverse momentum (right panels). [61] . . . . . 26
2.2 Dependence of $\sigma_{abs}$ on energy for the $J/\Psi$ at mid-rapidity [66] using the EKS98 and CTEQ61L nPDFs [67–70] . . . . . 28
2.3 Potential describing the $Q\bar{Q}$ pair interaction as function of the distance between the two quarks and temperature [80] . . . . . 29
2.4 Illustration of the dissociation of a quarkonium state and the hadronization of the free quarks into open heavy hadrons. . . . . 30
2.5 Illustration of the recombination of two uncorrelated quarks to form a quarkonium . . . . . 31
2.6 Dependence on multiplicity of the nuclear modification factor $R_{AA}$ for the Y(1S) (bottom panel) and of the integrated $R_{AA}$ for the Y(1S+2S+3S) (top panel) in Au-Au collisions at 200 GeV and U-U collisions at 193 GeV from the STAR experiment. [83] . . . . . 32
2.7 *Left panel:* Dependence on transverse momentum of the nuclear modification factor $R_{AA}$ for the Y(1S) and Y(2S) in Pb-Pb collisions at 2.76 TeV from the CMS experiment. *Right panel:* Dependence on rapidity. [84] . . . . . 33
2.8 Dependence on multiplicity of the nuclear modification factor $R_{AA}$ for the Y(1S) and Y(2S) in Pb-Pb collisions at 2.76 TeV from the CMS experiment. [84] . . . . . 33
2.9 *Left panel:* Dependence on transverse momentum of the $R_{AA}$ of the Y(1S) in Pb-Pb collisions at 5.02 TeV from the ALICE experiment. *Right panel:* Dependence on rapidity from ALICE and CMS. [85] . . . 34
2.10 Dependence on multiplicity of the nuclear modification factor $R_{AA}$ for the Y(1S) and Y(2S) in Pb-Pb collisions at 5.02 TeV from the ALICE experiment.[85] . . . . . 34
2.11 $J/\Psi$ $R_{AA}$ from STAR as function of multiplicity in Au-Au collisions at 200 GeV in two different rapidity range. [87] . . . . . 35

2.12 $J/\Psi$ $R_{AA}$ from CMS in Pb-Pb collisions at 2.76 and 5.02 TeV as function of rapidity (top left panel), multiplicity (top right panel) and transverse momentum (bottom panel).[88] . . . . . 36
2.13 $J/\Psi$ $R_{AA}$ from ALICE in Pb-Pb collisions at 2.76 TeV as function of multiplicity (left panel) and transverse momentum (right panel).[89] 36
2.14 Prompt $J/\Psi$ and $\Psi(2S)$ $R_{AA}$ from CMS in Pb-Pb collsions at 5.02 TeV as function of multiplicity (left panels) and transverse momentum (right panels) at central rapidities (top panels) and forward rapidity (bottom panels).[88] . . . . . 37
2.15 *Left panel:* Sequential suppression for $J/\Psi$. *Right panel:* Sequential suppression for $\Upsilon(1S)$. [33] . . . . . 38
2.16 Illustration of the dissociation of charmonium states through the disappearence of spectral functions [95]. . . . . 39
2.17 $\mathbf{p}_{\mathrm{T}}$ dependence of the $J/\Psi$ $R_{AA}$ in Pb-Pb collisions at $\sqrt{s_{NN}}$ = 2.76 TeV with the comovers interaction model (shadowed area) [102]. *Left panel:* Comparison to CMS [105, 106] data at mid-rapidity. *Right panel:* Comparison to CMS [105] data and ALICE [107] data at forward rapidity. . . . . 41
2.18 $J/\Psi$ transverse momentum spectrum in Pb-Pb collisions at $\sqrt{s_{NN}}$ = 5 TeV obtained from ALICE data [117] and comparison to results from the statistical hadronization model. Predictions for the $\Psi(2S)$ transverse momentum spectrum. [118]. . . . . 42
2.19 *Left panel:* Nuclear modification factor $R_{AA}$ for $J/\Psi$ dependence on charged particle multiplicity at forward rapidity obtained from the SHM and comparison to experimental data. *Right panel:* Same at mid-rapidity. Data are for Au-Au collisions from STAR (green points) [123] and PHENIX (blue points) [87, 124] and for Pb-Pb collisions from ALICE (red points) [89, 125]. . . . . 43
2.20 *Left panel:* Dependence on transverse momentum of the nuclear modification factor for the $\Upsilon(1S)$ and $\Upsilon(2S)$. *Left panel:* Dependence on multiplicity of the nuclear modification factor for the $\Upsilon(1S)$, $\Upsilon(2S)$ and $\Upsilon(3S)$. . . . . 45

3.1 Schematic view of an open quantum system . . . . . 49
3.2 Global picture of the open quantum systems evolution . . . . . 53

3.3 Main steps and assumptions of the derivation of a Lindblad equation 58
3.4 Evolution of the quarkonium states populations over time (left) and (right) comparison of ratios of bottomonium populations obtained with the master equation (symbols) and with expected Boltzmann distributions (solid) . . . . . 59
3.5 Evolution of the populations of quarkonium states over time obtained with the stochastic potential model . . . . . 60
3.6 Weights of the lowest 3 vacuum eigenstates for different temperatures and initial states without friction and stochastic forces (solid lines) and with friction and stochastic forces (dashed and thick lines, respectively with the vacuum and temperature dependant potentials) . 61
3.7 Occupation number of the ground and 1st excited state over time (left). Occupation number of the ground and 1st excited state over time with and without dissipation (right). . . . . 63
3.8 *Left panel:* Bottomonium $R_{AA}$ for the 30-50% class of centrality. *Right panel:* Same for the 50-100% class of centrality. The error bands are due to unconstrained transport coefficients used in the computation. 64
3.9 *Left panel:* $R_{AA}$ as a function of the number of participants for the first three Y states computed from coupled Boltzmann equations and compared to experimental data in $\sqrt{s_{NN}} = 2.76$ TeV Pb-Pb collisions. *Right panel:* $R_{AA}$ as a function of the number of participants for the $\Upsilon(2S)$ and $\chi_b(1P)$ states computed from coupled Boltzmann equations. 65
3.10 *Top left panel:* Fraction of surviving pairs at T = 150 MeV for 2, 10 and 50 initial pairs. *Top right panel:* Same for T = 190 MeV. *Bottom left panel:* Same for T = 220 MeV. *Bottom right panel:* Fraction of surviving pairs at T = 190 MeV for 10 initial bottomonium or charmonium pairs . . . 66

5.1 Real part of the potential for different temperatures in GeV (Left panel). Imaginary part of the potential for different temperatures in GeV (Right panel). . . . . 122
5.2 One-dimensional potential at different temperatures for the charmonia (left panel) and for the bottomonia (right panel). . . . . 123

5.3 (Left panel) Charmonium mass spectrum of the S states for the one-dimensional potential (solid lines) obtained from the expectation values of the Hamiltonian compared to the three-dimensional case (dashed lines). (Right panel) Same for the bottomonia. . . . . 124
5.4 (Left panel) Comparison of the root-mean-square radiuses of the charmonium S states obtained with the one and three-dimensional potentials. (Right panel) Same for the bottomonia. . . . . 124
5.5 (Left panel) Imaginary part of the one-dimensional potential for the bottomonia. (Right panel) Large distance behaviour of the imaginary part of the one and three-dimensional potentials for the bottomonia. 125
5.6 (Left pannel) Charmonium decay widths obtained with the one and three-dimensional potentials. (Right pannel) Same for bottomonia. . 126
5.7 Spectral decomposition of the imaginary part of the potential $\mathrm{Im}V^{1\mathrm{D}} = \alpha\,\mathrm{Im}V_c^{1\mathrm{D}} + \beta\,\mathrm{Im}V_s^{1\mathrm{D}}$ at different temperatures (in GeV) for the (left pannel) charmonia and (right pannel) bottomonia. . . . . 127
5.8 Evolution in time of $\mathrm{Tr}\,[\mathcal{D}_0(0)] - \mathrm{Tr}\,[\mathcal{D}_0(t)]$. . . . . 132
5.9 $\mathrm{Tr}\,[\mathcal{D}_0(0)] - \mathrm{Tr}\,[\mathcal{D}_0(20)]$ for $\Delta s = 0.04$,0.05,0.1 and 0.2 fm, with $s_{max} =$ 10 fm and $\Delta t = 0.1$ fm/c. . . . . 133
5.10 $\mathrm{Tr}\,[\mathcal{D}_0(0)] - \mathrm{Tr}\,[\mathcal{D}_0(20)]$ for $\Delta s = 0.02$,0.04 and 0.05 fm, with $s_{max} =$ 5 fm and $\Delta t = 0.1$ fm/c. . . . . 134
5.11 $\mathrm{Tr}\,[\mathcal{D}_0(0)] - \mathrm{Tr}\,[\mathcal{D}_{20}(0)]$ for $s_{max} = 2$,5 and 10 fm, with $\Delta s = 0.05$ fm and $\Delta t = 0.1$ fm/c. . . . . 135
5.12 $\mathrm{Tr}\,[\mathcal{D}_0(0)] - \mathrm{Tr}\,[\mathcal{D}_{20}(0)]$ for $s_{max} = 10$,15,20 and 25 fm, with $\Delta s =$ 0.1 fm and $\Delta t = 0.1$ fm/c. . . . . 135
5.13 $\mathrm{Tr}\,[\mathcal{D}_0(0)] - \mathrm{Tr}\,[\mathcal{D}_0(20)]$ for $\Delta t = 10^{-1}$, $10^{-2}$ and $10^{-3}$ fm/c, with $s_{max} = 10$ fm and $\Delta s = 0.05$ fm. . . . . 136
5.14 Cumulated distribution of the eigenvalues of $\mathcal{D}_s$ at $t$ = 20 fm/c with (blue line) and without (orange line) the $\mathcal{L}_4$ terms. . . . . 138
5.15 Projections on vacuum eigenstates for T = 300 MeV. . . . . 139

6.1 Evolution over time of the deviation from the equilibrium value of the trace of $\mathcal{D}_s$ (blue curves) and $\mathcal{D}_o$ (orange curves) for an initial singlet state (solid curves) and octet state (dotted curves). . . . . 142

6.2 Evolution over time of the deviation from the equilibrium value of the trace of $\mathcal{D}_s$ (blue curves) and $\mathcal{D}_o$ (orange curves) for an initial S-like singlet state, at T = 200 MeV (solid curves), 300 MeV (dotted curves) and 400 MeV (dashed curves). . . . . 143
6.3 Evolution over time of the weights of the first three vacuum eigenstates at T = 300 MeV in the QED-like case (solid curves) and in the QCD case (dotted curves) . . . . . 145
6.4 Evolution of the singlet density matrix $\mathcal{D}_s$ over time. From top left panel to bottom right panel: 0.1, 1, 5, 10, 15 and 20 fm/c . . . . . 146
6.5 *Left panel:* Evolution of the singlet density matrix $\mathcal{D}_s$ over time along the s= s′ axis. *Right panel :* Same along the s = -s′ axis . . . . . 147
6.6 Wigner transforms at different values of $\frac{s+s'}{2}$ and time. Three types of distributions appear: gaussian and positive Wigner distributions (top left panel), non-gaussian but still positive distributions (top right panel) and negative distributions (bottom panel). . . . . 148
6.7 Evolution of the mean squared momentum $\sqrt{\langle p^2 \rangle}$ over time at different values of $\frac{s+s'}{2}$. . . . . 149
6.8 Evolution of the singlet density matrix $\mathcal{D}_s$ over time. From left panel to right panel: 1, 10 and 20 fm/c. From top to bottom: medium temperature of 200 MeV, 300 MeV and 400 MeV . . . . . 150
6.9 *Left panel:* Evolution of the mean squared momentum $\sqrt{\langle p^2 \rangle}$ over time at different values of $\frac{s+s'}{2}$ for T = 200 MeV. *Right panel:* Same for T = 400 MeV. . . . . 151
6.10 Evolution of the mean squared momentum $\sqrt{\langle p^2 \rangle}$ for different values of $\frac{s+s'}{2}$ at t = 15 fm/c for a medium temperature T = 200, 300 and 400 MeV. For each temperature, the corresponding value of $\sqrt{\frac{MT}{2}}$ is shown by the dashed lines. . . . . 152
6.11 Evolution of the singlet density matrix $\mathcal{D}_s$ over time. From top left panel to bottom right panel: 0.1, 1, 5, 10, 15 and 20 fm/c . . . . . 153
6.12 *Left panel:* Evolution of the singlet density matrix $\mathcal{D}_s$ over time along the s= s′ axis. *Right panel :* Same along the s = -s′ axis . . . . . 154
6.13 Wigner distributions at $\frac{s+s'}{2}$ = 0 fm at different times. . . . . 154
6.14 Evolution of the mean squared momentum $\sqrt{\langle p^2 \rangle}$ over time at different values of $\frac{s+s'}{2}$. . . . . 155

6.15 *Left panel:* Evolution over time of the weights of the first three vacuum eigenstates with an initial 1S-like singlet state at T = 200 (solid curves), 300 (dotted curves) and 400 MeV (dashed curves). *Right panel:* Same but zoom on late time evolution. . . . . 156
6.16 *Left panel:*Evolution over time of the weights of the first three vacuum eigenstates at T = 300 MeV with an initial 1P-like singlet state. *Right panel:* Same with an initial 2S-like singlet state. . . . . 157
6.17 Evolution over time of the weights of the first three vacuum eigenstates at T = 300 MeV with an initial 1S-like singlet state (solid lines) and an initial P-like octet state (dotted lines). . . . . 158
6.18 Evolution over time of the weights of the first three vacuum eigenstates at T = 300 MeV with an initial 1S-like singlet state with a total pair momentum $p_{tot}$ = 0, 5 and 10 GeV. . . . . 159
6.19 *Left panel:*Evolution over time of the weights of the first three vacuum eigenstates for T = 200 MeV with (solid lines) and without (dashed lines) the $\mathcal{L}_4$ terms. *Right panel:* Same for T = 300 MeV. . . . . 160
6.20 Evolution over time of the weights of the first three vacuum eigenstates with an initial 1S-like singlet state with an initial medium temperature $T_0$ = 600 MeV. . . . . 161
6.21 Evolution of the singlet density matrix $\mathcal{D}_s$ over time with an initial temperature $T_0$ = 600 MeV. From top left panel to bottom right panel: 0.1, 1, 5, 10, 15 and 20 fm/c . . . . . 162
6.22 Evolution of the singlet density matrix $\mathcal{D}_s$ along the s = s′ axis over time for a medium with initial temperature $T_0$ = 600 MeV and for a medium with fixed temperature T = 300 MeV. From top left panel to bottom right panel: 0.1, 1, 5, 10, 15 and 20 fm/c. . . . . 163
6.23 Evolution of the mean squared momentum $\sqrt{\langle p^2 \rangle}$ over time at different values of $\frac{s+s'}{2}$ with an initial temperature $T_0$ = 600 MeV. . . . . 163

A.1 Diagrams representing the different types of terms we can encounter in the equations. [2] . . . . . 171

B.1 Principales étapes et hypothèses de la dérivation d'une équation de Lindblad . . . . . 181

B.2 *Gauche:* Partie réelle du potentiel à une dimension pour les bottomonia. *Droite:* Partie imaginaire du potentiel à une dimension pour les bottomonia. . . . . 184
B.3 Evolution au cours du temps des poids des trois premiers états propres du vide pour T = 300 MeV dans le cas sans (lignes pleines) et avec degrés de liberté de couleur (lignes pointillées) . . . . . 186
B.4 Evolution de l'opérateur densité singulet $\mathcal{D}_s$ au cours du temps. De haut en bas et de gauche à droite: 0.1, 1, 5, 10, 15 et 20 fm/c . . . . . 186
B.5 Evolution de l'impulsion carrée moyenne $\sqrt{\langle p^2 \rangle}$ au cours du temps pour différentes valeurs de $\frac{s+s'}{2}$. . . . . 187
B.6 Evolution au cours du temps des poids des trois premiers états propres du vide pour un état initial singulet type 1S, pour une température T = 200 (lignes pleines), 300 (lignes pointillées) et 400 MeV (lignes discontinues) . . . . . 188
B.7 Evolution au cours du temps des poids des trois premiers états propres du vide pour une température T = 300 MeV pour un état initial singulet type 1S (lignes pleines) et un état initial octet type P (lignes pointillées). . . . . 189
B.8 Evolution au cours du temps des poids des trois premiers états propres du vide pour une température initiale $T_0$ = 600 MeV pour un état initial singulet type 1S . . . . . 190

# List of Tables

2.1 Dissociation temperatures obtained from $\mathcal{L}$QCD calculations [94] with $T_C = 172.5$ MeV. Only an upper limit is given for the $\Upsilon(2S)$ and $\Upsilon(4S)$ due to the lack of data below this limit. . . . . 40

4.1 Summary of the terms contained in the minimal set . . . . . 116

5.1 Parameters for the real part of the 1D potential $\mathrm{Re}V_{\mathrm{1D}}$. . . . . 123
5.2 Coefficients for the imaginary part of the one-dimensional potential $\mathrm{Im}V^{\mathrm{1D}}$. 125
5.3 Values of $\mathrm{Tr}\left[\mathcal{D}_0(0)\right] - \mathrm{Tr}\left[\mathcal{D}_0(20)\right]$ for two different configurations . . 137
5.4 Parameters used for the resolution of the equations . . . . . 137

6.1 Values of the timescale $\tau$ for T = 200, 300 and 400 MeV. . . . . 144

# Introduction

It is theorized that under extreme temperatures and/or densities, such as the ones of the early Universe, nuclear matter reaches a new state, composed of deconfined quarks and gluons (while they are confined in usual hadronic matter), called Quark-Gluon Plasma (QGP). In the last forty years, theoretical and experimental physicists have carried an intensive study of the existence and the properties of this new state of matter. The only way on Earth to produce a QGP is to collide heavy ions at ultrarelativistic speeds in colliders like the *Relativistic Heavy Ion Collider* (RHIC) or the *Large Hadron Collider* (LHC). An observable of choice for the study of the Quark-Gluon Plasma is the so-called *quarkonia suppression*, which corresponds to a smaller production of quarkonia ( heavy $Q\bar{Q}$ composite particles) in heavy ion collisions compared to proton-proton collisions. This phenomenon, predicted in 1986 by Matsui and Satz [1], was studied intensively at colliders, where experiments revealed that the suppression is a very complex process, requiring a robust theoretical understanding. In recent years, a lot of work has been done towards a dynamical description of heavy quarkonia inside the QGP, using the open quantum systems formalism. In this framework, one can get a real-time description of a quantum system (the quarkonium) in interaction with a thermal bath (the QGP) by studying the system reduced density matrix. In this thesis we present an approach based on open quantum systems that aims at describing the dynamics of a heavy quarkonium inside the Quark-Gluon Plasma. The thesis is structured as follows:

The first chapter is focused on an introduction to the Standard Model of particles physics and to the Quark-Gluon Plasma. We first discuss the contents of the Standard Model and describe the theory of strong interactions, called Quantum Chromodynamics (QCD), and describe composite particles called quarkonia, and their production. We then explore the phase diagram of nuclear matter to introduce the Quark-Gluon Plasma, before describing how it is produced experimentally and finally review several observables used to study it.

The second chapter is dedicated to quarkonia suppression. We first describe the physical effects at play before reviewing experimental measurements on suppression at current colliders. In a second part, we present several model that aims at describing quarkonia suppression. We present their approaches, compare them to experimental results and discuss their assumptions.

In chapter 3, we present the open quantum systems (OQS) formalism. We describe the basics of this framework and show how to derive quantum master equations within it. We then review existing approaches based on the OQS formalism and focus on a specfic one developped by Blaizot & Escobedo [2] describing the dynamics of a $Q\bar{Q}$ pair in the QGP, which is the basis of this thesis work. In order to motivate our work, we discuss the shortcomings of their approach/

We present in chapter 4 the theoretical developments done during this thesis. We extend the equations derived by Blaizot & Escobedo to ensure they satisfy key properties of well-defined quantum master equations. We then prove that the equations satisfy unitarity and positivity and propose a strategy to get rid of divergences present in the equations.

The numerical strategy to resolve the equations is presented in chapter 5. We present the one-dimensional equations that will be resolved and a new potential, tailored for one-dimensional studies. We present the Crank-Nicolson method that will be used and determine numerical parameters by analyzing the numerical conservation of unitarity. We finish by briefly showing that positivity is satisfied numerically, validating the numerical implementation.

Finally in chapter 6, we resolve numerically the equations shown in chapter 5 to study the dynamics of a $c\bar{c}$ bar in the QGP, in the case of a medium with a fixed temperature and in the case of a cooling medium. In both cases, the $c\bar{c}$ pair density matrix is analyzed and the projection to vacuum eigenstates is done to study the evolution of the eigenstates weights.

# Chapter 1

# The Standard Model and the Quark-Gluon Plasma

This introductory chapter presents the basics of the Standard Model of particle physics and of an extreme state of matter called the Quark-Gluon Plasma (QGP). In the first section, the Standard Model of particle physics is briefly introduced, followed by an introduction to the theory of the strong interaction, called Quantum Chromodynamics (QCD). A focus on quarkonia and their production concludes the first section. In the second section, the QGP is introduced and several interesting probes used to study it are presented.

## 1.1 The Standard Model of particle physics

### 1.1.1 The Standard Model

Nowadays, it is known that matter is composed of molecules, which are composed of atoms, themselves composed of nuclei with electrons "orbiting" around them. It was then revealed, thanks to the experiments of Rutherford [3] and Chadwick [4], that nuclei are in fact composed of more elementary particles called protons and neutrons. First theorized by Gell-Mann [5] and Zweig [6], protons and neutrons were also revealed to be composed of smaller constituents, called quarks, which are (according to current knowledge) elementary particles. In parallel, the development of particle accelerators led to the discovery of many more composite particles, now called hadrons. In order to describe all known particles and their interactions, the Standard Model of particle physics was developped in the 70s. In this model, the particles are separated into two groups: bosons and fermions (see figure 1.1).

Bosons have an integer spin and are the mediators of the fundamental interactions. The photon ($\gamma$) is the mediator of the well-known electromagnetic interactions. The $W$ and $Z$ bosons are the mediators of the weak interaction, which is notably responsible for radioactive decays. Gluons ($g$) are the mediators of the strong interaction, which binds protons and neutrons inside the nuclei and also quarks inside hadrons. The Higgs boson is a special case as it does not mediate a specific interactions but gives their masses to elementary particles. Finally, a mediator for the gravitational force, called the graviton, may exist but is not yet observed. All bosons obey Bose-Einstein statistics as they have integer spins.

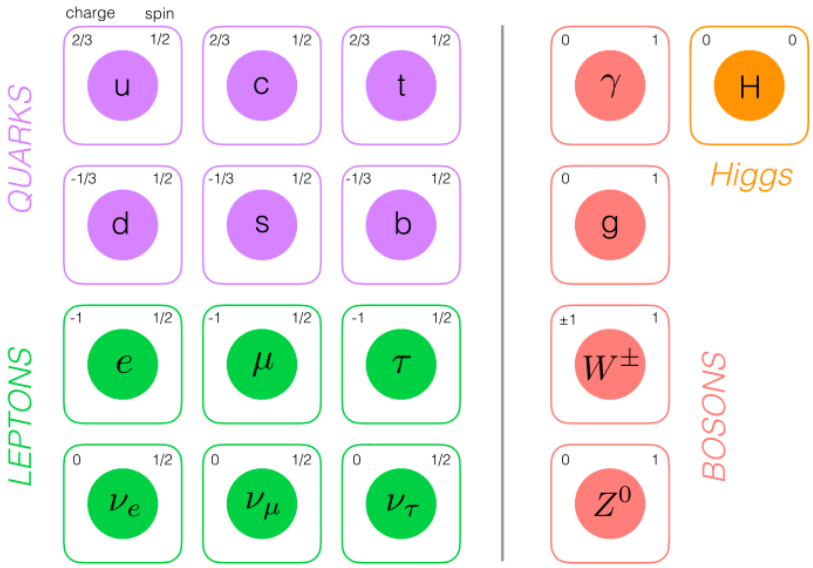


FIGURE 1.1 – Table of particles in the Standard Model. [7]

Fermions have a half-integer spin and compose matter. They are divided in 3 generations (or families) [8] with increasing masses. Each generation is composed of 2 quarks and 2 leptons, leading to 6 quarks (up, down, charm, strange, top and bottom) and 6 leptons (electron, muon, tau and their corresponding neutrinos). They all obey Fermi-Dirac statistics and must respect Pauli's exclusion principle. Due to the latter, two fermions can not be in the same quantum state. The existence of particles like the $\Delta^{++}$, which is composed of three up quarks, would obviously not respect it, therefore quarks must have another quantum number, called color [9]. Each quark carry a color (either blue, red or green by analogy with visible colors), which is the charge of the strong interaction (similar to the electric charge for the

electromagnetic interaction).

Through the years, the Standard Model was tested to a very high precision level and predicted many particles that were later discovered in particles accelerators and colliders such as the Higgs boson. [10, 11] However, while the Standard Model is undoubtedly successful, it also has its flaws. It can not describe gravitation or explain (among other important questions) neutrino oscillations [12, 13] and the matter-antimatter asymmetry in the universe, which indicates that it is a not a complete theory.

On a more formal aspect, the Standard Model is a relativistic quantum field theory [14] where dynamical fields describe particles. The interactions are related to the field gauge symmetries, which are internal transformations under which a Lagrangian is invariant. The work of Yang and Mills on gauge invariance [15] allowed to define a gauge symmetry under which the Standard Model is invariant: SU(3) $\times$ SU(2) $\times$ U(1). The U(1) symmetry is the basis for the electromagnetic interaction, the SU(2) symmetry is the basis for the weak interaction and the SU(3) symmetry is the basis for the strong interaction. The dynamics and interactions of particles are described by the Lagrangian of the Standard Model $\mathcal{L}_{SM}$, from which cross-sections for physical processes can be calculated. In this thesis, we will only focus on the strong interaction. However, the open quantum systems formalism that will be presented in chapter 3 go beyond this interaction, as it was originally used in condensed matter physics and quantum chemistry, which are based on Quantum Electrodynamics (QED), the theory of the electromagnetic interaction.

### 1.1.2 Quantum Chromodynamics

Within the Standard Model, the strong interaction is described by Quantum Chromodynamics (QCD) [16], which describes the dynamics of partons (quarks and gluons) and their interactions. As mentionned in section 1.1.1, quarks are represented by quarks fields denoted $\psi^i_j$, where $i$ goes from 1 to $N_c$ the number of colors (i.e. $N_c = 3$) and $j$ goes from 1 to $N_f$ the number of quark flavors (i.e. $N_f = 6$). The free quark field,

$$\psi_j = \begin{pmatrix} \psi_j^1 \\ \psi_j^2 \\ \psi_j^3 \end{pmatrix}, \tag{1.1}$$

Lagrangian writes [17, 18]:

$$\mathcal{L}_{free} = \bar{\psi}_j \left( i\gamma^\mu \partial_\mu - m_j \right) \psi_j, \tag{1.2}$$

where sums on $j$ and $\mu$ (a Lorentz index) are implicit.

The QCD Lagrangian has to be invariant under the SU(3) color gauge symmetry transformation:

$$\psi_j(x) \to \tilde{\psi}_j(x) = e^{-\theta^a(x) T^a} \psi_j(x), \tag{1.3}$$

where $a$ runs from 1 to 8, $\theta^a$ are real functions and $T^a$ the generators of the SU(3) group (related to the Gell-Mann matrices $\lambda^a$ by $T^a = \frac{\lambda^a}{2}$), defined by:

$$\left[ T^a, T^b \right] = i f^{abc} T^c, \tag{1.4}$$

with $f^{abc}$ the structure constants of SU(3).

However, the free quark Lagrangian defined as in equation (1.2) is not invariant under such transformation. To obtain the invariance, the $\partial_\mu$ derivative must be replaced by the covariant derivative:

$$D_\mu = \partial_\mu - i g_s T_a G_\mu^a, \tag{1.5}$$

where $g_s = \sqrt{4\pi\alpha_s}$ is the gauge coupling parameter and $G_\mu^a$ the eight gauge fields corresponding to gluons. This transformation leads to the introduction of interactions terms between quarks and gluons.

One also needs to add the gauge invariant Lagrangian for gluonic field, defined as:

$$\mathcal{L}_g = -\frac{1}{4} F^a_{\mu\nu}(x) F^{\mu\nu}_a(x), \tag{1.6}$$

where sums over $\mu$,$\nu$ and $a$ are implied. $F^a_{\mu\nu}$ is the gluonic field tensor, defined as:

$$F^a_{\mu\nu} = \partial_\mu G^a_\nu - \partial_\nu G^a_\mu - g_s f^{abc} G^b_\mu G^c_\nu. \tag{1.7}$$

The first two terms of the right-hand side of equation (1.7) describe the gluon free dynamics and are equivalent to the terms in the electromagnetic field tensor $F_{\mu\nu}$ in Quantum ElectroDynamics (QED). The last term describes the gluon self-interactions, arising from the non-Abelian nature of SU(3) (see equation (1.4)). The QCD Lagrangian thus writes:

$$\mathcal{L}_{QCD} = \bar{\psi}_j \left( i\gamma^\mu D_\mu - m_j \right) \psi_j - \frac{1}{4} F^a_{\mu\nu} F^{\mu\nu}_a. \tag{1.8}$$

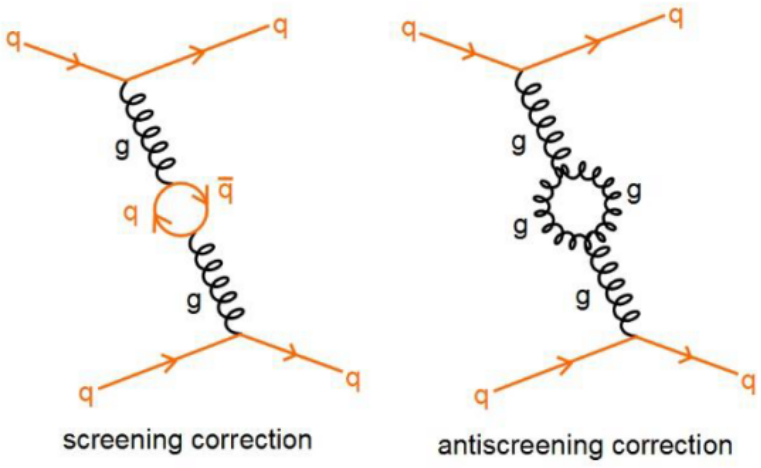


FIGURE 1.2 – *Left panel:* Gluon splitting into a virtual pair of quarks leading to screening. *Right panel:* Gluon self-interaction leading to antiscreening. [19]

The gluon self-interactions have important consequences on the properties of the strong interaction. When a gluon is exchanged during an interaction between two

colored particles, it is possible that the gluon splits into a virtual pair of quarks (see figure 1.2) at next-to-leading order (NLO) in the perturbative expansion. However, it can also self-interact (unlike the photon in QED for example), leading to different effects. In the case of a splitting into a virtual quark pair, the interactions between two partons will be screened [1] while in the case a gluon self-interacts and splits into a virtual gluon pair, antiscreening effects will arise. This leads to a modification of the interaction coupling and to the well-known "running" of the QCD coupling "constant" with respect to the energy transfered $Q$ between the two color charges (see figure 1.3) [2].

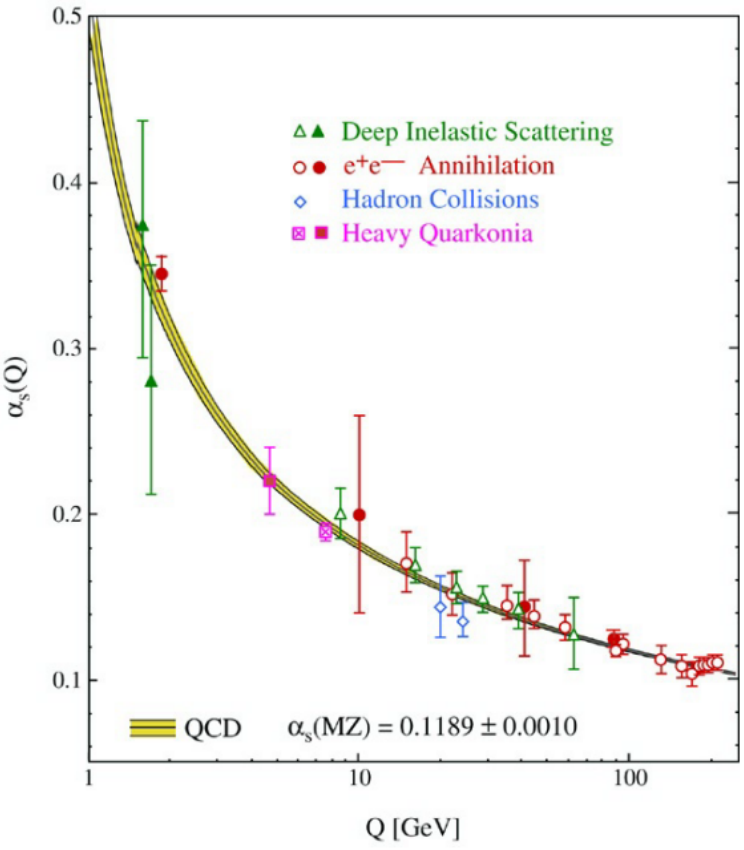


FIGURE 1.3 – QCD coupling constant as a function of the transfered energy Q between two color charges [20]

Two regimes can be observed, separated by the typical QCD energy scale $\Lambda_{QCD} \sim$

1. A similar effect exists in QED, where a photon creates a loop of charged particles, screening the electromagnetic interaction between two charged particles

2. The running of the coupling constant is also observed in QED, but in that case the coupling decreases at large distance, while it increases in QCD.

200 MeV:

— At high energies ($Q \geq \Lambda_{QCD}$) or small coupling constant ($\alpha_s \leq 1$), perturbative QCD (pQCD) can be applied. When $Q \gg \Lambda_{QCD}$, one reaches the asymptotic freedom regimes, where the interaction between two colored particles becomes weak. The color charges can then behave as if they were free (in the limit $Q \to \infty$).

— At low energies ($Q \leq \Lambda_{QCD}$) or large coupling constant ($\alpha_s \geq 1$), pQCD can not be applied anymore as the interaction becomes highly non-linear and the coupling is not small anymore. Non-perturbative methods, such as Lattice QCD ($\mathcal{L}$QCD), are needed. In this regime, partons are confined inside hadrons and can not be observed individually, a phenomenon known as confinement. In the Lund model [21] this is described as a consequence of the breaking of a gluon string into a quark-antiquark pair (see figure 1.4 . The interaction between two partons becoming stronger and stronger with increasing distance, it is more favorable energy-wise to create a pair, therefore converting the energy accumulated in the string.

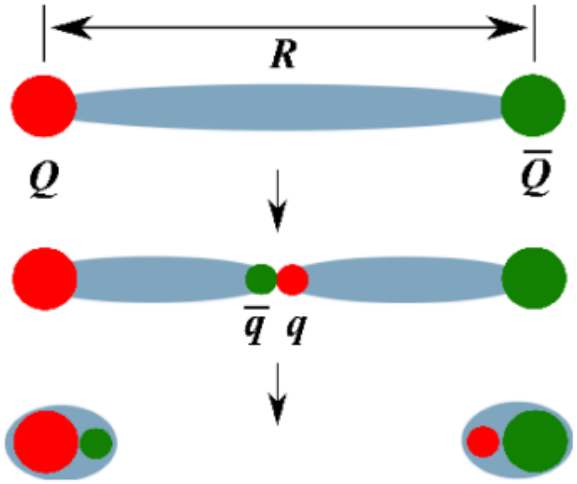


FIGURE 1.4 – Illustration of the gluon string breaking, leading to two new composite systems. [22]

Perturbative QCD allows expansions in power of $\alpha_s$ as $\alpha_s$ should be small where pQCD is applicable. For a given process, one should take into account all possible

Feynmann diagrams to obtain a precise prediction. The very high number of possible diagrams due to gluon self interactions (compared to QED) limits the order that can be attained in the perturbative expansion, thus limiting the precision of results even more than for pure QED processes. pQCD is usually considered applicable for energy scales superior to a few GeV.

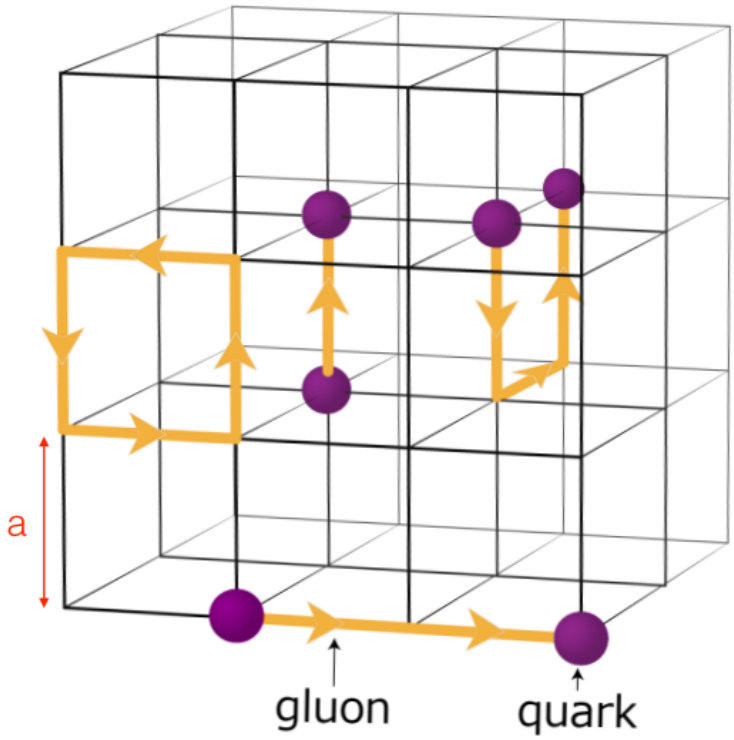


FIGURE 1.5 – Representation of the lattice used to discretize space-time in Lattice QCD. [7]

The Lattice QCD method was proposed in 1974 by Wilson [23] and explores the non-perturbative regime of QCD by numerically calculating Feynman's path integrals [24]. The principle of $\mathcal{L}$QCD is to discretize QCD on a four-dimensional Euclidian lattice[3] with step size $a$. Quark fields are situated on the the nodes of the lattice while gluon field propagate on the links between the nodes (see figure 1.5). The state of the system can be accessed through the partition function:

$$Z = \int [dx] e^{-S}, \tag{1.9}$$

3. This requires to perform a Wick rotation on the time variable, which limits the applicability of the method

where $S = \int d^4xL$ is the action. Note that due to the discretization procedure, $L$ is not the QCD Lagragian. However the action $S$ is discretized in such way that in the limit $a \to 0$, it is the QCD action.

Monte-Carlo algorithms can then evaluate the path integral by obtaining the most probable field configuration. $\mathcal{L}$QCD computations are thus very costly in terms of numerical computing power, limiting the lattice grid size and step available, therefore increasing the uncertainties on $\mathcal{L}$QCD results. Fortunately, the increasing computing power and new action modelizations help to reduce those uncertainties.

### 1.1.3 Quarkonia

Quarkonia are flavorless heavy mesons composed of a heavy quark and its own antiquark. Bound states composed of a charm and an anticharm quark are called *charmonia* while the states composed of a bottom and an antibottom quark are called *bottomonia*. Quarkonia composed of a top quark and antiquark (a topponia) are not expected to exist as the top quark decays too quickly to form a bound state due to its large mass. The mass spectra of charmonia and bottomonia are shown in figure 1.6.

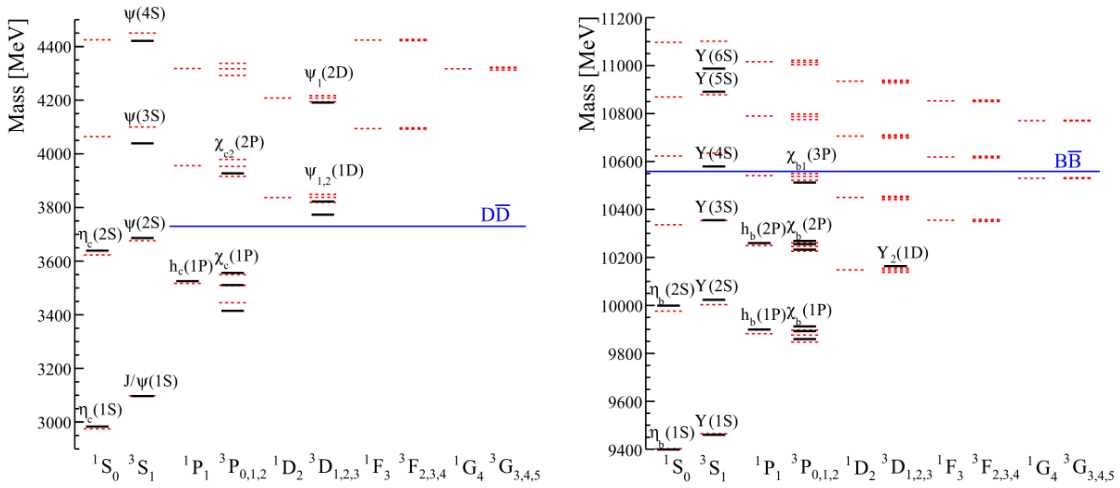


FIGURE 1.6 – *Left panel:* Mass spectrum of charmonia states. *Right panel:* Same for bottomonia states. [25]

**Quarkonium production**

The production of quarkonia involves perturbative and non-perturbative aspects of QCD. The production of the $Q\bar{Q}$ pair that will form the quarkonium is expected to be a perturbative process while its binding into a quarkonium is non-perturbative. In most of the models describing quarkonium production, a factorization between the pair production and its binding into a quarkonium is involved. Different approaches exist, mainly differing in their treatment of hadronization.

The Color Evaporation Model (CEM) [26, 27] connects the cross-section to produce a quarkonium to the cross-section to produce a $Q\bar{Q}$ pair in a range in invariant mass where hadronization into a quarkonium is expected to be possible. This range is between $2m_{\mathrm{q}}$ (the quark pair production mass threshold) and $2m_{\mathrm{H}}$ (the lightest open-heavy flavor hadron pair mass threshold). Therefore, one can express the cross-section as:

$$\sigma_{\Phi} = F_{\Phi} \int_{2m_{\mathrm{q}}}^{2m_{\mathrm{H}}} \frac{d\sigma_{Q\bar{Q}}}{dm_{Q\bar{Q}}} dm_{Q\bar{Q}}, \tag{1.10}$$

with $F_{\Phi}$ a phenomenological factor related to the probability that a pair hadronizes in the state $\Phi$. An example of such factor can be found in [28]. A factorization between the $Q\bar{Q}$ pair production and its binding is implied but do not rely on a factorization proof.

The Color Singlet Model (CSM) [29, 30] assumes that the quantum state of the pair do not evolve between its production and its hadronization. Assuming that quarkonia are non-relativistic bound states, the production cross-section can be expressed as the product of the production cross-section of a $Q\bar{Q}$ pair in a color singlet state with zero relative velocity and the same quantum numbers as the considered quarkonium state (i.e. for a $J/\Psi$, we have a $c\bar{c}$ pair with quantum numbers L = 0, J = 1 and S = 1) and of the square of the quarkonium wave function at the origin. The cross-section thus writes:

$$\sigma_{\Phi} = \sigma_{Q\bar{Q}} |\Psi_{\Phi}(0)|^2 \tag{1.11}$$

In the case of P-wave states, $|\Psi_{\Phi}(0)|^2$ obviously vanishes and its derivative $|\Psi'_{\Phi}(0)|^2$ should be used instead. Furthermore, when treating the decay of P-waves, the

CSM is affected by infrared divergences, which can be cured in the framework of Non-Relativistic QCD (NRQCD)

NRQCD [31, 32] is a rigorous effective field theory of QCD, based on the factorization of soft and hard scales, with a scale hierarchy $Mv^2 \gg Mv \gg \Lambda_{QCD} << M$. $v$ is the typical velocity if the heavy quark in the quarkonium rest frame ($v^2 \sim 0.3$ for the charmonium and $v^2 \sim 0.1$ for the bottomonium), $Mv$ is the typical momentum of the heavy quark in the quarkonium rest frame and $Mv^2$ is the binding energy of the quark and antiquark. In the NRQCD framework, the production cross-section is expressed in the following way:

$$\sigma_{\Phi} = \sum_{n} \sigma_{Q\bar{Q}[n]} \left\langle O^{\Phi}[n] \right\rangle , \tag{1.12}$$

with $\sigma_{Q\bar{Q}[n]}$ the production cross-section of a $Q\bar{Q}$ pair in the Fock state $n$ (which can be a color-octet state) and $\left\langle O^{\Phi}[n] \right\rangle$ long distance matrix elements (LDMEs) describing the hadronization $Q\bar{Q}[n] \rightarrow \Phi$, which are universal and extracted from experimental data.

Experimentally, the production of quarkonia can be separated in *non-prompt* production (only for charmonia) from the decays of B mesons and bottomonia and in *prompt* production, either from hadronization of $Q\bar{Q}$ pairs (so-called *direct* production) or from "feed-down" (decays) of excited quarkonia states. The contribution of direct production and feed-downs for the $J/\Psi$ and $\Upsilon$(1S) is shown in figure 1.7.

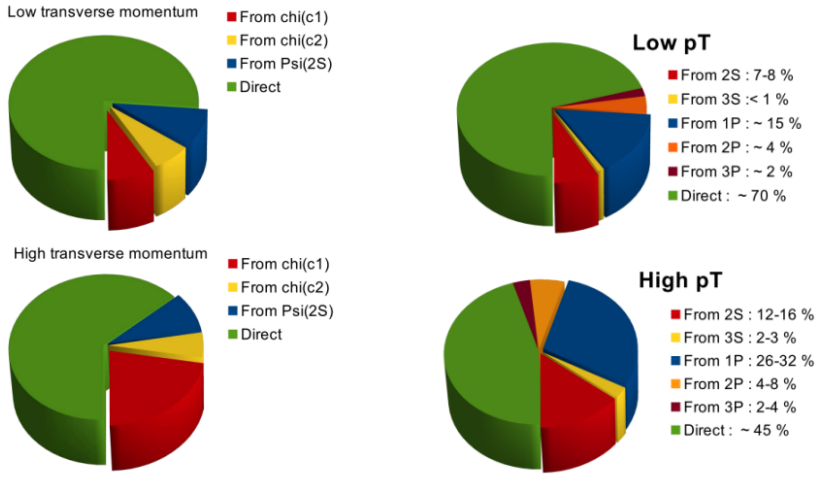


FIGURE 1.7 – *Left panels:* Sources of prompt $J/\Psi$. *Right panels:* Sources of prompt $\Upsilon$(1S). [33]

## 1.2 The Quark-Gluon Plasma

QCD is well tested in the perturbative regime but less in the non-perturbative regime. The Quark-Gluon Plasma (QGP) is a unique system to test the strong interaction and QCD predictions. Notably, QGP physics allow to study the equation of state of nuclear matter for high energy densities or the interactions between partons and a colored medium.

### 1.2.1 Phase diagram of the nuclear matter

To study the different phases of nuclear matter and the transitions between them, one can study its phase diagram. This phase diagram, represented on figure 1.8, is parametrized by two quantities: the temperature $T$ and the baryon chemical potential $\mu_B$.[4] As said in section 1.1, under normal conditions of temperature and baryon chemical potential, quarks and gluons are confined inside hadrons. However, QCD predicts that at extreme temperature and/or baryon chemical potential, a new state of nuclear matter exists, called the *Quark-Gluon Plasma* , where quarks and gluons are deconfined. This new phase of matter is supposed to be the state

4. The baryon chemical potential translates the change in free energy with respect to a change in baryon number composition.

of the universe a few microseconds after the Big Bang and may compose the core of neutron stars. Note that at very large chemical potential and low temperature, a color superconducting phase called Color-Flavor Locking is predicted [34].

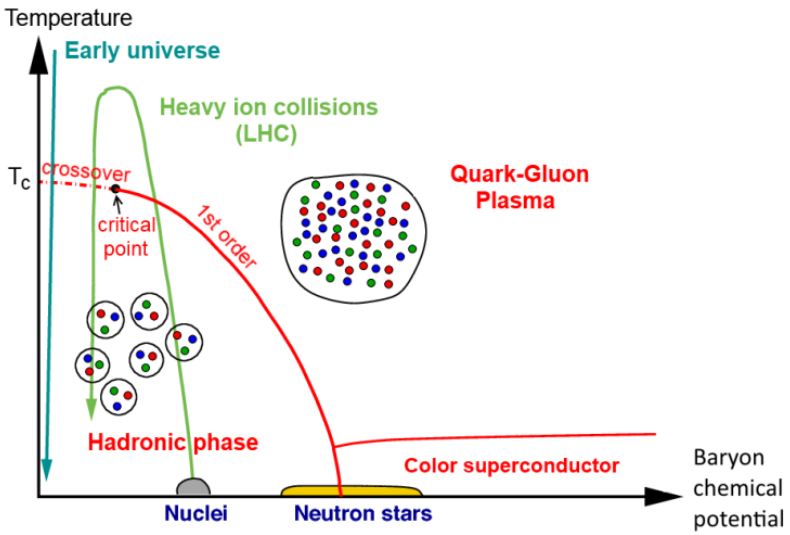


FIGURE 1.8 – Schematic view of the phase diagram of QCD as function of temperature and baryon chemical potential [19]

While it is impossible a priori to observe in Nature a Quark-Gluon Plasma, it is possible to produce small amounts of it at high-energy colliders (such as the *Relativistic Heavy Ion Collider* (RHIC) or the *Large Hadron Collider* (LHC)) in heavy ion collisions. As observed on figure 1.8, the QGP phase can exist at high temperatures but also at large values of $\mu_B$. The increase in temperature, and thus in energy, leads to a weaker coupling between partons, while the increase of the baryon chemical potential can be understood as an increase of the parton density, resulting in a larger net color charge density which leads to a screening of the interaction between the partons. The diagram predicts the existence of two types of transitions [35], a first order phase transition (discontinuity in the first derivative of the free energy), corresponding to a sudden phase transition and a *crossover*, corresponding to a smoother transition [5] where the medium is not purely hadronic nor deconfined. In all cases, the transition only occurs at a critical temperature $T_C$, which is estimated for example from Lattice QCD calculations [36] at $T_C \approx 175$ MeV at $\mu_B = 0$. The

5. Note however that a crossover is not a phase transition (in the Ehrenfest classification sense) as there are no discontinuities in the derivatives of the free energy, even though there is a change of phase.

point in the phase diagram separating the crossover and the first-order transition is called the *critical point* and its determination is an active field of research.

### 1.2.2 Heavy ion collisions

In order to produce a Quark-Gluon Plasma, extreme conditions of temperatures and/or density are needed. The only way to reach such conditions for now is to accelerate and collide heavy ions (U, Au, Pb, Cu....) at high energy colliders such as the RHIC and the LHC. The high amoiunt of nucleons contained in heavy ions and the ultrarelativistic velocities to which the ions are accelerated lead to the production of numerous particles in a very small volume which may satisfy the conditions required for the production of a deconfined state. If one assumes that a QGP is formed during a high-energy heavy ion collisions, the latter can be described by the Bjorken model [37], from the initial colliding ions to the hadrons observed in the experimental detectors (see figure 1.11. In this model, the collision is divided in 3 main phases phases: the pre-equilibrium phase, the expansion phase and the hadronization phase.

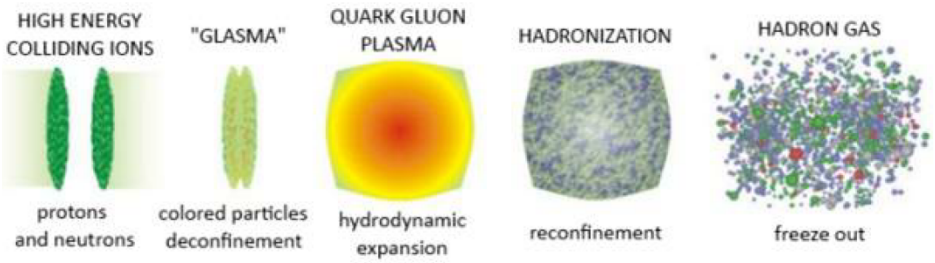


FIGURE 1.9 – Schematization of the whole evolution [19]

#### The initial collision and the pre-equilibrium phase

Due to relativistic effects, the initial ions are contracted along the beam axis, taking a "pancake" shape in the laboratory frame (see figure 1.10). The pre-equilibrium immediately follows the initial collision. This phase lasts for about 1 fm/c ($\sim 10^{-24}$ s) and it is during it that most hard processes occur and particles produced during this phase will witness the entire evolution and, as such, be interesting probes of the medium.

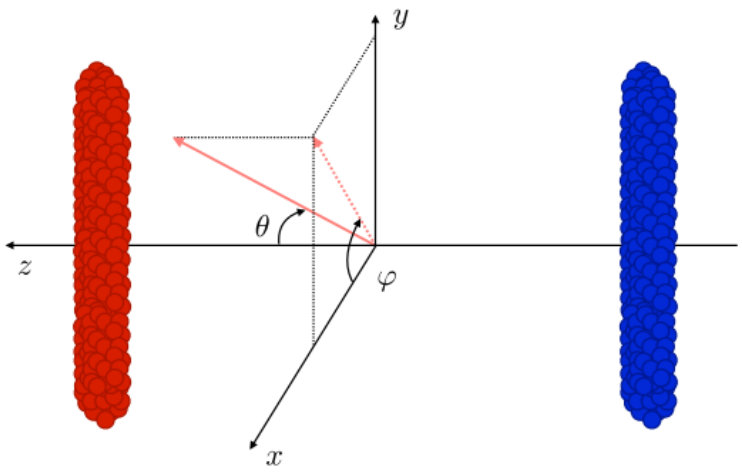


FIGURE 1.10 – Representation of the initial heavy-ion collision [7]

As the medium is not in thermal equilibrium during this phase, its theoretical description is difficult. Several models have been developped to describe the medium at the end of the pre-equilibrium phase:

— MC-Glauber [38]: Nuclei are described as ensembles of nucleons distributed according to a charge density distribution obtained experimentally.
— MC-KLN [39]: Based on the MC-Glauder model but incorporate the Color Glass Condensate (CGC) effective theory [40] which includes gluon saturation at small-$x$.
— IP-GLASMA [41]: Also based on the CGC, but also add fluctuations of color charges and partially treat the out-of-equilibrium evolution.
— Several transport models that evolves dynamically an out-of-equilibrium system to obtain initial conditions such as UrQMD [42] or EPOS [43].

**The QGP phase**

If the energy density is high enough, then a plasma is produced, which size depends on the initial energy density. This phase can last for up to 10 fm/c, depending on the initial size of the QGP. During it, interactions between partons occur, modifying their momentum distribution compared to collisions without formation of a QGP. At the same time, the medium expands quickly and brutally, expansion that can be described by hydrodynamical models [44, 45]. This expansion can last

up to 20 fm/c at current energies and lead to the progressive cooling of the QGP, until a critical temperature $T_C$ is reached, and a crossover occurs to an hadronic phase.

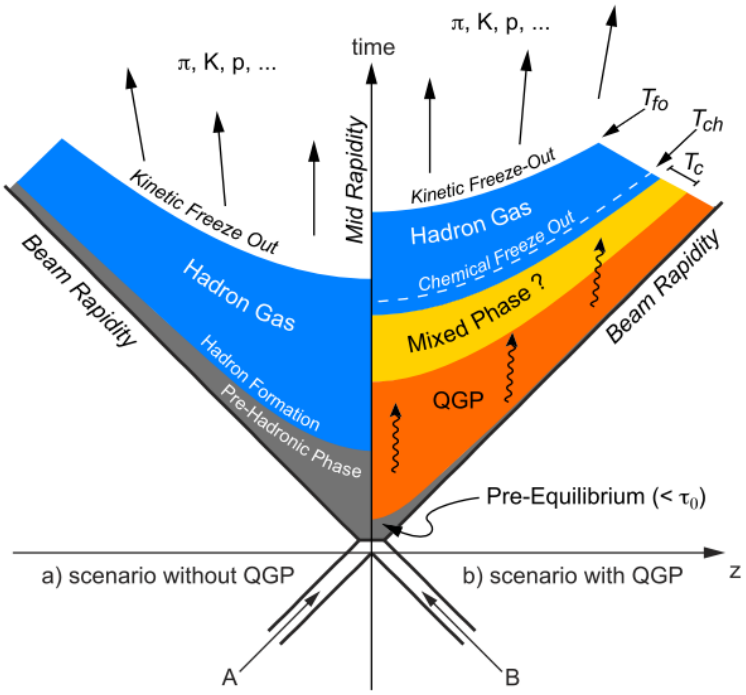


FIGURE 1.11 – Representation of the Björken scenario with and without a QGP phase [46]

### The hadronic phase

As the hadronic gas continues to cool down, it will first reach a chemical freeze-out temperature where the nature of particles is frozen as inelastic collisions stop. The gas finally reaches a kinetic freeze-out, where elastic collisions stop and the momentum distribution of particles is also frozen. The resulting hadrons can then propagate towards the detectors. For certain observables, it is necessary to take into account further interactions between hadrons, as it is done for example in the UrQMD model [42].

### 1.2.3 Probes of the QGP

We now present a list of probes used to study the Quark-Gluon Plasma in heavy ion collisions. They are usually separated into two categories: the *soft* probes, more affected by the physics near the freeze-out and the *hard* probes, which are known for being more sensitive to the plasma phase.

## Soft probes

#### Strangeness enhancement

It is one of the first proposed signatures of the formation of a QGP in nucleus-nucleus collisions [47, 48]. In proton-proton collisions, the production of strange hadrons is difficult. There are two ways of producing them:

— Direct production through $\pi\pi \rightarrow h\bar{h}$ processes. However, the production thresholds are quite high: 2.233 GeV for $\Lambda\bar{\Lambda}$, 2.642 GeV for $\Xi\bar{\Xi}$ and 3.344 GeV for $\Omega\bar{\Omega}$.

— Cascade production with the chain of processes: $\pi N \rightarrow K\Lambda$, $\pi\Lambda \rightarrow K\Xi$ and $\pi\Xi \rightarrow K\Omega$ (with $N$ denoting a nucleon). In this case the production thresholds are reduced (540, 560 and 710 MeV), but the production of multi-strange baryons is done through several processes, which is unlikely. [49]

However, in nucleus-nucleus collisions, to get strange hadrons in the final state, only the production of $s\bar{s}$ pairs is required, which only requires around 300 MeV as the strange quark mass gets smaller due to chiral symmetry restoration. On top of that, the gluon density in the deconfined phase is very high, favoring the production of a $s\bar{s}$ pair through gluon fusion $gg \rightarrow s\bar{s}$.[49] This should lead to an increase to the production of hyperons (strange baryons) in nucleus-nucleus collisions compared to proton-proton or proton-nucleus collisions.

Measurements at the LHC in Pb-Pb collisions of the production of hyperons and antihyperons, normalized by the production in p-Be collisions at the SPS showed an enhancement of the production of strange hadrons (see figure 1.12), interpreted as a sign of the presence of a QGP medium. This enhancement for greater for hadrons with multiple strange quarks (such as the $\Omega$) as they are less produced in p-Be collisions.

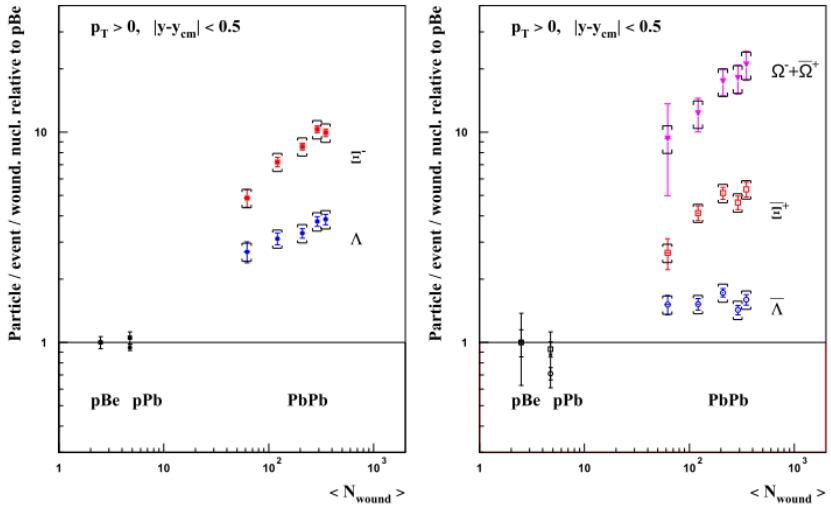


FIGURE 1.12 – Normalized production rates of hyperons and antihyperons in Pb-Pb collisions at $\sqrt{s_{NN}}$ = 17.3 GeV with respect to production rates in p-Be collisions measured by the NA57 experiment at the SPS [50]

### Thermal photons and leptons

The QGP medium radiates photons and $e^+e^-$ pairs (from pion annihilation $\pi\pi \rightarrow e^+e^-$) called *thermal* photons and leptons.[35, 51] This should lead to an excess in the mass invariant spectrum of $e^+e^-$ or transverse momentum $\mathbf{p}_T$ spectra of photons with respect to purely hadronic contributions. The NA54 experiment at the SPS measured the mass invariant spectrum of electron-positron pairs in p-p, p-Pb and Pb-Au collisions [52]. A good agreement in p-p and p-Pb collisions with predictions from hadronic processes was found and an excess at low masses was found for Pb-Au collisions. The PHENIX experiment at the RHIC measured an excess in the photon transverse momentum spectrum at low $\mathbf{p}_T$. [53] Those results indicate that a QGP medium is indeed formed in nucleus-nucleus collisions.

### Anisotropic flow

For peripheral collisions, the QGP medium has an almond shape (see figure 1.13). This induces a stronger pressure gradient in the reaction plane than elsewhere, which leads to different thrusts for partons depending on their distance to the reaction plane, resulting in an azimuthal anisotropy of the particle momentum distribution in the final state called *anisotropic flow*.

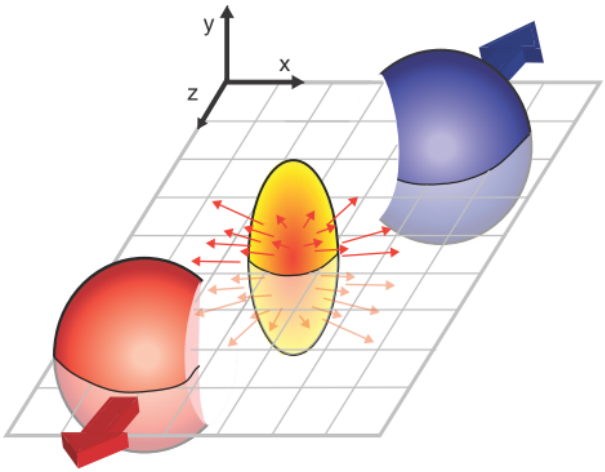


FIGURE 1.13 – Schematic view of a peripheral heavy ion collision. [7]

The final state particle yield can be decomposed as a Fourier series:

$$E\frac{d^3N}{d^3p} = \frac{1}{2\pi}\frac{d^2N}{p_T dp_T dy}\left(1 + \sum_{n=1}^{\infty} 2v_n \cos\left[n(\phi - \phi_{RP})\right]\right), \tag{1.13}$$

with $E$ the energy of the particle, $p$ its momentum, $p_T$ its transverse momentum, $\phi$ its azimuthal angle, $y$ the rapidity and $\phi_{RP}$ the reaction plane angle (see figure 1.14). The $v_n$ coefficients represent different anisotropies in the flow of particles in the medium.

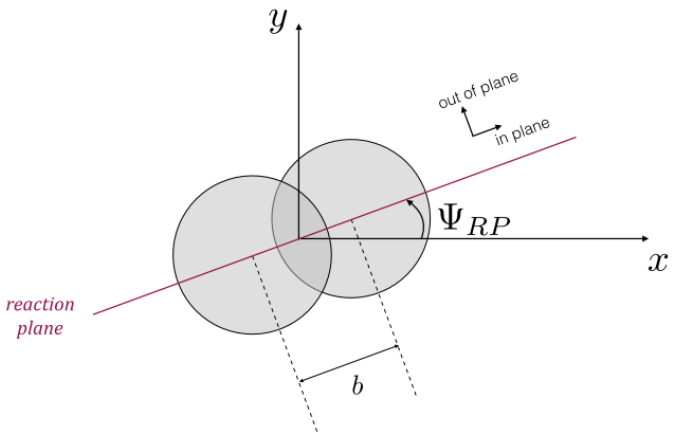


FIGURE 1.14 – Schematic view of the reaction plane. [7]

The $v_2$ coefficient, corresponding to the *elliptic flow* was measured at RHIC by the STAR and PHENIX experiments in Au-Au collisions (see figure 1.15 and found to be non-zero, confirming the presence of collective effects, which is consistent with the production of a QGP. However, measurements in p-p collisions at the LHC by the ATLAS experiment [54] also revealed a non-zero elliptic flow, which raises the question of whether the anisotropic flow is a good probe of the Quark-Gluon Plasma or if the proton-proton system is a good reference system without any collective effect.

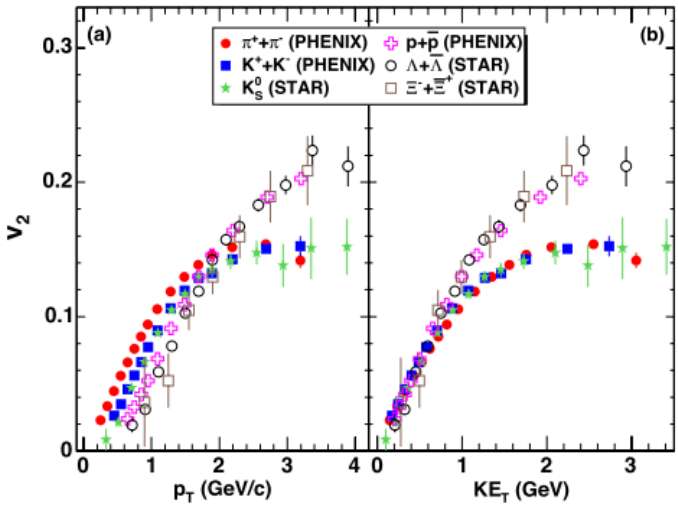


FIGURE 1.15 – $v_2$ coefficient measured by the PHENIX and STAR experiments in Au-Au collisions at $\sqrt{s_{NN}}$ = 200 GeV. [55]

## Hard probe

### Jet quenching

Proton-proton collisions are usually seen as a reference system in which no QGP is produced. The particle multiplicities in nucleus-nucleus collisions are then compared to the ones in proton-proton collisions, through the study of the nuclear modification factor $R_{AA}$, defined as:

$$R_{AA}(p_T, \eta) = \frac{d^2N^{AA}/d^2p_T\eta}{\langle N_{\text{coll}}\rangle\, d^2N^{pp}/d^2p_T\eta}, \tag{1.14}$$

where $p_T$ is the tranverse momentum of the particles and $\eta$ the pseudo-rapidity, defined as $\eta = -\ln\left[\tan\left(\frac{\theta}{2}\right)\right]$, with $\theta$ the angle of a particle relatively to the beam axis (usually defined as the z-axis). $\langle N_{\text{coll}} \rangle$ is the total number of binary collisions, which scales the multiplicities in nucleus-nucleus and proton-proton collisions. In the absence of a QGP medium, the $R_{AA}$ should be equal to 1, as the A-A collision would simply be a superposition of p-p collisions. However, in the presence of a medium, the $R_{AA}$ can be smaller than 1, indicating a *suppression* of the production of particles, or higher than 1, indicating an *enhancement* of the production.

Jets are a flux of collimated particles originating from the fragmentation of a highly energetic parton traversing the QGP. The partons from the jet interact in the medium and lose energy via gluonstrahlung (emission of gluons induced by the medium) or collisions with partons from the medium. This leads to a jet which energy is smaller than it would have been without the QGP medium, a phenomenon known as *jet quenching*. The resulting $R_{AA}$ then shows a suppression of the number of particles which depends on the centrality of the collision (see figure 1.16). It also shows a rise in the $R_{AA}$ for high transervse momentum.

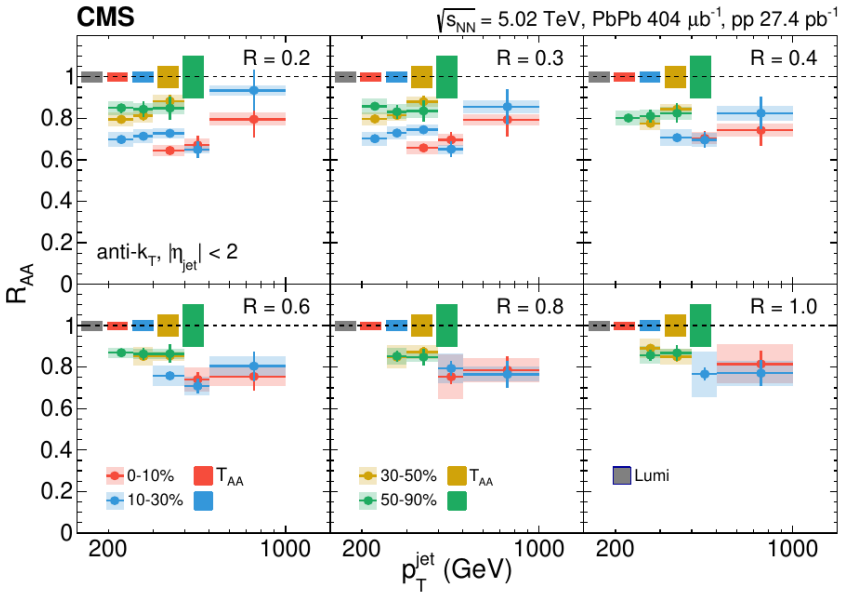


FIGURE 1.16 – Nuclear modification factor $R_{AA}$ as function of the jet transverse momentum for different centrality classes and isolation cone radius measured by CMS in Pb-Pb collisions at $\sqrt{s_{NN}}$ = 5.02 TeV [56].

The parton that created the jet is usually produced in a hard process, back-to-

back with another particle. The other particle can be another parton, leading to a "dijet" or a particle that will not lose energy in the medium such as a photon, leading to a "gamma-jet" event. This second case is of particular interest since one can get access to the initial energy of the parton, the gamme-jet system is thus a very good experimental probe of energy loss in the medium. [7, 57]

## 1.3 Summary

Experimental results presented in this chapter all seem to confirm the production of a new state of nuclear matter called Quark-Gluon Plasma in heavy ion collisions. We presented several probes of the QGP, testing different properties of the medium. Another very interesting probe is the so-called quarkonia suppression that occurs in heavy-ion collisions, which may be sensitive to the medium temperature. This observable will be central to the rest of this thesis, therefore we present in more details this observable, from both a theoretical and experimental point of view, in the next chapter.

# Chapter 2

# Phenomenology of quarkonia suppression

We will focus in this chapter on quarkonia suppression, which is an important observable of the Quark-Gluon Plasma. As the quarkonia are said to be suppressed when the number of detected quarkonia per binary nucleus-nucleus collision is smaller to the one in proton-proton collisions (once properly rescaled by the equivalent number of proton-proton collisions, $N_{\text{coll}}$), quarkonia suppression is usually quantified by the nuclear modification factor $R_{AA}$ defined in the previous chapter in equation (1.14). We will describe which effects play a role in the suppression of quarkonia and discuss experimental results from the RHIC and the LHC before presenting several types of models that aim at describing quarkonia suppression.

## 2.1 Quarkonia suppression and recombination

### 2.1.1 Cold nuclear effects on suppression

Those effects are usually classified in two categories: Initial cold nuclear effects, which happen before the creation of a $Q\bar{Q}$ pair, and final cold nuclear effects, which occur after the creation.

#### Shadowing and antishadowing

The main production mechanism for $Q\bar{Q}$ pairs production is gluon fusion. It depends on the initial gluon density, which can be described by *nuclear Parton Distribution Functions* (nPDFs) which use the DGLAP evolution equation [58–60] and describe the saturation of partons at small Björken $x$. In heavy ion collisions, the gluon

density of the colliding nuclei is modified by the interaction between the nucleons composing the nuclei. This can either either lead to a decrease (called *shadowing*) or increase (called *anti-shadowing*) of the heavy quark production depending on the energy and rapidity of the collisions. As shown on figure 2.1, the suppression for both charmonia and bottomonia decreases with increasing transverse momentum and becomes small at high-$\mathbf{p}_T$. It also decreases at large rapidities (both forward and backward) for both systems. Finally, the suppression is expected to be smaller for bottomonia than for charmonia as the probed energy fractions $x_1$ and $x_2$ of the colliding partons are larger for a given invariant energy.

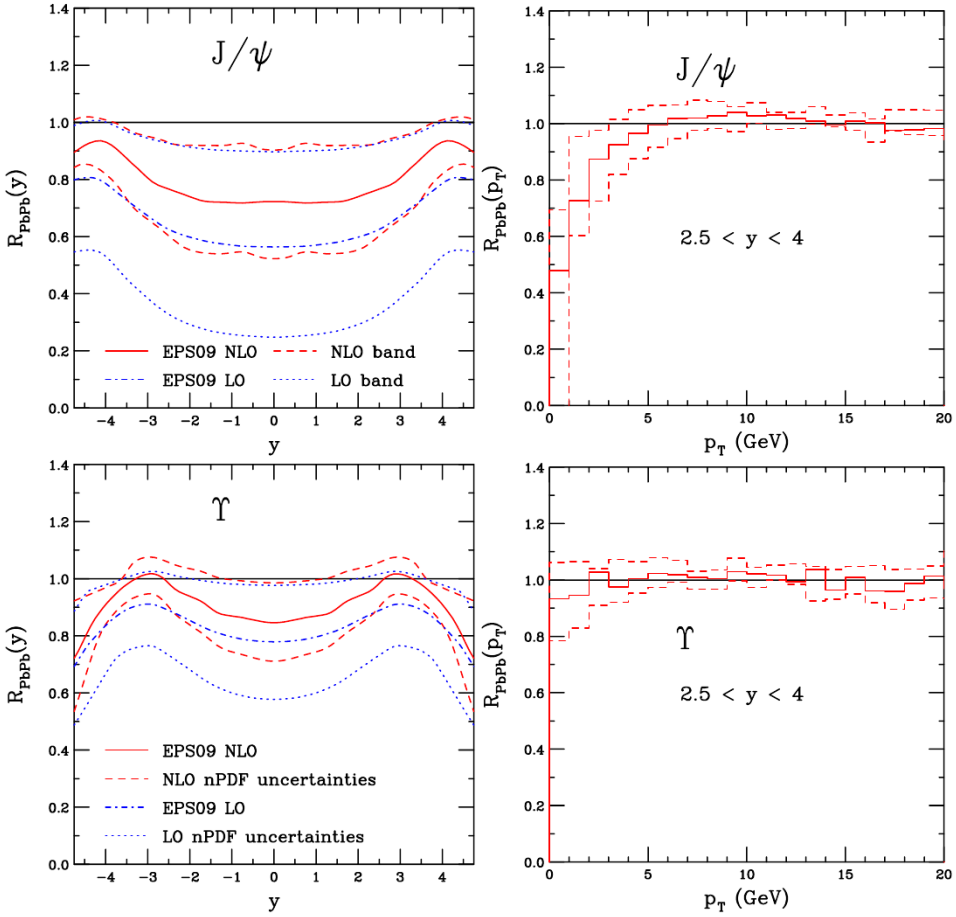


FIGURE 2.1 – Nuclear modification factor $R_{AA}$ for $J/\Psi$ (upper panels) and Υ (lower panels) using the EPS09 nPDFs as function of rapidity (left panels) and transverse momentum (right panels). [61]

One can also describe the parton saturation using the *Color Glass Condensate* (CGC) [40] effective theory, which is based on non-linear evolution equations such

as the Balitsky-Kovchegov (BK)[62–64] or JIMWLK equations.

### Cronin effect

In the initial stage of the collision, the initial parton from the projectile can scatter elastically multiple times on the colliding target nucleus. As they scatter, the partons acquire transverse momentum at each collision, which leads to a broadening of the quarkonium $\mathbf{p}_{\mathrm{T}}$ distributions in proton-nucleus and nucleus-nucleus collisions compared to proton-proton collisions. This broadening is known as the Cronin effect. [65]

### Nuclear absorption

It is a dissociation mechanism of quarkonia bound states induced by inelastic scatterings inside a nucleus with spectator nucleons in the final state. The survival probability of a quarkonium inside a nucleus can be expressed as:

$$S_{abs} = e^{-\rho_A \sigma_{abs} L}, \tag{2.1}$$

with $\rho_A$ the nuclear density, $\sigma_{abs}$ an effective cross-section for the quarkonium breaking and L the mean propagation length. The cross-section $\sigma_{abs}$ can be extracted from proton-nucleus collisions data and extrapolated to nucleus-nucleus collisions using the Glauber model.

As shown on figure 2.2, the cross-section $\sigma_{abs}$ decreases with the energy of the collision. Extrapolating the results to LHC energies leads to a negligeable cross-section and thus a negligeable effect of nuclear absorption in high energy heavy ion collisions.

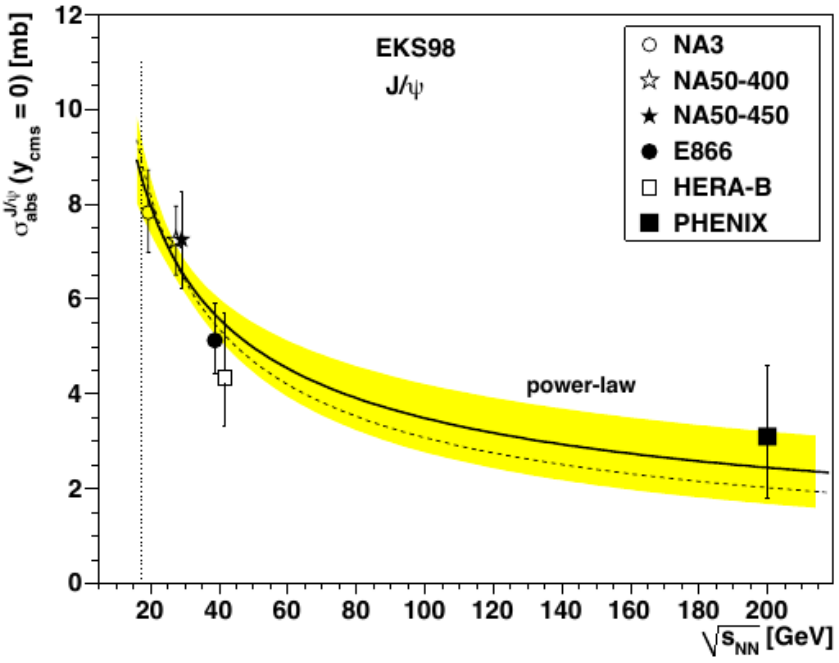


FIGURE 2.2 – Dependence of $\sigma_{abs}$ on energy for the $J/\Psi$ at mid-rapidity [66] using the EKS98 and CTEQ61L nPDFs [67–70]

**Parton energy loss**

The $Q\bar{Q}$ pairs produced during the collisions can lose energy in the nuclei, which may decrease its total momentum. This can lead to a lower quarkonium production at high $\mathbf{p}_T$. Parton energy loss arguments date back to the 90s, and the energy loss was considered to be moderate. A model describing parton coherent energy loss [71–75] showed that the energy loss is not moderate if we add the coherent energy loss mechanism. This model provides a good description of $J/\Psi$ suppression in proton-nucleus collisions over a large range of energies, from fixed-target to collider energies. However, its application to nucleus-nucleus collisions failed to reproduce experimental data overall, especially for the $\Upsilon(1S)$ at RHIC energies [76].

### 2.1.2 QGP effects on suppression

At zero temperature, the interaction potential between the quark and antiquark of the pair can be modelized by the Cornell potential [77]:

$$V(r) = -\frac{\alpha}{r} + \sigma r, \tag{2.2}$$

with the $\sigma r$ a term describing the non-perturbative confinement at long distance and $-\frac{\alpha}{r}$ a perturbative Coulombic interaction term at short distance. $\sigma$ is a string tension coefficient, that can be taken as $\sigma = (1.65 - \pi/12)/r_0^2$ (with $r_0 = 0.5$ fm) [78] and $\alpha = \pi/12$ a coefficient that can be determined by fitting to lattice results [79].

In the presence of a QGP medium, i.e at non-zero temperatures, the presence of color charges induces a Debye-like color screening of the $Q\bar{Q}$ interaction, which is similar to the screening of the electromagnetic interaction in a plasma composed of electrons and ions. As the density of color charges increases with temperature, the $Q\bar{Q}$ interaction is also more and more screened, as shown on figure 2.3, and its range is reduced.

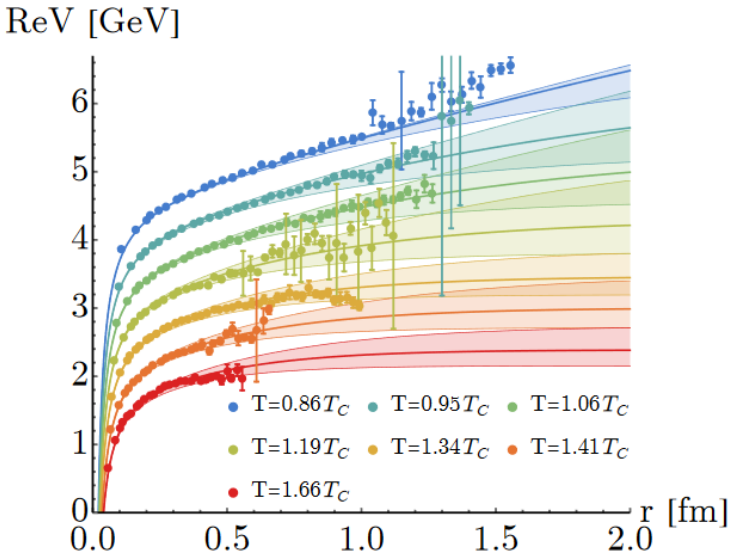


FIGURE 2.3 – Potential describing the $Q\bar{Q}$ pair interaction as function of the distance between the two quarks and temperature [80]

By analogy with an electromagnetic plasma, this range is usually described by the Debye radius, which is inversely proportionnal to the square root of the color charge density in the QGP. When the range of the interaction becomes smaller than

the quarkonium size, the strong interaction can not bind the quarkonium anymore. This leads to the bound state dissociation and to the suppression of the quarkonia production in the final state.

Alongside this static screening effect, there are also dynamical processes. The presence of light quarks and gluons in the medium will lead to collisions between the quarkonium and the medium particles. Those collisions may lead to the dissociation of the quarkonium through reactions of the type $g\ \Phi \rightarrow Q\bar{Q}$ (gluo-dissociation) or $p\ \Phi \rightarrow Q\bar{Q}p$ ("quasi-free" dissociation, with $p = q, \bar{q}, g$). [81, 82] This in turn will further suppress quarkonia production.

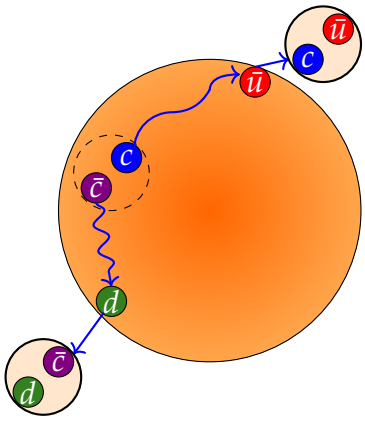


FIGURE 2.4 – Illustration of the dissociation of a quarkonium state and the hadronization of the free quarks into open heavy hadrons.

### 2.1.3 Recombination

The production of $c$ and $\bar{c}$ quarks is higher at high center of mass energies due to greater production cross-sections, as at the LHC. The high amount of $c$ quarks and antiquarks can lead to a phenomenon of *recombination* of those quarks into charmonia, increasing the production of such particles. This recombination can happen during the evolution, notably from quarks that come from dissociated pairs, or during the hadronization phase at the freeze-out as illustrated on figure 2.5. This recombination mechanism can therefore counterbalance the charmonium suppression which should be stronger at higher energy.

In the case of $b$ and $\bar{b}$ quarks, the production cross-section also increases with the

collision center of mass energy. However, the number of $b$ quarks and antiquarks in the medium remains small, even at high energies, and the contribution of the recombination mechanism to bottomonium production is still small.

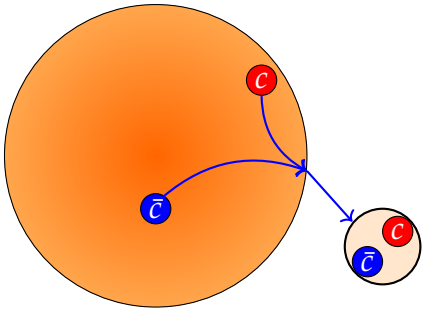


FIGURE 2.5 – Illustration of the recombination of two uncorrelated quarks to form a quarkonium

### 2.1.4 Experimental measurements at RHIC and LHC

In this section, we present experimental results from both RHIC and LHC experiments for bottomonia and charmonia suppression. [1]

#### Bottomonia

Results from Au-Au collisions at $\sqrt{s_{NN}}$ = 200 GeV and U-U collisions at $\sqrt{s_{NN}}$ = 193 GeV at RHIC show a strong suppression for the Y(1S) at high multiplicity (i.e. for more central collisions) and a stronger suppression in U-U collisions (see figure 2.6). Similar observations can be made for the integrated $R_{AA}$ measured of Y(1S+2S+3S), however, in that case, the suppression in U-U collision isn't stronger than in Au-Au collisions.

1. Results on quarkonia suppression at the SPS exist but will not be presented in this thesis

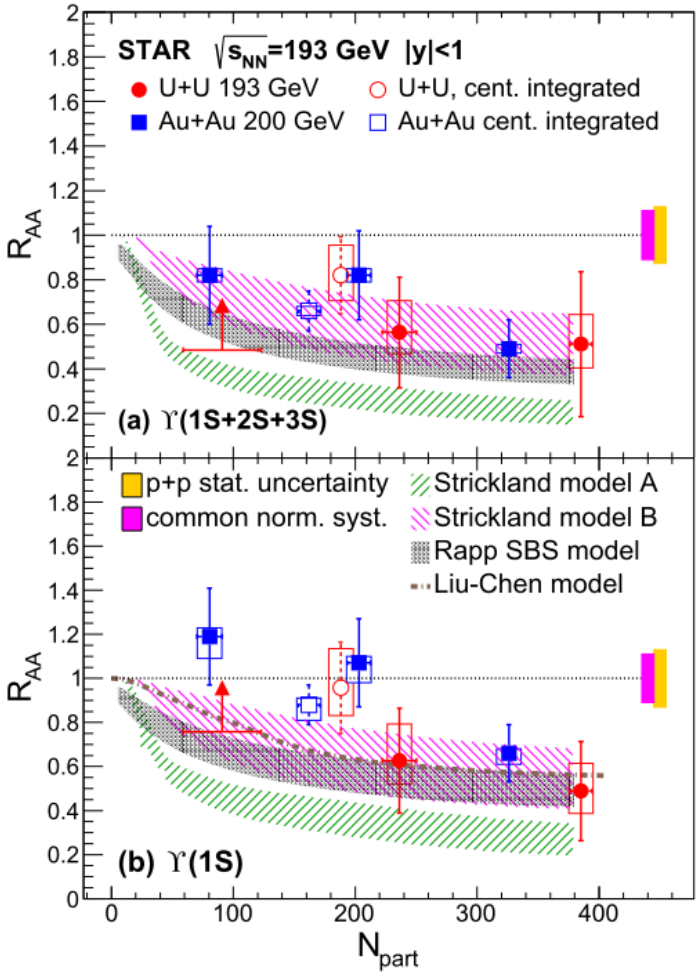


FIGURE 2.6 – Dependence on multiplicity of the nuclear modification factor $R_{AA}$ for the Y(1S) (bottom panel) and of the integrated $R_{AA}$ for the Y(1S+2S+3S) (top panel) in Au-Au collisions at 200 GeV and U-U collisions at 193 GeV from the STAR experiment. [83]

At the LHC, CMS measured the nuclear modification factor of the Y(1S) and Y(2S) in Pb-Pb collisions at $\sqrt{s_{NN}}$ = 2.76 TeV. They observed a stronger suppression of the Y(2S) compared to the Y(1S) for all kinematics. Compared to RHIC energies, the Y(1S) state is more suppressed at higher center of mass energies which is expected. No clear dependence on transverse momentum or rapidity was observed (see figure 2.7) but both Y states clearly show a stronger suppression at high multiplicity (see figure 2.8), which corroborates results from RHIC.

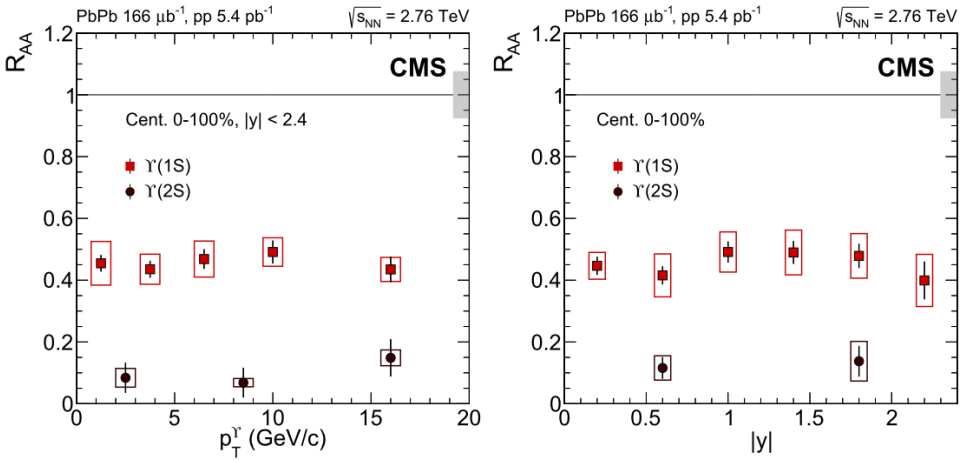


FIGURE 2.7 – *Left panel:* Dependence on transverse momentum of the nuclear modification factor $R_{AA}$ for the Υ(1S) and Υ(2S) in Pb-Pb collisions at 2.76 TeV from the CMS experiment. *Right panel:* Dependence on rapidity. [84]

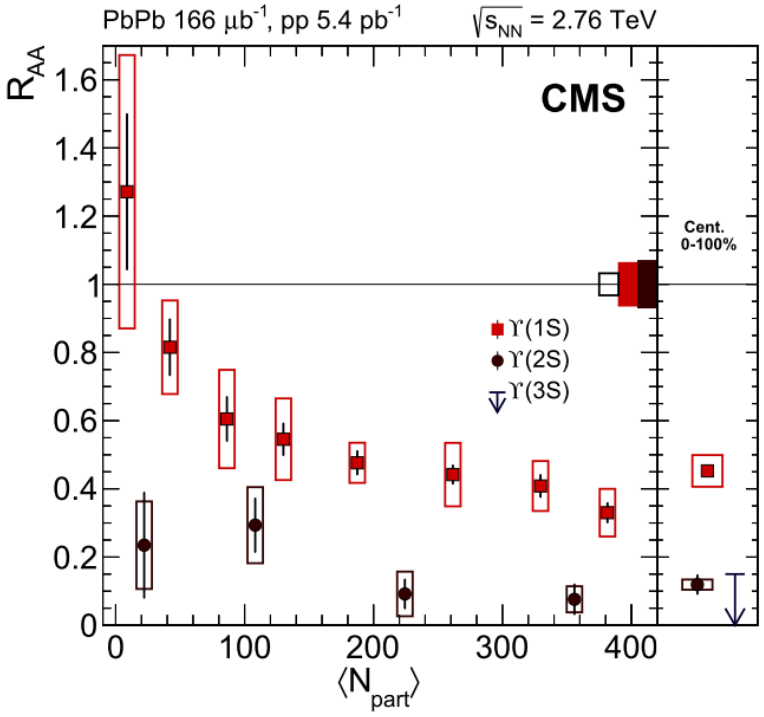


FIGURE 2.8 – Dependence on multiplicity of the nuclear modification factor $R_{AA}$ for the Υ(1S) and Υ(2S) in Pb-Pb collisions at 2.76 TeV from the CMS experiment. [84]

Finally, measurements of the $R_{AA}$ of the Y(1S) and Y(2S) with ALICE in Pb-Pb collisions at 5.02 TeV confirmed the stronger suppression of the Y(2S). No dependence on transverse momentum was observed but a decrease of the suppression at forward rapidity was shown for the Y(2S) (see figure 2.9) while an increase of the suppression was found for the Y(1S). As for CMS results, a stronger suppression of both Y(1S) and Y(2S) is observed at high multiplicity, which saturates for the most central collisions (see figure 2.10).

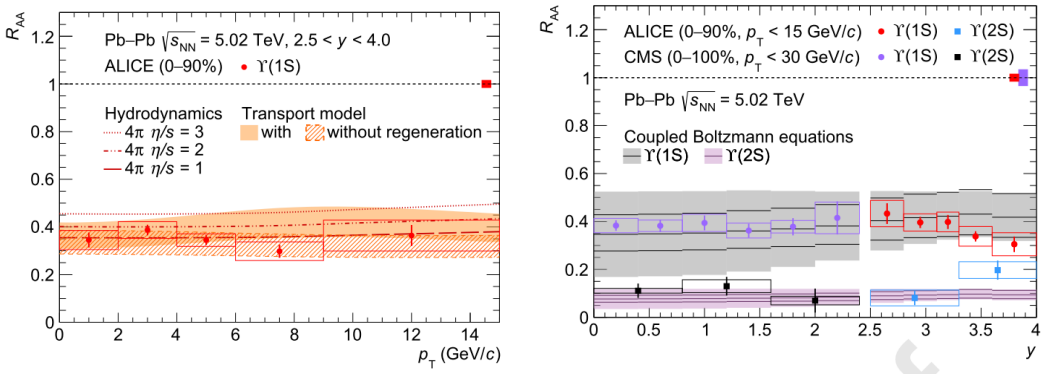


FIGURE 2.9 – *Left panel:* Dependence on transverse momentum of the $R_{AA}$ of the Y(1S) in Pb-Pb collisions at 5.02 TeV from the ALICE experiment. *Right panel:* Dependence on rapidity from ALICE and CMS. [85]

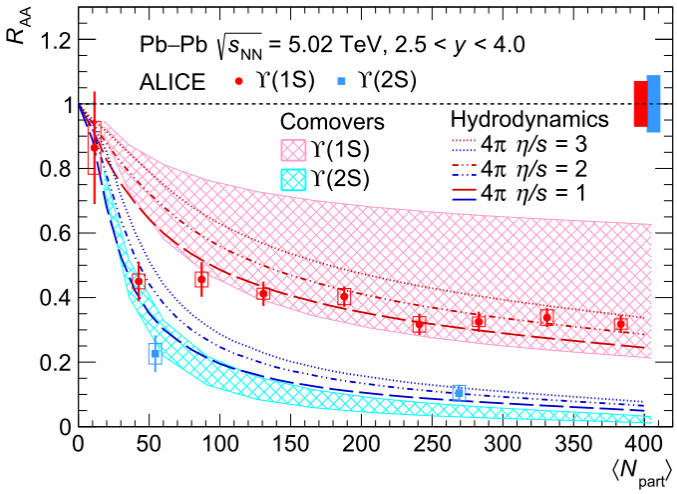


FIGURE 2.10 – Dependence on multiplicity of the nuclear modification factor $R_{AA}$ for the Y(1S) and Y(2S) in Pb-Pb collisions at 5.02 TeV from the ALICE experiment.[85]

The comparison of results from ALICE in Pb-Pb collisions at 2.76 and 5.02 TeV [86] shows a slightly reduced suppression at higher energies, indicating the presence of (still marginal) recombination for bottomonia.

### Charmonia

Measurements of the nuclear modification factor of the $J/\Psi$ at RHIC in Au-Au collisions at $\sqrt{s_{NN}} = 200$ GeV showed stronger suppression at forward rapidity than at mid-rapidity (see figure 2.11). Stronger suppression at high multiplicity (i.e. for more central collisions) was also observed. As of now, no data was published from RHIC experiments on $R_{AA}$ of the $\Psi$(2S) in A-A collisions.

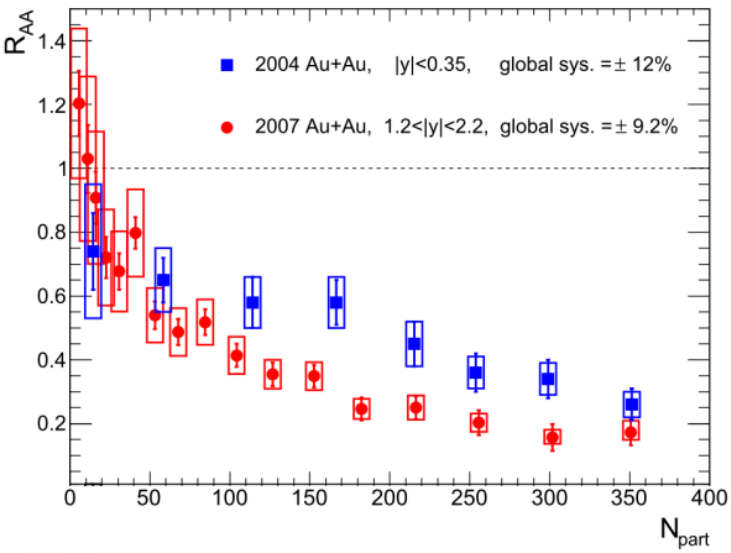


FIGURE 2.11 – $J/\Psi$ $R_{AA}$ from STAR as function of multiplicity in Au-Au collisions at 200 GeV in two different rapidity range. [87]

At the LHC, measurements in Pb-Pb collisions at 2.76 and 5.02 TeV by CMS for transverse momentum higher than 6.5 GeV showed no dependence on rapidity (see figure 2.12). Similar suppression with respect to multiplicity as RHIC is obtained with a slightly higher suppression at higher energies.

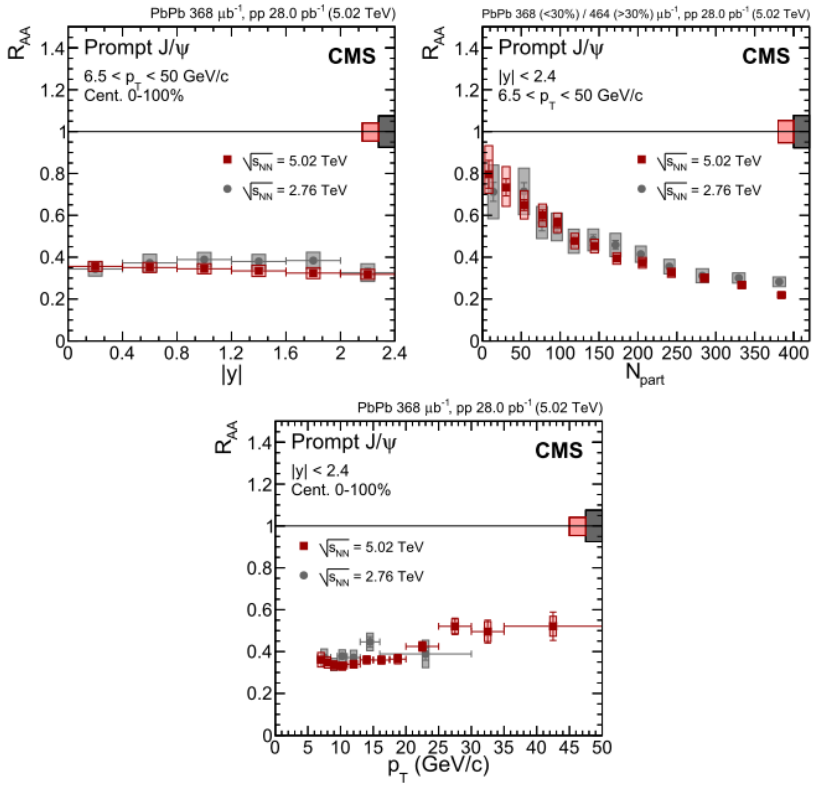


FIGURE 2.12 – $J/\Psi$ $R_{AA}$ from CMS in Pb-Pb collisions at 2.76 and 5.02 TeV as function of rapidity (top left panel), multiplicity (top right panel) and transverse momentum (bottom panel).[88]

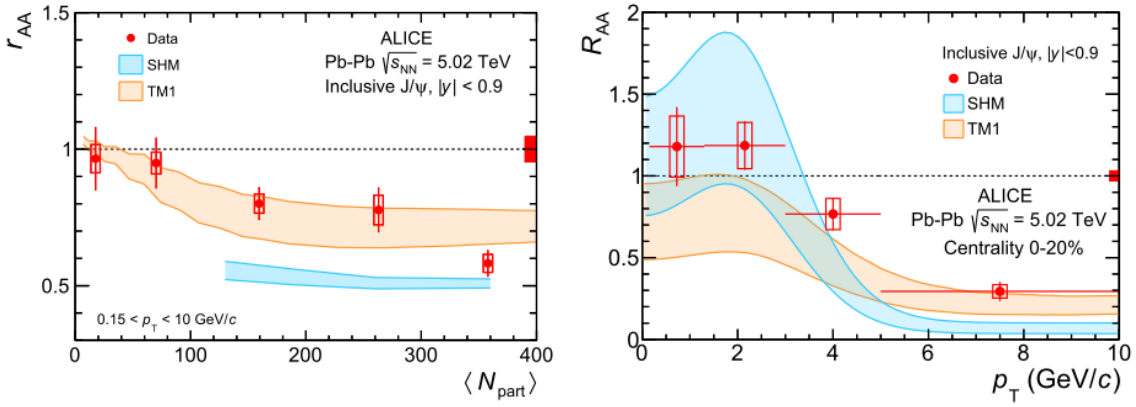


FIGURE 2.13 – $J/\Psi$ $R_{AA}$ from ALICE in Pb-Pb collisions at 2.76 TeV as function of multiplicity (left panel) and transverse momentum (right panel).[89]

ALICE measured the $J/\Psi$ $R_{AA}$ at low transverse momentum and also observed

an increase of the suppression with respect to multiplicity (see figure 2.13). At very low $\mathbf{p}_T$ (0-2 GeV), an enhancement of the $J/\Psi$ production is observed, indicative of recombination of $c$ and $\bar{c}$ quarks in the medium, while a significant suppression (> 50%) is observed for transverse momenta between 3 and 10 GeV. This can be explained as recombination is a process that is less relevant at higher transverse momentum.

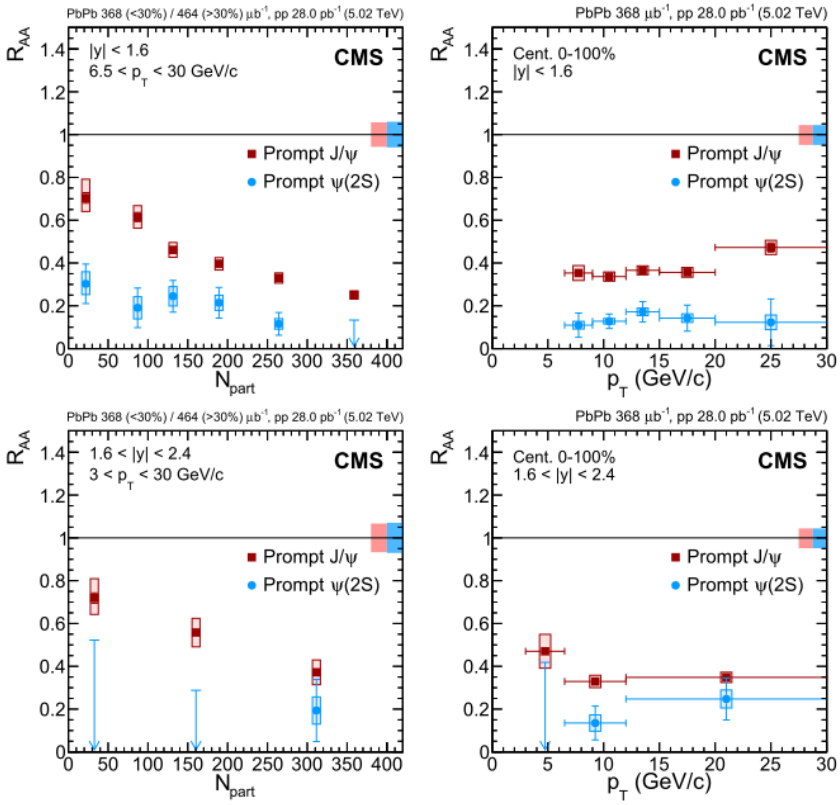


FIGURE 2.14 – Prompt $J/\Psi$ and $\Psi(2S)$ $R_{AA}$ from CMS in Pb-Pb collsions at 5.02 TeV as function of multiplicity (left panels) and transverse momentum (right panels) at central rapidities (top panels) and forward rapidity (bottom panels).[88]

Measurements of the $\Psi(2S)$ suppression were done by CMS in Pb-Pb collision at 5.02 TeV. A stronger suppression of the $\Psi(2S)$ compared to $J/\Psi$ was observed with respect to multiplicity and transverse momentum (for $\mathbf{p}_T > 6.5$ GeV) at mid-rapidity. However, at more forward rapidity, the uncertainties on the $\Psi(2S)$ $R_{AA}$ remain quite large but suppression is still observed to be stronger nonetheless.

## 2.2 Theoretical models of quarkonia suppression

In this section, we review the main models that try to describe quarkonia suppression in heavy-ion collisions.

### 2.2.1 Sequential suppression

Matsui & Satz [1] first predicted quarkonium suppression as a sign of the formation of a Quark-Gluon Plasma. As described in section 2.1.2, the screening of the interaction between the quark and antiquark is described by the Debye screening radius $r_D$, which decreases with increasing temperature. If the Debye radius gets smaller than the radius of a quarkonium state, the quarkonium will dissociate.

The idea of sequential suppression is that for each quarkonium state, there exists a dissociation temperature $T_\Phi^d$ for which $r_D < r_\Phi$, where $r_\Phi$ is the mean radius of quarkonium state $\Phi$. At the start of the QGP phase, if the temperature of the medium is higher than $T_\Phi^d$, the state is melted and the heavy quarks evolve freely in the medium. If this scenario is realized, then one should observe a suppression by steps for each state with the most excited states being the most suppressed. Quarkonia suppression can then be seen as a early time thermometer of the plasma.

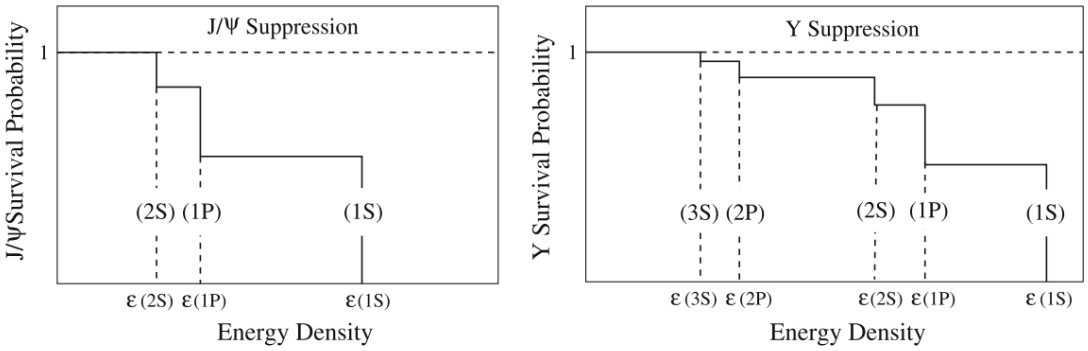


FIGURE 2.15 – *Left panel:* Sequential suppression for $J/\Psi$. *Right panel:* Sequential suppression for $\Upsilon(1S)$. [33]

In this approach, one needs to determine the dissociation temperatures $T_\Phi^d$, which is not obvious. Two main methods are usually used to determine them. One can either model the interquark potential $V(r,T)$ (by parametrizing it, or by using $\mathcal{L}$QCD results) [78, 90, 91] or compute the quarkonium spectral functions using $\mathcal{L}$QCD

[92–94]. In the latter case, the dissociation temperature of the quarkonium state $\Phi$ is obtained when the peak in the spectral function corresponding to the state $\Phi$ disappears (see figure 2.16).

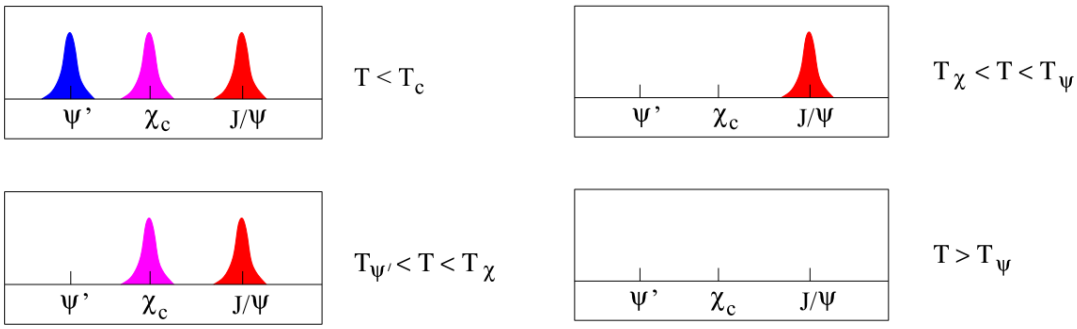


FIGURE 2.16 – Illustration of the dissociation of charmonium states through the disappearence of spectral functions [95].

The sequential suppression model assumes that the whole dynamics of quarkonium in the medium is decided in the early stage of the QGP phase, which is also assumed to be stationnary as far as its effects on quarkonia are concerned. If the medium initial temperature is greater than the dissociation temperature $T_\Phi^d$ of the quarkonium $\Phi$, then the state is melted and the $Q\bar{Q}$ pair evolves freely until hadronization. In that case the $Q\bar{Q}$ pair decorrelates quickly which is not obvious as residual interactions are still present. If the medium initial temperature is lower than the dissociation temperature, then the state is formed and evolves adiabatically without any dissociation or transitions to other states which is also highly debatable. In another version of the sequential suppression model, where the medium is assumed to be quasi-stationnary, the quarkonium formation times are taken into account and the dissociation temperatures are compared to the medium local temperature after such a formation time. However, the determination of the dissociation temperatures and formation times remains complicated as different prescriptions can result in different values and as the physics which is continuous is replaced by discretized criteria.

| State | $J/\Psi$ | $\Psi(2S)$ | $\Upsilon(1S)$ | $\Upsilon(2S)$ | $\Upsilon(3S)$ | $\Upsilon(4S)$ |
|---|---|---|---|---|---|---|
| $T_{diss}/T_C$ | $1.37^{+0.08}_{-0.07}$ | $< 0.95$ | $2.66^{+0.49}_{-0.14}$ | $1.25^{+0.17}_{-0.05}$ | $1.01^{+0.03}_{-0.03}$ | $< 0.95$ |

TABLE 2.1 – Dissociation temperatures obtained from $\mathcal{L}$QCD calculations [94] with $T_C = 172.5$ MeV. Only an upper limit is given for the $\Psi(2S)$ and $\Upsilon(4S)$ due to the lack of data below this limit.

### 2.2.2 Co-movers

This model [96–100] was originally introduced to explain the "abnormal" suppression of charmonia in proton-nucleus collisions at SPS. It takes into account shadowing and nuclear absorption effects, which are described by suppression factors $S^{\text{sh}}$ and $S^{\text{abs}}$, with the latter defined in a similar fashion as in section 2.1.1 (see equation (2.1)). It originally described the suppression of the production of quarkonia caused by inelastic interactions with the "co-moving" hadrons (i.e. with similar rapidity as the quarkonium) of the type $Q\bar{Q} + h_{co} \rightarrow D/B + \bar{D}/\bar{B} + X$ during the hadronization phase ($D$ and $B$ refer to either $D$ or $B$ generic mesons). The model was later extended to also take into account recombination by the same mechanism [101], via reactions of the type $D/B + \bar{D}/\bar{B} \rightarrow Q\bar{Q} + X$. This dissociation or recombination due to co-movers is described by another suppression factor $S^{\text{co}}$, which is derived from a rate equation governing the final state quarkonium density:

$$S^{co} = \exp\left(-\sigma_{co}\left[N^{co} - \frac{N_Q N_{\bar{Q}}}{N_\Phi}\right]\ln\left[\frac{N_{co}}{N_f}\right]\right), \tag{2.3}$$

where $N_Q$ and $N_\Phi$ are respectively the densities of the considered heavy quark and quarkonium state and $\sigma_{co}$ is the quarkonium dissociation cross-section with the comoving medium of density $N_{co}$.

The model is in overall good agreement with data from A-A collisions at LHC [102] (see figure 2.17) and RHIC [101]. It was also applied to excited charmonium states (in p-A collisions) [103] and to bottomonia [104]. However, the nature of co-movers is not clearly identified and the cross-sections used are tuned and are not related to QCD.

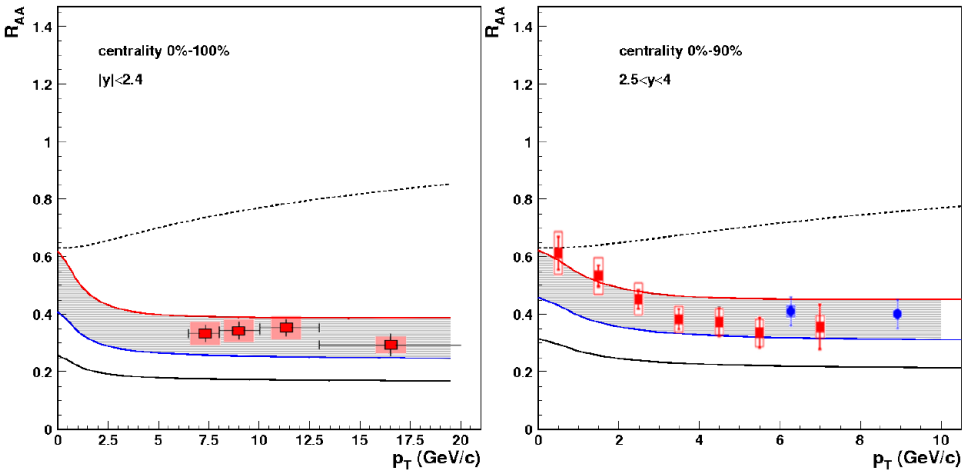


FIGURE 2.17 – $\mathbf{p}_{\mathrm{T}}$ dependence of the $J/\Psi$ $R_{AA}$ in Pb-Pb collisions at $\sqrt{s_{NN}} = 2.76$ TeV with the comovers interaction model (shadowed area) [102]. *Left panel:* Comparison to CMS [105, 106] data at mid-rapidity. *Right panel:* Comparison to CMS [105] data and ALICE [107] data at forward rapidity.

### 2.2.3 Statistical hadronization

The statistical hadronization model (SHM) was first used to describe light hadrons multiplicity [108–111] and then also applied to quarkonia yields [112–114]. It is based on the possible production of quarkonia at the phase boundary from recombination of uncorrelated $Q$ and $\bar{Q}$. The $Q\bar{Q}$ pairs produced by the initial collision are screened in the QGP at the start of the deconfined phase and only uncorrelated quark and antiquarks remain as all correlations are considered to disappear. The single heavy quarks freely evolve in the medium and then hadronize at the phase boundary into open hadrons or quarkonia, based on their statistical weights and masses. This production mechanism requires the number of uncorrelated heavy quarks in the medium to be non-negligeable compared to the number of light quarks. It depends on the number of initial $Q\bar{Q}$ pairs produced at the start of the collision, which should increase with the center of mass energy and centrality of the collision. At the LHC, one expects the production of a hundred of $Q\bar{Q}$ pairs [115] and ten times less at the RHIC [116], therefore the contribution should be important at LHC energies and moderate at RHIC energies. The number of $c\bar{c}$ pairs produced is also expected to be much greater than the number of $b\bar{b}$ pairs, this production

mechanism should thus not be dominant for bottomonia.

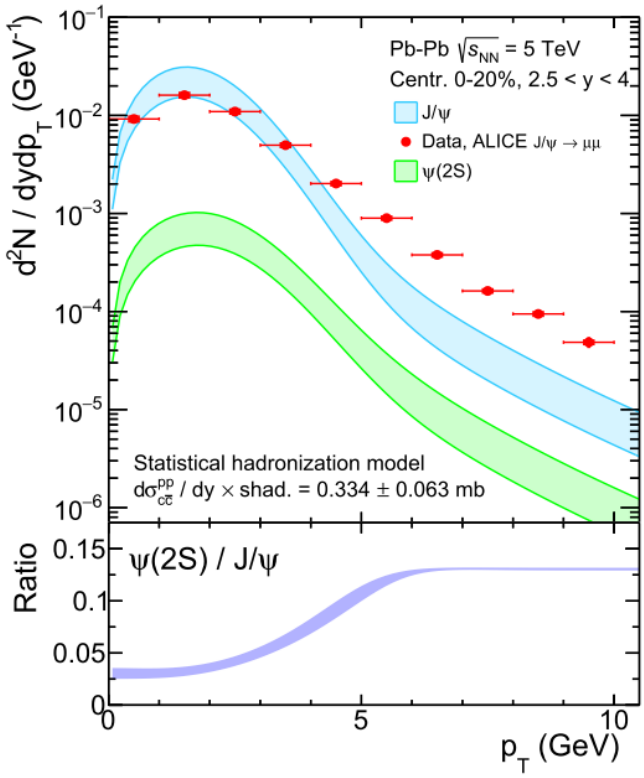


FIGURE 2.18 – $J/\Psi$ transverse momentum spectrum in Pb-Pb collisions at $\sqrt{s_{NN}}$ = 5 TeV obtained from ALICE data [117] and comparison to results from the statistical hadronization model. Predictions for the $\Psi(2S)$ transverse momentum spectrum. [118].

The statistical hadronization model reproduces well data from RHIC on the $J/\Psi$ $R_{AA}$ dependence on rapidity and centrality and data from the NA50 experiment at the SPS on the $\Psi(2S)/J/\Psi$ ratio [119, 120]. More recent results show a good agreement with ALICE data on the $J/\Psi$ transverse momentum spectrum at mid rapidity and low $\mathbf{p}_T$ [118]. A discrepancy at high $\mathbf{p}_T$ is observed (see figure 2.18) and is expected as the statistical recombination is a low $\mathbf{p}_T$ phenomenon (because it only applies to thermalized charm quarks). Predictions for the $\Psi(2S)$ were also made. Results on the dependence on charged particles multiplicity of the $J/\Psi$ $R_{AA}$ at midrapidity and forward rapidity were shown in [121]. A good agreement within uncertainties with RHIC data was observed as well as with ALICE data (see figure

2.19). The statistical hadronization model also made predictions on $J/\Psi$ and $\Psi(2S)$ yields for 5.02 TeV Pb-Pb collisions [122].

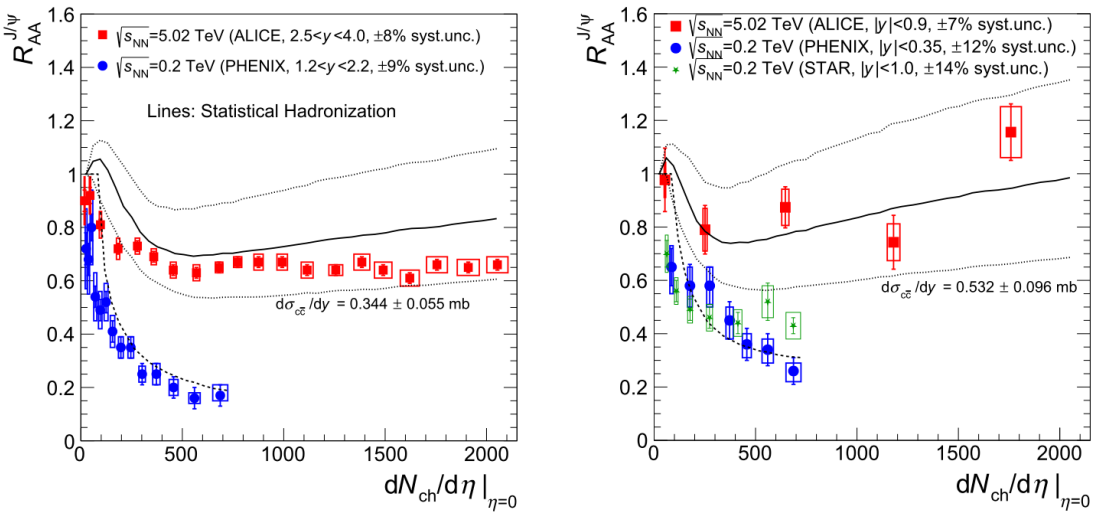


FIGURE 2.19 – *Left panel:* Nuclear modification factor $R_{AA}$ for $J/\Psi$ dependence on charged particle multiplicity at forward rapidity obtained from the SHM and comparison to experimental data. *Right panel:* Same at mid-rapidity. Data are for Au-Au collisions from STAR (green points) [123] and PHENIX (blue points) [87, 124] and for Pb-Pb collisions from ALICE (red points) [89, 125].

Despite its successes, this model makes several assumptions regarding charmonia that are debatable. First of all, and contrary to the sequential suppression model, it assumes that the fate of quarkonia is decided at a quasi-stationnary phase boundary. The initial $c\bar{c}$ pairs are assumed to be completely dissociated and then equilibrate with the medium. Both assumptions are questionable as it is not obvious that the heavy quarks completely thermalize in the dynamic medium [126] and it is also not obvious that the initial pairs completely decorrelate. Finally, it is implied that the quarkonia production is "instantaneous", even though production timescales for heavy quarks are rather long due to their masses.

### 2.2.4 Transport models

Transport models rely on a more dynamical view of the dissociation and recombination and usually include most of the effects affecting quarkonia production

(shadowing, nuclear absorption...). Feed-down from excited quarkonia and non-prompt charmonia from b-decays are also included and formation times are taken into account [127]. They usually describe the phase-space distribution of quarkonia in the QGP using the relativistic Boltzmann or Langevin equation, from which one can obtain, assuming a spatially homogeneous medium and the thermalization of open heavy states, the rate equation:

$$\frac{\mathrm{d}N_\Phi}{\mathrm{d}\tau} = -\Gamma_\Phi(T)\left[N_\Phi - N_\Phi^{eq}(T)\right], \tag{2.4}$$

with $\tau$ the proper time, $N_\Phi$ the number of quarkonia $\Phi$, $\Gamma_\Phi$ the inelastic reaction rate (taking into account both dissociation and recombination) and $N_\Phi^{eq}$ the quarkonium equilibrium limit.

The reaction rate $\Gamma_\Phi$ is computed from inelastic scattering processes of quarkonia on the particles present in the medium. Two processes are relevant: 1) if the state $\Phi$ is tightly bound (i.e. if its binding energy $E_b$ is greater than the medium temperature $T$), gluo-dissociation $g\Phi \rightarrow Q\bar{Q}$ is dominant [81] and 2) if the state $\Phi$ is loosely bound (i.e. $E_b < T$), it is the "quasi-free" dissociation $p\Phi \rightarrow Q\bar{Q}p$ ($p = g, q, \bar{q}$) that is dominant. [82]

To describe the medium space-time evolution, transport models usually use an isotropically expanding fireball model, which reproduces measured hadrons yields and $\mathbf{p}_\mathrm{T}$ spectra while also resembles basic features of hydrodynamical models. [128] The single heavy quarks in the medium are evolved with a Boltzmann equation containing an additionnal diffusive term obtained from the elastic cross-section of the $Qp \rightarrow Qp$ process.

The two main transport models are the TAMU model from Zhao et al. and the THU model from Liu et al. [129, 130]. The TAMU model was applied to both charmonia [131] and bottomonia[132]. More recent results obtained from the TAMU model on the dependence on $\mathbf{p}_\mathrm{T}$ and multiplicity of the $J/\Psi$ and $\Psi(2S)$ $R_{AA}$ for Pb-Pb collisions at $\sqrt{s_{NN}}$ = 5.02 TeV can be found in [133] and can be found in [134] for case of the Y with comparison to CMS data (see figure 2.20).

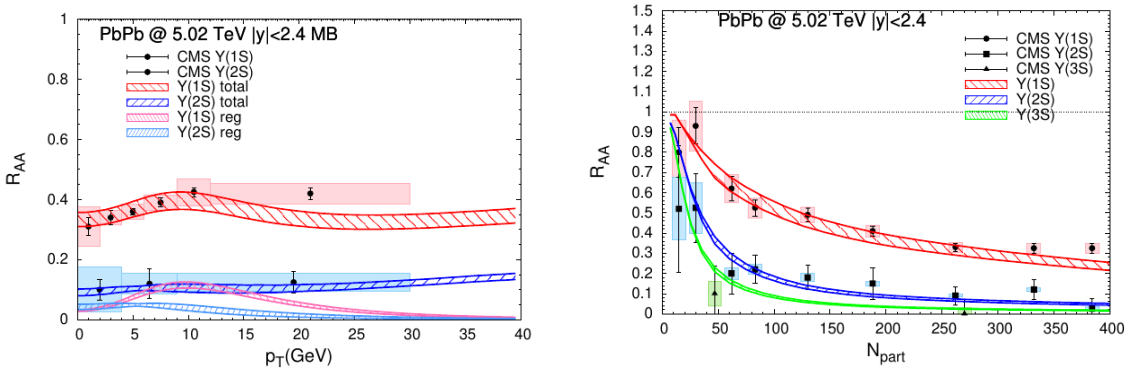


FIGURE 2.20 – *Left panel:* Dependence on transverse momentum of the nuclear modification factor for the $\Upsilon(1S)$ and $\Upsilon(2S)$. *Left panel:* Dependence on multiplicity of the nuclear modification factor for the $\Upsilon(1S)$, $\Upsilon(2S)$ and $\Upsilon(3S)$.

While transport models are a more dynamical approach to quarkonia suppression, the rates for dissociation and recombination are obtained from inelastic cross-sections, which can be questionable as:

— The initial and final states can not be defined asymptotically, which is one of the postulates of cross-sections [14]

— All quantum effects are not taken into account

## 2.3 Summary

We presented in this chapter a review of the various aspects of quarkonia suppression. This suppression is the result of the interplay between cold nuclear matter effects, dissociative effects in the QGP medium and recombination of heavy quarks into quarkonia. We discussed experimental results from both RHIC and LHC and presented four types of model that aims at describing quarkonia suppression. Those models are in overall good agremment with experimental data, but their assumptions are often questionnable. Instead, one can turn its attention to the real-time dynamics of heavy quarkonia in the Quark-Gluon Plasma, which is a very complex quantum field theory problem at finite temperature. In recent years, a lot of efforts in the theoretical community has be done towards such a real-time description using the open quantum systems formalism. In this framework, one can treat a $Q\bar{Q}$ pair as a quantum system in interaction with an environment, which is the QGP. In the

next chapter, we review this formalism and several models that were developped in the past ten years to tackle the problem of quarkonia suppression.

# Chapter 3

# Open Quantum Systems

Heavy quarkonium physics requires to understand the reaction of a heavy $Q\bar{Q}$ pair to a Quark-Gluon Plasma environment with which it is not initially equilibrated. If the system degrees of freedom can be separated in an environment E and a subsystem S, we can describe it through the open quantum system formalism. This framework is used extensively, notably in condensed matter physics, and in the past years, it has also been applied to the case of heavy quarkonia. Indeed, thanks to the hierarchy of scales at play, one can separate the QGP (the environment) from the $Q\bar{Q}$ pairs (the subsystem).

We give in this chapter an introduction to this formalism, applied to the case of a heavy $Q\bar{Q}$ pair in interaction with the Quark-Gluon Plasma. We will first introduce the concept of open quantum systems before deriving a very general quantum master equation called the Lindblad equation that describes the subsystem dynamics. We will then make a review of the various approaches that have been used in the community to describe quarkonium dynamics using open quantum systems. Finally, the last part of this chapter will be devoted to the discussion of an approach by Jean-Paul Blaizot and Miguel Escobedo [2], which will be the basis of the work presented in the following chapters.

## 3.1 Density operator and quantum master equations

The quantum state of a system can be described by an object called a density operator. A density matrix is a representation of this operator, obtained by choosing a basis in the space the operator acts on. In the remaining part of this manuscript, both terms may be used interchangeably but one has to keep in mind that they do

not strictly point to the same objects.

Let us consider the case of a quantum system with N possible states, labelled $|\psi_i\rangle$, with $i$ going from 1 to N. The most general expression of the density operator (denoted $\rho$) describing the system is:

$$\rho = \sum_i p_i \left|\psi_i\right\rangle \left\langle\psi_i\right| , \tag{3.1}$$

with $p_i$ the probability for the system to be in the state $|\psi_i\rangle$ and $\sum_i p_i = 1$.

If there is only one index $i$ for which $p_i \neq 0$ then we simply have

$$\rho = \left|\psi_i\right\rangle \left\langle\psi_i\right| , \tag{3.2}$$

and the system state is called a *pure* state (note that in this specific case, one may also call the density operator a *projector* on the state $|\psi_i\rangle$). If the system is not in a pure state, it is said to be in a *mixed* state. We can then see the density operator as a generalization of state vectors, in the sense that the latter can only describe pure states, while the former can describe both pure and mixed states.

Let us now consider a system with an initial state $\rho(t_0)$ at a time $t_0$. The evolution of the density operator $\rho$ is then given by:

$$\rho(t) = \mathrm{U}(t, t_0)\rho(t_0)\mathrm{U}^\dagger(t, t_0), \tag{3.3}$$

with $\mathrm{U}(t, t_0)$ an evolution operator from time $t_0$ to time $t$, defined as:

$$\mathrm{U}(t, t_0) = Te^{-i\int_{t_0}^{t} ds H(s)}, \tag{3.4}$$

where $H(t)$ is the time-dependant Hamiltonian of the system and T the time-ordering operator.

By differentiating (3.4) with respect to time, we get an equation of motion for the density operator:

$$\frac{d}{dt}\rho(t) = -i\left[H(t), \rho(t)\right] . \tag{3.5}$$

This equation is known as the (Liouville)-von Neumann equation. By analogy with the classical Liouville equation, equation (3.5) can also be written as:

$$\frac{d}{dt}\rho(t) = \mathcal{L}(t)\rho(t). \tag{3.6}$$

$\mathcal{L}$ is often called the Liouville super-operator (because it is an operator acting on another operator) and is here defined such that $\mathcal{L}(t)\rho(t) = -i\,[H(t), \rho(t)]$.
Equations (3.5) and (3.6), describing the evolution of the density operator, are called *quantum master equations*.

## 3.2 Dynamics of open quantum systems

In section (3.1), we only considered the case of a closed system, and described its dynamics by introducing a density operator. In this section, we describe the dynamics of an open quantum system. As previously said, an open quantum system is composed of a quantum subsystem S in interaction with an environment E. We assume here that the total system S+E is closed. As time evolves, the state of the subsystem will change due to its interactions with the environment and its own internal dynamics. One is usually not interested in the dynamics of the total system but in the dynamics of the subsystem S, which is in general non-unitary, due to its correlations with the environment.

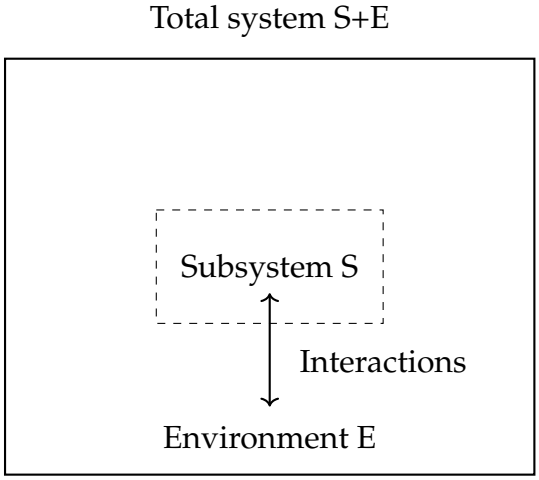


FIGURE 3.1 – Schematic view of an open quantum system

The Hilbert space of the total system is given by $\mathcal{H} = \mathcal{H}_S \otimes \mathcal{H}_E$, with $\otimes$ denoting the tensor product and $\mathcal{H}_S(\mathcal{H}_E)$ the system (the environment) Hilbert space. The Hamiltonian $H(t)$ of the total system can then be then written in a general way:

$$H(t) = H_S \otimes \mathbb{1}_E + \mathbb{1}_S \otimes H_E + H_{int}(t), \tag{3.7}$$

with $H_S$ the subsystem's free Hamiltonian, $H_E$ the environment free Hamiltonian and $H_{int}(t)$ the Hamiltonian describing the interactions between the system and the environment which can be time-dependent.

In the physical case of interest, the subsystem is the heavy $Q\bar{Q}$ pair and the environment is the QGP. Therefore, we can write the Hamiltonian of our total system in the same way as in (3.7):

$$H_{sys}(t) = H_{Q\bar{Q}} \otimes \mathbb{1}_{QGP} + \mathbb{1}_{Q\bar{Q}} \otimes H_{QGP} + H_{int}(t). \tag{3.8}$$

Recalling the equation (3.5), the equation of motion describing the evolution of our total system is:

$$\frac{d}{dt}\rho(t) = -i\left[H_{sys}(t), \rho(t)\right]. \tag{3.9}$$

As we are only interested by the dynamics of the heavy quark-antiquark subsystem, we introduce its *reduced density operator*, denoted $\rho_{Q\bar{Q}}$. It is obtained by tracing out the QGP degrees of freedom, which is done by performing the partial trace of the global density matrix on the Hilbert space of the QGP:

$$\rho_{Q\bar{Q}} = \mathrm{Tr}_{QGP}[\rho]. \tag{3.10}$$

Recalling (3.3), we can evolve in time the initial reduced density operator for the pair:

$$\rho_{Q\bar{Q}}(t) = \mathrm{Tr}_{QGP}\left[\mathrm{U}(t,0)\rho(0)\mathrm{U}^{\dagger}(t,0)\right], \tag{3.11}$$

assuming the following factorization of the initial density operator:

$$\rho(0) = \rho_{Q\bar{Q}}(0) \otimes \rho_{QGP}(0), \tag{3.12}$$

where $\rho_{QGP}(t)$ is the reduced density operator for the QGP and $\mathrm{U}(t,0) = Te^{-\int_0^t ds H_{int}(s)}$.

This evolution is non-unitary (contrary to the evolution of the total density operator), which leads to dissipative effects as we shall see later. Until that point, no major approximations were made and the quantum master equation obtained is still quite general. The next section will introduce a more specific class of quantum master equations that are widely used to describe the dynamics of heavy quarkonia, called the *Lindblad equation*.

## 3.3 The Linblad equation

Before going further, it is useful to look at the different relevant timescales of our system, since further approximations will rely on hierarchies between them. In the physical problem we are interested in, there are 3 relevant timescales:

— $\tau_E$ the environment correlation timescale along which correlations in the QGP decay.
— $\tau_S$ the subsystem intrinsic timescale, estimated through $\Delta E \times \tau_S \sim 1$ with $\Delta E$ the typical energy gap between two of the subsystem eigenenergies.
— $\tau_R$ the subsystem relaxation timescale, i.e. the typical timescale needed for the initially unequilibrated subsystem to go back to equilibrium with its environment.

We can rewrite the evolution equation of $\rho_{Q\bar{Q}}$ (3.11) in the following way:

$$\rho_{Q\bar{Q}}(t) = V(t)\rho_{Q\bar{Q}}(0), \tag{3.13}$$

where $V(t)$ is called a dynamical map. This map is in general quite complicated, however, there exists a class of systems for which $V(t)$ satisfies the following property:

$$V(t_1)V(t_2) = V(t_1 + t_2) \tag{3.14}$$

This property means that there are no memory effects and that the next step in the

evolution of the subsystem only depends on its current state. If this property is satisfied, the subsystem dynamics is said to be *Markovian*.

There is a specific regime where the hierarchy of timescales will allow us to neglect those effects: when $\tau_R$ and $\tau_E$ can be separated and $\tau_R \gg \tau_E$, meaning that the environment correlations decay fast on the timescale set by the subsystem relaxation. In this specific regime, we can write:

$$\frac{\mathrm{d}}{\mathrm{d}t}\rho_{Q\bar{Q}}(t) = \mathcal{L}\rho_{Q\bar{Q}}(t), \tag{3.15}$$

where $\mathcal{L}$ is a generator of $V$ such that $V(t) = e^{\mathcal{L}t}$.

The most general form for (3.15) was derived by Gorini, Kossakowski and Sudarshan [135] and independantly by Lindblad [136] and is called the *Gorini-Kossakowski-Sudarshan-Lindblad* (GKSL) or simply *Lindblad* equation:

$$\frac{\mathrm{d}}{\mathrm{d}t}\rho_{Q\bar{Q}}(t) = -i\Big[H_{Q\bar{Q}}, \rho_{Q\bar{Q}}(t)\Big] + \sum_i \gamma_i \left[L_i \rho_{Q\bar{Q}}(t) L_i^\dagger - \frac{1}{2}\Big\{L_i L_i^\dagger, \rho_{Q\bar{Q}}(t)\Big\}\right]. \tag{3.16}$$

The $L_i$ are called Lindblad operators and encode the subsystem's interaction with the environment. This equation is particularly interesting since it preserves three fundamental properties of $\rho_{Q\bar{Q}}$:

— positivity: $\langle\psi_i|\rho_{Q\bar{Q}}|\psi_i\rangle \geq 0 \quad \forall\, |\psi_i\rangle$
— hermiticity: $\rho^\dagger_{Q\bar{Q}} = \rho_{Q\bar{Q}}$
— unitarity: $\mathrm{Tr}\Big[\rho_{Q\bar{Q}}\Big] = 1$.

The derivation of the Lindblad equation actually involves several approximations. In sections 3.4 to 3.6, we show how to derive it for a general physical system, in two regimes of interest : the quantum optical limit and the quantum brownian motion.

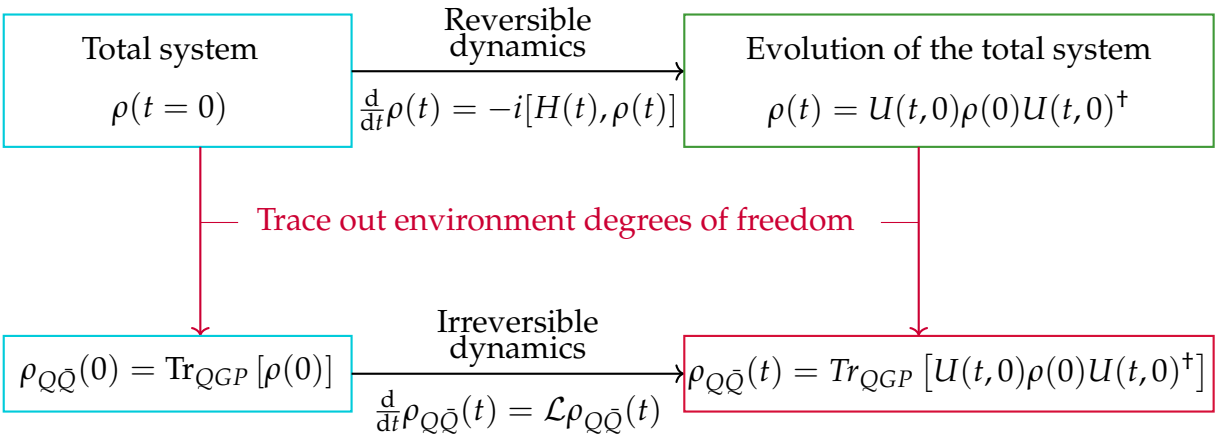


FIGURE 3.2 – Global picture of the open quantum systems evolution

## 3.4 Weak coupling limit and Born-Markov approximation

We now want to derive the Lindblad equation from a microscopic theory. This derivation is based on a chain of approximations with the first one being that we assume a weak coupling between the subsystem and the environment.

In the interaction representation, the Von Neumann equation (3.5) is written as:

$$\frac{\mathrm{d}}{\mathrm{d}t}\rho(t) = -i[H_{int}(t), \rho(t)], \tag{3.17}$$

with $H_{int}$ the interaction Hamiltonian.

The formal solution of (3.17) is:

$$\rho(t) = \rho(0) - i\int_0^t ds[H_{int}(s), \rho(s)]. \tag{3.18}$$

By substituting (3.18) in (3.17), we get:

$$\frac{\mathrm{d}}{\mathrm{d}t}\rho(t) = -i[H_{int}(t), \rho(0)] - \int_0^t ds[H_{int}(t), [H_{int}(s), \rho(s)]]. \tag{3.19}$$

The evolution of the reduced density operator is obtained by performing the partial trace on the environment degrees of freedom:

$$\frac{\mathrm{d}}{\mathrm{d}t}\rho_S(t) = -\int_0^t ds\, \mathrm{Tr}_E\left[[H_{int}(t), [H_{int}(s), \rho(s)]]\right], \tag{3.20}$$

where we assume $\mathrm{Tr}_E\left\{[H_{int}(t), \rho(0)]\right\} = 0$.

The weak coupling approximation we mentionned earlier allows us to use the ansatz that $\rho(s) = \rho_S(s) \otimes \rho_E(0)$. It is justified when the environment is large enough to not be affected by the subsystem thanks to the weak coupling between the two. This is know as the *Born* approximation.

In the case where $\tau_R \gg \tau_E$, we can replace $\rho_S(s)$ by $\rho_S(t)$, which is known as the *Markovian* approximation. Moreover, due to the timescale hierarchy involved here, the initial environment correlations are lost for times $t \sim \tau_R$, which allows us to extend the time integration domain in (3.20) to $(-\infty, t)$. Finally, performing the change of variables $s = t - s$, we get the following master equation:

$$\frac{\mathrm{d}}{\mathrm{d}t}\rho_S(t) = -\int_0^\infty ds\, \mathrm{Tr}_E\left\{[H_{int}(t), [H_{int}(t-s), \rho_S(t) \otimes \rho_E(0)]]\right\}. \tag{3.21}$$

This equation is not yet a Lindblad equation. Depending on the timescales hierarchy considered, two limits can be defined:

— $\tau_R \gg \tau_E$ ; $\tau_R \gg \tau_S$ : the quantum optical limit
— $\tau_R \gg \tau_E$ ; $\tau_S \gg \tau_E$ : the quantum brownian motion

In each of those regimes, another approximation is needed to get the Lindblad equation. Sections 3.5 and 3.6 are devoted to its derivation in each of those limits.

## 3.5 The quantum optical limit

The quantum optical regime is reached when the system satisfies the hierarchy of scales $\tau_R \gg \tau_S$. This is typically satisfied when considering a quantum optical system (a two-level atom interacting with a gas of photons for example), hence the name of this limit.

By introducing a spectral decomposition of the subsystem's Hamiltonian $H_S$, we can rewrite $H_{int}$ so that [137]:

$$H_{int}(t) = \sum_{n,\omega} e^{-i\omega t} O_S^n(\omega) \otimes O_E^n(t) = \sum_{n,\omega} e^{i\omega t} O_S^{n\dagger}(\omega) \otimes O_E^n(t), \tag{3.22}$$

with $O_S^n$ and $O_E^n$ operators of the subsystem and environment.

By injecting (3.22) in (3.21), we get:

$$\begin{aligned} \frac{\mathrm{d}}{\mathrm{d}t}\rho_S(t) = \sum_{\omega,\omega'} \sum_{n,m} e^{i(\omega'-\omega)t} \int_0^\infty ds e^{i\omega s} \operatorname{Tr}_E \left[\rho_E(0) O_E^n(t) O_E^m(t-s)\right] \\ \times \left[O_S^m(\omega)\rho_S(t) O_S^{n\dagger}(\omega') - O_S^{n\dagger}(\omega') O_S^m(\omega)\rho_S(t)\right] + h.c, \end{aligned} \tag{3.23}$$

where $h.c$ denotes the hermitian conjugate.

The phase factor $e^{i(\omega'-\omega)t}$ is oscillating with the timescale $\tau_S$. Since we are in the regime where $\tau_R \gg \tau_S$, in the timescale $\tau_R$, only the $\omega = \omega'$ phase factor remains. This is known as the *rotating wave approximation*. Adding to that the assumption that the environment is invariant under time translation, the master equation reads:

$$\frac{\mathrm{d}}{\mathrm{d}t}\rho_S(t) = \sum_{\omega} \sum_{n,m} \Gamma_{nm}(\omega) \left[O_S^m(\omega)\rho_S(t) O_S^{n\dagger}(\omega') - O_S^{n\dagger}(\omega') O_S^m(\omega)\rho_S(t)\right] + h.c \tag{3.24}$$

with $\Gamma_{nm}(\omega) = \int_0^\infty ds e^{i\omega s} \operatorname{Tr}_E \left[\rho_E(0) O_E^n(s) O_E^m(0)\right]$.

This $\Gamma_{nm}(\omega)$ can then be decomposed into :

$$\Gamma_{nm}(\omega) = \frac{1}{2}\gamma_{nm}(\omega) + iS_{nm}(\omega) \;\; ; \;\; \gamma^*_{nm}(\omega) = \gamma_{mn}(\omega) \;\; ; \;\; S^*_{nm}(\omega) = S_{mn}(\omega), \quad (3.25)$$

leading to the following quantum master equation:

$$\begin{aligned}\frac{\mathrm{d}}{\mathrm{d}t}\rho_S(t) &= -i[\Delta H_S, \rho_S(t)] \\ &+ \sum_{\omega}\sum_{n,m}\gamma_{nm}(\omega)\left[O^m_S(\omega)\rho_S(t)O^{n\dagger}_S(\omega) - \frac{1}{2}\left\{O^{n\dagger}_S(\omega)O^m_S(\omega), \rho_S(t)\right\}\right], \end{aligned} \quad (3.26)$$

with $\Delta H_S = \sum_{\omega}\sum_{n,m} S_{nm}(\omega)O^{n\dagger}_S(\omega)O^m_S(\omega)$ a modification to the subsystem Hamiltonian due to the coupling to the environment called the *Lamb shift*.

Finally, to obtain the Lindblad equation, one has to come back to the Schrödinger representation and choosing an appropriate linear combination of O operators in order to diagonalize $\gamma_{nm}$ and rescale it to $\delta_{nm}$.

## 3.6 The quantum brownian motion

We mentionned in 3.4 that there is another limit of interest, the *quantum Brownian motion*. Similarly to the previous section, we can approximate (3.21) by using a specific hierarchy of timescales. If $\tau_S \gg \tau_E$, i.e. if the subsystem dynamics is slow compared to that of the environment, we are in the quantum brownian regime. The latter can be seen as the quantum counterpart of the well-known Brownian motion.

A more explicit form of equation (3.21) is:

$$\begin{aligned}\frac{\mathrm{d}}{\mathrm{d}t}\rho_S(t) = \int_0^{\infty} ds \sum_{n,m} &\mathrm{Tr}_E\left[\rho_E(0)O^n_E(t)O^m_E(t-s)\right] \\ &\times \left[O^m_S(t-s)\rho_S(t)O^n_S(t) - O^n_S(t)O^m_S(t-s)\rho_S(t)\right] + h.c.\end{aligned} \quad (3.27)$$

The approximation involved in the quantum Brownian motion limit is to approxi-

mate the subsystem operators $O_S$ using the gradient expansion:

$$O_S^n(t-s) \approx O_S^n(t) - s\dot{O}_S^n(t) + \cdots \tag{3.28}$$

This approximation is only valid because the environment correlations only exist for a short time ($\tau_E \ll \tau_S$).

Assuming once again that the environment is invariant under time translation, we introduce the following quantities:

$$\begin{aligned} \int_0^\infty ds\, \mathrm{Tr}_E\left[\rho_E(0) O_E^n(s) O_E^m(0)\right] &= \frac{1}{2}\gamma_{nm} + iS_{nm} \\ \int_0^\infty ds\, s\, \mathrm{Tr}_E\left[\rho_E(0) O_E^n(s) O_E^m(0)\right] &= \eta_{nm}, \end{aligned} \tag{3.29}$$

with, $\gamma_{nm}^*(\omega) = \gamma_{mn}(\omega)$ and $S_{nm}^*(\omega) = S_{mn}(\omega)$. Those quantities are the environment correlations functions at zero frequency.

We then obtain the following quantum master equation:

$$\begin{aligned} \frac{\mathrm{d}}{\mathrm{d}t}\rho_S(t) = \sum_{n,m}\Bigg[ & \gamma_{nm}\left[O_S^m(t)\rho_S(t)O_S^n(t) - \frac{1}{2}\{O_S^n(t)O_S^m(t), \rho_S(t)\}\right] \\ & - iS_{nm}[O_S^n(t)O_S^m(t)\rho_S(t) - \rho_S(t)O_S^n(t)O_S^m(t)] \\ & - \eta_{nm}\left[\dot{O}_S^m(t)\rho_S(t)O_S^n(t) - O_S^n(t)\dot{O}_S^m(t)\rho_S(t)\right] \\ & - \eta_{nm}^*\left[O_S^n(t)\rho_S(t)\dot{O}_S^m(t) - \rho_S(t)\dot{O}_S^m(t)O_S^n(t)\right]\Bigg]. \end{aligned} \tag{3.30}$$

If we assume that $\gamma_{nm}^{-1}$ exists (i.e. that $\gamma_{nm}$ is a positive definite matrix), then we can turn (3.30) into a Lindblad equation:

$$\frac{\mathrm{d}}{\mathrm{d}t}\rho_S(t) = -i[\Delta H_S, \rho_S(t)] + \sum_{n,m}\gamma_{nm}\left[\tilde{O}_S^m(t)\rho_S(t)\tilde{O}_S^{n\dagger}(t) - \frac{1}{2}\left\{\tilde{O}_S^{n\dagger}(t)\tilde{O}_S^m(t), \rho_S(t)\right\}\right], \tag{3.31}$$

where we redefined the $O_S^n$ operators:

$$\tilde{O}_S^n(t) \equiv O_S^n(t) - \sum_{mk}\gamma_{nm}^{-1}\eta_{mk}\dot{O}_S^k(t) \quad \tilde{O}_S^{n\dagger}(t) \equiv O_S^n(t) - \sum_{mk}\eta_{mk}^*\dot{O}_S^k(t)\gamma_{mn}^{-1}, \tag{3.32}$$

and the subsystem Hamiltonian:

$$\Delta H_S \equiv \sum_{nm} S_{nm}O_S^n(t)O_S^m(t) + \frac{i}{2}\sum_{nm}\left[\eta_{nm}O_S^n(t)\dot{O}_S^m(t) - \eta_{nm}^*\dot{O}_S^m(t)O_S^n(t)\right]. \tag{3.33}$$

Until now, we have not derived any quantum master equation specifically for the physical problem of a heavy quarkonium in interaction with the Quark-Gluon Plasma. We will now make a review of the various open quantum systems approaches that were used in recent years to tackle the problem of quarkonium dynamics inside the QGP.

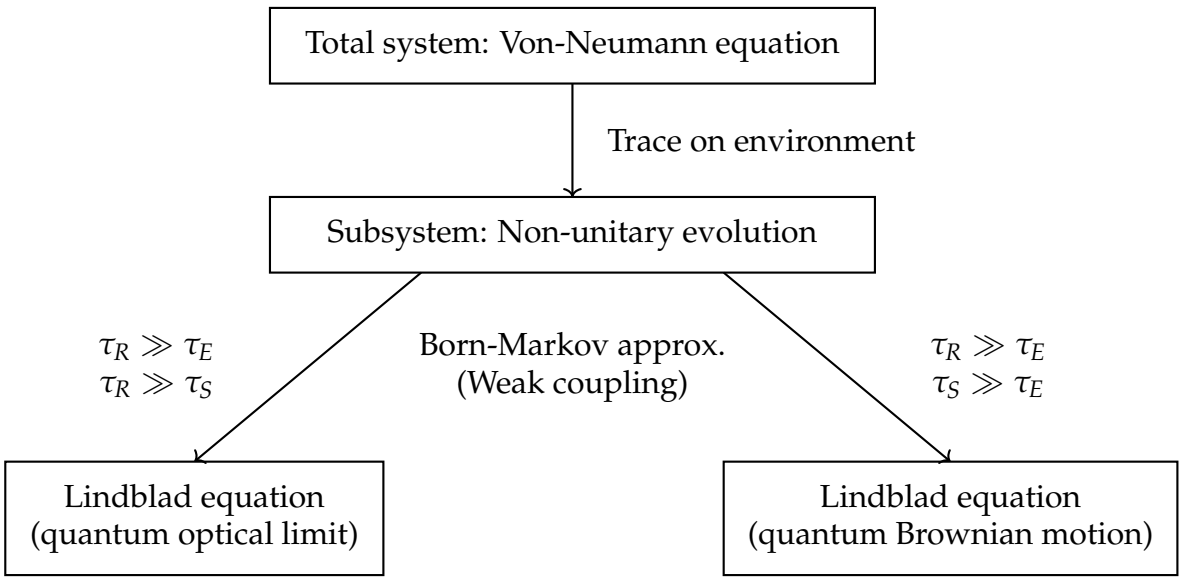


FIGURE 3.3 – Main steps and assumptions of the derivation of a Lindblad equation

## 3.7 Quarkonia as open quantum systems

In this section, we present several approaches based on open quantum systems that were developped in recent years. We start with early approaches, that were more phenomenology oriented before describing the most recent ones that are all derived from QCD first principles but use different strategies [1].

### 3.7.1 Early phenomenological approaches

Borghini and Gombeaud [138] proposed a phenomenological model based on the Einstein rate equation:

$$\frac{\mathrm{d}}{\mathrm{d}t}\rho_{ii}^{S}(t) = -\sum_{k\neq i}\Gamma_{i\to k}\rho_{ii}^{S}(t) + \sum_{k\neq i}\Gamma_{k\to i}\rho_{kk}^{S}(t) \tag{3.34}$$

with $\Gamma_{i\to k}$ the transition rate from quarkonium state $i$ to $k$ and $\rho_{ii}^{S}(t)$ the $i^{th}$ quarkonium state population. Those transition rates are given by Fermi's golden rule and the interaction between the heavy quark and antiquark is taken as the vacuum Coulomb potential.

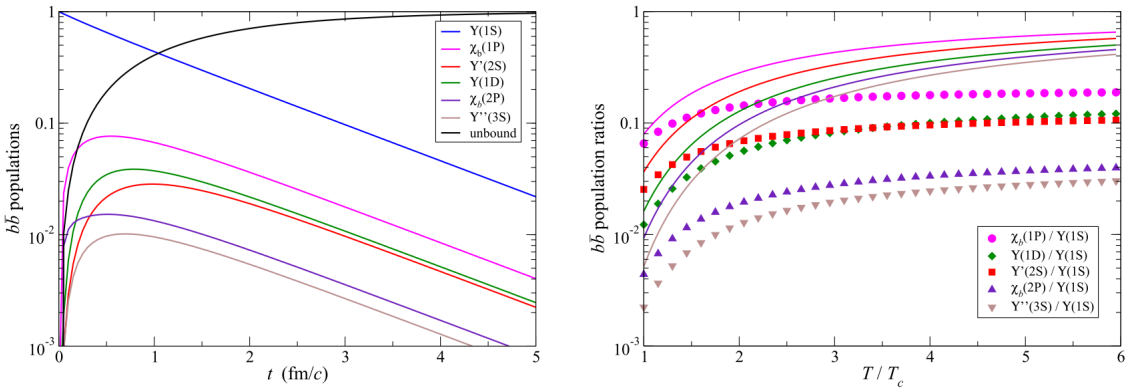


FIGURE 3.4 – Evolution of the quarkonium states populations over time (left) and (right) comparison of ratios of bottomonium populations obtained with the master equation (symbols) and with expected Boltzmann distributions (solid)

As shown on figure 3.4, they observed that at a constant temperature, all the bottomonium states they considered decayed at the same rate after a transient phase.

1. A more focused review can be found in [137]

They also observed a discrepancy between the temperature dependance of ratios of the bottomonium populations after the transient phase and in the case of a thermally equilibrated system (expected to follow a Boltzmann distribution). This difference is due to an incomplete modelling of the transitions between bound and free states.

Young and Dusling [139] used the Caldeira-Leggett [140] model to study the effect of interactions with the Quark-Gluon Plasma on the heavy quark-antiquark correlators. More precisely, they looked at how the masses, potential and drag force affected those correlators.

Akamatsu and Rothkopf [141] derived a quantum master equation and added a stochastic term in the unitary evolution operator.

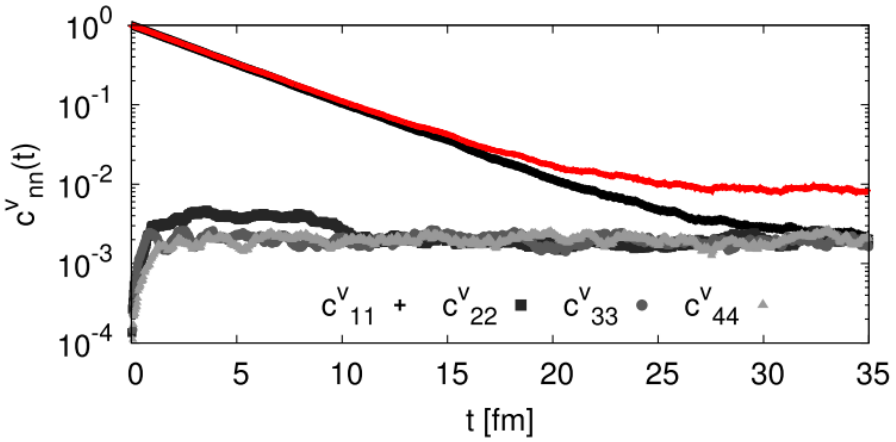


FIGURE 3.5 – Evolution of the populations of quarkonium states over time obtained with the stochastic potential model

This leads to decoherence and an exponential suppression of the ground states (see figure 3.5). However, their model lacks a friction term, which causes the system to be unable to reach thermalization as friction effects become important at later times and leads to uniform state populations at late times. The absence of friction also leads to the rise of the energy of the system.

### 3.7.2 Katz and Gossiaux

Katz and Gossiaux [142] proposed another approach based on a Langevin-like extension of the Schrödinger equation called the *Schrödinger-Langevin* equation (SLE):

$$i\hbar\frac{\mathrm{d}}{\mathrm{d}t}\Psi(x,t) = \left[H_0 + \hbar A\left(S(x,t) - \int \Psi^*(x,t)S(x,t)\Psi(x,t)dx\right) - xF_R(t)\right] \times \Psi(x,t) \tag{3.35}$$

where $A$ is a friction coefficient, $S(x,t)$ the real phase of the wavefunction and $F_R(t)$ a fluctuation operator.

In particular they applied this formalism in one dimension to the case of bottomonia suppression in ultra-relativistic heavy ion collisions [143].

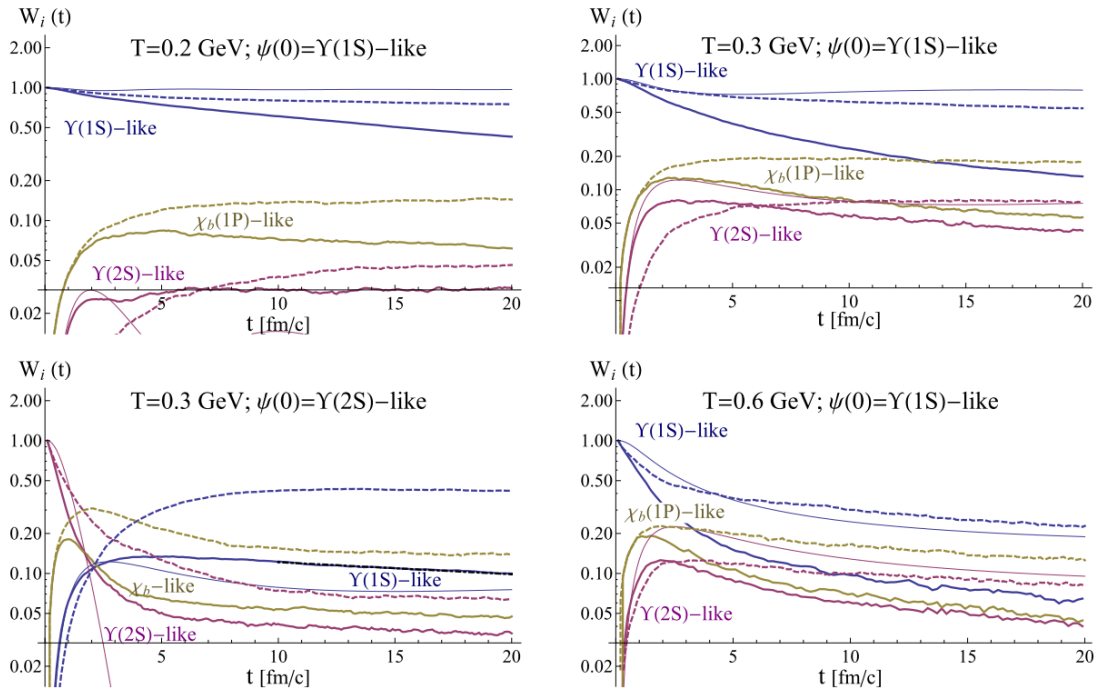


FIGURE 3.6 – Weights of the lowest 3 vacuum eigenstates for different temperatures and initial states without friction and stochastic forces (solid lines) and with friction and stochastic forces (dashed and thick lines, respectively with the vacuum and temperature dependant potentials)

Similarly to Borghini & Gombeaud [138] in section 3.7.1, they observed an asymptotic regime with uniform decay for all states considered after a transient phase (see figure 3.6). The latter was interpreted as a re-equilibration leading to a mixed state in thermal equilibrium with the environment. They also noted that stochastic forces had a greater role in destroying the bottomonium states at small temperatures while screening had a greater role at high temperatures.

This is one of the first approaches based on a stochastic Schrödinger equation, which includes both a stochastic force and friction. However, it is not derived from first QCD principles and can not be related to a Lindblad equation (for more details on their approach, see also [19]).

### 3.7.3 Akamatsu et al.: Quarkonium quantum master equation in the Lindblad form

Akamatsu [144] first derived a quantum master equation for a heavy quarkonium system. He later extended [145] this work using the influence functionnal formalism [146], which is the path-integral form of open quantum systems to derive a master equation in the Lindblad form. He derived in this paper explicit Lindblad equations for both the case of a single heavy quark and of a heavy quarkonium. He also derived the equivalent stochastic Schrödinger equation for the heavy quarkonium using a stochastic potential as in [141].

This stochastic Schrödinger equation was then resolved in one dimension [147], in the case of an expanding QGP following a Björken-like expansion for both charmonia and bottomonia. It should be noted that only the color singlet sector was considered in the resolution. In this paper, it was shown that the decoherence induced by the noise terms was an important mechanism for quarkonium suppression. A dependance on the system (bottomonium or charmonium) was also observed. An extension of this work to the case of a 3-dimensionnal system and taking into account the complete color structure was done in [148].

Another strategy to resolve the Lindblad equation derived in [145] was presented in [149] in the case of a single heavy quark in one dimension. In this paper, another type of stochastic Schrödinger equation was derived, using the *Quantum State Dif-*

*fusion* method [150][151]. This approach was then generalized to the heavy quarkonium case in one dimension in [152].

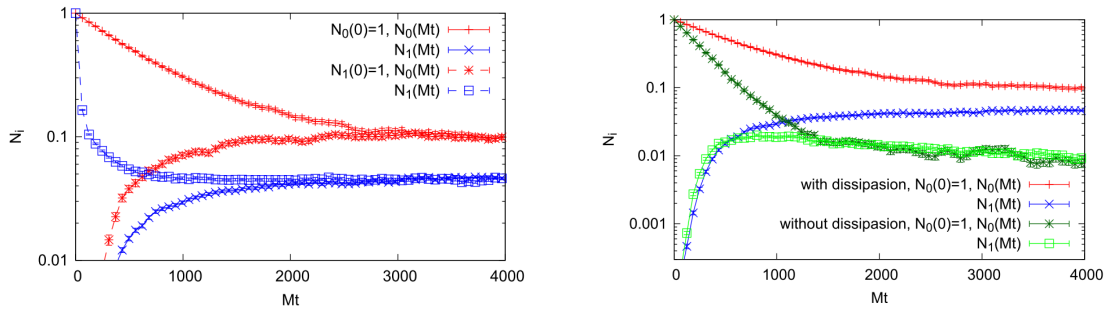


(A) (B)

FIGURE 3.7 – Occupation number of the ground and 1st excited state over time (left). Occupation number of the ground and 1st excited state over time with and without dissipation (right).

As shown on figure 3.7, they obtained for a fixed temperature a thermal steady state independent of the initial state, and which follows a Boltzmann distribution of the population. They also observed the differences that appear when the dissipative term is not included, both in the initial evolution and the late-time steady state. This is due to the fact that disspation prevents the pair from dissociating and balances the thermal fluctuations. They compared the results for both charmonia and bottomonia and also extended the analysis to the case of a cooling QGP medium [147].

More recently, a direct resolution of the Lindblad equation in the one dimensionnal case and for the singlet color space was done using a novel difference operator in [153].

### 3.7.4 Brambilla et al.: A pNRQCD based quantum master equation approach

Brambilla et al. used the potential Non-Relativistic QCD (pNRQCD) [154][155], an effective field theory formalism to derive a quantum master equation in the Lindblad form to describe quarkonium dynamics inside the Quark-Gluon Plasma [156][157]. They used pNRQCD to compute the evolution operators for the reduced

density matrix and only considered S-like and P-like states by performing an expansion in spherical harmonics to simplify the problem. They resolved those equation in an evolving medium following a Björken expansion for the bottomonium system.

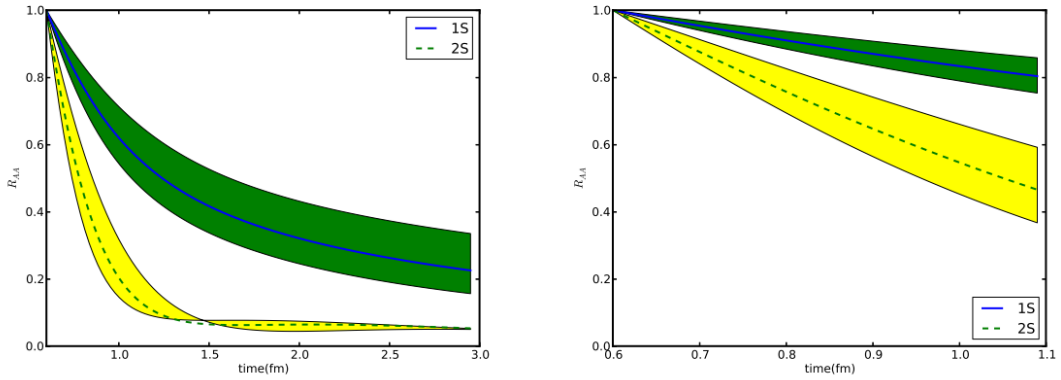


FIGURE 3.8 – *Left panel:* Bottomonium $R_{AA}$ for the 30-50% class of centrality. *Right panel:* Same for the 50-100% class of centrality. The error bands are due to unconstrained transport coefficients used in the computation.

As shown in figure 3.8, they observed that for mid-central collisions, the 2S state reached a steady state and is more strongly suppressed than in peripheral collisions.

They recently also turned their equation into a stochastic Schrödinger equation [158], using a different method than Akamatsu et al.[152] called the *Monte-Carlo Wave Function* method [159] and using transport coefficients computed in [160]. They published their code as an open-source package called QTraj [161], which they recently used to study the suppression and elliptic flow of bottomonia at the LHC [162]. Their results on the nuclear modification factors are in good agreement with experimental data and the predicted elliptic flow is compatible within experimental uncertainty with the data.

### 3.7.5 Yao et al.: Boltzmann equation derived from pNRQCD effective theory

Yao and Mehen [163] derived some coupled Boltzmann transport equations using the pNRQCD formalism, the include dissociation and recombination. More precisely, they first derived a Lindblad equation from first principles, using pNRQCD

to describe the interaction Hamiltonian. Then, they used the Wigner transform of the density matrix to derive the Boltzmann equation. The derivation of a transport equation from an effective field theory is of particular relevance as compared to models based on cross-sections for the dissociation and recombination rates like in [164][165].

They later applied this approach to study bottomonium dynamics in heavy ion collisions [166]. They resolved numerically the coupled Boltzmann equations using Monte-Carlo techniques and compared their results to experimental data from the LHC and RHIC.

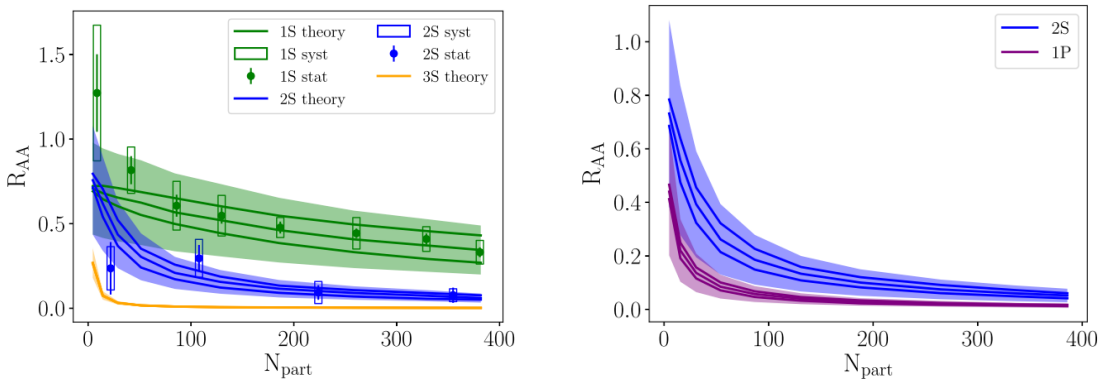


(A) (B)

FIGURE 3.9 – *Left panel:* $R_{AA}$ as a function of the number of participants for the first three Y states computed from coupled Boltzmann equations and compared to experimental data in $\sqrt{s_{NN}} = 2.76$ TeV Pb-Pb collisions. *Right panel:* $R_{AA}$ as a function of the number of participants for the $\Upsilon(2S)$ and $\chi_b(1P)$ states computed from coupled Boltzmann equations.

Their results on $R_{AA}$ (see figure 3.9) are compatible with experimental data from the LHC, but are still subject to large uncertainties. They may not be compatible with RHIC data, where more precise measurements are needed. They also made a prediction on the suppression of $\Upsilon(2S)$ and $\chi_b(1P)$, concluding that the $\chi_b(1P)$ may be more suppressed than the $\Upsilon(2S)$ due to the recombination mechanism. Yao et al. also plan to extend this work to the charmonia states. A complete review of this approach can be found in [167].

### 3.7.6 Blaizot et al.: Quantum dynamics of heavy quarks in the QGP

The final approach we will address in this section is an approach by Blaizot et al. [168]. Using the influence functionnal formalism, they first derived a quantum master equation for a heavy quark-antiquark pair in the case of an Abelian plasma. They then performed a semi-classical approximation to get a Langevin equation. This allow them to treat multiple pairs at the same time, which remains a theoretical challenge, and is mandatory if one wants to make accurate predictions for charmonia at the LHC.

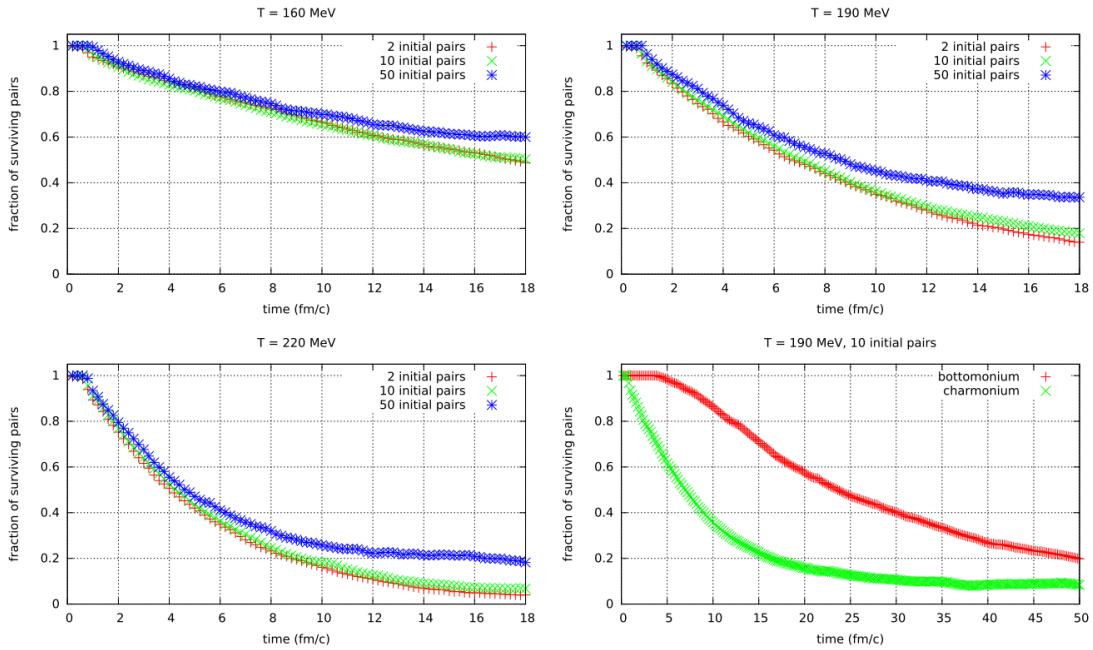


FIGURE 3.10 – *Top left panel:* Fraction of surviving pairs at T = 150 MeV for 2, 10 and 50 initial pairs. *Top right panel:* Same for T = 190 MeV. *Bottom left panel:* Same for T = 220 MeV. *Bottom right panel:* Fraction of surviving pairs at T = 190 MeV for 10 initial bottomonium or charmonium pairs

They computed the fraction of surviving pairs over time (see figure 3.10) at different temperatures and for different amounts of pairs. From those results, they infered the dissociation and recombinaison rates of the pairs. As could be expected, they observed lower survival fractions at higher temperatures. They also observed the effect of recombination when the amount of pairs involved is large, as the survival fractions were higher for a large amount of pairs. They also showed that the

bottomonium states survive more than charmonium states, for the same amount of initial pairs, which is also expected.

While derived from first principles, the quantum master equation is not a Lindblad equation, as positivity is not preserved. This was resolved in [169] where De Boni extended the derivation to get a master equation preserving positivity by adding quadratic terms by hand.

As we mentionned, this approach has the merit to tackle the challenging problem of multiple $Q\bar{Q}$ pairs. The next section of this chapter is devoted to the extension of this work to the case of a non-Abelian plasma (i.e. a proper Quark-Gluon Plasma), which will be the basis of the work presented in the remaining chapters of this thesis.

## 3.8 Quantum dynamics of heavy quarks in the QGP and semi-classical approximation

In this section we present the approach from Blaizot and Escobedo [2] in the case of a non-Abelian plasma. Their approach is based on two main approximations: 1) a weak coupling between the heavy quarks and the plasma constituents and 2) a fast plasma response to the perturbation caused by the heavy quarks compared to the typical timescales of the heavy quarks. We start from the von Neumann equation:

$$\frac{\mathrm{d}}{\mathrm{d}t}\mathcal{D} = -i[H, \mathcal{D}] \tag{3.36}$$

with $H = H_0 + H_1$; $H_0 = H_{Q\bar{Q}} + H_{QGP}$ where $H_{Q\bar{Q}}$ is the free Hamiltonian of the pair and $H_{QGP}$ is the QGP Hamiltonian; $H_1 = -g \int_r A_0^a(r) n^a(r)$ the interaction between the plasma and the heavy quarks, where $n^a(r)$ is the color charge density of the heavy quarks, $A_0^a$ is the chromo-electric potential and $r$ the distance between the quark and antiquark. A sum on the color index $a$ is implied.

As we did in section 3.4, we can get the following equation in the interaction representation:

$$\frac{\mathrm{d}}{\mathrm{d}t}\mathcal{D}^I = -i\Big[H_1(t), \mathcal{D}^I(t_0)\Big] - \int_{t_0}^{t} dt' \Big[H_1(t), \Big[H_1(t'), \mathcal{D}^I(t')\Big]\Big] \tag{3.37}$$

Thanks to the weak coupling approximation, we can factorize the density matrix:

$$\mathcal{D}^I(t) = \mathcal{D}^I_{Q\bar{Q}}(t) \otimes \mathcal{D}^I_{QGP}(t_0) \tag{3.38}$$

Performing the trace over the environment degrees of freedom, we obtain:

$$\begin{aligned}\frac{\mathrm{d}}{\mathrm{d}t}\mathcal{D}^I_{Q\bar{Q}} = -\int_{t_0}^{t} dt' \int_{\mathbf{x},\mathbf{x}'} \Big( &\Big[n^a(t,\mathbf{x}), n^a(t',\mathbf{x}')\mathcal{D}^I_{Q\bar{Q}}(t')\Big]\Delta^{>}(t-t',\mathbf{x}\text{ - }\mathbf{x}') \\ &+ \Big[\mathcal{D}^I_{Q\bar{Q}}(t')n^a(t',\mathbf{x}'), n^a(t,\mathbf{x})\Big]\Delta^{<}(t-t',\mathbf{x}\text{ - }\mathbf{x}')\Big)\end{aligned} \tag{3.39}$$

where the $\Delta$ are the gauge field correlators in the plasma, defined as:

$$\begin{aligned}\mathrm{Tr}_{QGP}\Big[A^b_0(t_1,\mathbf{x})\mathcal{D}^I_{QGP}(t_0)A^a_0(t_2,\mathbf{x}')\Big] &= \delta^{ab}\Delta^{>}(t_2-t_1,\mathbf{x}'\text{ - }\mathbf{x}) \\ &= \delta^{ab}\Delta^{<}(t_1-t_2,\mathbf{x}\text{ - }\mathbf{x}')\end{aligned} \tag{3.40}$$

As in section 3.6, we can apply the Markovian approximation and replace $\mathcal{D}^I(t')$ by $\mathcal{D}^I(t)$ in (3.39). If we now go back to the Schrödinger representation and define $\tau = t - t'$, we get:

$$\begin{aligned}&\frac{\mathrm{d}}{\mathrm{d}t}\mathcal{D}_{Q\bar{Q}} + i\Big[H_{Q\bar{Q}}, \mathcal{D}_{Q\bar{Q}}\Big] = \\ &\quad - \int_{\mathbf{x},\mathbf{x}'}\int_0^{t-t_0} d\tau \Big[n^a_{\mathbf{x}}, U_{Q\bar{Q}}(\tau)n^a_{\mathbf{x}'}U^{\dagger}_{Q\bar{Q}}(\tau)\mathcal{D}_{Q\bar{Q}}(t)\Big]\Delta^{>}(\tau,\mathbf{x}\text{ - }\mathbf{x}') \\ &\quad - \int_{\mathbf{x},\mathbf{x}'}\int_0^{t-t_0} d\tau \Big[\mathcal{D}_{Q\bar{Q}}(t)U_{Q\bar{Q}}(\tau)n^a_{\mathbf{x}'}U^{\dagger}_{Q\bar{Q}}(\tau), n^a_{\mathbf{x}}\Big]\Delta^{<}(\tau,\mathbf{x}\text{ - }\mathbf{x}')\end{aligned} \tag{3.41}$$

Since only small values of $\tau$ are relevant, we can perform a series expansion of the evolution operators $U : e^{-iH_{Q\bar{Q}}\tau} \simeq 1 - iH_{Q\bar{Q}}\tau$. Keeping only terms up to linear order

in $\tau$, we have:

$$U_{Q\bar{Q}}(\tau)n^a_{\mathbf{x}'}U^\dagger_{Q\bar{Q}}(\tau) = U^\dagger_{Q\bar{Q}}(-\tau)n^a_{\mathbf{x}'}U_{Q\bar{Q}}(-\tau) = n^a_{\mathbf{x}'}(-\tau) \tag{3.42}$$

with $n^a_{\mathbf{x}'}(-\tau) = n^a_{\mathbf{x}'}(\tau) - \tau\dot{n}^a_{\mathbf{x}'}(-\tau)$. This gives us [2]:

$$\begin{aligned}\frac{\mathrm{d}}{\mathrm{d}t}\mathcal{D}_{Q\bar{Q}} + i\Big[H_{Q\bar{Q}}, \mathcal{D}_{Q\bar{Q}}\Big] \simeq &- \int_{\mathbf{x},\mathbf{x}'}\Big[n^a_{\mathbf{x}}, n^a_{\mathbf{x}'}\mathcal{D}_{Q\bar{Q}}\Big]\int_0^\infty d\tau\Delta^>(\tau, \mathbf{x}\text{ - }\mathbf{x}') \\ &- \int_{\mathbf{x},\mathbf{x}'}\Big[\mathcal{D}_{Q\bar{Q}}n^a_{\mathbf{x}'}, n^a_{\mathbf{x}}\Big]\int_0^\infty d\tau\Delta^<(\tau, \mathbf{x}\text{ - }\mathbf{x}') \\ &+ \int_{\mathbf{x},\mathbf{x}'}\Big[n^a_{\mathbf{x}}, \dot{n}^a_{\mathbf{x}'}\mathcal{D}_{Q\bar{Q}}\Big]\int_0^\infty d\tau\tau\Delta^>(\tau, \mathbf{x}\text{ - }\mathbf{x}') \\ &+ \int_{\mathbf{x},\mathbf{x}'}\Big[\mathcal{D}_{Q\bar{Q}}\dot{n}^a_{\mathbf{x}'}, n^a_{\mathbf{x}}\Big]\int_0^\infty d\tau\tau\Delta^<(\tau, \mathbf{x}\text{ - }\mathbf{x}')\end{aligned} \tag{3.43}$$

It can be shown [170][171] that the time integrals involves the zero-frequency time-ordered propagator $\Delta(\omega = 0)$ which is identified to a complex potential $V(r) + iW(r)$. This complex potential has been derived using the Har Thermal Loop (HTL) perturbation theory [170][171] in [172][173]. We finally get the quantum master equation:

$$\frac{\mathrm{d}}{\mathrm{d}t}\mathcal{D}_{Q\bar{Q}} = \mathcal{L}\mathcal{D}_{Q\bar{Q}} \tag{3.44}$$

with $\mathcal{L} = \mathcal{L}_0 + \mathcal{L}_1 + \mathcal{L}_2 + \mathcal{L}_3$ and:

$$\begin{aligned}\mathcal{L}_0\mathcal{D}_{Q\bar{Q}} &= -i\Big[H_{Q\bar{Q}}, \mathcal{D}_{Q\bar{Q}}\Big] \\ \mathcal{L}_1\mathcal{D}_{Q\bar{Q}} &= -\frac{i}{2}\int_{\mathbf{x},\mathbf{x}'}V(\mathbf{x}\text{ - }\mathbf{x}')\Big[n^a_{\mathbf{x}}n^a_{\mathbf{x}'}, \mathcal{D}_{Q\bar{Q}}\Big] \\ \mathcal{L}_2\mathcal{D}_{Q\bar{Q}} &= \frac{1}{2}\int_{\mathbf{x},\mathbf{x}'}W(\mathbf{x}\text{ - }\mathbf{x}')\left(\Big\{n^a_{\mathbf{x}}n^a_{\mathbf{x}'}, \mathcal{D}_{Q\bar{Q}}\Big\} - 2n^a_{\mathbf{x}}\mathcal{D}_{Q\bar{Q}}n^a_{\mathbf{x}'}\right) \\ \mathcal{L}_3\mathcal{D}_{Q\bar{Q}} &= \frac{i}{4T}\int_{\mathbf{x},\mathbf{x}'}W(\mathbf{x}\text{ - }\mathbf{x}')\left(\Big[n^a_{\mathbf{x}'}, \dot{n}^a_{\mathbf{x}'}\mathcal{D}_{Q\bar{Q}}\Big] - \Big[n^a_{\mathbf{x}'}, \mathcal{D}_{Q\bar{Q}}\dot{n}^a_{\mathbf{x}'}\Big]\right)\end{aligned} \tag{3.45}$$

2. Like in section 3.4, we extended the time integration domain to (0,∞).

If we omit the $\mathcal{L}_3$ terms, the equation (3.45) has the same structure as of a Lindblad equation. Unfortunately, the $\mathcal{L}_3$ terms are responsible for the breaking of positivity and thus this master equation can not be put in the Lindblad form. This positivity breaking problem will be further investigated and resolved in chapter 4.
The color charge density for a heavy quark-antiquark pair in QCD is given by:

$$n^a_{\mathbf{x}} = \delta(\mathbf{x} - \mathbf{r}) t^a \otimes \mathbb{1} - \mathbb{1} \otimes \delta(\mathbf{x} - \mathbf{r}) \tilde{t}^a \tag{3.46}$$

We then decompose the reduced density matrix into a color singlet and a color octet components:

$$\mathcal{D}_{Q\bar{Q}} = \mathcal{D}_s \, |s\rangle\langle s| + \mathcal{D}_o \sum_c |o^c\rangle\langle o^c| \tag{3.47}$$

with $|s\rangle\langle s|$ a projector on a color singlet state and $|o^c\rangle\langle o^c|$ a projector on a color octet state. We now have the following coupled equations:

$$\frac{\mathrm{d}}{\mathrm{d}t} \begin{pmatrix} \mathcal{D}_s \\ \mathcal{D}_o \end{pmatrix} (\mathbf{r}_1, \mathbf{r}_2, \mathbf{r}'_1, \mathbf{r}'_2) = \mathcal{L} \begin{pmatrix} \mathcal{D}_s \\ \mathcal{D}_o \end{pmatrix} (\mathbf{r}_1, \mathbf{r}_2, \mathbf{r}'_1, \mathbf{r}'_2) \tag{3.48}$$

where $\mathbf{r}_1$ and $\mathbf{r}_2$ are the coordinates of the quark and antiquark and the $\mathbf{r}'_1$ and $\mathbf{r}'_2$ are conjugated variables that were introduced to keep the time real in the derivation. We have $\mathcal{L} = \begin{pmatrix} \mathcal{L}_{ss} & \mathcal{L}_{so} \\ \mathcal{L}_{os} & \mathcal{L}_{oo} \end{pmatrix}$ where the $\mathcal{L}_{ss,so,os,oo}$ operators describe color state transitions. Introducing the following notation $W_{ab} = W(\mathbf{r}_a - \mathbf{r}_b)$, we define:

$$\begin{aligned} W_a &= W_{11'} + W_{22'} \quad W_b = W_{21'} + W_{12'} \\ W_c &= W_{12} + W_{1'2'} \quad W_\pm = W_a \pm W_b, \end{aligned} \tag{3.49}$$

one can write the different expressions for the $\mathcal{L}$ operators (see Appendix A for details on the computation):

$$
\begin{aligned}
\mathcal{L}^0_{ss} &= \mathcal{L}^0_{oo} = \frac{1}{2M}\left[\nabla^2_{\mathbf{r}_1} + \nabla^2_{\mathbf{r}_2} + \nabla^2_{\mathbf{r}'_1} + \nabla^2_{\mathbf{r}'_2}\right] \\
\mathcal{L}^1_{ss} &= C_F[V_{12} - V_{1'2'}] \quad \mathcal{L}^1_{oo} = -\frac{1}{2N_c}[V_{12} - V_{1'2'}] \\
\mathcal{L}^2_{ss} &= C_F[2W(0) - W_c] \\
\mathcal{L}^2_{oo} &= 2C_F W(0) + \frac{1}{2N_c}W_c - \frac{N_c^2-2}{2N_c}W_a + \frac{1}{N_c}W_b \\
\mathcal{L}^2_{so} &= -C_F W_- \qquad \mathcal{L}^2_{os} = -\frac{1}{2N_c}W_- \\
\mathcal{L}^3_{ss} &= \frac{C_F}{4MT}\left[2\nabla^2 W(0) - \nabla^2 W_c - \nabla W_c \cdot \nabla_c\right] \\
\mathcal{L}^3_{oo} &= \frac{C_F}{2MT}\nabla^2 W(0) + \frac{1}{4MT}\frac{1}{2N_c}\left[\nabla^2 W_c + \nabla W_c \cdot \nabla_c\right] \\
&\quad - \frac{1}{4MT}\left\{\frac{N_c^2-2}{2N_c}\left[\nabla^2 W_- + \nabla W_- \cdot \nabla_-\right] + \frac{N_c}{4}\left[\nabla^2 W_+ + \nabla W_+ \cdot \nabla_+\right]\right\} \\
\mathcal{L}^3_{so} &= -\frac{C_F}{4MT}\left[\nabla^2 W_- + \nabla W_- \cdot \nabla_-\right] \\
\mathcal{L}^3_{os} &= -\frac{1}{4MT}\frac{1}{2N_c}\left[\nabla^2 W_- + \nabla W_- \cdot \nabla_-\right]
\end{aligned}
\tag{3.50}
$$

with $\nabla W_c \cdot \nabla_c = \nabla_1 W_{12} \cdot (\nabla_1 - \nabla_2) + \nabla_{1'} W_{1'2'} \cdot (\nabla_{1'} - \nabla_{2'})$ and similar notations.

Blaizot & Escobedo used another set of variables more relevant for the analysis, based on the center of masses and relative coordinates,

$$
\begin{aligned}
\mathcal{R} &= \frac{\mathbf{R} + \mathbf{R}'}{2} \quad \Upsilon = \mathbf{R} - \mathbf{R}' \\
y &= \mathbf{s} - \mathbf{s}' \quad r = \frac{\mathbf{s} + \mathbf{s}'}{2}
\end{aligned}
\tag{3.51}
$$

where $R, R', s$ and $s'$ are defined by:

$$
\begin{aligned}
\mathbf{R} &= \frac{\mathbf{r}_1 + \mathbf{r}_2}{2} \quad \mathbf{R}' = \frac{\mathbf{r}'_1 + \mathbf{r}'_2}{2} \\
\mathbf{s} &= \mathbf{r}_1 - \mathbf{r}_2 \quad \mathbf{s}' = \mathbf{r}'_1 - \mathbf{r}'_2.
\end{aligned}
\tag{3.52}
$$

The $y$ variable measures the deviation from a diagonal matrix, which is reached in the classical limit. They then performed a small-$y$ expansion, that can be then interpreted as a semi-classical approximation:

$$W(y) \simeq W(0) + \frac{1}{2} y \cdot \mathcal{H}(0) \cdot y + \cdots \tag{3.53}$$

with $\mathcal{H}(y)$ the Hessian matrix of W.

They then performed a Wigner transform on the resulting equations, leading to a Langevin equation. The correlation of the noise in this Langevin equation is given by the second order derivative of the imaginary part of the potential W. The latter Langevin equation can be used to simulate multiple $Q\bar{Q}$ pairs simultaneously, which is still a challenging problem. The work of Blaizot & Escobedo is truly pionneering since it was one of the first approaches which uses a Langevin equation derived from a master equation.

However, several issues remain:

— The validity of the semi-classical approximation was never verified by actually solving the equations directly and only motivated by a scale analysis. A more systematic study of the feasability of a semi-classical treatment is thus needed to find out if there exists a physical regime where it is possible. If such regime exists, the simultaneous treatment of multiple pairs, which is crucial for phenomenology, would be accessible.

— The coupled master equations derived in their paper break positivity as will be explicitely shown in the next chapter in section 4.4. This limits the validity range of those equations.

— Blaizot & Escobedo mentionned that it is possible to get Lindblad equations (albeit not in the Lindblad form) by adding higher-order terms, However, they have not derived those terms, assuming them to be subleading and without significant effects on the dynamics. The importance of those terms will be studied in this thesis.

— The present quantum master equations were never resolved directly, which is a challenging problem, to explore all the physics they contain.

All of this leads us to the approach that will be developped in the remaining chapters of this thesis. In chapter 4, we first follow the procedure described in their original paper to derive properly the higher-order terms that will restore the positivity of the reduced density operator. We will show that the new equations derived satisfy the properties of a Lindblad equation. Then, in chapter 5, we will proceed to show how we resolve numerically the new equations that will be derived without performing the semi-classical approximation. Finally, in chapter 6, we will study the dynamics of a heavy quarkonium in the Quark-Gluon Plasma and test the range of validity of the semi-classical approximation.

# Chapter 4

# Extension of the Blaizot-Escobedo equations and restoration of positivity

In this chapter, we develop a strategy to treat one of the major shortcomings of the approach by Blaizot & Escobedo, the breaking of positivity. To do so, we first follow a procedure to derive new terms that should restore positivity. We will then prove that both unitarity and positivity are preserved with the new equations. The last part will be devoted to the treatment of divergences that arise in the new equations. This will lead to a global strategy to study the dynamics of a heavy quarkonium in the Quark-Gluon Plasma, which will be done in chapter 6.

## 4.1 Alternative time discretization

In the appendix B of their paper [2], Blaizot & Escobedo used another time discretization to derive their master equations, which leads to some new terms they however never derived completely in the direct space. They started from the following equation (equation B.9 in their paper):

$$\begin{aligned}\frac{\mathrm{d}}{\mathrm{d}t}\mathcal{D}_{Q\bar{Q}}(t)+i\Big[H_Q,\mathcal{D}_{Q\bar{Q}}(t)\Big] &= -\frac{i}{2}\int_{\mathbf{x},\mathbf{x}'}V(\mathbf{x}\text{-}\mathbf{x}')\Big[n^a_{\mathbf{x}}n^a_{\mathbf{x}'},\mathcal{D}_{Q\bar{Q}}\Big]\\ &+\frac{1}{2}\int_{\mathbf{x},\mathbf{x}'}W(\mathbf{x}\text{-}\mathbf{x}')\Big(\Big\{n^a_{\mathbf{x}}n^a_{\mathbf{x}'},\mathcal{D}_{Q\bar{Q}}\Big\}-2n^a_{\mathbf{x}}\mathcal{D}_{Q\bar{Q}}n^a_{\mathbf{x}'}\Big)\\ &-\frac{i}{4T}\int_{\mathbf{x},\mathbf{x}'}W(\mathbf{x}\text{-}\mathbf{x}')\Big(\dot{n}^a_{\mathbf{x}}\mathcal{D}_{Q\bar{Q}}n^a_{\mathbf{x}'}-n^a_{\mathbf{x}}\mathcal{D}_{Q\bar{Q}}\dot{n}^a_{\mathbf{x}'}\Big)\\ &-\frac{i}{8T}\int_{\mathbf{x},\mathbf{x}'}W(\mathbf{x}\text{-}\mathbf{x}')\Big\{\mathcal{D}_{Q\bar{Q}},[\dot{n}^a_{\mathbf{x}},n^a_{\mathbf{x}'}]\Big\}.\end{aligned}\tag{4.1}$$

The equation (4.1) doesn't preserve positivity, however, it is possible to transform it to this end. One can first notice that up to the second line, the equation (4.1) is a Lindblad equation. Moreover, it is possible to obtain the third and fourth lines of equation (4.1), by performing the following transformation in the second line:

$$\frac{1}{2}\int_{\mathbf{x},\mathbf{x}'} W(\mathbf{x}\text{-}\mathbf{x}')\left(\left\{\left(n^a_{\mathbf{x}}-\frac{i}{4T}\dot{n}^a_{\mathbf{x}}\right)\left(n^a_{\mathbf{x}'}+\frac{i}{4T}\dot{n}^a_{\mathbf{x}'}\right),\mathcal{D}_{Q\bar{Q}}\right\}\right.$$
$$\left.-2\left(n^a_{\mathbf{x}}+\frac{i}{4T}\dot{n}^a_{\mathbf{x}}\right)\mathcal{D}_{Q\bar{Q}}\left(n^a_{\mathbf{x}'}-\frac{i}{4T}\dot{n}^a_{\mathbf{x}'}\right)\right). \tag{4.2}$$

Equation (4.2) generates three types of terms:

— The terms without any $\dot{n}$, which correspond to the second line of equation (4.1) and are the original $\mathcal{L}_2$ terms.

— The terms linear in $\dot{n}$, which correspond to the third and fourth lines of equation (4.1). They will be refered later as $\mathcal{L}'_3$ (since they are different from the original $\mathcal{L}_3$ terms).

— The terms quadratic in $\dot{n}$, which correspond to higher order terms in $\frac{1}{MT}$ and are the new terms that will restore the positivity. They will be refered as $\mathcal{L}_4$ terms.

We will follow the same procedure as in Appendix A of this thesis to derive the new terms: we first derive them in the QED case and identify the $\mathcal{L}_{QQ,a}$,$\mathcal{L}_{Q\bar{Q},a}$,$\mathcal{L}_{QQ,b}$ and $\mathcal{L}_{Q\bar{Q},b}$ operators. The equations in the QCD case can then be easily derived using those operators. A small disclaimer is necessary: in the following sections, the operators may be written as $\mathcal{L}_{3,QQ,a}$ or $\mathcal{L}^3_{QQ,a}$ (and similar notations for higher order terms) but both notations point to the same operators.

### 4.1.1 Derivation of the $\mathcal{L}'_3$ terms

By observing the terms of the form $n\mathcal{D}_{Q\bar{Q}}\dot{n}$ or $\dot{n}\mathcal{D}_{Q\bar{Q}}n$, which correspond to the $\mathcal{L}^3_{QQ,b}$ and $\mathcal{L}^3_{Q\bar{Q},b}$ operators, in both discretizations, we see that they are actually the same. The computation is thus straightforward and one gets (as in equations (3.49)

and (3.50)):

$$\begin{aligned}\langle \mathbf{r}_1\mathbf{r}_2|\mathcal{L}_{QQ,b}\mathcal{D}_{Q\bar{Q}}|\mathbf{r}_1'\mathbf{r}_2'\rangle &= -\frac{1}{4MT}[\Delta W_a + \nabla W_a\cdot\nabla_a]\,\langle \mathbf{r}_1\mathbf{r}_2|\mathcal{D}_{Q\bar{Q}}|\mathbf{r}_1'\mathbf{r}_2'\rangle \\ \langle \mathbf{r}_1\mathbf{r}_2|\mathcal{L}_{Q\bar{Q},b}\mathcal{D}_{Q\bar{Q}}|\mathbf{r}_1'\mathbf{r}_2'\rangle &= \frac{1}{4MT}[\Delta W_b + \nabla W_b\cdot\nabla_b]\,\langle \mathbf{r}_1\mathbf{r}_2|\mathcal{D}_{Q\bar{Q}}|\mathbf{r}_1'\mathbf{r}_2'\rangle\,. \end{aligned} \tag{4.3}$$

In the new discretization, the $\mathcal{L}^3_{QQ,a}$ and $\mathcal{L}^3_{Q\bar{Q},a}$ contributions correspond to:

$$\mathcal{L}'_{3a}\mathcal{D}_{Q\bar{Q}} = \frac{i}{8T}\int_{\mathbf{x}\mathbf{x}'} W_{\mathbf{x}\mathbf{x}'}\Big[\mathcal{D}_{Q\bar{Q}}n_{\mathbf{x}}\dot{n}_{\mathbf{x}'} + n_{\mathbf{x}}\dot{n}_{\mathbf{x}'}\mathcal{D}_{Q\bar{Q}} - \mathcal{D}_{Q\bar{Q}}\dot{n}_{\mathbf{x}'}n_{\mathbf{x}} - \dot{n}_{\mathbf{x}'}n_{\mathbf{x}}\mathcal{D}_{Q\bar{Q}}\Big]. \tag{4.4}$$

By comparing with the original discretization, one can see that:

$$\mathcal{L}'_{3a}\mathcal{D}_{Q\bar{Q}} = \frac{1}{2}\mathcal{L}_{3a}\mathcal{D}_{Q\bar{Q}} + \frac{i}{8T}\int_{\mathbf{x}\mathbf{x}'} W_{\mathbf{x}\mathbf{x}'}\Big[\mathcal{D}_{Q\bar{Q}}n_{\mathbf{x}}\dot{n}_{\mathbf{x}'} - \dot{n}_{\mathbf{x}'}n_{\mathbf{x}}\mathcal{D}_{Q\bar{Q}}\Big]. \tag{4.5}$$

Let us start by computing the second term of the right-hand side of equation (4.5). Introducing completion relations, we obtain:

$$\begin{aligned}&\frac{i}{8T}\int_{\mathbf{x}\mathbf{x}'} W_{\mathbf{x}\mathbf{x}'}\,\langle \mathbf{r}_1\mathbf{r}_2|\mathcal{D}_{Q\bar{Q}}n_{\mathbf{x}}\dot{n}_{\mathbf{x}'}|\mathbf{r}_1'\mathbf{r}_2'\rangle \\ =&\frac{i}{8T}\int_{\substack{\mathbf{x}\mathbf{x}'\\ \mathbf{a}\mathbf{a}'\\ \mathbf{b}\mathbf{b}'}} W_{\mathbf{x}\mathbf{x}'}\,\langle \mathbf{r}_1\mathbf{r}_2|\mathcal{D}_{Q\bar{Q}}|\mathbf{a}\mathbf{a}'\rangle\,\langle \mathbf{a}\mathbf{a}'|n_{\mathbf{x}}|\mathbf{b}\mathbf{b}'\rangle\,\langle \mathbf{b}\mathbf{b}'|\dot{n}_{\mathbf{x}'}|\mathbf{r}_1'\mathbf{r}_2'\rangle\,, \end{aligned} \tag{4.6}$$

with $W_{\mathbf{x}\mathbf{x}'} = W(\mathbf{x}-\mathbf{x}')$. As shown in Appendix A the expressions of the charge density matrix elements and their derivatives are :

$$\begin{aligned}\langle \mathbf{r}_1\mathbf{r}_2|n_{\mathbf{x}}|\mathbf{r}_1'\mathbf{r}_2'\rangle &= \delta_{11'}\delta_{22'}[\delta_{\mathbf{x}1} - \delta_{\mathbf{x}1'}] \\ \langle \mathbf{r}_1\mathbf{r}_2|\dot{n}_{\mathbf{x}}|\mathbf{r}_1'\mathbf{r}_2'\rangle &= -\frac{1}{2iM}[\nabla_1\delta_{11'}]\cdot\nabla_{\mathbf{x}}[\delta_{\mathbf{x}1'} + \delta_{\mathbf{x}1}]\delta_{22'} \\ &\quad + \frac{1}{2iM}[\nabla_2\delta_{22'}]\cdot\nabla_{\mathbf{x}}[\delta_{\mathbf{x}2'} + \delta_{\mathbf{x}2}]\delta_{11'}, \end{aligned} \tag{4.7}$$

with $\delta_{11'} = \delta^{(3)}(\mathbf{r}_1 - \mathbf{r}'_1)$, $\delta_{\mathbf{x}1'} = \delta^{(3)}(\mathbf{x} - \mathbf{r}'_1)$ and similar notations.

The equations (4.6) and (4.7)

$$\begin{aligned}
&\frac{i}{8T}\int_{\substack{\mathbf{xx'}\\ \mathbf{aa'}\\ \mathbf{bb'}}} W_{\mathbf{xx'}} \left\langle \mathbf{r}_1\mathbf{r}_2\right|\mathcal{D}_{Q\bar{Q}}\left|\mathbf{aa'}\right\rangle \left\langle \mathbf{aa'}\right|n_{\mathbf{x}}\left|\mathbf{bb'}\right\rangle \left\langle \mathbf{bb'}\right|\dot{n}_{\mathbf{x'}}\left|\mathbf{r}'_1\mathbf{r}'_2\right\rangle \\
=&\frac{1}{16MT}\int_{\substack{\mathbf{xx'}\\ \mathbf{aa'}\\ \mathbf{bb'}}} W_{\mathbf{xx'}} \left\langle \mathbf{r}_1\mathbf{r}_2\right|\mathcal{D}_{Q\bar{Q}}\left|\mathbf{aa'}\right\rangle \delta_{\mathbf{ab}}\delta_{\mathbf{a'b'}}[\delta_{\mathbf{xa}} - \delta_{\mathbf{xb}}] \\
&\qquad\times\Big\{[\nabla_{\mathbf{b'}}\delta_{\mathbf{b'}2'}]\cdot\nabla_{\mathbf{x'}}[\delta_{\mathbf{x'}2'} + \delta_{\mathbf{x'b'}}]\delta_{\mathbf{b}1'} \\
&\qquad\quad -[\nabla_{\mathbf{b}}\delta_{\mathbf{b}1'}]\cdot\nabla_{\mathbf{x'}}[\delta_{\mathbf{x'}1'} + \delta_{\mathbf{x'b}}]\delta_{\mathbf{b'}2'}\Big\} \\
=&\frac{1}{16MT}\int_{\substack{\mathbf{xx'}\\ \mathbf{aa'}}} [W_{\mathbf{ax'}} - W_{\mathbf{a'x'}}] \left\langle \mathbf{r}_1\mathbf{r}_2\right|\mathcal{D}_{Q\bar{Q}}\left|\mathbf{aa'}\right\rangle \\
&\qquad\times\Big\{[\nabla_{\mathbf{a'}}\delta_{\mathbf{a'}2'}]\cdot\nabla_{\mathbf{x'}}[\delta_{\mathbf{x'}2'} + \delta_{\mathbf{x'a'}}]\delta_{\mathbf{a}1'} \\
&\qquad\quad -[\nabla_{\mathbf{a}}\delta_{\mathbf{a}1'}]\cdot\nabla_{\mathbf{x'}}[\delta_{\mathbf{x'}1'} + \delta_{\mathbf{x'a}}]\delta_{\mathbf{a'}2'}\Big\}.
\end{aligned} \tag{4.8}$$

Performing first an integration by parts on $\mathbf{x}'$ then on either $\mathbf{a}$ or $\mathbf{a}'$ depending on the term, and using the fact that $\nabla W(0) = 0$, one finds:

$$\begin{aligned}
&\frac{i}{8T}\int_{\mathbf{xx'}} W_{\mathbf{xx'}} \left\langle \mathbf{r}_1\mathbf{r}_2\right|\mathcal{D}_{Q\bar{Q}} n_{\mathbf{x}}\dot{n}_{\mathbf{x'}}\left|\mathbf{r}'_1\mathbf{r}'_2\right\rangle \\
=&\frac{1}{8MT}[\Delta W(0) + \Delta W_{1'2'} + \nabla W_{1'2'}\cdot\nabla_{1'2'}] \left\langle \mathbf{r}_1\mathbf{r}_2\right|\mathcal{D}_{Q\bar{Q}}\left|\mathbf{r}'_1\mathbf{r}'_2\right\rangle .
\end{aligned} \tag{4.9}$$

One can see that the last term of equation (4.5) will lead to the same contribution with $1' \to 1$ and $2' \to 2$. We recall the expression for $\mathcal{L}_{3a}$:

$$\mathcal{L}_{3a}\mathcal{D}_{Q\bar{Q}} = \frac{1}{4MT}[2\Delta W(0) - \Delta W_{12} - \Delta W_{1'2'} - \nabla W_{12}\cdot\nabla_{12} - \nabla W_{1'2'}\cdot\nabla_{1'2'}]\mathcal{D}_{Q\bar{Q}}, \tag{4.10}$$

which gives us, using (4.5) and (4.9):

$$\left\langle \mathbf{r}_1\mathbf{r}_2\right|\mathcal{L}'_{3a}\mathcal{D}_{Q\bar{Q}}\left|\mathbf{r}'_1\mathbf{r}'_2\right\rangle = \frac{1}{4MT}[2\Delta W(0)]\left\langle \mathbf{r}_1\mathbf{r}_2\right|\mathcal{D}_{Q\bar{Q}}\left|\mathbf{r}'_1\mathbf{r}'_2\right\rangle . \tag{4.11}$$

In the new discretization, the $\mathcal{L}^3_{Q\bar{Q},a}$ operator is actually null while the $\mathcal{L}^3_{QQ,a}$ one remains unchanged. Later in the chapter, we will see that this difference will have consequences on how the conservation of the trace (i.e. unitarity) is realized.

### 4.1.2 Derivation of the $\mathcal{L}_4$ terms

The terms corresponding to $\mathcal{L}_{4a}$ are given by:

$$\left\langle \mathbf{r}_1\mathbf{r}_2\right|\mathcal{L}_{4a}\mathcal{D}_{Q\bar{Q}}\left|\mathbf{r}'_1\mathbf{r}'_2\right\rangle = \frac{1}{32T^2}\int_{\mathbf{x}\mathbf{x}'} W_{\mathbf{x}\mathbf{x}'}\left\langle \mathbf{r}_1\mathbf{r}_2\right|\left(\dot{n}_{\mathbf{x}}\dot{n}_{\mathbf{x}'}\mathcal{D}_{Q\bar{Q}} - \mathcal{D}_{Q\bar{Q}}\dot{n}_{\mathbf{x}}\dot{n}_{\mathbf{x}'}\right)\left|\mathbf{r}'_1\mathbf{r}'_2\right\rangle , \tag{4.12}$$

while the one corresponding to $\mathcal{L}_{4b}$ is:

$$\left\langle \mathbf{r}_1\mathbf{r}_2\right|\mathcal{L}_{4b}\mathcal{D}_{Q\bar{Q}}\left|\mathbf{r}'_1\mathbf{r}'_2\right\rangle = -\frac{1}{16T^2}\int_{\mathbf{x}\mathbf{x}'} W_{\mathbf{x}\mathbf{x}'}\left\langle \mathbf{r}_1\mathbf{r}_2\right|\dot{n}_{\mathbf{x}'}\mathcal{D}_{Q\bar{Q}}\dot{n}_{\mathbf{x}}\left|\mathbf{r}'_1\mathbf{r}'_2\right\rangle . \tag{4.13}$$

Following the same procedure as in section 4.1.1, the $\mathcal{L}_{4b}$ contribution becomes:

$$\begin{aligned}
&\int_{\substack{\mathbf{x}\mathbf{x}'\\ \mathbf{a}\mathbf{a}'\\ \mathbf{b}\mathbf{b}'}} W_{\mathbf{x}\mathbf{x}'}\left\langle \mathbf{r}_1\mathbf{r}_2\right|\dot{n}_{\mathbf{x}'}\mathcal{D}_{Q\bar{Q}}\dot{n}_{\mathbf{x}}\left|\mathbf{r}'_1\mathbf{r}'_2\right\rangle \\
&= -\frac{1}{4M^2}\int_{\substack{\mathbf{x}\mathbf{x}'\\ \mathbf{a}\mathbf{a}'\\ \mathbf{b}\mathbf{b}'}} W_{\mathbf{x}\mathbf{x}'}\{[\nabla_2\delta_{2\mathbf{a}'}]\cdot\nabla_{\mathbf{x}'}[\delta_{\mathbf{x}'\mathbf{a}'}+\delta_{\mathbf{x}'2}]\delta_{1\mathbf{a}} - [\nabla_1\delta_{1\mathbf{a}}]\cdot\nabla_{\mathbf{x}'}[\delta_{\mathbf{x}'\mathbf{a}}+\delta_{\mathbf{x}'1}]\delta_{2\mathbf{a}'}\} \\
&\quad\times\{[\nabla_{\mathbf{b}'}\delta_{\mathbf{b}'2'}]\cdot\nabla_{\mathbf{x}}[\delta_{\mathbf{x}2'}+\delta_{\mathbf{x}\mathbf{b}'}]\delta_{\mathbf{b}1'} - [\nabla_{\mathbf{b}}\delta_{\mathbf{b}1'}]\cdot\nabla_{\mathbf{x}}[\delta_{\mathbf{x}1'}+\delta_{\mathbf{x}\mathbf{b}}]\delta_{\mathbf{b}'2'}\} \\
&\quad\times\left\langle \mathbf{a}\mathbf{a}'\right|\mathcal{D}_{Q\bar{Q}}\left|\mathbf{b}\mathbf{b}'\right\rangle .
\end{aligned} \tag{4.14}$$

There are 4 terms to compute in the right-hand size of equation (4.14), the first one being:

$$\mathcal{L}_{4b1} = -\frac{1}{4M^2}\int_{\substack{\mathbf{x}\mathbf{x}'\\ \mathbf{a}'\mathbf{b}'}} W_{\mathbf{x}\mathbf{x}'}[\nabla_2\delta_{2\mathbf{a}'}]\cdot\nabla_{\mathbf{x}'}[\delta_{\mathbf{x}'\mathbf{a}'}+\delta_{\mathbf{x}'2}] \times[\nabla_{\mathbf{b}'}\delta_{\mathbf{b}'2'}]\cdot\nabla_{\mathbf{x}}[\delta_{\mathbf{x}2'}+\delta_{\mathbf{x}\mathbf{b}'}]\left\langle \mathbf{r}_1\mathbf{a}'\middle|\mathcal{D}_{Q\bar{Q}}\middle|\mathbf{r}_1'\mathbf{b}'\right\rangle . \tag{4.15}$$

We first integrate by parts on $\mathbf{x}$ and $\mathbf{x}'$, then use the relation $\nabla_A\delta_{AB} = -\nabla_B\delta_{AB}$ and finally proceed to integrate by parts on $\mathbf{a}'$ and $\mathbf{b}'$, resulting in:

$$\mathcal{L}_{4b1} = -\frac{1}{4M^2}\left[-\partial^4 W_{22'} - 2\nabla\nabla^2 W_{22'}\cdot\nabla_{22'} + 4\partial_i\partial_j W_{22'}\partial_2^i\partial_2^j\right]\left\langle \mathbf{r}_1\mathbf{r}_2\middle|\mathcal{D}_{Q\bar{Q}}\middle|\mathbf{r}_1'\mathbf{r}_2'\right\rangle , \tag{4.16}$$

where $\nabla\nabla^2 W_{22'}$ has to be understood as gradients with respect to the variable of $W$, taken at $\mathbf{r}_2 - \mathbf{r}_2'$. One can see that the last term of the equation (4.14) will be the exact same as with $\mathcal{L}_{4b1}$ , with $2 \to 1$ and $2' \to 1'$, giving us:

$$\mathcal{L}_{4b4} = -\frac{1}{4M^2}\left[-\partial^4 W_{11'} - 2\nabla\nabla^2 W_{11'}\cdot\nabla_{11'} + 4\partial_i\partial_j W_{11'}\partial_1^i\partial_{1'}^j\right]\left\langle \mathbf{r}_1\mathbf{r}_2\middle|\mathcal{D}_{Q\bar{Q}}\middle|\mathbf{r}_1'\mathbf{r}_2'\right\rangle . \tag{4.17}$$

Similarly, the second term of (4.14):

$$\mathcal{L}_{4b2} = \frac{1}{4M^2}\int_{\substack{\mathbf{x}\mathbf{x}'\\ \mathbf{a}'\mathbf{b}}} W_{\mathbf{x}\mathbf{x}'}[\nabla_2\delta_{2\mathbf{a}'}]\cdot\nabla_{\mathbf{x}'}[\delta_{\mathbf{x}'\mathbf{a}'}+\delta_{\mathbf{x}'2}] \times[\nabla_{\mathbf{b}}\delta_{\mathbf{b}1'}]\cdot\nabla_{\mathbf{x}}[\delta_{\mathbf{x}1'}+\delta_{\mathbf{x}\mathbf{b}}]\left\langle \mathbf{r}_1\mathbf{a}'\middle|\mathcal{D}_{Q\bar{Q}}\middle|\mathbf{b}\mathbf{r}_2'\right\rangle , \tag{4.18}$$

leads to:

$$\mathcal{L}_{4b2} = \frac{1}{4M^2}\left[-\partial^4 W_{21'} - 2\nabla\nabla^2 W_{21'}\cdot\nabla_{21'} + 4\partial_i\partial_j W_{21'}\partial_2^i\partial_{1'}^j\right]\left\langle \mathbf{r}_1\mathbf{r}_2\middle|\mathcal{D}_{Q\bar{Q}}\middle|\mathbf{r}_1'\mathbf{r}_2'\right\rangle . \tag{4.19}$$

Once again, it is possible to obtain the last remaining term by performing the change $2 \to 1$ and $1' \to 2'$ in equation (4.19), giving us:

$$\mathcal{L}_{4b3} = \frac{1}{4M^2}\left[-\partial^4 W_{12'} - 2\nabla\nabla^2 W_{12'}\cdot\nabla_{12'} + 4\partial_i\partial_j W_{12'}\partial_1^i\partial_{2'}^j\right]\left\langle \mathbf{r}_1\mathbf{r}_2\middle|\mathcal{D}_{Q\bar{Q}}\middle|\mathbf{r}_1'\mathbf{r}_2'\right\rangle . \tag{4.20}$$

As there are no exchanges between a quark and a antiquark ($1 \leftrightarrow 1'$ or $2 \leftrightarrow 2'$) in the $\mathcal{L}_{4b1}$ and $\mathcal{L}_{4b4}$ contributions, they correspond to the $\mathcal{L}_{QQ,b}$ operator, while the other two contributions correspond to the $\mathcal{L}_{Q\bar{Q},b}$ operator. Regrouping the terms and using the $W_a$ and $W_b$ notations introduced in the previous chapter, we obtain:

$$\begin{aligned}
\mathcal{L}_{QQ,b} &= \frac{1}{64M^2T^2}\left[-\partial^4 W_a - 2\nabla\nabla^2 W_a\cdot\nabla_a + 4\partial_i\partial_j W_a\left(\partial^i\partial^j\right)^a\right]\\
\mathcal{L}_{Q\bar{Q},b} &= \frac{1}{64M^2T^2}\left[\partial^4 W_b + 2\nabla\nabla^2 W_b\cdot\nabla_b - 4\partial_i\partial_j W_b\left(\partial^i\partial^j\right)^b\right],
\end{aligned} \tag{4.21}$$

with the following definition:

$$\partial_i\partial_j W_a\left(\partial^i\partial^j\right)^a = \partial_i\partial_j W_{11'}\partial_1^i\partial_{1'}^j + \partial_i\partial_j W_{22'}\partial_2^i\partial_{2'}^j, \tag{4.22}$$

and similar definitions for $W_b$ and $W_c$.

There are 3 types of terms at the $\mathcal{L}_4$ level:

— Terms involving no derivatives on $\mathcal{D}_{Q\bar{Q}}$, they will be refered later as $\mathcal{L}_4^{cst}$ terms.

— Terms involving $1^{st}$ order derivatives of $\mathcal{D}_{Q\bar{Q}}$, they will be refered as $\mathcal{L}_4^{lin}$.

— Terms involving $2^{nd}$ order derivatives of $\mathcal{D}_{Q\bar{Q}}$, they will be refered as $\mathcal{L}_4^{quad}$.

We now treat the $\mathcal{L}_{4a}$ terms given by equation (4.12). We only compute the first term of the right-hand side of the equation (4.12) since a closer inspection shows that the contribution from the second term can be obtained from the first one by performing the change $(1,2) \to (1',2')$. The term under consideration is the following:

$$
\begin{aligned}
&\int_{\substack{\mathbf{x}\mathbf{x}'\\ \mathbf{a}\mathbf{a}'\\ \mathbf{b}\mathbf{b}'}} W_{\mathbf{x}\mathbf{x}'} \left\langle \mathbf{r}_1\mathbf{r}_2\right| \dot{n}_{\mathbf{x}}\dot{n}_{\mathbf{x}'}\mathcal{D}_{Q\bar{Q}}\left|\mathbf{r}_1'\mathbf{r}_2'\right\rangle \\
&= -\frac{1}{4M^2}\int_{\substack{\mathbf{x}\mathbf{x}'\\ \mathbf{a}\mathbf{a}'\\ \mathbf{b}\mathbf{b}'}} W_{\mathbf{x}\mathbf{x}'}\{[\nabla_2\delta_{2\mathbf{a}'}]\cdot\nabla_{\mathbf{x}}[\delta_{\mathbf{x}\mathbf{a}'}+\delta_{\mathbf{x}2}]\delta_{1\mathbf{a}} - [\nabla_1\delta_{1\mathbf{a}}]\cdot\nabla_{\mathbf{x}}[\delta_{\mathbf{x}\mathbf{a}}+\delta_{\mathbf{x}'1}]\delta_{2\mathbf{a}'}\} \\
&\quad\times\{[\nabla_{\mathbf{a}'}\delta_{\mathbf{a}'\mathbf{b}'}]\cdot\nabla_{\mathbf{x}'}[\delta_{\mathbf{x}'\mathbf{b}'}+\delta_{\mathbf{x}'\mathbf{a}'}]\delta_{\mathbf{a}\mathbf{b}} - [\nabla_{\mathbf{a}}\delta_{\mathbf{a}\mathbf{b}}]\cdot\nabla_{\mathbf{x}'}[\delta_{\mathbf{x}'\mathbf{b}}+\delta_{\mathbf{x}'\mathbf{a}}]\delta_{\mathbf{a}'\mathbf{b}'}\} \\
&\quad\times\left\langle \mathbf{b}\mathbf{b}'\right|\mathcal{D}_{Q\bar{Q}}\left|\mathbf{r}_1'\mathbf{r}_2'\right\rangle . \qquad (4.23)
\end{aligned}
$$

Just as before, it is only useful to compute two terms of equation (4.23), as the other two can be obtained from them by performing adequate change of variables. The first contribution writes:

$$
\begin{aligned}
\mathcal{L}^1_{4a1} = -\frac{1}{4M^2}\int_{\substack{\mathbf{x}\mathbf{x}'\\ \mathbf{a}'\mathbf{b}'}} & W_{\mathbf{x}\mathbf{x}'}[\nabla_2\delta_{2\mathbf{a}'}]\cdot\nabla_{\mathbf{x}}[\delta_{\mathbf{x}\mathbf{a}'}+\delta_{\mathbf{x}2}] \\
&\times[\nabla_{\mathbf{a}'}\delta_{\mathbf{a}'\mathbf{b}'}]\cdot\nabla_{\mathbf{x}'}[\delta_{\mathbf{x}'\mathbf{b}'}+\delta_{\mathbf{x}'\mathbf{a}'}]\left\langle \mathbf{r}_1\mathbf{b}'\right|\mathcal{D}_{Q\bar{Q}}\left|\mathbf{r}_1'\mathbf{r}_2'\right\rangle . \qquad (4.24)
\end{aligned}
$$

Using the same procedure as for the $\mathcal{L}_{4b}$ terms, one finds (using $\nabla\nabla^2 W(0) = 0$, thanks to isotropy):

$$
\mathcal{L}^1_{4a1} = \frac{1}{4M^2}\left[\partial^4 W(0) + 4\partial_i\partial_j W(0)\partial_2^i\partial_{2'}^j\right]\left\langle \mathbf{r}_1\mathbf{r}_2\right|\mathcal{D}_{Q\bar{Q}}\left|\mathbf{r}_1'\mathbf{r}_2'\right\rangle . \qquad (4.25)
$$

The second term is given by:

$$
\begin{aligned}
\mathcal{L}^1_{4a2} = \frac{1}{4M^2}\int_{\substack{\mathbf{x}\mathbf{x}'\\ \mathbf{a}'\mathbf{b}}} & W_{\mathbf{x}\mathbf{x}'}[\nabla_2\delta_{2\mathbf{a}'}]\cdot\nabla_{\mathbf{x}}[\delta_{\mathbf{x}\mathbf{a}'}+\delta_{\mathbf{x}2}] \\
&\times[\nabla_1\delta_{1\mathbf{b}}]\cdot\nabla_{\mathbf{x}'}[\delta_{\mathbf{x}'\mathbf{b}'}+\delta_{\mathbf{x}'1}]\left\langle \mathbf{b}\mathbf{a}'\right|\mathcal{D}_{Q\bar{Q}}\left|\mathbf{r}_1'\mathbf{r}_2'\right\rangle . \qquad (4.26)
\end{aligned}
$$

which leads to:

$$\mathcal{L}^1_{4a2} = \frac{1}{4M^2}\left[\partial^4 W_{12} + +2\nabla\nabla^2 W_{12}\cdot\nabla_{12} + 4\partial_i\partial_j W_{12}\partial_1^i\partial_2^j\right]\left\langle \mathbf{r}_1\mathbf{r}_2\middle|\mathcal{D}_{Q\bar{Q}}\middle|\mathbf{r}_1'\mathbf{r}_2'\right\rangle. \quad (4.27)$$

The third term is immediately obtained from (4.27) as one can see that it leads to the same contribution. The last term is obtained from (4.25) by replacing $2 \to 1$. Regrouping all the terms leads to:

$$\begin{aligned}\mathcal{L}^1_{4a} =& \frac{1}{64M^2T^2}\Bigg[\partial^4 W(0) + 2\partial_i\partial_j W(0)\left[\partial_1^i\partial_1^j + \partial_2^i\partial_2^j\right] \\ &+\partial^4 W_{12} + 2\nabla\nabla^2 W_{12}\cdot\nabla_{12} - 4\partial_i\partial_j W_{12}\partial_1^i\partial_2^j\Bigg]\left\langle \mathbf{r}_1\mathbf{r}_2\middle|\mathcal{D}_{Q\bar{Q}}\middle|\mathbf{r}_1'\mathbf{r}_2'\right\rangle. \quad (4.28)\end{aligned}$$

The contribution $\mathcal{L}^2_{4a}$ obtained from the second term of (4.23) is obtained by doing the change $(1,2) \to (1',2')$ in $\mathcal{L}^1_{4a}$. Regrouping both contributions, we can identify the $\mathcal{L}_{QQ,a}$ and $\mathcal{L}_{Q\bar{Q},a}$ operators, written as:

$$\begin{aligned}\mathcal{L}_{QQ,a} &= \frac{1}{64M^2T^2}\left[2\partial^4 W(0) + 2\partial_i\partial_j W(0)\left(\partial_1^i\partial_1^j + \partial_{1'}^i\partial_{1'}^j + \partial_2^i\partial_2^j + \partial_{2'}^i\partial_{2'}^j\right)\right], \\ \mathcal{L}_{Q\bar{Q},a} &= \frac{1}{64M^2T^2}\left[\partial^4 W_c + 2\nabla\nabla^2 W_c\cdot\nabla_c - 4\partial_i\partial_j W_c\left(\partial^i\partial^j\right)^c\right]. \quad (4.29)\end{aligned}$$

### 4.1.3 Derivation for QCD

From the terms derived in the QED-like case at each level, we can obtain the equations in the QCD case, by constructing the $\mathcal{L}_{ss}$,$\mathcal{L}_{so}$,$\mathcal{L}_{os}$ and $\mathcal{L}_{oo}$ operators as explained in Appendix A:

$$\mathcal{L}_{ss} = C_F\Big[\mathcal{L}_{QQ,a} + \mathcal{L}_{Q\bar{Q},a}\Big], \quad \mathcal{L}_{so} = C_F\Big[\mathcal{L}_{QQ,b} + \mathcal{L}_{Q\bar{Q},b}\Big], \quad \mathcal{L}_{os} = \frac{1}{2N_c}\Big[\mathcal{L}_{QQ,b} + \mathcal{L}_{Q\bar{Q},b}\Big],$$
$$\mathcal{L}_{oo} = C_F\mathcal{L}_{QQ,a} - \frac{1}{2N_c}\mathcal{L}_{Q\bar{Q},a} + \frac{N_c^2-2}{2N_c}\mathcal{L}_{QQ,b} - \frac{1}{N_c}\mathcal{L}_{Q\bar{Q},b}. \tag{4.30}$$

The different operators involve different types of transitions. In the case of $\mathcal{L}_{ss}$, only direct transitions with even $\Delta L$ (L being the angular momentum) are present. In the case of both $\mathcal{L}_{so}$ and $\mathcal{L}_{os}$, we only have transitions where $\Delta L$ is odd, meaning than singlet to octet or octet to singlet transitions will change parity. Finally, in the case of $\mathcal{L}_{oo}$ both types of transitions are present, so we have transitions between octet color states that change parity and other that do not.

Before studying the conservation of unitarity and positivity, we will perform another approximation to simplify the equations we derived.

## 4.2 Reduction of the center of mass degrees of freedom

In this section, we will perform a quite common reduction, which consists in tracing out the center of mass degrees of freedom. Since the pair is heavy and weakly interacts with the medium, the center of mass motion does not vary much and it seems legitimate that we can integrate it out. However, for some of the terms at the $\mathcal{L}_4$ level, this will not be the case, leading to terms depending on the total momentum of the pair. To do so, we first introduce the center of mass and relative coordinates:

$$\begin{aligned} \mathbf{R} &= \frac{\mathbf{r}_1 + \mathbf{r}_2}{2}, \quad & \mathbf{R}' &= \frac{\mathbf{r}_1' + \mathbf{r}_2'}{2}, \\ \mathbf{s} &= \mathbf{r}_1 - \mathbf{r}_2, & \mathbf{s}' &= \mathbf{r}_1' - \mathbf{r}_2', \end{aligned} \tag{4.31}$$

and the reduced density operator in the center of mass:

$$\left\langle \mathbf{s}\middle|\mathcal{D}\middle|\mathbf{s}'\right\rangle = \int d^3\mathbf{R}d^3\mathbf{R}'\delta^{(3)}\left(\mathbf{R}-\mathbf{R}'\right)\left\langle \mathbf{R}\mathbf{s}\middle|\mathcal{D}\middle|\mathbf{R}'\mathbf{s}'\right\rangle. \tag{4.32}$$

It is then possible to formulate the time derivative of $\langle \mathbf{s}|\mathcal{D}|\mathbf{s}'\rangle$:

$$\frac{\mathrm{d}}{\mathrm{d}t}\langle \mathbf{s}|\mathcal{D}|\mathbf{s}'\rangle = \int d^3\mathbf{R}d^3\mathbf{R}'\delta^{(3)}(\mathbf{R}-\mathbf{R}')\langle \mathbf{R}\mathbf{s}|\mathcal{L}\mathcal{D}|\mathbf{R}'\mathbf{s}'\rangle . \tag{4.33}$$

The goal is to show that the right-hand side of the equation 4.33 can be expressed as an operator only acting on $\langle \mathbf{s}|\mathcal{D}|\mathbf{s}'\rangle$, which is not trivial. We will start from the $\mathcal{L}_0$ terms and go through each level.

### 4.2.1 Reduction of the $\mathcal{L}_0$ terms

We had for both $\mathcal{D}_s$ and $\mathcal{D}_o$:

$$\mathcal{L}_0\mathcal{D}_{121'2'} = -i\left(\frac{\mathbf{p}_1^2+\mathbf{p}_2^2-\mathbf{p}_{1'}^2-\mathbf{p}_{2'}^2}{2M}\right)\mathcal{D}_{121'2'}, \tag{4.34}$$

with $\mathcal{L}_0\mathcal{D}_{121'2'} = \langle \mathbf{r}_1\mathbf{r}_2|\mathcal{L}_0\mathcal{D}|\mathbf{r}_1'\mathbf{r}_2'\rangle$ and $\mathcal{D}_{121'2'} = \langle \mathbf{r}_1\mathbf{r}_2|\mathcal{D}|\mathbf{r}_1'\mathbf{r}_2'\rangle$.

Using (4.32), we have:

$$\nabla_1 = \frac{1}{2}\nabla_R + \nabla_s, \quad \nabla_2 = \frac{1}{2}\nabla_R - \nabla_s, \tag{4.35}$$

and similar notations for the conjugated variables.

We then get:

$$\langle \mathbf{R}\mathbf{s}|\mathcal{L}_0\mathcal{D}|\mathbf{R}'\mathbf{s}'\rangle = \frac{i\hbar^2}{2M}\left(\frac{1}{2}\Delta_R + 2\Delta_s - \frac{1}{2}\Delta_{R'} - 2\Delta_{s'}\right)\langle \mathbf{R}\mathbf{s}|\mathcal{D}|\mathbf{R}'\mathbf{s}'\rangle . \tag{4.36}$$

By going to the Fourier space for the $\mathbf{R}$ and $\mathbf{R}'$ variables, we have:

$$\begin{aligned}\langle \mathbf{s}|\mathcal{D}|\mathbf{s}'\rangle &= \int d^3\mathbf{k}d^3\mathbf{k}'\delta^{(3)}(\mathbf{k}-\mathbf{k}')\,\langle \mathbf{k}\mathbf{s}|\mathcal{D}|\mathbf{k}'\mathbf{s}'\rangle \\ \langle \mathbf{s}|\mathcal{L}_0\mathcal{D}|\mathbf{s}'\rangle &= \int d^3\mathbf{k}d^3\mathbf{k}'\delta^{(3)}(\mathbf{k}-\mathbf{k}')\,\langle \mathbf{k}\mathbf{s}|\mathcal{L}_0\mathcal{D}|\mathbf{k}'\mathbf{s}'\rangle\,, \end{aligned} \tag{4.37}$$

while from (4.36):

$$\langle \mathbf{k}\mathbf{s}|\mathcal{L}_0\mathcal{D}|\mathbf{k}'\mathbf{s}'\rangle = \frac{i\hbar^2}{2M}\left(2[\Delta_s-\Delta_{s'}]+\frac{1}{2}\left[\|\mathbf{k}\|^2-\|\mathbf{k}'\|^2\right]\right)\langle \mathbf{k}\mathbf{s}|\mathcal{D}|\mathbf{k}'\mathbf{s}'\rangle\,. \tag{4.38}$$

One easily sees that we obtain:

$$\langle \mathbf{s}|\mathcal{L}_0\mathcal{D}|\mathbf{s}'\rangle = \frac{i\hbar^2}{M}(\Delta_s-\Delta_{s'})\,\langle \mathbf{s}|\mathcal{D}|\mathbf{s}'\rangle\,, \tag{4.39}$$

which is indeed properly formulated as an operator acting on $\langle \mathbf{s}|\mathcal{D}|\mathbf{s}'\rangle$.

### 4.2.2 Reduction of the $\mathcal{L}_1$ terms

We have at the $\mathcal{L}_1$ level:

$$\mathcal{L}_1\mathcal{D}_{121'2'} = iC(V_{12}-V_{1'2'})\mathcal{D}_{121'2'}, \tag{4.40}$$

with C a color factor: $C_F$ for $\mathcal{D}_s$ and $-\frac{1}{2N_c}$ for $\mathcal{D}_o$.

As the potentials here are expressed as functions of the relative variables[1], the reduction of the center of mass degrees of freedom is immediate:

$$\langle \mathbf{s}|\mathcal{L}_1\mathcal{D}|\mathbf{s}'\rangle = iC\left[V(\mathbf{s})-V(\mathbf{s}')\right]\langle \mathbf{s}|\mathcal{D}|\mathbf{s}'\rangle\,. \tag{4.41}$$

1. The behaviour of the potential could depend on the speed of the $c\bar{c}$ pair, which would involve operators acting on $\mathbf{R}$ and $\mathbf{R}'$

### 4.2.3 Reduction of the $\mathcal{L}_2$ terms

Starting from the $\mathcal{L}_2$ level, we will treat separately the $\mathcal{L}_{QQ,a}$, $\mathcal{L}_{Q\bar{Q},a}$, $\mathcal{L}_{QQ,b}$ and $\mathcal{L}_{Q\bar{Q},b}$ terms in the QED case. The QCD case is restored by using the combinations given in equation (4.30). Starting with the $\mathcal{L}_{QQ,a}$ term:

$$\mathcal{L}^2_{QQ,a}\mathcal{D}_{121'2'} = 2W(0)\mathcal{D}_{121'2'}, \tag{4.42}$$

the reduction is immediate and we obtain:

$$\left\langle \mathbf{s}\middle|\mathcal{L}^2_{QQ,a}\mathcal{D}\middle|\mathbf{s}'\right\rangle = 2W(0)\left\langle \mathbf{s}\middle|\mathcal{D}\middle|\mathbf{s}'\right\rangle. \tag{4.43}$$

The $\mathcal{L}_{Q\bar{Q},a}$ term are given by:

$$\mathcal{L}^2_{Q\bar{Q},a}\mathcal{D}_{121'2'} = -[W_{12} + W_{1'2'}]\mathcal{D}_{121'2'}. \tag{4.44}$$

Similarly to the $\mathcal{L}_1$ level, this leads to:

$$\left\langle \mathbf{s}\middle|\mathcal{L}^2_{Q\bar{Q},a}\mathcal{D}\middle|\mathbf{s}'\right\rangle = -\left[W(\mathbf{s}) + W(\mathbf{s}')\right]\left\langle \mathbf{s}\middle|\mathcal{D}\middle|\mathbf{s}'\right\rangle. \tag{4.45}$$

We continue by looking at the $\mathcal{L}_{QQ,b}$ term:

$$\mathcal{L}^2_{QQ,b}\mathcal{D}_{121'2'} = -[W_{11'} + W_{22'}]\mathcal{D}_{121'2'}. \tag{4.46}$$

According to the change of variables (4.32), we have:

$$\begin{aligned}\mathbf{r}_1 - \mathbf{r}'_1 &= \mathbf{R} - \mathbf{R}' + \frac{\mathbf{s}-\mathbf{s}'}{2},\\ \mathbf{r}_2 - \mathbf{r}'_2 &= \mathbf{R} - \mathbf{R}' - \frac{\mathbf{s}-\mathbf{s}'}{2}.\end{aligned} \tag{4.47}$$

Using the relation$W(-\mathbf{r}) = -W(\mathbf{r})$, we perform the reduction and obtain, thanks to

the equation (4.32):

$$\langle \mathbf{s}|\mathcal{L}^2_{Q\bar{Q},b}\mathcal{D}|\mathbf{s}'\rangle = -2W\left(\frac{\mathbf{s}-\mathbf{s}'}{2}\right)\langle \mathbf{s}|\mathcal{D}|\mathbf{s}'\rangle\,. \tag{4.48}$$

Finally, we have the $\mathcal{L}_{Q\bar{Q},b}$ term:

$$\mathcal{L}^2_{Q\bar{Q},b}\mathcal{D}_{121'2'} = -[W_{12'}+W_{21'}]\mathcal{D}_{121'2'}. \tag{4.49}$$

Once again, using (4.32), we have:

$$\begin{aligned}\mathbf{r}_1-\mathbf{r}_2' &= \mathbf{R}-\mathbf{R}'+\frac{\mathbf{s}+\mathbf{s}'}{2},\\ \mathbf{r}_2-\mathbf{r}_1' &= \mathbf{R}-\mathbf{R}'-\frac{\mathbf{s}+\mathbf{s}'}{2},\end{aligned} \tag{4.50}$$

which leads to:

$$\langle \mathbf{s}|\mathcal{L}^2_{Q\bar{Q},b}\mathcal{D}|\mathbf{s}'\rangle = 2W\left(\frac{\mathbf{s}+\mathbf{s}'}{2}\right)\langle \mathbf{s}|\mathcal{D}|\mathbf{s}'\rangle\,. \tag{4.51}$$

### 4.2.4 Reduction of the $\mathcal{L}_3'$ terms

We proceed in the same way and evaluate the reduction of the $\mathcal{L}_{QQ,a}$ term at the $\mathcal{L}_3'$ level:

$$\mathcal{L}^{3'}_{QQ,a}\mathcal{D}_{121'2'} = \frac{1}{2MT}\Delta W(0)\mathcal{D}_{121'2'}, \tag{4.52}$$

which immediately gives us:

$$\langle \mathbf{s}|\mathcal{L}^{3'}_{QQ,a}\mathcal{D}|\mathbf{s}'\rangle = \frac{\hbar^2}{4MT}\Delta W(0)\langle \mathbf{s}|\mathcal{D}|\mathbf{s}'\rangle\,, \tag{4.53}$$

where we restored proper $\hbar$ counting so that the term clearly has the dimension of an energy. We will restore the $\hbar$ constants for every term from now on. The $\mathcal{L}_{Q\bar{Q},a}$ term is equal to zero and thus trivial, so we proceed with the $\mathcal{L}_{QQ,b}$ term:

$$\mathcal{L}^{3'}_{Q\bar{Q},b}\mathcal{D}_{121'2'} = \frac{1}{4MT}[\Delta W_{11'} + \Delta W_{22'} + \nabla W_{11'}\cdot\nabla_{11'} + \nabla W_{22'}\cdot\nabla_{22'}]\mathcal{D}_{121'2'}, \quad (4.54)$$

where we have:

$$\begin{aligned}\nabla_{11'} &= \nabla_1 - \nabla_{1'} = \frac{1}{2}(\nabla_R - \nabla_{R'}) + \nabla_s - \nabla_{s'},\\ \nabla_{22'} &= \nabla_2 - \nabla_{2'} = \frac{1}{2}(\nabla_R - \nabla_{R'}) - \nabla_s + \nabla_{s'}.\end{aligned} \quad (4.55)$$

Combining the equations (4.54) and (4.55), we get:

$$\begin{aligned}\left\langle \mathbf{Rs}\middle|\mathcal{L}^{3'}_{Q\bar{Q},b}\mathcal{D}\middle|\mathbf{R's'}\right\rangle = \frac{1}{4MT}\Bigg\{&\Delta W\left(\mathbf{R}-\mathbf{R'}+\frac{\mathbf{s}-\mathbf{s'}}{2}\right) + \Delta W\left(\mathbf{R}-\mathbf{R'}-\frac{\mathbf{s}-\mathbf{s'}}{2}\right)\\ &+\nabla W\left(\mathbf{R}-\mathbf{R'}+\frac{\mathbf{s}-\mathbf{s'}}{2}\right)\cdot\left[\frac{1}{2}(\nabla_R-\nabla_{R'})+\nabla_s-\nabla_{s'}\right]\\ &+\nabla W\left(\mathbf{R}-\mathbf{R'}-\frac{\mathbf{s}-\mathbf{s'}}{2}\right)\cdot\left[\frac{1}{2}(\nabla_R-\nabla_{R'})-\nabla_s+\nabla_{s'}\right]\Bigg\}\\ &\times\left\langle \mathbf{Rs}\middle|\mathcal{D}\middle|\mathbf{R's'}\right\rangle.\end{aligned} \quad (4.56)$$

Using the relation $\nabla W(-\mathbf{r}) = -\nabla W(\mathbf{r})$, we easily see from the equation (4.56) that no dependence on $\mathbf{R}$ or $\mathbf{R}'$ after the trace on $\mathbf{R}$ and $\mathbf{R}'$:

$$\left\langle \mathbf{s}\middle|\mathcal{L}^{3'}_{Q\bar{Q},b}\mathcal{D}\middle|\mathbf{s'}\right\rangle = \frac{\hbar^2}{2MT}\left[\Delta W\left(\frac{\mathbf{s}-\mathbf{s'}}{2}\right)+\nabla W\left(\frac{\mathbf{s}-\mathbf{s'}}{2}\right)\cdot(\nabla_{\mathbf{s}}-\nabla_{\mathbf{s'}})\right]\left\langle \mathbf{s}\middle|\mathcal{D}\middle|\mathbf{s'}\right\rangle. \quad (4.57)$$

Finally, from the $\mathcal{L}_{Q\bar{Q},b}$ term:

$$\mathcal{L}^{3'}_{Q\bar{Q},b}\mathcal{D}_{121'2'} = \frac{1}{4MT}[\Delta W_{12'} + \Delta W_{21'} + \nabla W_{12'}\cdot\nabla_{12'} + \nabla W_{21'}\cdot\nabla_{21'}]\mathcal{D}_{121'2'}, \quad (4.58)$$

where we have:

$$\nabla_{12'} = \nabla_1 - \nabla_{1'} = \frac{1}{2}(\nabla_R - \nabla_{R'}) + \nabla_s + \nabla_{s'},$$
$$\nabla_{21'} = \nabla_1 - \nabla_{1'} = \frac{1}{2}(\nabla_R - \nabla_{R'}) - \nabla_s - \nabla_{s'}, \tag{4.59}$$

Again, combining the equations (4.58) and (4.59) yields:

$$\begin{aligned}\left\langle \mathbf{Rs}\middle|\mathcal{L}^{3'}_{Q\bar{Q},b}\mathcal{D}\middle|\mathbf{R's'}\right\rangle = \frac{1}{4MT}\Bigg\{&\Delta W\left(\mathbf{R}-\mathbf{R'}+\frac{\mathbf{s}+\mathbf{s'}}{2}\right)+\Delta W\left(\mathbf{R}-\mathbf{R'}-\frac{\mathbf{s}+\mathbf{s'}}{2}\right)\\&+\nabla W\left(\mathbf{R}-\mathbf{R'}+\frac{\mathbf{s}-\mathbf{s'}}{2}\right)\cdot\left[\frac{1}{2}(\nabla_R-\nabla_{R'})+\nabla_s+\nabla_{s'}\right]\\&+\nabla W\left(\mathbf{R}-\mathbf{R'}-\frac{\mathbf{s}-\mathbf{s'}}{2}\right)\cdot\left[\frac{1}{2}(\nabla_R-\nabla_{R'})-\nabla_s-\nabla_{s'}\right]\Bigg\}\\&\times\left\langle \mathbf{Rs}\middle|\mathcal{D}\middle|\mathbf{R's'}\right\rangle,\end{aligned} \tag{4.60}$$

and we obtain after the trace:

$$\left\langle \mathbf{s}\middle|\mathcal{L}^{3'}_{Q\bar{Q},b}\mathcal{D}\middle|\mathbf{s'}\right\rangle = \frac{\hbar^2}{2MT}\left[\Delta W\left(\frac{\mathbf{s}+\mathbf{s'}}{2}\right)+\nabla W\left(\frac{\mathbf{s}-\mathbf{s'}}{2}\right)\cdot(\nabla_{\mathbf{s}}+\nabla_{\mathbf{s'}})\right]\left\langle \mathbf{s}\middle|\mathcal{D}\middle|\mathbf{s'}\right\rangle. \tag{4.61}$$

### 4.2.5 Reduction of the $\mathcal{L}_4$ terms

We end the reduction of the center of mass degrees of freedom with the $\mathcal{L}_4$ terms. The $\mathcal{L}_{QQ,a}$ term writes:

$$\begin{aligned}\mathcal{L}^4_{QQ,a}\mathcal{D}_{121'2'} = \frac{1}{64M^2T^2}\Big[&2\partial^4 W(0)+2\partial_i\partial_j W(0)\left(\partial_1^i\partial_1^j+\partial_2^i\partial_2^j\right.\\&\left.+\partial_{1'}^i\partial_{1'}^j+\partial_{2'}^i\partial_{2'}^j\right)\Big]\mathcal{D}_{121'2'}.\end{aligned} \tag{4.62}$$

We have:

$$\partial_1^i \partial_1^j + \partial_2^i \partial_2^j = \frac{1}{2}\partial_R^i \partial_R^j + 2\partial_s^i \partial_s^j, \tag{4.63}$$

with similar notations for primed variables.

In contrast to other $\mathcal{L}$ levels, there are still terms in $\partial_R$, which inhibits the reduction in general. One can however still perform it assuming special dependences on $\mathbf{R}$ and $\mathbf{R}'$. Assuming for instance a state with perfectly defined total momentum, we have:

$$\mathcal{D}_{121'2'} = e^{i\mathbf{p}_{tot}\cdot(\mathbf{R}-\mathbf{R}')} \left\langle \mathbf{s} \middle| \mathcal{D} \middle| \mathbf{s}' \right\rangle . \tag{4.64}$$

Then, we obtain:

$$\begin{aligned} \left\langle \mathbf{s} \middle| \mathcal{L}^4_{Q\bar{Q},a} \mathcal{D} \middle| \mathbf{s}' \right\rangle = \frac{\hbar^4}{64M^2T^2} \Big[ & 2\partial^4 W(0) + 4\partial_i\partial_j W(0) \left[ \partial^i_{\mathbf{s}} \partial^j_{\mathbf{s}} + \partial^i_{\mathbf{s}'} \partial^j_{\mathbf{s}'} \right] \\ & -2\mathbf{p}_{tot} \cdot \mathcal{H}(0) \cdot \mathbf{p}_{tot} \Big] \left\langle \mathbf{s} \middle| \mathcal{D} \middle| \mathbf{s}' \right\rangle , \end{aligned} \tag{4.65}$$

with $\mathcal{H}$ the Hessian matrix of W.

We see that at the $\mathcal{L}_4$ level there are terms depending on the velocity of the state, which was not the case at the other levels. For the $\mathcal{L}^4_{Q\bar{Q},a}$ operator, we have:

$$\begin{aligned} \mathcal{L}^4_{Q\bar{Q},a} \mathcal{D}_{121'2'} = \frac{1}{64M^2T^2} \Big[ & \partial^4 W_{12} + \partial^4 W_{1'2'} + 2\nabla\nabla^2 W_{12} \cdot \nabla_{12} \\ & + 2\nabla\nabla^2 W_{1'2'} \cdot \nabla_{1'2'} - 4\partial_i\partial_j W_{12} \partial_1^i \partial_2^j \\ & -4\partial_i\partial_j W_{1'2'} \partial_{1'}^i \partial_{2'}^j \Big] \mathcal{D}_{121'2'}, \end{aligned} \tag{4.66}$$

with:

$$\partial_1^i \partial_2^j = \frac{1}{4}\partial_R^i \partial_R^j - \partial_s^i \partial_s^j, \tag{4.67}$$

and a similar notation for the conjugated variables.

We obtain after performing the trace on $\mathbf{R}$ and $\mathbf{R}'$:

$$\begin{aligned}\left\langle \mathbf{s}\middle|\mathcal{L}^4_{Q\bar{Q},a}\mathcal{D}\middle|\mathbf{s}'\right\rangle = \frac{\hbar^4}{64M^2T^2}\Big[&\partial^4 W(\mathbf{s}) + \partial^4 W(\mathbf{s}') + 4\nabla\nabla^2 W(\mathbf{s})\cdot\nabla_{\mathbf{s}} \\ &+ 4\nabla\nabla^2 W(\mathbf{s}')\cdot\nabla_{\mathbf{s}'} + 4\partial_i\partial_j W(\mathbf{s})\partial^i_{\mathbf{s}}\partial^j_{\mathbf{s}} \\ &+ 4\partial_i\partial_j W(\mathbf{s}')\partial^i_{\mathbf{s}'}\partial^j_{\mathbf{s}'} + \mathbf{p}_{tot}\cdot\mathcal{H}(\mathbf{s})\cdot\mathbf{p}_{tot} \\ &+ \mathbf{p}_{tot}\cdot\mathcal{H}(\mathbf{s}')\cdot\mathbf{p}_{tot}\Big]. \end{aligned} \tag{4.68}$$

Then, for the $\mathcal{L}^4_{QQ,b}$ term:

$$\begin{aligned}\mathcal{L}^4_{QQ,b}\mathcal{D}_{121'2'} = \frac{1}{64M^2T^2}\Big[&-\partial^4 W_{11'} - \partial^4 W_{22'} + 2\nabla\nabla^2 W_{11'}\cdot\nabla_{11'} \\ &+ 2\nabla\nabla^2 W_{22'}\cdot\nabla_{22'} - 4\partial_i\partial_j W_{11'}\partial^i_1\partial^j_{1'} \\ &- 4\partial_i\partial_j W_{22'}\partial^i_2\partial^j_{2'}\Big]\mathcal{D}_{121'2'}, \end{aligned} \tag{4.69}$$

with:

$$\begin{aligned}\partial^i_1\partial^j_{1'} &= \frac{1}{4}\partial^i_R\partial^j_{R'} + \partial^i_s\partial^j_{s'} + \frac{1}{2}\partial^i_R\partial^j_{s'} + \frac{1}{2}\partial^i_s\partial^j_{R'}, \\ \partial^i_2\partial^j_{2'} &= \frac{1}{4}\partial^i_R\partial^j_{R'} + \partial^i_s\partial^j_{s'} - \frac{1}{2}\partial^i_R\partial^j_{s'} - \frac{1}{2}\partial^i_s\partial^j_{R'}. \end{aligned} \tag{4.70}$$

Using the parity of the derivatives of W, we get:

$$\begin{aligned}\left\langle \mathbf{s}\middle|\mathcal{L}^4_{Q\bar{Q},b}\mathcal{D}\middle|\mathbf{s}'\right\rangle = \frac{\hbar^4}{64M^2T^2}\Big[&-2\partial^4 W\left(\frac{\mathbf{s}-\mathbf{s}'}{2}\right) - 4\nabla\nabla^2 W\left(\frac{\mathbf{s}-\mathbf{s}'}{2}\right)\cdot[\nabla_{\mathbf{s}}-\nabla_{\mathbf{s}'}]\\ &+ 8\partial_i\partial_j W\left(\frac{\mathbf{s}-\mathbf{s}'}{2}\right)\partial^i_{\mathbf{s}}\partial^j_{\mathbf{s}'}\\ &+ 2\mathbf{p}_{tot}\cdot\mathcal{H}\left(\frac{\mathbf{s}-\mathbf{s}'}{2}\right)\cdot\mathbf{p}_{tot}\Big]\left\langle \mathbf{s}\middle|\mathcal{D}\middle|\mathbf{s}'\right\rangle . \end{aligned} \tag{4.71}$$

And finally we proceed with the reduction of the $\mathcal{L}^4_{Q\bar{Q},b}$ term:

$$\begin{aligned}\mathcal{L}^4_{Q\bar{Q},b}\mathcal{D}_{121'2'} = \frac{1}{64M^2T^2}\Big[&\partial^4 W_{12'} + \partial^4 W_{21'} + 2\nabla\nabla^2 W_{12'}\cdot\nabla_{12'}\\ &+ 2\nabla\nabla^2 W_{21'}\cdot\nabla_{21'} - 4\partial_i\partial_j W_{21'}\partial^i_2\partial^j_{1'}\\ &-4\partial_i\partial_j W_{21'}\partial^i_2\partial^j_{1'}\Big]\mathcal{D}_{121'2'}, \end{aligned} \tag{4.72}$$

with:

$$\begin{aligned}\partial^i_1\partial^j_{2'} &= \frac{1}{4}\partial^i_R\partial^j_{R'} - \partial^i_s\partial^j_{s'} - \frac{1}{2}\partial^i_R\partial^j_{s'} + \frac{1}{2}\partial^i_s\partial^j_{R'},\\ \partial^i_2\partial^j_{1'} &= \frac{1}{4}\partial^i_R\partial^j_{R'} - \partial^i_s\partial^j_{s'} + \frac{1}{2}\partial^i_R\partial^j_{s'} - \frac{1}{2}\partial^i_s\partial^j_{R'}. \end{aligned} \tag{4.73}$$

Once again, using the parity of the derivatives of W, we obtain:

$$\begin{aligned}\left\langle \mathbf{s}\middle|\mathcal{L}^4_{Q\bar{Q},b}\mathcal{D}\middle|\mathbf{s}'\right\rangle = \frac{\hbar^4}{64M^2T^2}\Big[&2\partial^4 W\left(\frac{\mathbf{s}+\mathbf{s}'}{2}\right) + 4\nabla\nabla^2 W\left(\frac{\mathbf{s}+\mathbf{s}'}{2}\right)\cdot[\nabla_{\mathbf{s}}+\nabla_{\mathbf{s}'}]\\ &+ 8\partial_i\partial_j W\left(\frac{\mathbf{s}+\mathbf{s}'}{2}\right)\partial^i_{\mathbf{s}}\partial^j_{\mathbf{s}'}\\ &- 2\mathbf{p}_{tot}\cdot\mathcal{H}\left(\frac{\mathbf{s}+\mathbf{s}'}{2}\right)\cdot\mathbf{p}_{tot}\Big]\left\langle \mathbf{s}\middle|\mathcal{D}\middle|\mathbf{s}'\right\rangle . \end{aligned} \tag{4.74}$$

The terms involving $\mathbf{p}_{tot}$ do not represent an energy loss but a different internal

dynamics when we consider a pair with fixed velocity.

In section 4.1.3, we mentionned that different types of transitions were involved. A simple calculation can show that transitions with even $DeltaL$ correspond to terms only depending on $\mathbf{s}$ or $\mathbf{s}'$ which are only present in $\mathcal{L}_{QQ,a}$ or $\mathcal{L}_{Q\bar{Q},a}$ terms while transitions with odd $DeltaL$ correspond to terms depending on combinations of $\mathbf{s}$ and $\mathbf{s}'$ which are only present in $\mathcal{L}_{QQ,b}$ or $\mathcal{L}_{Q\bar{Q},b}$. This imply that a color transition will indeed always change the parity. On the contrary transitions not changing the color state (singlet→singlet or from an octet to the same octet) will not change the parity.

Now that the reduction of the center of mass degrees of freedom is done, we can proceed to prove that the trace and positivity are indeed preserved.

## 4.3 Conservation of the trace

We now demonstrate explicitely the trace conservation for the new equations in the QCD case. The trace of either $\mathcal{D}_s$ or $\mathcal{D}_o$ is not conserved, however, there is a combination for which it is:

$$\frac{\mathrm{d}}{\mathrm{d}t}\,\mathrm{Tr}\left[\mathcal{D}_s + \left(N_c^2 - 1\right)\mathcal{D}_o\right] = 0, \tag{4.75}$$

which is simply the sum of all possible color states.

The procedure will be the following: we will compute the trace at the $\mathcal{L}_2$ level, then at the $\mathcal{L}_3$ and $\mathcal{L}_4$ levels. The trace should be conserved level by level as the prefactors are different for each level ($\frac{1}{4MT}$ for $\mathcal{L}_3$, $\frac{1}{64M^2T^2}$ for $\mathcal{L}_4$...). The first two levels $\mathcal{L}_0$ and $\mathcal{L}_1$ obviously conserve the trace as they are akin to a Schrödinger equation. At each level, we will compute the trace of the $\mathcal{L}_{ss}$, $\mathcal{L}_{so}$, $\mathcal{L}_{os}$ and $\mathcal{L}_{oo}$ operators, before regrouping all terms to compute (4.75), written as:

$$\mathrm{Tr}\left[\frac{\mathrm{d}}{\mathrm{d}t}\mathcal{D}_s + \left(N_c^2-1\right)\frac{\mathrm{d}}{\mathrm{d}t}\mathcal{D}_o\right] = \mathrm{Tr}\Big[\Big\{\mathcal{L}_{ss} + \left(N_c^2-1\right)\mathcal{L}_{os}\Big\}\mathcal{D}_s + \Big\{\mathcal{L}_{so} + \left(N_c^2-1\right)\mathcal{L}_{oo}\Big\}\mathcal{D}_o\Big], \tag{4.76}$$

therefore, we are going to prove that:

$$\begin{aligned}\mathrm{Tr}\left[\Big\{\mathcal{L}_{ss} + \left(N_c^2-1\right)\mathcal{L}_{os}\Big\}\mathcal{D}_s\right] &= 0,\\ \mathrm{Tr}\left[\Big\{\mathcal{L}_{so} + \left(N_c^2-1\right)\mathcal{L}_{oo}\Big\}\mathcal{D}_o\right] &= 0.\end{aligned} \tag{4.77}$$

The $\mathcal{L}_{ss}$ term represents in reality a loss of the singlet probability while the $\mathcal{L}_{os}$ term represents the gain term of the same quantity from the perspective of the octet. The $\mathcal{L}_{oo}$ term correspond to a net loss of the octet density to the singlet density with the octet to octet losses compensating each other. The quantity lost in the octet sector is gained in the singlet sector and is represented by the $\mathcal{L}_{so}$ term.

### 4.3.1 Trace at the $\mathcal{L}_2$ level

From the trace on $\mathcal{D}_s$, combining equations (4.30), (4.43) and (4.45), we have:

$$\mathcal{L}_{ss}\mathcal{D}_s = C_F\left[2W(0) - W(\mathbf{s}) - W(\mathbf{s}')\right]\mathcal{D}_s(s,s'). \tag{4.78}$$

The trace is then given by:

$$\begin{aligned}\mathrm{Tr}\left[\mathcal{L}_{ss}\mathcal{D}_s\right] &= C_F\int d^3\mathbf{s}d^3\mathbf{s}'\delta^{(3)}\left(\mathbf{s}-\mathbf{s}'\right)\left[2W(0) - W(\mathbf{s}) - W(\mathbf{s}')\right]\mathcal{D}_s(s,s')\\ &= 2C_F\int d^3\mathbf{s}[W(0) - W(\mathbf{s})]\mathcal{D}_s(s,s),\end{aligned} \tag{4.79}$$

where we will simply note $\mathcal{D}_s(s,s)$ as $\mathcal{D}_s$ (and a similar notation later for $\mathcal{D}_o$).

Combining equations (4.30), (4.48) and (4.51), the $\mathcal{L}_{os}$ term writes:

$$\mathcal{L}_{os}\mathcal{D}_s = \frac{1}{N_c}\left[-W\left(\frac{\mathbf{s}-\mathbf{s}'}{2}\right) + W\left(\frac{\mathbf{s}+\mathbf{s}'}{2}\right)\right]\mathcal{D}_s(s,s'). \tag{4.80}$$

Performing the trace, we obtain:

$$\mathrm{Tr}\,[\mathcal{L}_{os}\mathcal{D}_s] = \frac{1}{N_c}\int d^3\mathbf{s}[-W(0)+W(s)], \tag{4.81}$$

from which it is immediate to see that:

$$\mathrm{Tr}\left[\left\{\mathcal{L}_{ss} + \left(N_c^2-1\right)\mathcal{L}_{os}\right\}\mathcal{D}_s\right] = 0. \tag{4.82}$$

For the trace on $\mathcal{D}_o$, the $\mathcal{L}_{so}$ term is the same as $\mathcal{L}_{os}$, with a different color factor, leading to:

$$\mathrm{Tr}\,[\mathcal{L}_{so}\mathcal{D}_o] = C_F\int d^3\mathbf{s}[-W(0)+W(s)]\mathcal{D}_s. \tag{4.83}$$

Finally, following equation (4.30), the $\mathcal{L}_{oo}$ contribution is given by:

$$\begin{aligned}\mathcal{L}_{oo}\mathcal{D}_o = \Big[&2C_F W(0) + \frac{1}{2N_c}\left(W(\mathbf{s})+W(\mathbf{s}')\right)\\ &-\frac{N_c^2-2}{N_c}W\left(\frac{\mathbf{s}-\mathbf{s}'}{2}\right) - \frac{1}{N_c}W\left(\frac{\mathbf{s}+\mathbf{s}'}{2}\right)\Big]\mathcal{D}_o(s,s'),\end{aligned} \tag{4.84}$$

from which we obtain:

$$\mathrm{Tr}\,[\mathcal{L}_{oo}\mathcal{D}_o] = \frac{1}{N_c}\int d^3\mathbf{s}[W(0)-W(\mathbf{s})]\mathcal{D}_o. \tag{4.85}$$

Regrouping $\mathcal{L}_{so}$ and $\mathcal{L}_{oo}$, we get:

$$\mathrm{Tr}\left[\left\{\mathcal{L}_{so} + \left(N_c^2-1\right)\mathcal{L}_{oo}\right\}\mathcal{D}_o\right] = 0, \tag{4.86}$$

thus proving that the trace is conserved at the $\mathcal{L}_2$ level.

### 4.3.2 Trace at the $\mathcal{L}_3'$ level

The global factor $\frac{\hbar^2}{4MT}$ will be omitted for simplicity as it is common to all $\mathcal{L}_3'$ terms. From equation (4.53), the trace on the $\mathcal{L}_{ss}$ term is straightforward:

$$\mathrm{Tr}\left[\mathcal{L}_{ss}\mathcal{D}_s\right] = 2C_F \int d^3\mathbf{s}\Delta W(0)\mathcal{D}_s. \tag{4.87}$$

Combining equations (4.57) and (4.61), the term $\mathcal{L}_{os}$ writes:

$$\begin{aligned}\mathcal{L}_{os}\mathcal{D}_s = \frac{1}{N_c}\Big[-\Delta W\left(\frac{\mathbf{s}-\mathbf{s}'}{2}\right) + \Delta W\left(\frac{\mathbf{s}+\mathbf{s}'}{2}\right) - \nabla W\left(\frac{\mathbf{s}-\mathbf{s}'}{2}\right)\cdot(\nabla_{\mathbf{s}} - \nabla_{\mathbf{s}'}) \\ + \nabla W\left(\frac{\mathbf{s}+\mathbf{s}'}{2}\right)\cdot(\nabla_{\mathbf{s}} + \nabla_{\mathbf{s}'})\Big]\mathcal{D}_s(\mathbf{s},\mathbf{s}').\end{aligned} \tag{4.88}$$

Using the relation $\nabla W(0) = 0$, we get:

$$\mathrm{Tr}\left[\mathcal{L}_{os}\mathcal{D}_s\right] = \frac{1}{N_c}\int d^3\mathbf{s}[-\Delta W(0) + \Delta W(\mathbf{s}) + \nabla W(\mathbf{s})\cdot(\nabla_{\mathbf{s}} + \nabla_{\mathbf{s}'})]\mathcal{D}_s(\mathbf{s}), \tag{4.89}$$

with $\mathcal{D}_s(\mathbf{s}) = \mathcal{D}_s(\mathbf{s},\mathbf{s}')\big|_{\mathbf{s}=\mathbf{s}'}$. Regrouping equations (4.87) and (4.89), we obtain:

$$\begin{aligned}\mathrm{Tr}\left[\left\{\mathcal{L}_{ss} + \left(N_c^2-1\right)\mathcal{L}_{os}\right\}\mathcal{D}_s\right] = 2C_F\int d^3\mathbf{s}[\Delta W(\mathbf{s}) + \nabla W(\mathbf{s})\cdot(\nabla_{\mathbf{s}} + \nabla_{\mathbf{s}'})] \\ \times\, \mathcal{D}_s(\mathbf{s}).\end{aligned} \tag{4.90}$$

We can write:

$$\begin{aligned}\nabla W(\mathbf{s})\cdot(\nabla_{\mathbf{s}} + \nabla_{\mathbf{s}'})\mathcal{D}_s &= \nabla W(\mathbf{s})\cdot\left(\mathcal{D}_s^{(1,0)} + \mathcal{D}_s^{(0,1)}\right) \\ &= \nabla W(\mathbf{s})\cdot\nabla\mathcal{D}_s(\mathbf{s}),\end{aligned} \tag{4.91}$$

with the second $\nabla$ representing a total derivative on $\mathbf{s}$. We thus have:

$$\mathrm{Tr}\left[\left\{\mathcal{L}_{ss}+\left(N_c^2-1\right)\mathcal{L}_{os}\right\}\mathcal{D}_s\right]=2C_F\int d^3\mathbf{s}\nabla[\mathcal{D}_s\nabla W(\mathbf{s})]=0. \tag{4.92}$$

One can notice here something that will be important in the next chapters. At the $\mathcal{L}_2$ level, the trace was conserved locally in $\mathbf{s}$ (that is for each value of $\mathbf{s}$ in the integrand) since terms exactly compensated each other. Here, we still need to perform the integral on $\mathbf{s}$ to prove that this quantity is indeed equal to 0. Analytically, this has not much of an importance, however this is not the case numerically as we shall see in chapter 5.

Just as we did at the $\mathcal{L}_2$ level, we have:

$$\mathrm{Tr}\left[\mathcal{L}_{so}\mathcal{D}_o\right]=2C_F\int d^3\mathbf{s}[-\Delta W(0)+\Delta W(\mathbf{s})+\nabla W(\mathbf{s})\cdot(\nabla_{\mathbf{s}}+\nabla_{\mathbf{s}'})]\mathcal{D}_o(\mathbf{s}). \tag{4.93}$$

As for the $\mathcal{L}_{oo}$ term, we have:

$$\begin{aligned}\mathcal{L}_{oo}\mathcal{D}_o=\Bigg[&2C_FW(0)\\&-\frac{N_c^2-2}{N_c}\left(\Delta W\left(\frac{\mathbf{s}-\mathbf{s}'}{2}\right)+\nabla W\left(\frac{\mathbf{s}-\mathbf{s}'}{2}\right)\cdot(\nabla_{\mathbf{s}}-\nabla_{\mathbf{s}'})\right)\\&-\frac{2}{N_c}\left(\Delta W\left(\frac{\mathbf{s}+\mathbf{s}'}{2}\right)+\nabla W\left(\frac{\mathbf{s}+\mathbf{s}'}{2}\right)\cdot(\nabla_{\mathbf{s}}+\nabla_{\mathbf{s}'})\right)\Bigg]\mathcal{D}_o(\mathbf{s},\mathbf{s}').\end{aligned} \tag{4.94}$$

Using relation (4.91) and equations (4.93) and (4.94), we compute the trace:

$$\mathrm{Tr}\left[\mathcal{L}_{oo}\mathcal{D}_o\right]=\int d^3\mathbf{s}\left[\frac{1}{N_c}\Delta W(0)-\frac{2}{N_c}\{\Delta W(\mathbf{s})+\nabla W(\mathbf{s})\cdot(\nabla_{\mathbf{s}}+\nabla_{\mathbf{s}'})\}\right]\mathcal{D}_o(\mathbf{s}). \tag{4.95}$$

Which finally leads to, after integration on $\mathbf{s}$:

$$\mathrm{Tr}\left[\left\{\mathcal{L}_{so}+\left(N_c^2-1\right)\mathcal{L}_{oo}\right\}\mathcal{D}_o\right]=0. \tag{4.96}$$

The trace at the $\mathcal{L}_3'$ level is thus conserved.

### 4.3.3 Trace at the $\mathcal{L}_4$ level

The global factor $\frac{\hbar^4}{64M^2T^2}$ will be omitted for simplicity as it is common to all $\mathcal{L}_4$ terms. The procedure is the same as before, we will simply give directly the expression of the trace of each operator. Using equations (4.65) and (4.68), the trace of the $\mathcal{L}_{ss}$ term is given by:

$$\begin{aligned}\mathrm{Tr}\left[\mathcal{L}_{ss}\mathcal{D}_s\right]=C_F\int d^3\mathbf{s}\Big[&2\partial^4\{W(0)+W(\mathbf{s})\}+4\nabla\nabla^2W(\mathbf{s})\cdot(\nabla_{\mathbf{s}}+\nabla_{\mathbf{s}'})\\&+4\partial_i\partial_j[W(0)+W(\mathbf{s})]\left\{\partial^i_{\mathbf{s}}\partial^j_{\mathbf{s}}+\partial^i_{\mathbf{s}'}\partial^j_{\mathbf{s}'}\right\}\\&-2\mathbf{p}_{tot}\cdot\mathcal{H}(0)\cdot\mathbf{p}_{tot}+2\mathbf{p}_{tot}\cdot\mathcal{H}(\mathbf{s})\cdot\mathbf{p}_{tot}\Big]\mathcal{D}_s.\end{aligned} \tag{4.97}$$

We proceed with the trace of $\mathcal{L}_{os}$, using the fact that $\nabla\nabla^2W(0)=0$ and equations (4.71) and (4.74):

$$\begin{aligned}\mathrm{Tr}\left[\mathcal{L}_{os}\mathcal{D}_s\right]=\frac{1}{N_c}\int d^3\mathbf{s}\Big[&\partial^4\{-W(0)+W(\mathbf{s})\}+2\nabla\nabla^2W(\mathbf{s})\cdot(\nabla_{\mathbf{s}}+\nabla_{\mathbf{s}'})\\&+4\partial_i\partial_j[W(0)+W(\mathbf{s})]\partial^i_{\mathbf{s}}\partial^j_{\mathbf{s}'}\\&+\mathbf{p}_{tot}\cdot\mathcal{H}(0)\cdot\mathbf{p}_{tot}-\mathbf{p}_{tot}\cdot\mathcal{H}(\mathbf{s})\cdot\mathbf{p}_{tot}\Big]\mathcal{D}_s.\end{aligned} \tag{4.98}$$

Regrouping both terms, we obtain:

$$\begin{aligned}\mathrm{Tr}\left[\left\{\mathcal{L}_{ss}+\left(N_c^2-1\right)\mathcal{L}_{os}\right\}\mathcal{D}_s\right] = 4C_F\int d^3\mathbf{s}\Big[&\partial_i\partial_j W(0)\left\{\partial^i_{\mathbf{s}}\partial^j_{\mathbf{s}}+\partial^i_{\mathbf{s}'}\partial^j_{\mathbf{s}'}+2\partial^i_{\mathbf{s}}\partial^j_{\mathbf{s}'}\right\}\\ &+\partial^4 W(\mathbf{s})+2\nabla\nabla^2 W(\mathbf{s})\cdot(\nabla_{\mathbf{s}}+\nabla_{\mathbf{s}'})\\ &+\partial_i\partial_j W(\mathbf{s})\left\{\partial^i_{\mathbf{s}}\partial^j_{\mathbf{s}}+\partial^i_{\mathbf{s}'}\partial^j_{\mathbf{s}'}+2\partial^i_{\mathbf{s}}\partial^j_{\mathbf{s}'}\right\}\Big]\mathcal{D}_s. \quad (4.99)\end{aligned}$$

One can show that:

$$\partial_i\partial_j W(0)\left\{\partial^i_{\mathbf{s}}\partial^j_{\mathbf{s}}+\partial^i_{\mathbf{s}'}\partial^j_{\mathbf{s}'}+2\partial^i_{\mathbf{s}}\partial^j_{\mathbf{s}'}\right\}\mathcal{D}_s = \partial_i\partial_j W(0)\nabla^i_{\mathbf{s}}\nabla^j_{\mathbf{s}}\mathcal{D}_s, \quad (4.100)$$

and that:

$$\begin{aligned}&\Big[\partial^4 W(\mathbf{s})+2\nabla\nabla^2 W(\mathbf{s})\cdot(\nabla_{\mathbf{s}}+\nabla_{\mathbf{s}'})+\partial_i\partial_j W(\mathbf{s})\left\{\partial^i_{\mathbf{s}}\partial^j_{\mathbf{s}}+\partial^i_{\mathbf{s}'}\partial^j_{\mathbf{s}'}+2\partial^i_{\mathbf{s}}\partial^j_{\mathbf{s}'}\right\}\Big]\mathcal{D}_s\\ &=\nabla^i_{\mathbf{s}}\nabla^j_{\mathbf{s}}\left[\mathcal{D}_s\partial_i\partial_j W(\mathbf{s})\right]. \quad (4.101)\end{aligned}$$

Both contributions vanish when performing the remaining integration on $\mathbf{s}$, leading to:

$$\mathrm{Tr}\left[\left\{\mathcal{L}_{ss}+\left(N_c^2-1\right)\mathcal{L}_{os}\right\}\mathcal{D}_s\right] = 0. \quad (4.102)$$

As already observed with $\mathcal{L}'_3$, the conservation is not local.

The trace of $\mathcal{L}_{so}$ is straightforward:

$$\begin{aligned}\mathrm{Tr}\left[\mathcal{L}_{so}\mathcal{D}_o\right] = 2C_F\int d^3\mathbf{s}\Big[&\partial^4\{-W(0)+W(\mathbf{s})\}+2\nabla\nabla^2 W(\mathbf{s})\cdot(\nabla_{\mathbf{s}}+\nabla_{\mathbf{s}'})\\ &+4\partial_i\partial_j[W(0)+W(\mathbf{s})]\partial^i_{\mathbf{s}}\partial^j_{\mathbf{s}'}\\ &+\mathbf{p}_{tot}\cdot\mathcal{H}(0)\cdot\mathbf{p}_{tot}-\mathbf{p}_{tot}\cdot\mathcal{H}(\mathbf{s})\cdot\mathbf{p}_{tot}\Big]\mathcal{D}_o. \quad (4.103)\end{aligned}$$

Whereas the trace of $\mathcal{L}_{oo}$ is given by:

$$\begin{aligned}\mathrm{Tr}\left[\mathcal{L}_{oo}\mathcal{D}_o\right] = \int d^3\mathbf{s}\Bigg[&2C_F\Big(\partial^4 W(0) + \partial_i\partial_j W(0)\Big\{\partial^i_{\mathbf{s}}\partial^j_{\mathbf{s}} + \partial^i_{\mathbf{s}'}\partial^j_{\mathbf{s}'}\Big\}\Big)\\ &- \frac{1}{N_c}\Big(\partial^4 W(\mathbf{s}) + 2\nabla\nabla^2 W(\mathbf{s})\cdot(\nabla_{\mathbf{s}} + \nabla_{\mathbf{s}'}) - 2\partial_i\partial_j W(\mathbf{s})\Big\{\partial^i_{\mathbf{s}}\partial^j_{\mathbf{s}} + \partial^i_{\mathbf{s}'}\partial^j_{\mathbf{s}'}\Big\}\Big)\\ &+ \frac{N_c^2-2}{N_c}\Big(\partial^4 W(0) + 4\partial_i\partial_j W(0)\partial^i_{\mathbf{s}}\partial^j_{\mathbf{s}'}\Big)\\ &- \frac{2}{N_c}\Big(\partial^4 W(\mathbf{s}) + 2\nabla\nabla^2 W(\mathbf{s})\cdot(\nabla_{\mathbf{s}} + \nabla_{\mathbf{s}'}) + 4\partial_i\partial_j W(\mathbf{s})\partial^i_{\mathbf{s}}\partial^j_{\mathbf{s}'}\Big)\\ &- \frac{1}{N_c}\mathbf{p}_{tot}\cdot\mathcal{H}(0)\cdot\mathbf{p}_{tot} + \frac{1}{N_c}\mathbf{p}_{tot}\cdot\mathcal{H}(\mathbf{s})\cdot\mathbf{p}_{tot}\Bigg]\mathcal{D}_o. \end{aligned} \tag{4.104}$$

Regrouping all the terms in equations (4.103) and (4.104) and performing the integration on $\mathbf{s}$ using relations (4.100) and (4.101), we get:

$$\mathrm{Tr}\left[\Big\{\mathcal{L}_{so} + \Big(N_c^2 - 1\Big)\mathcal{L}_{oo}\Big\}\mathcal{D}_o\right] = 0. \tag{4.105}$$

The new equations indeed preserve the trace, but it is not conserved locally in $\mathbf{s}$ as it was with the original equations. Now that we have demonstrated this conservation, we will study the positivity.

## 4.4 Positivity

In the new discretization, positivity conservation is ensured by construction. Nonetheless, it is still interesting to demonstrate it and see how it is realized. Let us recall the Lindblad equation:

$$\frac{\mathrm{d}}{\mathrm{d}t}\rho = -i[H,\rho] + \sum_i^N \gamma_i\left(L_i\rho L_i^\dagger - \frac{1}{2}\Big\{L_i L_i^\dagger, \rho\Big\}\right). \tag{4.106}$$

By adopting a basis in which $\rho$ is diagonal, we define the weights $w_n = \langle n|\rho|n\rangle$, with $|n\rangle$ one of the eigenstates of $\rho$. In the case $N = 1$, we have:

$$\begin{aligned}\dot{w}_n &= \sum_m L_{nm} w_m L^\dagger_{mn} - L^\dagger_{nm} L_{mn} w_n \\ &= \sum_m L_{nm} w_m L^*_{nm} - L^*_{mn} L_{mn} w_n. \end{aligned} \tag{4.107}$$

Defining $t_{nm} \equiv L_{nm} L^*_{nm} > 0$, we obtain:

$$\dot{w}_n = \sum_m t_{nm} w_m - t_{mn} w_n, \tag{4.108}$$

with $t_{nm} w_m$ a gain term from the $m$ state and $t_{mn} w_n$ a loss term from the $n$ state. If all $t_{mn}$ are positive, then we can define $\Gamma_n = \sum_m t_{mn}$ so that (4.108) becomes:

$$\dot{w}_n = -\Gamma_n w_n + s, \tag{4.109}$$

where $s$ is a source term which is strictly positive. Even if we consider $s = 0$, $w_n$ can not become negative, which preserves positivity.

Starting from the $\mathcal{L}_2$ level, we will derive systematically the gain term $t_{nm}$ and show that it is positively defined at each level before demonstrating how to retrieve the terms leading to the associated loss term $t_{mn}$ at the $\mathcal{L}_2$ and $\mathcal{L}'_3$ levels. We will first prove the positivity conservation in the simpler case where color degrees of freedom are ignored. We will then analyse the full QCD case. Contrary to the trace, positivity is not conserved level by level and we will need to combine $\mathcal{L}_3$ and $\mathcal{L}_4$ terms to conserve it.

### 4.4.1 Positivity at the $\mathcal{L}_2$ level

We define $\mathcal{D}_{Q\bar{Q}} = \sum_l w_l \, |l\rangle\langle l|$ with $w_l \geq 0$. We have at the $\mathcal{L}_2$ level:

$$\begin{aligned}\dot{w}_n = \langle n|\dot{\mathcal{D}}_{Q\bar{Q}}|n\rangle &= \langle n|\mathcal{L}_2 \mathcal{D}_{Q\bar{Q}}|n\rangle \\ &= \int d^3\mathbf{s} d^3\mathbf{s}' \, \langle n|\mathbf{s}\rangle \, \langle \mathbf{s}|\mathcal{L}_2 \mathcal{D}_{Q\bar{Q}}|\mathbf{s}'\rangle \, \langle \mathbf{s}'|n\rangle \,, \end{aligned} \tag{4.110}$$

where we separate $\mathcal{L}_2$ in $\mathcal{L}_{2a}$ and $\mathcal{L}_{2b}$ which correspond respectively to a loss term and a gain term as we shall see. We will start with $\mathcal{L}_{2b}$ by assuming that we can write:

$$W(\mathbf{r}) = -\int d^3\mathbf{q}\rho(\mathbf{q})\left(e^{i\mathbf{q}\cdot\mathbf{r}} - 1\right), \tag{4.111}$$

where $\rho(\mathbf{q})$ is the spectral density of $W$ which is even with respect to $\mathbf{q}$, the gain term can then be written as:

$$\begin{aligned} -2\left(W\left(\frac{\mathbf{s}-\mathbf{s}'}{2}\right) - W\left(\frac{\mathbf{s}+\mathbf{s}'}{2}\right)\right) &= 2\int d^3\mathbf{q}\rho(\mathbf{q})\left(e^{i\frac{\mathbf{q}}{2}\cdot(\mathbf{s}-\mathbf{s}')} - e^{i\frac{\mathbf{q}}{2}\cdot(\mathbf{s}+\mathbf{s}')}\right) \\ &= 4\int d^3\mathbf{q}\rho(\mathbf{q})\sin\left(\frac{\mathbf{q}}{2}\cdot\mathbf{s}\right)\sin\left(\frac{\mathbf{q}}{2}\cdot\mathbf{s}'\right). \end{aligned} \tag{4.112}$$

We thus have for the gain term:

$$\dot{w}_n = 4\sum_l w_l \int d^3\mathbf{s}d^3\mathbf{s}'\psi_l(\mathbf{s})\psi_l^*(\mathbf{s}')\psi_n^*(\mathbf{s})\psi_n(\mathbf{s}')\int d^3\mathbf{q}\rho(\mathbf{q})\sin\left(\frac{\mathbf{q}}{2}\cdot\mathbf{s}\right)\sin\left(\frac{\mathbf{q}}{2}\cdot\mathbf{s}'\right). \tag{4.113}$$

By defining the transition amplitude:

$$T_{nl}(\mathbf{q}) \equiv 2\int d^3\mathbf{s}\psi_n^*(\mathbf{s})\sin\left(\frac{\mathbf{q}}{2}\cdot\mathbf{s}\right)\psi_l(\mathbf{s}), \tag{4.114}$$

the equation (4.113) becomes:

$$\dot{w}_n = \sum_l w_l \int d^3\mathbf{q}\rho(\mathbf{q})T_{nl}(\mathbf{q})T_{ln}(\mathbf{q}). \tag{4.115}$$

One can note that the transition amplitude $T_{nl}(\mathbf{q})$ changes the parity of $\psi_l(\mathbf{s})$. Since one has $T_{ln}(\mathbf{q}) = T_{nl}^*(\mathbf{q})$, we immediately have:

$$\begin{aligned}\dot{w}_n &= \sum_l w_l \int d^3\mathbf{q}\rho(\mathbf{q})|T_{nl}(\mathbf{q})|^2 \\ &= \sum_l w_l t_{nl},\end{aligned} \tag{4.116}$$

where we defined $t_{nl} \equiv \int d^3\mathbf{q}\rho(\mathbf{q})\left|T_{nl}(\mathbf{q})\right|^2$.
$\mathcal{L}_{2b}$ corresponds to a gain term. Similarly, for $\mathcal{L}_{2a}$, we can write:

$$\dot{w}_n = 2w_n \int d^3\mathbf{q}\rho(\mathbf{q}) \int d^3\mathbf{s}\psi_n(\mathbf{s})\psi_n^*(\mathbf{s})\left(e^{i\mathbf{q}\cdot\mathbf{s}} - 1\right), \tag{4.117}$$

where, using parity arguments, only the real part contributes:

$$\begin{aligned}\dot{w}_n &= -2w_n \int d^3\mathbf{q}\rho(\mathbf{q}) \int d^3\mathbf{s}\psi_n(\mathbf{s})\psi_n^*(\mathbf{s})[1-\cos(\mathbf{q}\cdot\mathbf{s})] \\ &= -4w_n \int d^3\mathbf{q}\rho(\mathbf{q}) \int d^3\mathbf{s}\psi_n(\mathbf{s})\psi_n^*(\mathbf{s}) \sin\left(\frac{\mathbf{q}}{2}\cdot\mathbf{s}\right)^2 \\ &= -4w_n \int d^3\mathbf{q}\rho(\mathbf{q}) \int d^3\mathbf{s}d^3\mathbf{s}'\delta^{(3)}(\mathbf{s}-\mathbf{s}')\psi_n^*(\mathbf{s}') \sin\left(\frac{\mathbf{q}}{2}\cdot\mathbf{s}'\right)\sin\left(\frac{\mathbf{q}}{2}\cdot\mathbf{s}\right)\psi_n(\mathbf{s}).\end{aligned} \tag{4.118}$$

Using a completion relation $\delta^{(3)}(\mathbf{s}-\mathbf{s}') = \sum_l \psi_l(\mathbf{s}')\psi_l^*(\mathbf{s})$, we get:

$$\begin{aligned}\dot{w}_n &= -4w_n \sum_l \int d^3\mathbf{q}\rho(\mathbf{q}) \int d^3\mathbf{s}d^3\mathbf{s}'\psi_n^*(\mathbf{s}') \sin\left(\frac{\mathbf{q}}{2}\cdot\mathbf{s}'\right)\psi_l(\mathbf{s}')\psi_l^*(\mathbf{s})\sin\left(\frac{\mathbf{q}}{2}\cdot\mathbf{s}\right)\psi_n(\mathbf{s}). \\ &= -\sum_l \int d^3\mathbf{q}\rho(\mathbf{q})T_{nl}(\mathbf{q})T_{ln}(\mathbf{q})w_n \\ &= -\sum_l t_{ln}w_n,\end{aligned} \tag{4.119}$$

which is indeed the associated loss term.

Combining the gain and loss terms, we obtain the formulation of a master equation as shown at the start of this section with equation (4.108) if and only if $\rho(\mathbf{q})$ is

globally positive as the $t_{ln}$ are positive only if it is the case.

### 4.4.2 Positivity at the $\mathcal{L}_3'$ level

Similarly to the $\mathcal{L}_2$ level, one can start again with the gain term, associated to the $\mathcal{L}_{3b}'$ terms given in section 4.2.4. We first focus on the Laplacian term. With:

$$W\left(\frac{\mathbf{s}+\mathbf{s}'}{2}\right) - W\left(\frac{\mathbf{s}-\mathbf{s}'}{2}\right) = \int d^3\mathbf{s}\rho(\mathbf{q})\left[e^{i\frac{\mathbf{q}}{2}\cdot(\mathbf{s}-\mathbf{s}')} - e^{i\frac{\mathbf{q}}{2}\cdot(\mathbf{s}+\mathbf{s}')}\right], \tag{4.120}$$

we have:

$$\begin{aligned}\frac{\hbar^2}{2MT}\left(\Delta W\left(\frac{\mathbf{s}+\mathbf{s}'}{2}\right) - \Delta W\left(\frac{\mathbf{s}-\mathbf{s}'}{2}\right)\right) &= -\frac{\hbar^2}{2MT}\int d^3\mathbf{s}\rho(\mathbf{q})\|\mathbf{q}\|^2\left[e^{i\frac{\mathbf{q}}{2}\cdot(\mathbf{s}-\mathbf{s}')} - e^{i\frac{\mathbf{q}}{2}\cdot(\mathbf{s}+\mathbf{s}')}\right] \\ &= -\frac{\hbar^2}{MT}\int d^3\mathbf{s}\rho(\mathbf{q})\|\mathbf{q}\|^2\sin\left(\frac{\mathbf{q}}{2}\cdot\mathbf{s}\right)\sin\left(\frac{\mathbf{q}}{2}\cdot\mathbf{s}'\right).\end{aligned} \tag{4.121}$$

And one obtains, using the definition (4.114) :

$$\dot{w}_n = -\frac{\hbar^2}{4MT}\sum_l \int d^3\mathbf{s}\rho(\mathbf{q})\|\mathbf{q}\|^2|T_{nl}(\mathbf{q})|^2 w_l \tag{4.122}$$

For the second contribution in $\mathcal{L}_{3b}'$, we have:

$$\begin{aligned}\nabla W\left(\frac{\mathbf{s}+\mathbf{s}'}{2}\right) &= \int d^3\mathbf{q}\rho(\mathbf{q})\mathbf{q}\cdot\sin\left(\frac{\mathbf{q}}{2}\cdot\{\mathbf{s}+\mathbf{s}'\}\right) \\ &= \int d^3\mathbf{q}\rho(\mathbf{q})\mathbf{q}\cdot\left[\sin\left(\frac{\mathbf{q}}{2}\cdot\mathbf{s}\right)\cos\left(\frac{\mathbf{q}}{2}\cdot\mathbf{s}'\right) + \sin\left(\frac{\mathbf{q}}{2}\cdot\mathbf{s}'\right)\cos\left(\frac{\mathbf{q}}{2}\cdot\mathbf{s}\right)\right].\end{aligned} \tag{4.123}$$

We also have:

$$\nabla W\left(\frac{\mathbf{s}-\mathbf{s}'}{2}\right) = \int d^3\mathbf{q}\rho(\mathbf{q})\mathbf{q}\cdot\left[\sin\left(\frac{\mathbf{q}}{2}\cdot\mathbf{s}\right)\cos\left(\frac{\mathbf{q}}{2}\cdot\mathbf{s}'\right) - \sin\left(\frac{\mathbf{q}}{2}\cdot\mathbf{s}'\right)\cos\left(\frac{\mathbf{q}}{2}\cdot\mathbf{s}\right)\right]. \tag{4.124}$$

Using those relations we get:

$$\begin{aligned}&\frac{\hbar^2}{2MT}\left[\nabla W\left(\frac{\mathbf{s}+\mathbf{s}'}{2}\right)\cdot(\nabla_{\mathbf{s}}+\nabla_{\mathbf{s}'})-\nabla W\left(\frac{\mathbf{s}-\mathbf{s}'}{2}\right)\cdot(\nabla_{\mathbf{s}}-\nabla_{\mathbf{s}'})\right]\\&=\frac{\hbar^2}{MT}\int d^3\mathbf{q}\rho(\mathbf{q})\left[\sin\left(\frac{\mathbf{q}}{2}\cdot\mathbf{s}\right)\cos\left(\frac{\mathbf{q}}{2}\cdot\mathbf{s}'\right)\mathbf{q}\cdot\nabla_{\mathbf{s}'}+\sin\left(\frac{\mathbf{q}}{2}\cdot\mathbf{s}'\right)\cos\left(\frac{\mathbf{q}}{2}\cdot\mathbf{s}\right)\mathbf{q}\cdot\nabla_{\mathbf{s}}\right].\end{aligned} \tag{4.125}$$

We thus have:

$$\begin{aligned}\dot{w}_n=\frac{\hbar^2}{MT}\sum_l\int d^3\mathbf{q}\rho(\mathbf{q})\int d^3\mathbf{s}d^3\mathbf{s}'\psi_n(\mathbf{s}')\psi_n^*(\mathbf{s})\Big[&\sin\left(\frac{\mathbf{q}}{2}\cdot\mathbf{s}\right)\cos\left(\frac{\mathbf{q}}{2}\cdot\mathbf{s}'\right)\mathbf{q}\cdot\nabla_{\mathbf{s}'}\\&+\sin\left(\frac{\mathbf{q}}{2}\cdot\mathbf{s}'\right)\cos\left(\frac{\mathbf{q}}{2}\cdot\mathbf{s}\right)\mathbf{q}\cdot\nabla_{\mathbf{s}}\Big]\psi_l(\mathbf{s})\psi_l^*(\mathbf{s}')w_l.\end{aligned} \tag{4.126}$$

We define new transition operators:

$$T_{nl}^{(3)}(\mathbf{q})\equiv\frac{\hbar^2}{2MT}\int d^3\mathbf{s}\psi_n^*(\mathbf{s})\cos\left(\frac{\mathbf{q}}{2}\cdot\mathbf{s}\right)\mathbf{q}\cdot\nabla_{\mathbf{s}}\psi_l(\mathbf{s}). \tag{4.127}$$

As the $T_{nl}(\mathbf{q})$ operators, those new transition operators also change the parity of $\psi_l(\mathbf{s})$. Using those newly defined operators and the previous $T_{nl}$ operators from equation (4.114), we obtain:

$$\dot{w}_n=\sum_l\int d^3\mathbf{q}\rho(\mathbf{q})\left[T_{nl}(\mathbf{q})T_{nl}^{(3)*}(\mathbf{q})+T_{nl}^*(\mathbf{q})T_{nl}^{(3)}(\mathbf{q})\right]w_l. \tag{4.128}$$

Combining (4.115),(4.122) and (4.128), $t_{nl}$ writes:

$$t_{nl}\equiv\int d^3\mathbf{q}\rho(\mathbf{q})\left[\left(1-\frac{\hbar^2\|\mathbf{q}\|^2}{4MT}\right)|T_{nl}(\mathbf{q})|^2+\left(T_{nl}(\mathbf{q})T_{nl}^{(3)*}(\mathbf{q})+c.c\right)\right] \tag{4.129}$$

which is not positively defined.

We now study the associated loss term, by first studying the contribution associated to (4.128). To do so, we go back to equation (4.126) and perform the change $l \leftrightarrow n$:

$$\frac{\dot{w}_n}{w_n} = -\frac{\hbar^2}{MT}\sum_l \int d^3\mathbf{q}\rho(\mathbf{q}) \int d^3\mathbf{s}d^3\mathbf{s}'\psi_l(\mathbf{s}')\psi_l^*(\mathbf{s})\Big[\sin\Big(\frac{\mathbf{q}}{2}\cdot\mathbf{s}\Big)\cos\Big(\frac{\mathbf{q}}{2}\cdot\mathbf{s}'\Big)\mathbf{q}\cdot\nabla_{\mathbf{s}'} + \sin\Big(\frac{\mathbf{q}}{2}\cdot\mathbf{s}'\Big)\cos\Big(\frac{\mathbf{q}}{2}\cdot\mathbf{s}\Big)\mathbf{q}\cdot\nabla_{\mathbf{s}}\Big]\psi_n(\mathbf{s})\psi_n^*(\mathbf{s}'). \tag{4.130}$$

Using the completion relation, one finds:

$$\begin{aligned}\frac{\dot{w}_n}{w_n} &= -\frac{\hbar^2}{MT}\int d^3\mathbf{q}\rho(\mathbf{q}) \int d^3\mathbf{s}\Big[\sin\Big(\frac{\mathbf{q}}{2}\cdot\mathbf{s}\Big)\cos\Big(\frac{\mathbf{q}}{2}\cdot\mathbf{s}\Big)\mathbf{q}\cdot\nabla_{\mathbf{s}} \\ &\qquad + \sin\Big(\frac{\mathbf{q}}{2}\cdot\mathbf{s}\Big)\cos\Big(\frac{\mathbf{q}}{2}\cdot\mathbf{s}\Big)\mathbf{q}\cdot\nabla_{\mathbf{s}}\Big]\psi_n(\mathbf{s})\psi_n^*(\mathbf{s}). \\ &= -\frac{\hbar^2}{2MT}\int d^3\mathbf{q}\rho(\mathbf{q}) \int d^3\mathbf{s}\sin(\mathbf{q}\cdot\mathbf{s})\mathbf{q}\cdot\nabla_{\mathbf{s}}(\psi_n^*(\mathbf{s})\psi_n(\mathbf{s})).\end{aligned} \tag{4.131}$$

Integrating by parts, we obtain:

$$\frac{\dot{w}_n}{w_n} = \frac{\hbar^2}{2MT}\int d^3\mathbf{q}\rho(\mathbf{q})\|\mathbf{q}\|^2 \int d^3\mathbf{s}|\psi_n(\mathbf{s})|^2\cos(\mathbf{q}\cdot\mathbf{s}). \tag{4.132}$$

Following the same procedure for the loss term associated to equation (4.128), we obtain:

$$\frac{\dot{w}_n}{w_n} = \frac{\hbar^2}{2MT}\int d^3\mathbf{q}\rho(\mathbf{q})\|\mathbf{q}\|^2 \int d^3\mathbf{s}|\psi_n(\mathbf{s})|^2(1-\cos(\mathbf{q}\cdot\mathbf{s})). \tag{4.133}$$

Regrouping both contributions leads to the following loss term:

$$\frac{\dot{w}_n}{w_n} = \frac{\hbar^2}{2MT}\int d^3\mathbf{q}\rho(\mathbf{q})\|\mathbf{q}\|^2 \int d^3\mathbf{s}|\psi_n(\mathbf{s})|^2 = \frac{\hbar^2}{2MT}\Delta W(0), \tag{4.134}$$

which is exactly $\mathcal{L}'_{3a}$.

We showed that the $\mathcal{L}'_3$ contribution by itself can't form master equation terms preserving positivity. We shall now demonstrate that adding the $\mathcal{L}_4$ contribution leads to conservation of positivity.

### 4.4.3 Positivity at the $\mathcal{L}_4$ level

We start with the gain term given by the contributions $\mathcal{L}_{4b}^{quad}$, $\mathcal{L}_{4b}^{lin}$ and $\mathcal{L}_{4b}^{cst}$ defined in section 4.1.2. The $\mathcal{L}_{4b}^{quad}$ term is:

$$\mathcal{L}_{4b}^{quad} = \frac{\hbar^4}{8M^2T^2}\left[\partial_i\partial_j W\left(\frac{\mathbf{s}-\mathbf{s}'}{2}\right)\partial_{\mathbf{s}}^i\partial_{\mathbf{s}'}^j + \partial_i\partial_j W\left(\frac{\mathbf{s}+\mathbf{s}'}{2}\right)\partial_{\mathbf{s}}^i\partial_{\mathbf{s}'}^j\right]. \tag{4.135}$$

Using the spectral decomposition of $W$, we obtain:

$$\begin{aligned}\partial_i\partial_j W\left(\frac{\mathbf{s}+\mathbf{s}'}{2}\right) &= \int d^3\mathbf{q}\rho(\mathbf{q})q_iq_j\left[\cos\left(\frac{\mathbf{q}}{2}\cdot(\mathbf{s}+\mathbf{s}')\right) + i\sin\left(\frac{\mathbf{q}}{2}\cdot(\mathbf{s}+\mathbf{s}')\right)\right] \\ &= \int d^3\mathbf{q}\rho(\mathbf{q})q_iq_j\cos\left(\frac{\mathbf{q}}{2}\cdot(\mathbf{s}+\mathbf{s}')\right),\end{aligned} \tag{4.136}$$

where we used parity considerations. Similarly:

$$\partial_i\partial_j W\left(\frac{\mathbf{s}-\mathbf{s}'}{2}\right) = \int d^3\mathbf{q}\rho(\mathbf{q})q_iq_j\cos\left(\frac{\mathbf{q}}{2}\cdot(\mathbf{s}-\mathbf{s}')\right). \tag{4.137}$$

We can then write:

$$\mathcal{L}_{4b}^{quad} = \frac{\hbar^4}{4M^2T^2}\int d^3\mathbf{q}\rho(\mathbf{q})\left[\cos\left(\frac{\mathbf{q}}{2}\cdot\mathbf{s}\right)\mathbf{q}\cdot\nabla_{\mathbf{s}}\right]\left[\cos\left(\frac{\mathbf{q}}{2}\cdot\mathbf{s}'\right)\mathbf{q}\cdot\nabla_{\mathbf{s}'}\right]. \tag{4.138}$$

Proceeding as for the $\mathcal{L}_2$ and $\mathcal{L}_3'$ contributions, we obtain:

$$\dot{w}_n = \sum_l \int d^3\mathbf{s} d^3\mathbf{s}' \psi_n(\mathbf{s}') \psi_n^*(\mathbf{s}) \int d^3\mathbf{q} \rho(\mathbf{q}) \left[ \cos\left(\frac{\mathbf{q}}{2} \cdot \mathbf{s}\right) \frac{\hbar^2 \mathbf{q} \cdot \nabla_{\mathbf{s}}}{2MT} \right] \times \left[ \cos\left(\frac{\mathbf{q}}{2} \cdot \mathbf{s}'\right) \frac{\hbar^2 \mathbf{q} \cdot \nabla_{\mathbf{s}'}}{2MT} \right] \psi_l(\mathbf{s}) \psi_l^*(\mathbf{s}') w_l, \tag{4.139}$$

where we can recognize the $T_{nl}^{(3)}(\mathbf{q})$ operators we introduced with equation (4.127) so that:

$$\dot{w}_n = \sum_l \int d^3\mathbf{q} \rho(\mathbf{q}) T_{nl}^{(3)}(\mathbf{q}) T_{nl}^{(3)*}(\mathbf{q}) w_l. \tag{4.140}$$

We can see something really interesting by regrouping the results from equations (4.115), (4.128) and (4.139):

$$t_{nl}^{pos} \equiv \int d^3\mathbf{q} \rho(\mathbf{q}) \left| T_{nl}(\mathbf{q}) + T_{nl}^{(3)}(\mathbf{q}) \right|^2, \tag{4.141}$$

which is positively defined. This grouping of terms will be of particular interest in the following section as we shall see.

The $\mathcal{L}_{4b}^{lin}$ contribution writes:

$$\mathcal{L}_{4b}^{lin} = \frac{\hbar^4}{16M^2T^2} \left[ -\nabla\nabla^2 W\left(\frac{\mathbf{s}-\mathbf{s}'}{2}\right) \cdot (\nabla_{\mathbf{s}} - \nabla_{\mathbf{s}'}) + \nabla\nabla^2 W\left(\frac{\mathbf{s}+\mathbf{s}'}{2}\right) \cdot (\nabla_{\mathbf{s}} + \nabla_{\mathbf{s}'}) \right]. \tag{4.142}$$

The spectral decomposition of W gives us:

$$\nabla\nabla^2 W\left(\frac{\mathbf{s}+\mathbf{s}'}{2}\right) = -\int d^3\mathbf{q} \rho(\mathbf{q}) \|\mathbf{q}\|^2 \mathbf{q} \left[ \sin\left(\frac{\mathbf{q}}{2} \cdot \mathbf{s}\right) \cos\left(\frac{\mathbf{q}}{2} \cdot \mathbf{s}'\right) + \sin\left(\frac{\mathbf{q}}{2} \cdot \mathbf{s}'\right) \cos\left(\frac{\mathbf{q}}{2} \cdot \mathbf{s}\right) \right], \tag{4.143}$$

and:

$$\nabla\nabla^2 W\left(\frac{\mathbf{s}-\mathbf{s}'}{2}\right) = -\int d^3\mathbf{q}\rho(\mathbf{q})\|\mathbf{q}\|^2\mathbf{q}\Big[\sin\left(\frac{\mathbf{q}}{2}\cdot\mathbf{s}\right)\cos\left(\frac{\mathbf{q}}{2}\cdot\mathbf{s}'\right) - \sin\left(\frac{\mathbf{q}}{2}\cdot\mathbf{s}'\right)\cos\left(\frac{\mathbf{q}}{2}\cdot\mathbf{s}\right)\Big]. \tag{4.144}$$

Combining equations (4.142),(4.143) and (4.144) leads to:

$$\mathcal{L}_{4b}^{lin} = -\frac{\hbar^4}{8M^2T^2}\int d^3\mathbf{q}\rho(\mathbf{q})\|\mathbf{q}\|^2\Big[\sin\left(\frac{\mathbf{q}}{2}\cdot\mathbf{s}\right)\cos\left(\frac{\mathbf{q}}{2}\cdot\mathbf{s}'\right)\mathbf{q}\cdot\nabla_{\mathbf{s}'} + \sin\left(\frac{\mathbf{q}}{2}\cdot\mathbf{s}'\right)\cos\left(\frac{\mathbf{q}}{2}\cdot\mathbf{s}\right)\mathbf{q}\cdot\nabla_{\mathbf{s}}\Big], \tag{4.145}$$

which gives the following term:

$$\dot{w}_n = -\sum_l \int d^3\mathbf{q}\rho(\mathbf{q})\frac{\|\mathbf{q}\|^2}{8MT}\Big[T_{nl}(\mathbf{q})T_{nl}^{(3)*}(\mathbf{q}) + T_{nl}^{*}(\mathbf{q})T_{nl}^{(3)}(\mathbf{q})\Big]w_l. \tag{4.146}$$

Finally, the $\mathcal{L}_{4b}^{cst}$ term is given by:

$$\mathcal{L}_{4b}^{cst} = \frac{\hbar^4}{32M^2T^2}\left[-\partial^4 W\left(\frac{\mathbf{s}-\mathbf{s}'}{2}\right) + \partial^4 W\left(\frac{\mathbf{s}+\mathbf{s}'}{2}\right)\right]. \tag{4.147}$$

One has:

$$\begin{aligned}\partial^4 W\left(\frac{\mathbf{s}+\mathbf{s}'}{2}\right) &= -\int d^3\mathbf{q}\rho(\mathbf{q})\|\mathbf{q}\|^4\cos\left(\frac{\mathbf{q}}{2}\cdot\left[\mathbf{s}+\mathbf{s}'\right]\right)\\ \partial^4 W\left(\frac{\mathbf{s}-\mathbf{s}'}{2}\right) &= -\int d^3\mathbf{q}\rho(\mathbf{q})\|\mathbf{q}\|^4\cos\left(\frac{\mathbf{q}}{2}\cdot\left[\mathbf{s}-\mathbf{s}'\right]\right).\end{aligned} \tag{4.148}$$

By taking into account the parities, we have:

$$\mathcal{L}_{4b}^{cst} = \int d^3\mathbf{q}\rho(\mathbf{q})\left[\frac{\hbar^2\|\mathbf{q}\|^2}{8MT}2\sin\left(\frac{\mathbf{q}}{2}\cdot\mathbf{s}\right)\right]\left[\frac{\hbar^2\|\mathbf{q}\|^2}{8MT}2\sin\left(\frac{\mathbf{q}}{2}\cdot\mathbf{s}'\right)\right], \tag{4.149}$$

which leads to:

$$\dot{w}_n = \sum_l \int d^3\mathbf{q}\rho(\mathbf{q})\left|\frac{\hbar^2\|\mathbf{q}\|^2}{8MT}T_{nl}(\mathbf{q})\right|^2 w_l. \tag{4.150}$$

Regrouping the equations (4.139),(4.146) and (4.150), one obtains the gain term at the $\mathcal{L}_4$ level:

$$\begin{aligned}\dot{w}_n = \sum_l \int d^3\mathbf{q}\rho(\mathbf{q})\Bigg[&T_{nl}^{(3)}(\mathbf{q})T_{nl}^{(3)*}(\mathbf{q}) + \frac{\hbar^4\|\mathbf{q}\|^4}{64M^2T^2}|T_{nl}(\mathbf{q})|^2 \\ &-\frac{\|\mathbf{q}\|^2}{8MT}\left[T_{nl}(\mathbf{q})T_{nl}^{(3)*}(\mathbf{q}) + T_{nl}^{*}(\mathbf{q})T_{nl}^{(3)}(\mathbf{q})\right]\Bigg]w_l\end{aligned} \tag{4.151}$$

Regrouping the equations (4.129) and (4.151) and redefining $T_{nl}(\mathbf{q})$ such that $\tilde{T}_{nl}(\mathbf{q}) = \left(1 - \frac{\hbar^2\|\mathbf{q}\|^2}{8MT}\right)T_{nl}(\mathbf{q})$, we finally obtain the gain term for the $\mathcal{L}_2$,$\mathcal{L}_3'$ and $\mathcal{L}_4$ levels:

$$t_{nl} \equiv \int d^3\mathbf{q}\rho(\mathbf{q})\left|\tilde{T}_{nl}(\mathbf{q}) + T_{nl}^{(3)}(\mathbf{q})\right|^2, \tag{4.152}$$

indeed proving that the new equation preserves positivity if $\rho(\mathbf{q})$ is globally positive.

We will not demonstrate how to derive the associated loss term, however it is compatible with $\mathcal{L}_{4a}$ and the procedure is the same as the one used to derive the loss terms at the $\mathcal{L}_2$ and $\mathcal{L}_3'$ levels. Another point that should be discussed is the contribution of the $\mathbf{p}_{tot}$ terms. It is easy to show that for these terms, the gain part writes:

$$t_{nl} \equiv \frac{\hbar^4}{64M^2T^2}\int d^3\mathbf{q}\rho(\mathbf{q})(\mathbf{p}_{tot}\cdot\mathbf{q})^2|T_{nl}(\mathbf{q})|^2, \tag{4.153}$$

which also preserves positivity.

### 4.4.4 Full QCD case

We now prove that positivity is preserved when taking into account the color degrees of freedom. For that, we will proceed in the same way as in sections sections 4.4.1 to 4.4.3 and interpret the QCD operators in terms of transition rates.

**$\mathcal{L}_2$ level:**

In the octet-octet color sector we have [2]:

$$\mathcal{L}_{2b}^{oo} = -\left(\frac{N_c^2-4}{4N_c}W_- + \frac{N_c}{4}W_+\right), \tag{4.154}$$

with $W_\pm$ defined in chapter 3 with the equation (3.49).

The $W_-$ term was leading to:

$$\dot{w}_n^o = \sum_l \frac{N_c^2-4}{4N_c} t_{nl} w_n^o. \tag{4.155}$$

For the $W_+$ term, one has:

$$\dot{w}_n^o = \sum_l \frac{N_c}{4} t_{nl}^+ w_n^o, \tag{4.156}$$

with $t_{nl}^+ = \int d^3\mathbf{q}\rho(\mathbf{q})\left|T_{nl}^+(\mathbf{q})\right|^2$ and:

$$T_{nl}^+(\mathbf{q}) \equiv 2\int d^3\mathbf{s}\psi_n^*(\mathbf{s})\cos\left(\frac{\mathbf{q}}{2}\cdot\mathbf{s}\right)\psi_l(\mathbf{s}). \tag{4.157}$$

2. It is more convenient to write the terms this way to exploit the results already obtained

One immediately sees that $T^{+}_{nl}(\mathbf{q})$ do not change the parity of $\psi_l(\mathbf{s})$. This implies that $\mathcal{L}_{oo}$ has terms changing the parity and other that do not. The terms associated to singlet↔octet transitions are proportional to $W_-$, with color factors specific to each type of transition. Therefore, the gain terms have the same structure as those given by the equation (4.155) and preserve positivity.

Taking into account the associated loss term for both octet→octet and octet→singlet transitions (computed in the same way as in section 4.4.1, one obtains:

$$\mathcal{L}^{oo}_{2a} = 2C_F W(0) + \frac{1}{2N_c} W_c, \tag{4.158}$$

which indeed corresponds to what we had in section 3.8.

**$\mathcal{L}'_3$ level:**

As for the $\mathcal{L}_2$ level, the gain term for singlet↔octet transitions is the same as in the QED case with a different color factor (this will also be the case to the $\mathcal{L}_4$ level gain terms). The octet→octet gain term has two contributions: one that is the same as in the QED case with a $\frac{N_c^2-4}{2N_c}$ color factor and another "$W_+$":

$$\mathcal{L}^{oo,+}_{3b} = -\frac{\hbar^2}{4MT}\frac{N_c}{4}[\Delta W_+ + \nabla W_+ \cdot \nabla_+]. \tag{4.159}$$

The computation is the same as for the QED case. Combining this contribution and the one from the $\mathcal{L}_2$ level, one gets:

$$t^{+}_{nl} = \int d^3\mathbf{q}\rho(\mathbf{q})\left[\left(1 - \frac{\hbar^2\|\mathbf{q}\|^2}{4MT}\right)\left|T^{+}_{nl}(\mathbf{q})\right|^2 + \left(T^{+}_{nl}(\mathbf{q})T^{+(3)*}_{nl}(\mathbf{q}) + c.c\right)\right], \tag{4.160}$$

with $T^{+(3)}_{nl}(\mathbf{q}) = \frac{\hbar^2}{2MT}\int d^3\mathbf{s}\psi^*_n(\mathbf{s})\sin\left(\frac{\mathbf{q}}{2}\cdot\mathbf{s}\right)\mathbf{q}\cdot\nabla_{\mathbf{s}}\psi_l(\mathbf{s})$.

We will not show how to derive the loss term at the $\mathcal{L}'_3$ level but the procedure is the same as before.

**$\mathcal{L}_4$ level:**

Proceeding as in the previous section, the $\mathcal{L}_{4b}^{quad}$ term for octet→octet transitions writes:

$$\dot{w}_n^o = \sum_l \frac{N_c}{4} \int d^3\mathbf{q}\rho(\mathbf{q}) T_{nl}^{+(3)} T_{nl}^{+(3)*}(\mathbf{q}) w_l^o. \tag{4.161}$$

As in the QED case, combining the same contributions as in equation (4.141) leads to an interesting result:

$$t_{nl}^{pos,+} \equiv \int d^3\mathbf{q}\rho(\mathbf{q}) \left| T_{nl}^{+}(\mathbf{q}) - T_{nl}^{+(3)}(\mathbf{q}) \right|^2. \tag{4.162}$$

Note that in the QCD case, there is a "-" sign and not a "+" sign. This grouping will be very useful in the last section of this chapter. We now treat the $\mathcal{L}_{4b}^{lin}$ term, giving us:

$$\dot{w}_n^o = \frac{N_c}{4} \sum_l \int d^3\mathbf{q}\rho(\mathbf{q}) \frac{\hbar^2\|\mathbf{q}\|^2}{8MT} \left[ T_{nl}^{+}(\mathbf{q}) T_{nl}^{+(3)*}(\mathbf{q}) + T_{nl}^{+*}(\mathbf{q}) T_{nl}^{+(3)}(\mathbf{q}) \right] w_l^o. \tag{4.163}$$

Finally, we focus on the $\mathcal{L}_{4b}^{cst}$ term, leading to:

$$\dot{w}_n^o = \frac{N_c}{4} \sum_l \int d^3\mathbf{q}\rho(\mathbf{q}) \left| \frac{\hbar^2\|\mathbf{q}\|^2}{8MT} T_{nl}^{+}(\mathbf{q}) \right|^2 w_l^o. \tag{4.164}$$

Regrouping the contributions from all three levels, one finally finds:

$$t_{nl}^{+} \equiv \int d^3\mathbf{q}\rho(\mathbf{q}) \left| \tilde{T}_{nl}^{+}(\mathbf{q}) - T_{nl}^{+(3)}(\mathbf{q}) \right|^2, \tag{4.165}$$

with $\tilde{T}_{nl}^{+}(\mathbf{q}) = \left(1 - \frac{\hbar^2\|\mathbf{q}\|^2}{8MT}\right) T_{nl}^{+}(\mathbf{q})$.

We can see that positivity is indeed preserved in the QCD case if $\rho(\mathbf{q})$ is globally positive. We will not prove it here for the terms involving $\mathbf{p}_{tot}$ but the procedure is the same. We will also not show how to derive the loss term at the $\mathcal{L}_4$ level but the procedure is the same as before.

## 4.5 UV divergences and minimal set

The equations presented in 4.1 are positivity and trace preserving which are key properties of well-defined master equations. However, they involve $3^{rd}$ and $4^{th}$ derivatives of the imaginary part of the potential W, which are actually divergent if we take the expression of W derived from HTL perturbation theory:

$$W(\mathbf{r}) \propto \int d^3\mathbf{z} \frac{\|\mathbf{z}\|^2}{\left(\|\mathbf{z}\|^2 - 1\right)^2}\left(1 - \frac{\sin(\mathbf{z}\cdot\mathbf{r})}{\mathbf{z}\cdot\mathbf{r}}\right). \tag{4.166}$$

For example, one can show that $\partial^4 W(0)$ is UV-divergent.

As we go higher and higher in the order of the derivatives of the imaginary part W, we leave the domain of validity of the Hard Thermal Loop approximation that is used to derive W, leading to the UV-divergences found. We will hereafter explain the pragmatic method that we adopt that avoids those divergences while embedding most of the terms identified in the $\mathcal{L}_2$, $\mathcal{L}'_3$ and $\mathcal{L}_4$ operators. We showed in equation (4.141) that a specific grouping of terms was enough to ensure that positivity is preserved. This grouping will be referred as the *minimal set* and it does not lead to UV divergences By only taking those terms (alongside the corresponding $\mathcal{L}_a$ terms and the terms depending on $p_{tot}$) we neglect several others, especially at the $\mathcal{L}'_3$ level. It is however possible to regenerate most of the missing terms by redefining the imaginary part W of the complex potential in the following way:

$$\tilde{W}(\mathbf{r}) \equiv -\int d^3\mathbf{q}\rho(\mathbf{q})\left(1 - \frac{\hbar^2\|\mathbf{q}\|^2}{8MT}\right)\left(e^{i\mathbf{q}\cdot\mathbf{r}} - 1\right). \tag{4.167}$$

Using this new potential in the minimal set of equations, most of the missing terms are regenerated and even higher order terms (that we could call $\mathcal{L}_5$, $\mathcal{L}_6$...) are generated. Those higher order terms are supposed to be truly negligeable, as $\mathcal{L}_4$ terms are already subleading. However, the potential (4.167) still leads to some UV divergences

This leads us to the actual strategy that we will retain for the study of the dynamics of a heavy quarkonium:

— We take the so-called minimal set of terms.

— We use the redefined imaginary part W to regenerate most terms, using the following prescription to avoid the divergencies of the prescription used in equation (4.167):

$$\tilde{\rho}(\mathbf{q}) = \frac{\rho(\mathbf{q})}{\left(1 + \frac{\hbar^2 \|\mathbf{q}\|^2}{8MT}\right)^2}. \tag{4.168}$$

Using this redefined potential has an additional advantage. It ensures that higher order (> 2) derivatives of W are now regularized and not divergent anymore. This is crucial since $3^{rd}$ order derivatives remain in the final equations. The type of terms contained in the minimal set are regrouped in table 4.1 (without any prefactor).

| Level | Terms |
|---|---|
| $\mathcal{L}_0$,$\mathcal{L}_1$,$\mathcal{L}_2$ | all |
| $\mathcal{L}_3$ | $\nabla W(\mathbf{s}) \cdot \nabla_{\mathbf{s}}$ |
| | $\nabla W(\mathbf{s}') \cdot \nabla_{\mathbf{s}'}$ |
| | $\nabla W\left(\frac{\mathbf{s}-\mathbf{s}'}{2}\right) \cdot (\nabla_{\mathbf{s}} - \nabla_{\mathbf{s}'})$ |
| | $\nabla W\left(\frac{\mathbf{s}+\mathbf{s}'}{2}\right) \cdot (\nabla_{\mathbf{s}} + \nabla_{\mathbf{s}'})$ |
| $\mathcal{L}_4$ | $p_{\text{tot}}$ terms |
| | $\nabla^2 W(0)\left(\nabla^2_{\mathbf{s}} + \nabla^2_{\mathbf{s}'}\right)$ |
| | $\nabla^2 W(\mathbf{s}) \nabla^2_{\mathbf{s}}$ |
| | $\nabla^2 W(\mathbf{s}') \nabla^2_{\mathbf{s}'}$ |
| | $\nabla \nabla^2 W(\mathbf{s}) \cdot \nabla_{\mathbf{s}}$ |
| | $\nabla \nabla^2 W(\mathbf{s}') \cdot \nabla_{\mathbf{s}'}$ |
| | $\nabla^2 W\left(\frac{\mathbf{s}-\mathbf{s}'}{2}\right) \nabla_{\mathbf{s}} \nabla_{\mathbf{s}'}$ |
| | $\nabla^2 W\left(\frac{\mathbf{s}+\mathbf{s}'}{2}\right) \nabla_{\mathbf{s}} \nabla_{\mathbf{s}'}$ |

TABLE 4.1 – Summary of the terms contained in the minimal set

## 4.6 Conclusion

In this chapter, we derived the new master equations that we will use to describe the quarkonium dynamics. We proved that they indeed preserves the trace and positivity of the reduced density operator and we provided a strategy to properly treat divergences. Before applying those equations to study the dynamics of a heavy quarkonium, we show how the resolution is performed in the next chapter.

# Chapter 5

# Numerical implementation

In chapter 4, we presented new equations, extending the work done by Blaizot & Escobedo [2], now exhibiting the properties of a Lindblad equation. This chapter aims to present the numerical implementation of those equations and the numerical scheme used to resolve them, in a one dimensional case. A new phenomenological complex potential, developped to be better suited for one dimensional studies, is also presented. The numerical code is finally tested to ensure that the trace of the density matrix and its positivity, which are preserved analytically as proved in chapter 4, are also preserved numerically.

## 5.1 One-dimensionnal equations

One last simplification will be made: the resolution of the equations derived in chapter 4 will not be done in three dimensions and is limited to the one-dimensionnal case. This simplification will reduce the computational cost required to resolve the equations while still allowing to gain insight on the dynamics and especially on the validity of the semi-classical approximation [1]. The transformation to one-dimensionnal equations is straightforward and one obtains:

1. Another strategy would be to perform a expansion on the first spherical harmonics and then treat the one-dimensional radial space

$$
\begin{aligned}
\mathcal{L}_{ss} = & \frac{i\hbar^2c^2}{M}\left[\partial_s^2 - \partial_{s'}^2\right] - C_F\left[V(s) - V(s')\right] \\
& + C_F\left[2W(0) - W(s) - W(s')\right] \\
& - \frac{\hbar^2c^2C_F}{2MT}\left[W'(s)\partial_s + W'(s')\partial_{s'}\right] \\
& + \frac{\hbar^4c^4C_F}{64M^2T^2}\left[4W''(0)\left(\partial_s^2 + \partial_{s'}^2\right) - 2p_{tot}^2W''(0)\right] \\
& + \frac{\hbar^4c^4C_F}{64M^2T^2}\left[4W''(s)\partial_s^2 + 4W''(s')\partial_{s'}^2 + 4W'''(s)\partial_s\right] \\
& + \frac{\hbar^4c^4C_F}{64M^2T^2}\left[4W'''(s')\partial_{s'} + p_{tot}^2W''(s) + p_{tot}^2W''(s')\right]
\end{aligned}
$$

$$
\begin{aligned}
\mathcal{L}_{so} = & C_F\left[-2W\left(\frac{s-s'}{2}\right) + 2W\left(\frac{s+s'}{2}\right)\right] \\
& + \frac{\hbar^2c^2C_F}{2MT}\left[-W'(\frac{s-s'}{2})(\partial_s - \partial_{s'}) + W'(\frac{s+s'}{2})(\partial_s + \partial_{s'})\right] \\
& + \frac{\hbar^4c^4C_F}{8M^2T^2}\left[W''\left(\frac{s-s'}{2}\right)\partial_s\partial_{s'} + W''\left(\frac{s+s'}{2}\right)\partial_s\partial_{s'}\right] \\
& + \frac{\hbar^4c^4C_F}{32M^2T^2}\left[p_{tot}^2W''\left(\frac{s-s'}{2}\right) - p_{tot}^2W''\left(\frac{s+s'}{2}\right)\right]
\end{aligned}
$$

$$
\begin{aligned}
\mathcal{L}_{os} = & \frac{1}{2N_c}\left[-2W\left(\frac{s-s'}{2}\right) + 2W\left(\frac{s+s'}{2}\right)\right] \\
& + \frac{1}{2N_c}\frac{\hbar^2c^2}{2MT}\left[-W'(\frac{s-s'}{2})(\partial_s - \partial_{s'}) + W'(\frac{s+s'}{2})(\partial_s + \partial_{s'})\right] \\
& + \frac{1}{2N_c}\frac{\hbar^4c^4}{8M^2T^2}\left[W''\left(\frac{s-s'}{2}\right)\partial_s\partial_{s'} + W''\left(\frac{s+s'}{2}\right)\partial_s\partial_{s'}\right] \\
& + \frac{1}{2N_c}\frac{\hbar^4c^4}{32M^2T^2}\left[p_{tot}^2W''\left(\frac{s-s'}{2}\right) - p_{tot}^2W''\left(\frac{s+s'}{2}\right)\right]
\end{aligned}
$$

$$
\begin{aligned}
\mathcal{L}_{oo} = & \frac{i\hbar^2c^2}{M}\left[\partial_s^2 - \partial_{s'}^2\right] + \frac{1}{2N_c}\left[V(s) - V(s')\right] \\
& + 2C_F W(0) + \frac{1}{2N_c}[W(s) + W(s)] \\
& - \frac{N_c^2-2}{N_c} W\left(\frac{s-s'}{2}\right) - \frac{2}{N_c} W\left(\frac{s+s'}{2}\right) \\
& + \frac{1}{2N_c}\frac{\hbar^2c^2}{2MT}\left[W'(s)\partial_s + W'(s')\partial_{s'}\right] \\
& - \frac{N_c^2-2}{2N_c}\frac{\hbar^2c^2}{2MT} W'(\frac{s-s'}{2})(\partial_s - \partial_{s'}) \\
& - \frac{1}{N_c}\frac{\hbar^2c^2}{2MT} W'(\frac{s+s'}{2})(\partial_s + \partial_{s'}) \\
& + \frac{\hbar^4c^4C_F}{64M^2T^2}\left[4W''(0)\left(\partial_s^2 - \partial_{s'}^2\right) - 2p_{tot}^2 W''(0)\right] \\
& - \frac{1}{2N_c}\frac{\hbar^4c^4}{64M^2T^2}\left[4W''(s)\partial_s^2 + 4W''(s')\partial_{s'}^2 + 4W'''(s)\partial_s\right] \\
& - \frac{1}{2N_c}\frac{\hbar^4c^4}{64M^2T^2}\left[4W'''(s')\partial_{s'} + p_{tot}^2 W''(s) + p_{tot}^2 W''(s')\right] \\
& + \frac{N_c^2-2}{2N_c}\frac{\hbar^4c^4C_F}{64M^2T^2}\left[8W''\left(\frac{s-s'}{2}\right)\partial_s\partial_{s'} + 2p_{tot}^2 W''\left(\frac{s-s'}{2}\right)\right] \\
& - \frac{1}{N_c}\frac{\hbar^4c^4C_F}{64M^2T^2}\left[8W''\left(\frac{s+s'}{2}\right)\partial_s\partial_{s'} - 2p_{tot}^2 W''\left(\frac{s+s'}{2}\right)\right], \qquad (5.1)
\end{aligned}
$$

with:

$$
\hbar\frac{\mathrm{d}}{\mathrm{d}t}\mathcal{D}_s = \mathcal{L}_{ss}\mathcal{D}_s + \mathcal{L}_{so}\mathcal{D}_o
$$

$$
\hbar\frac{\mathrm{d}}{\mathrm{d}t}\mathcal{D}_o = \mathcal{L}_{os}\mathcal{D}_s + \mathcal{L}_{oo}\mathcal{D}_o. \qquad (5.2)
$$

One should note that the color factors associated to the $\mathcal{L}_1$ terms have changed compared to chapter 4. For the color singlet equation, we have $-C_F$ instead of $C_F$ and for the color octet equation, we have $\frac{1}{2N_c}$ instead of $-\frac{1}{2N_c}$. This difference is due to a change of convention in the expression of the potential derived in the

perturbative Hard Thermal Loop formalism in the paper from Blaizot & Escobedo [2] and its expression in [172], which is the one we are using.

In one dimension, several potentials have been used [149, 152, 153, 169], usually based on a tunable parameter to explore different regimes. The connection to phenomenology using those potentials is often difficult due to the disconnection from quantitative quarkonium physics. There is thus a need for a more suited one-dimensional potential.

## 5.2 One dimensional potential for quarkonia in the Quark-Gluon Plasma

N.B.: This section is mostly inspired by the paper "One-dimensional imaginary potentials for quarkonia in a quark-gluon plasma" written by Katz, Delorme and Gossiaux [174].

In this section, we propose a one dimensional potential based on a three dimensional potential inspired by lattice data [80, 94]. This potential aims to reproduce properties from the original 3D potential which are the decay widths of the eigenstates and their masses, which depend on temperature.

### 5.2.1 Generalized Gauss law model

Lattice QCD results can provide three dimensional potentials that are relevant for phenomenology. In particular, a potential based on the linear response theory and a generalized Gauss law ansatz was proposed [80, 94]. This potential can be decomposed in two parts: a Coulombic part $V_C$, which is equivalent to the HTL potential derived in [172, 173] and a string-like part $V_S$ which is linear at vanishing temperatures. The potential writes:

$$\mathrm{Re}\, V = \mathrm{Re}\, V_C + \mathrm{Re}\, V_S + c \qquad \mathrm{Im}\, V = \mathrm{Im}\, V_C + \mathrm{Im}\, V_S, \tag{5.3}$$

with $c$ a constant and the Couombic part given by:

$$\mathrm{Re}\, V_C(r) = -\alpha_s \left[ m_D + \frac{e^{-m_D r}}{r} \right] \quad , \quad \mathrm{Im}\, V_C(r) = \alpha_s T \phi(m_D r)$$

$$\phi(r) = 2 \int_0^\infty dz \frac{z}{(z^2+1)^2} \left( 1 - \frac{\sin(zr)}{zr} \right), \tag{5.4}$$

with $\alpha_s$ the QCD running coupling constant and $m_D$ the Debye mass. The string part writes:

$$\mathrm{Re}\, V_S(r) = \frac{2\sigma}{m_D} - \frac{e^{-m_D r}(2 + m_D r)\sigma}{m_D} \qquad \mathrm{Im}\, V_S(r) = \frac{\sigma T}{m_D} \chi(m_D r)$$

$$\chi(r) = 2 \int_0^\infty dp \frac{2 - 2\cos(pr) - pr\sin(pr)}{\sqrt{p^2 + \Delta_D^2}(p^2+1)^2}, \tag{5.5}$$

with $\sigma$ a phenomenological parameter corresponding to the string constant and $\Delta_D = \frac{\Delta}{m_D} \approx 3.0369$ with $\Delta$ a regularization scale. The QCD running coupling constant $\alpha_s$ is computed at one loop and at scale $2\pi T$:

$$\alpha_s(T) = \frac{g^2(T)}{4\pi} = \frac{2\pi}{\left(11 - \frac{2}{3} n_f\right) \log\left(\frac{2\pi T}{\Lambda_{\mathrm{QCD}}}\right)}, \tag{5.6}$$

with $n_f = 3$ massless flavors and the QCD scale taken to be $\Lambda_{\mathrm{QCD}} = 0.250$ GeV [2, 175]. The Debye mass $m_D$ is given by its HTL approximation:

$$m_D^2(T) = \frac{2\pi}{3}(6 + n_f)\alpha_s T^2 = \frac{3}{2} g^2 T^2. \tag{5.7}$$

The real and imaginary part of the three dimensional potential are shown in figure 5.1.

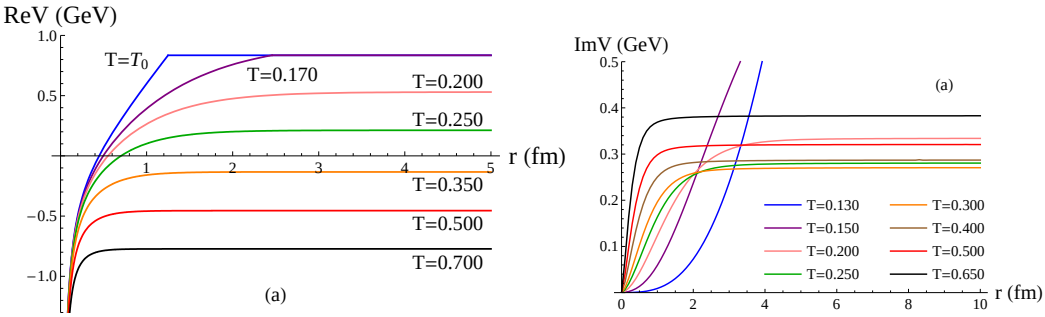


FIGURE 5.1 – Real part of the potential for different temperatures in GeV (Left panel). Imaginary part of the potential for different temperatures in GeV (Right panel).

### 5.2.2 Real part of the one dimensional potential

The one dimensional real part of the potential is parametrized to reproduce the mass spectrum temperature dependance of the three dimensional potential. The real part is saturated to the large distance three dimensional potential value in order to mimic the temperature dependant Debye screening. The real part is parametrizeed in the following way:

$$\mathrm{Re}V_{1\mathrm{D}}(x,T) = \begin{cases} 1/2\,K|x|\,e^{-\mu_1|x|} + \mu_2 + C & \text{when} \quad 1/2\,K|x|\,e^{-\mu_1|x|} + \mu_2 + C < V_{\mathrm{SB}} \\ V_{\mathrm{SB}} & \text{when} \quad 1/2\,K|x|\,e^{-\mu_1|x|} + \mu_2 + C \geq V_{\mathrm{SB}} \end{cases} \tag{5.8}$$

with

$$\mu_1(x,T) = a_1\,(T-T_0)^{b_1}\,e^{-\lambda(T-T_0)\,|x|} \qquad \mu_2(T) = a_2\,(T-T_0)^{b_2} \tag{5.9}$$

with $V_{\mathrm{SB}} \approx 0.835\,\mathrm{GeV}$ and $T_0 \approx 0.126$ such that $m_D(T_0) = 0$.

The $\mu_2$ term leads to a decrease in the mass spectrum values as temperature increases. The $e^{-\mu_1|x|}$ term curves the potential at intermediate distances and cancels at large distances due to the $e^{-\lambda(T-T_0)|x|}$ factor. All the values of the parameters of the real part of the potential are summed up in table 5.1 for the charmonia and bottomonia.

| Re$V_{1D}$ parameters | $K$ | $C$ | $a_1$ | $b_1$ | $\lambda$ | $a_2$ | $b_2$ |
|---|---|---|---|---|---|---|---|
| Charmonia | 1.724 | -0.115 | 7.5 | 0.98 | 1.5 | -0.96 | 0.97 |
| Bottomonia | 2.692 | -0.55 | 7.7 | 1.15 | 1.5 | -0.58 | 1.15 |

TABLE 5.1 – Parameters for the real part of the 1D potential Re$V_{1D}$.

The potentials for both charmonia and bottomonia are shown in figure 5.2.

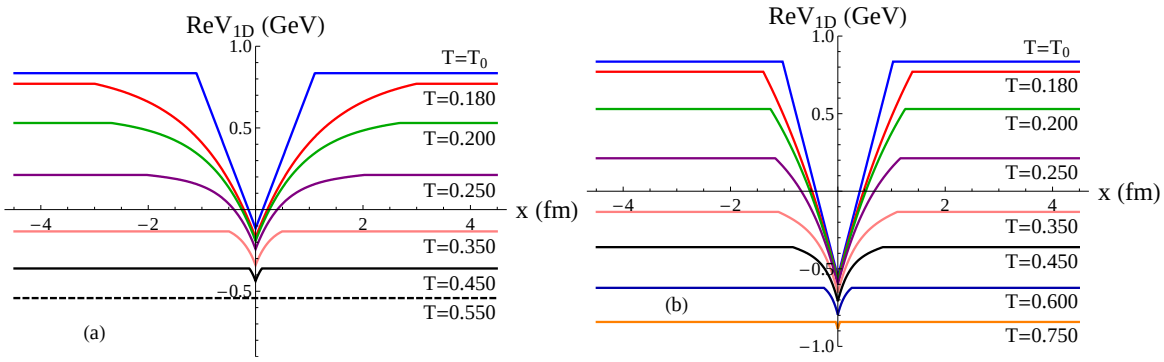


FIGURE 5.2 – One-dimensional potential at different temperatures for the charmonia (left panel) and for the bottomonia (right panel).

One feature of this one-dimensional potential is the dependence on the heavy quark mass although it is not the case for the three dimensional potential. This dependence arises as the focus is made on keeping the phenomenological features of the three dimensional potential and not the exact expression. One can note that in the bottomonia case, the well of the potential is deeper and narrower than in the charmonia case due to larger $K$ and smaller $C$.

The temperature dependence of the mass spectra obtained from the one dimensional and three dimensional potentials is compared for the two systems in figure 5.3

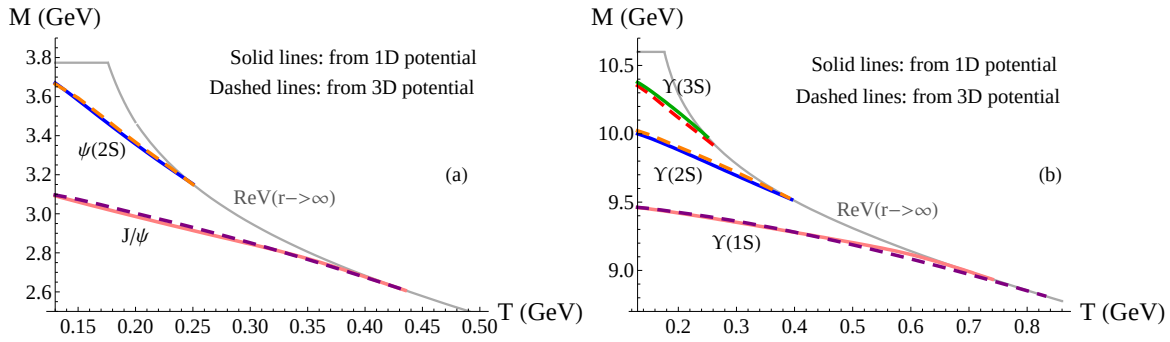


FIGURE 5.3 – (Left panel) Charmonium mass spectrum of the S states for the one-dimensional potential (solid lines) obtained from the expectation values of the Hamiltonian compared to the three-dimensional case (dashed lines). (Right panel) Same for the bottomonia.

In the charmonia case, both mass spectra are in good agreement at any temperature. In the bottomonia case, the agreement is up to $T \approx 550$MeV, which includes the QGP physics expected range of temperatures.

The lack of a Coulombic part in the one dimensional potential compared to the three dimensional case leads to significant differences in the root mean square radii of S states, especially at high temperatures (see figure 5.4). The S states radii are larger for the three dimensional potential, the difference being smaller for the 2S state than for the 1S state.

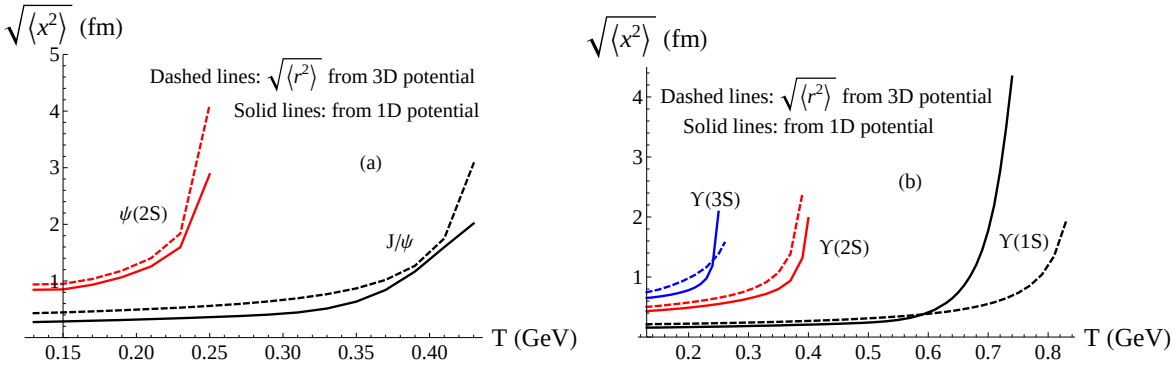


FIGURE 5.4 – (Left panel) Comparison of the root-mean-square radiuses of the charmonium S states obtained with the one and three-dimensional potentials. (Right panel) Same for the bottomonia.

### 5.2.3 Imaginary part of the one dimensional potential

The imaginary part is parametrized to reproduce at best the temperature dependence of the three dimensional decay widths. The one dimensional imaginary part is obtained by symmetrizing the radial imaginary part of the three dimensional potential and adding two parameters which allows some tuning:

$$\mathrm{Im}\, V^{1D}(x,T) = \alpha\, \mathrm{Im}\, V_C(|x|,T) + \beta\, \mathrm{Im}\, V_S(|x|,T). \tag{5.10}$$

This allows to retain the small distance harmonic behaviour and the large distance asymptotic behaviour from the three dimensional potential. The best parameters $\alpha$ and $\beta$ are given in table 5.2.

| $\mathrm{Im}V_{1D}$ coefficients | $\alpha$ | $\beta$ |
|---|---|---|
| Charmonia | 1.7 | 0.8 |
| Bottomonia | 1.4 | 0.9 |

TABLE 5.2 – Coefficients for the imaginary part of the one-dimensional potential $\mathrm{Im}V^{1D}$.

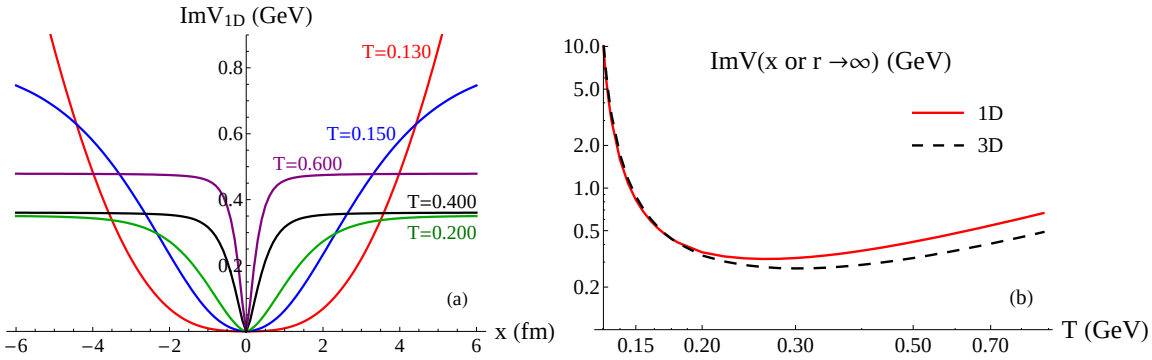


FIGURE 5.5 – (Left panel) Imaginary part of the one-dimensional potential for the bottomonia. (Right panel) Large distance behaviour of the imaginary part of the one and three-dimensional potentials for the bottomonia.

Figure 5.5 shows the imaginary part of the bottomonia potential for different temperatures. One can also observe a difference in the large distance asymptotic value of the potentials, from $T \approx 250$MeV, due to the effect of the coefficient $\alpha$ which raises the large distance saturation.

The decay widths are obtained by using the eigenstates obtained with Re $V^{1D}$ and computing the expectation value of Im $V^{1D}$. Figure 5.6 shows the decay widths for charmonium and bottomonium states obtained with the one dimensional and three dimensional potentials.

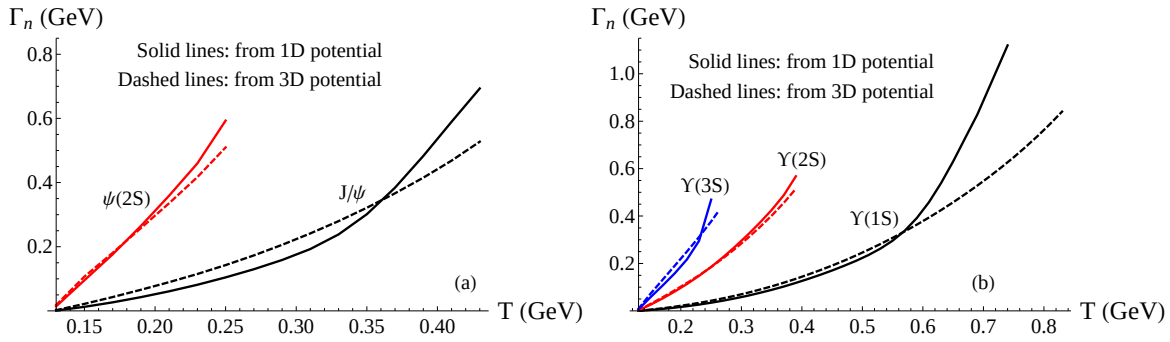


FIGURE 5.6 – (Left pannel) Charmonium decay widths obtained with the one and three-dimensional potentials. (Right pannel) Same for bottomonia.

The one dimensional decay widths are in good agreement with the three dimensional ones, with the exception of the $J/\Psi$ state. The discrepancy at high temperature for the $\Upsilon(1S)$ state is notably due to the large distance differences in the bottomonium potential (see figure 5.5). One should also note that this discrepancy is at temperatures where the states are almost unbound.

### 5.2.4 Spectral decomposition

It can be shown that to ensure positivity of the Lindblad equation, the spectral decomposition of the imaginary part of the potential must be globally either positive or negative (see section 4.4.1), depending on the convention used. In the case of the one dimensional potential, it can be computed analytically. The Fourier transform of the Coulombic part writes:

$$\mathrm{Im}\tilde{V}_c^{1\mathrm{D}} = \frac{\alpha_s T}{2\pi}\int_{-\infty}^{\infty} dx\,\phi\left(\frac{m_D}{\hbar c}|x|\right)\cos(qx), \tag{5.11}$$

which leads to, after integration by parts:

$$\mathrm{Im}\tilde{V}_c^{1\mathrm{D}} = \frac{\alpha_s T}{2}\left[\frac{q}{q^2+(\frac{m_D}{\hbar c})^2} + \frac{\hbar c}{m_D}\left(\arctan\left(\frac{\hbar c}{m_D}q\right) - \frac{\pi}{2}\right)\right], \tag{5.12}$$

where the $-\frac{\pi}{2}$ term is added to get rid of the asymptotic value. The string part spectral decomposition is obtained in the same way:

$$\mathrm{Im}\tilde{V}_s^{1\mathrm{D}} = \frac{\sigma T}{2\pi m_D^2}\int_{-\infty}^{\infty} dx\,\chi\left(\frac{m_D}{\hbar c}|x|\right)\cos(qx), \tag{5.13}$$

leading to:

$$\mathrm{Im}\tilde{V}_s^{1\mathrm{D}} = -\frac{\sigma T\hbar c}{m_D^3}\left[\frac{2}{\sqrt{{\Delta_D}^2+\left(\frac{\hbar c}{m_D}q\right)^2}\left(1+\left(\frac{\hbar c}{m_D}q\right)^2\right)^2}+\frac{{\Delta_D}^2\left(1-3\left(\frac{\hbar c}{m_D}q\right)^2\right)-4\left(\frac{\hbar c}{m_D}q\right)^4}{\left(1+\left(\frac{\hbar c}{m_D}q\right)^2\right)^3\left({\Delta_D}^2+\left(\frac{\hbar c}{m_D}q\right)^2\right)^{3/2}}\right]. \tag{5.14}$$

The spectral decomposition of the imaginary part of the potential is shown in figure 5.7. One can see that $\mathrm{Im}\,\tilde{V}^{1D}$ is indeed negative for all $q$ and all temperatures considered. The spectral decomposition is thus negative and the one dimensional imaginary part will satisfy the positivity requirement of the Lindblad equation.

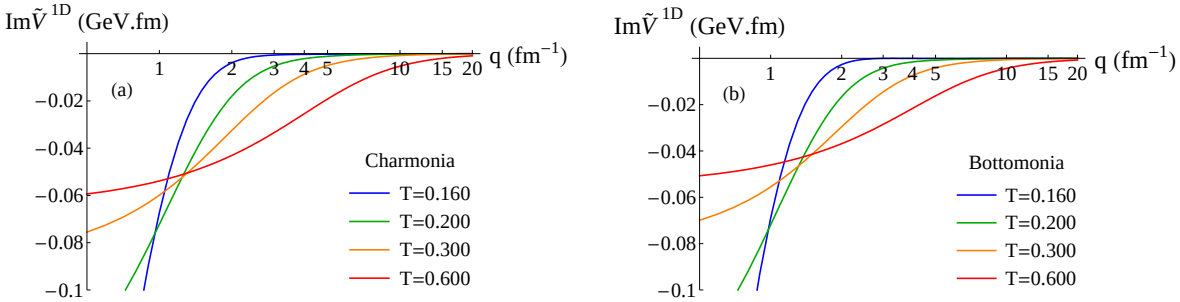


FIGURE 5.7 – Spectral decomposition of the imaginary part of the potential $\mathrm{Im}V^{1\mathrm{D}} = \alpha\,\mathrm{Im}V_c^{1\mathrm{D}} + \beta\,\mathrm{Im}V_s^{1\mathrm{D}}$ at different temperatures (in GeV) for the (left pannel) charmonia and (right pannel) bottomonia.

Now that we have a suitable one dimensional potential, we present how the equations will be resolved.

## 5.3 Numerical method

We present in this section the numerical algorithm that will be used to resolve the equations.

The differential equations that will be resolved can be written as:

$$\frac{\mathrm{d}}{\mathrm{d}t}\mathcal{D}(s,s') = g\Big(\mathcal{D};\ \partial_s\mathcal{D};\ \partial_{s'}\mathcal{D};\ \partial_s^2\mathcal{D};\ \partial_{s'}^2\mathcal{D};\ \partial_s\partial_{s'}\mathcal{D}\Big), \tag{5.15}$$

where $\mathcal{D}$ is either $\mathcal{D}_s$ or $\mathcal{D}_o$ and $g$ a function. For simplicity, the right-hand side will be written as $g(\mathcal{D})$.

The equations are discretized on a grid of size $[-s_{max}; s_{max}] \times [-s_{max}; s_{max}]$ with a spatial step $\Delta s$ for both the $s$ and $s'$ axis. Those parameters with be determined in section 5.4. The equations are resolved using the Crank-Nicolson [176] method and become:

$$\frac{\mathcal{D}_{i,j}^{t+1} - \mathcal{D}_{i,j}^{t}}{\Delta t} = \frac{1}{2}\Big[g\Big(\mathcal{D}_{i,j}^{t+1}\Big) + g\Big(\mathcal{D}_{i,j}^{t}\Big)\Big], \tag{5.16}$$

with $g\Big(\mathcal{D}_{i,j}^{t}\Big)$ the value of the density matrix at point $(i,j)$ of the grid at time $t$ and $\Delta t$ the time step, also to be determined in section 5.4. $i$ is an index on the $s'$ axis and $j$ is an index on the $s$ axis.

As one can see, a system of equations has to be resolved to obtain $\mathcal{D}_{i,j}^{t+1}$, the Crank-Nicolson method is said to be an *implicit* method. It has a higher computing cost (and this will limit the accessible parameters phase space as we shall see in section 5.4) than an *explicit* method like the Runge-Kutta method [2] and is more difficult to implement. However, explicit methods proved to be unstable for the equations considered, hence the choice of this method, as implicit methods are more stable.

The time derivative is discretized using the Crank-Nicolson method and we choose to discretize the spatial derivatives on $\mathcal{D}_{i,j}$ using a central difference scheme:

2. In this case, the value of $\mathcal{D}_{i,j}^{t+1}$ would be obtained explicitely without resolving any equation.

$$\partial_s \mathcal{D}_{i,j} = \frac{\mathcal{D}_{i,j+1} - \mathcal{D}_{i,j-1}}{2\Delta s} \qquad \partial_{s'} \mathcal{D}_{i,j} = \frac{\mathcal{D}_{i+1,j} - \mathcal{D}_{i-1,j}}{2\Delta s}$$
$$\partial_s^2 \mathcal{D}_{i,j} = \frac{\mathcal{D}_{i,j+1} + \mathcal{D}_{i,j-1} - 2\mathcal{D}_{i,j}}{(\Delta s)^2} \quad \partial_{s'}^2 \mathcal{D}_{i,j} = \frac{\mathcal{D}_{i+1,j} + \mathcal{D}_{i-1,j} - 2\mathcal{D}_{i,j}}{(\Delta s)^2}$$
$$\partial_s \partial_{s'} \mathcal{D}_{i,j} = \frac{\mathcal{D}_{i+1,j+1} - \mathcal{D}_{i+1,j-1} - \mathcal{D}_{i-1,j+1} + \mathcal{D}_{i+1,j+1}}{4(\Delta s)^2}. \tag{5.17}$$

At the edges, those definitions can obviously not be used and forward and backward difference schemes are used instead. (5.16) can be written in another form to better show the system that needs to be resolved:

$$\mathcal{D}_{i,j}^{t+1} - \frac{1}{2}\Delta t \; g\left(\mathcal{D}_{i,j}^{t+1}\right) = \mathcal{D}_{i,j}^{t} + \frac{1}{2}\Delta t \; g\left(\mathcal{D}_{i,j}^{t}\right), \tag{5.18}$$

which can be put in matrix form:

$$\mathbf{A}\mathbf{x} = \mathbf{b}, \tag{5.19}$$

with $\mathbf{b}$ a vector containing all values of $\mathcal{D}_{i,j}^{t} + \frac{1}{2}\Delta t \; g\left(\mathcal{D}_{i,j}^{t}\right)$, $\mathbf{x}$ a vector containing all values of $\mathcal{D}_{i,j}^{t+1}$, which are to be determined, and $\mathbf{A} = \mathbb{1} - \frac{1}{2}\Delta t \; \mathbf{g}_M$ a matrix where $\mathbb{1}$ is the identity matrix and $\mathbf{g}_M$ a matrix representing $g$ such that $\mathbf{g}_M \mathbf{x} = g\left(\mathcal{D}_{i,j}^{t+1}\right)$.

The vector $\mathbf{x}$ is constructed in the following way:

$$\mathbf{x} = \begin{pmatrix} \mathcal{D}_{s;0,0}^{t+1} \\ \mathcal{D}_{o;0,0}^{t+1} \\ \mathcal{D}_{s;0,1}^{t+1} \\ \mathcal{D}_{o;0,1}^{t+1} \\ \vdots \\ \mathcal{D}_{s;N,N}^{t+1} \\ \mathcal{D}_{o;N,N}^{t+1} \end{pmatrix}, \tag{5.20}$$

and a similar construction for $\mathbf{b}$ with $\mathcal{D}_{0,0}^{t}$. $\mathbf{x}$ and $\mathbf{b}$ are thus $2N^2$-dimensionnal

vectors, and $\mathbf{A}$ is thus a $2N^2 \times 2N^2$ matrix. Taking into account the discretization scheme used for the spatial derivatives, one may recognize that $\mathbf{A}$ is a block-tridiagonal matrix of the form (for $N = 3$):

$$\mathbf{A} = \begin{pmatrix} \mathbf{A}_0 & \mathbf{B}_0 & 0 \\ \mathbf{C}_0 & \mathbf{A}_1 & \mathbf{B}_0 \\ 0 & \mathbf{C}_1 & \mathbf{A}_2 \end{pmatrix}, \tag{5.21}$$

with $\mathbf{A}_i$,$\mathbf{B}_i$,$\mathbf{C}_i$ matrices of dimension $2N \times 2N$ (in the $N = 3$ case, they are of dimension $6 \times 6$ and $\mathbf{A}$ of dimension $18 \times 18$).

Using this property, the systems of equations (5.19) can be resolved using the Block Tridiagonal algorithm, which is the generalization of the famous Thomas algorithm [177] (or tridiagonal matrix algorithm) to the case of block tridiagonal matrices. This method is based on a block LU decomposition. For the $N = 3$ case, we have:

$$\mathbf{L} = \begin{pmatrix} \mathbb{1} & 0 & 0 \\ \mathbf{L}_1 & \mathbb{1} & 0 \\ 0 & \mathbf{L}_2 & \mathbb{1} \end{pmatrix} \quad \mathbf{L} = \begin{pmatrix} \mathbf{U}_0 & \mathbf{B}_0 & 0 \\ 0 & \mathbf{U}_1 & \mathbf{B}_1 \\ 0 & 0 & \mathbf{U}_2 \end{pmatrix}. \tag{5.22}$$

For a general value of N, the $\mathbf{L}_i$ and $\mathbf{U}_i$ are determined by:

$$\begin{aligned} &\mathbf{U}_0 = \mathbf{A}_0 \\ &\mathbf{L}_i\mathbf{U}_{i-1} = \mathbf{C}_i \qquad i : 1 \to N-1 \\ &\mathbf{U}_i = \mathbf{A}_i - \mathbf{L}_i\mathbf{B}_{i-1} \qquad i : 1 \to N-1. \end{aligned} \tag{5.23}$$

The system (5.19) can then be resolved with:

$$\begin{aligned}
&\mathbf{y}_0 = \mathbf{b}_0 \\
&\mathbf{y}_i = \mathbf{b}_i - \mathbf{L}_i \mathbf{y}_{i-1} \qquad i : 1 \to N-1
\end{aligned}$$

$$\begin{aligned}
&\mathbf{U}_{N-1}\mathbf{x}_{N-1} = \mathbf{y}_{N-1} \\
&\mathbf{U}_i \mathbf{x}_i = \mathbf{y}_i - \mathbf{b}_i \mathbf{x}_{i+1} \qquad i : N-2 \to 0.
\end{aligned} \tag{5.24}$$

We will now proceed to benchmark the numerical code by first checking if the trace is conserved numerically. This will allow us to also determine the parameters that will be used for the resolution.

## 5.4 Trace conservation and determination of numerical parameters

Three numerical parameters need to be determined:
— the grid size $s_{max}$
— the spatial step $\Delta s$
— the time step $\Delta t$.

One also has to verify that the trace is conserved. As a first test, the following parameters are chosen:

$$s_{max} = 10 \text{ fm} \quad \Delta s = 0.05 \text{ fm} \quad \Delta t = 0.1 \text{ fm/c}. \tag{5.25}$$

The procedure is as follows: we resolve the equation until $t = 20$ fm/c and compute at each time the trace of the density matrix and compare it to the trace of the density matrix at the start of the evolution ($t = 0$ fm/c). This will give us the deviation from trace conservation during the whole evolution in time.

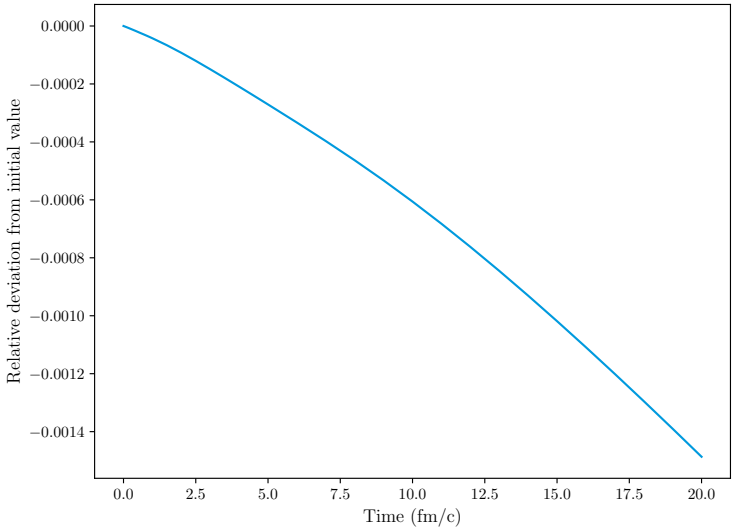


FIGURE 5.8 – Evolution in time of $\mathrm{Tr}\left[\mathcal{D}_0(0)\right] - \mathrm{Tr}\left[\mathcal{D}_0(t)\right]$.

Figure 5.8 shows the evolution in time of $\mathrm{Tr}\left[\mathcal{D}_0(0)\right] - \mathrm{Tr}\left[\mathcal{D}_0(t)\right]$ where $\mathcal{D}_0 = \frac{1}{N_c^2}\left(\mathcal{D}_s + \left[N_c^2 - 1\right]\mathcal{D}_o\right)$. The trace of $\mathcal{D}_0$ should be conserved as proved in chapter 4. One can see a clear deviation from the analytical result as one would expect a constant value. As it is a numerical resolution, this behaviour is expected as numerical results are always subject to errors. However, one would expect a smaller deviation than what is obtained here if it was purely round-off errors.

In chapter 4, it was shown that the conservation of trace required at the $\mathcal{L}_3'$ and $\mathcal{L}_4$ levels to perform an integration to be realized. The numerical computation of this integral is not exact and its precision depends on the spatial step $\Delta s$. On top of that, one can show that the discretization scheme used for the terms $\propto \partial_s \partial_{s'} \mathcal{D}$ also contributes to the error. Indeed, these terms appear in the computation of the trace in groupings of the form $\partial_s^2 \mathcal{D} + \partial_{s'}^2 \mathcal{D} + 2\partial_s \partial_{s'} \mathcal{D}$. One can show that errors from each terms due to the discretization schemes do not cancel each other, leading to non-conservation of the trace. This problem was already observed in the literature and a strategy to resolve it was proposed very recently in [153].

This strategy will not be used in this work. Instead, we choose to minimize the deviation from conservation. To do so, the effect of each parameters on it is studied,

with only one parameter varying at a time and the other two fixed. We then resolve the equations until $t = 20$ fm/c and compute $\mathrm{Tr}\,[\mathcal{D}_0(0)] - \mathrm{Tr}\,[\mathcal{D}_0(20)]$. We start by studying the effect of the spatial step $\Delta s$. We fix $\Delta t = 0.1$ fm/c and $s_{max} = 10$ fm and resolve the equations for $\Delta s = 0.04$,0.05,0.1 and 0.2 fm.

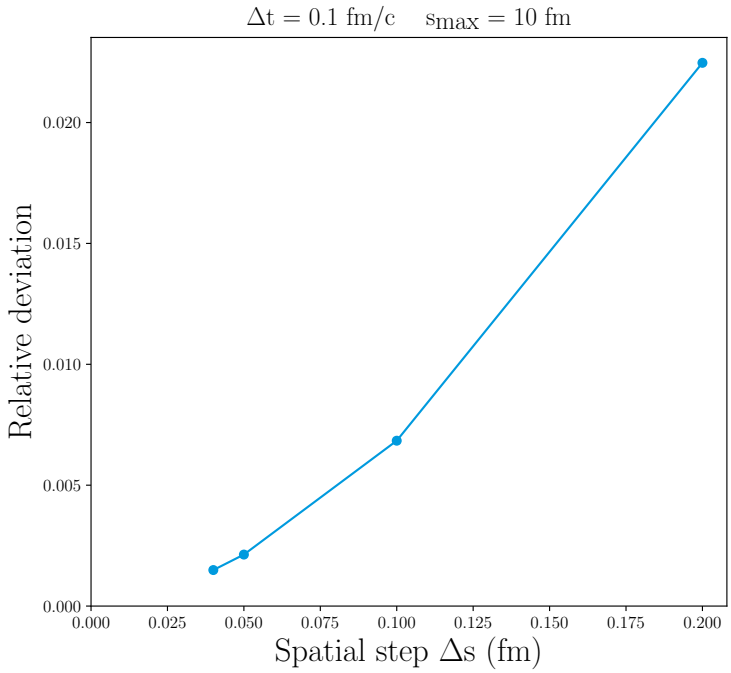


FIGURE 5.9 – $\mathrm{Tr}\,[\mathcal{D}_0(0)] - \mathrm{Tr}\,[\mathcal{D}_0(20)]$ for $\Delta s = 0.04$,0.05,0.1 and 0.2 fm, with $s_{max} = 10$ fm and $\Delta t = 0.1$ fm/c.

Figure 5.9 show a clear effect of the spatial step on the error on the trace. Due to memory limitations, it is not possible to go to values of $\Delta s$ smaller than 0.04 fm with $s_{max}$ = 10 fm. We see that the error is smaller at smaller $\Delta s$, as expected. One can also note that the error seems to reach a plateau around $\Delta s$ = 0.04 fm. To verify this hypothesis, we reduce the grid size to $s_{max}$ = 5 fm, and resolve the equations for $\Delta s$ = 0.05,0.04 and 0.02 fm.

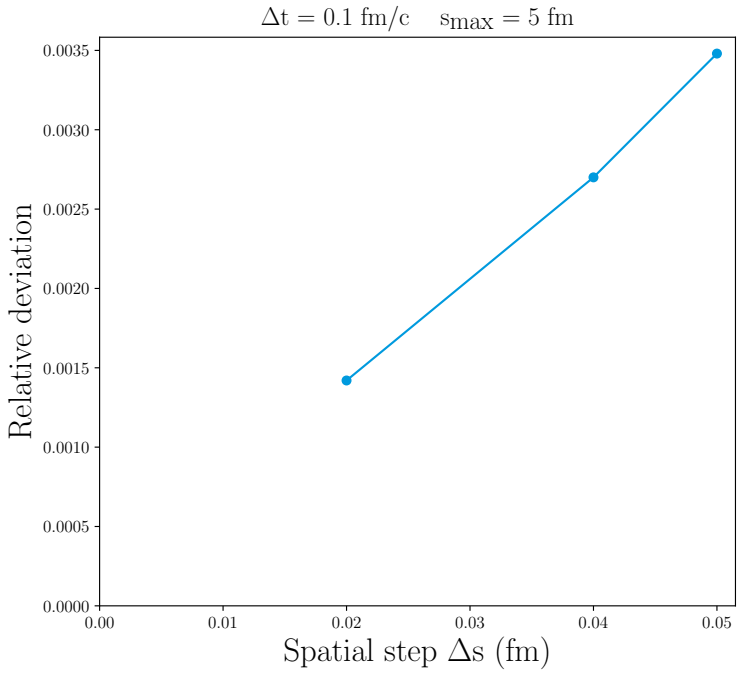


FIGURE 5.10 – $\mathrm{Tr}\,[\mathcal{D}_0(0)] - \mathrm{Tr}\,[\mathcal{D}_0(20)]$ for $\Delta s = 0.02$,0.04 and 0.05 fm, with $s_{max} = 5$ fm and $\Delta t = 0.1$ fm/c.

Figure 5.10 confirms that the reduction of the error is smaller when taking an even smaller $\Delta s$. However, we will determine $\Delta s$ after we study the effect of $s_{max}$. We fix $\Delta s$ = 0.05 fm and $\Delta t$ = 0.1 fm/c and resolve the equations with $s_{max}$ = 2,5 and 10 fm.

We see on figure 5.11 that the deviation from trace conservation is indeed influenced by the grid size, as the deviation is smaller at large grid sizes. To see if the reduction of the deviation is still significant at higher $s_{max}$, we fix this time $\Delta s = 0.1$ fm and resolve the equations for $s_{max}$ = 10,15,20 and 25 fm.

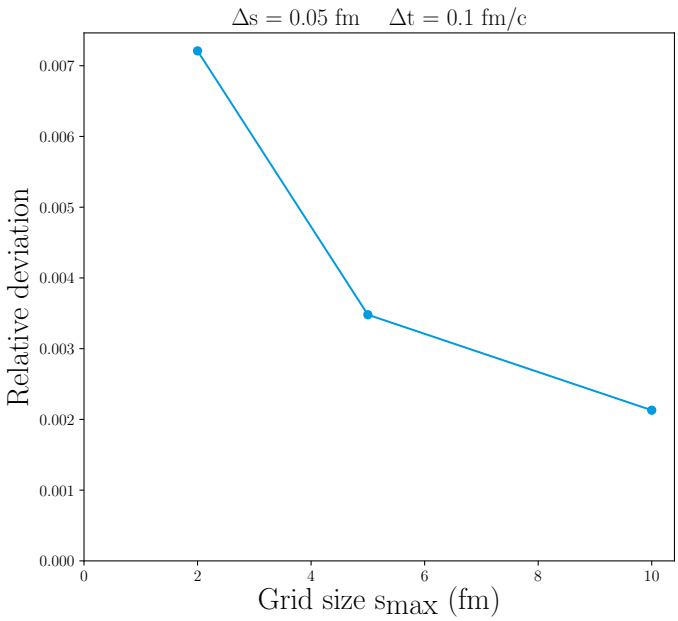


FIGURE 5.11 – $\mathrm{Tr}\left[\mathcal{D}_0(0)\right] - \mathrm{Tr}\left[\mathcal{D}_{20}(0)\right]$ for $s_{max}$ = 2,5 and 10 fm, with $\Delta s = 0.05$ fm and $\Delta t = 0.1$ fm/c.

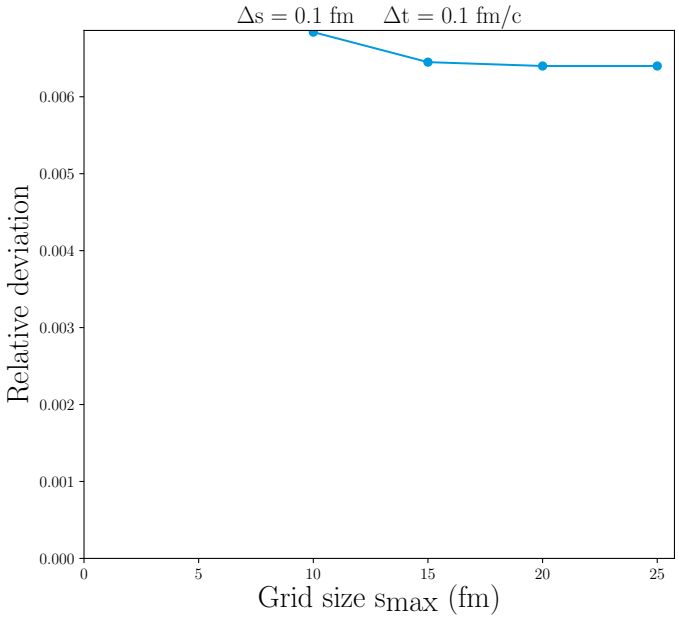


FIGURE 5.12 – $\mathrm{Tr}\left[\mathcal{D}_0(0)\right] - \mathrm{Tr}\left[\mathcal{D}_{20}(0)\right]$ for $s_{max}$ = 10,15,20 and 25 fm, with $\Delta s = 0.1$ fm and $\Delta t = 0.1$ fm/c.

As seen on figure 5.12, a plateau is indeed reached at very large $s_{max}$. It seems to be reasonable to take a grid size of at least 15 fm based on those observations, however, again due to computing resources limitations, a larger spatial step will be needed.

We finally study the effect of the time step $\Delta t$. We fix $s_{max} = 10$ fm, $\Delta s = 0.05$ fm and choose $\Delta t = 10^{-1}, 10^{-2}$ and $10^{-3}$ fm/c.

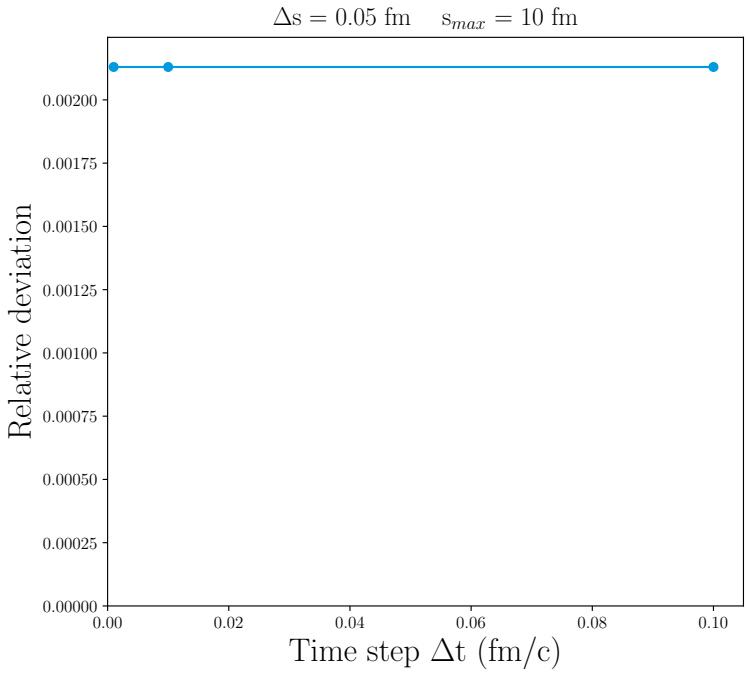


FIGURE 5.13 – $\mathrm{Tr}\left[\mathcal{D}_0(0)\right] - \mathrm{Tr}\left[\mathcal{D}_0(20)\right]$ for $\Delta t = 10^{-1}$, $10^{-2}$ and $10^{-3}$ fm/c, with $s_{max} = 10$ fm and $\Delta s = 0.05$ fm.

Figure 5.13 shows no effect of the time step $\Delta t$ at a $10^{-4}$ precision level. We choose to fix $\Delta t = 0.1$ fm/c as it will not add truncation errors to the computation while decreasing the computation time.

To fix both the spatial step and the grid size, we have 3 constraints:

— $s_{max}$ should be chosen as large as possible, to minimize the deviation from trace conservation but also to avoid finite grid size effects at the boundaries.

— $\Delta s$ should be chosen as small as possible to minimize the errors and the deviation.

— The computing resources are limited (a rough estimate is a maximum grid of $500 \times 500$ points due to the resolution method), thus a compromise between grid size and spatial step has to be found.

Among several, we will retain the following two configurations: either we choose $s_{max} = 15$ fm and $\Delta s = 0.06$ fm or we choose $s_{max} = 10$ fm and $\Delta s = 0.04$ fm.

| $s_{max}$ (fm) | $\Delta s$ (fm) | $\mathrm{Tr}\left[\mathcal{D}_0(0)\right] - \mathrm{Tr}\left[\mathcal{D}_0(20)\right]$ |
|---|---|---|
| 15 | 0.06 | $2.550 \times 10^{-3}$ |
| 10 | 0.04 | $1.487 \times 10^{-3}$ |

TABLE 5.3 – Values of $\mathrm{Tr}\left[\mathcal{D}_0(0)\right] - \mathrm{Tr}\left[\mathcal{D}_0(20)\right]$ for two different configurations

Table 5.3 gives the deviation from trace conservation in both cases. We can clearly see from the results that the most important parameter is the spatial step as the second case with $\Delta s = 0.04$ fm leads to a smaller deviation. We recap in table 5.4 the parameters that will be used in chapter 6.

| $s_{max}$ (fm) | $\Delta s$ (fm) | $\Delta t$ (fm/c) |
|---|---|---|
| 10 | 0.04 | 0.1 |

TABLE 5.4 – Parameters used for the resolution of the equations

## 5.5 Positivity conservation

The last check we perform is the one on positivity. One has:

$$\mathbf{A}\mathbf{x} = \lambda \mathbf{x}, \tag{5.26}$$

where $\mathbf{A}$ is a square matrix, $\mathbf{x}$ one of its eigenvectors and $\lambda$ the associated eigenvalue. Multiplying by $\mathbf{x}^T$ on each side, one finds:

$$\mathbf{x}^T \mathbf{A}\mathbf{x} = \lambda \mathbf{x}^T \mathbf{x}. \tag{5.27}$$

$\mathbf{x}^T \mathbf{x}$ is obviously positive so the sign of the left-hand side depends on the sign of the

eigenvalue $\lambda$.

A matrix $\mathbf{A}$ is positive definite if $\mathbf{x}^T\mathbf{A}\mathbf{x} > 0 \ \forall$ non-zero $\mathbf{x}$ and positive semidefinite if the condition is $\geq 0$. As $\mathbf{x}$ is obviously non-zero as it is an eigenvector, there exists a link between matrix positivity and the eigenvalues sign of said matrix:

— If $\lambda > 0 \ \forall \ \lambda$, the matrix is positive definite.

— If $\lambda \geq 0 \ \forall \ \lambda$, the matrix is positive semidefinite.

The check of the positivity preservation is fairly straightforward. One would need to compute the eigenvalues of the evolution operator and verify that none of them is negative. This would guarantee that the positivity is preserved for any intial state. We choose another way of doing it. We resolve the equations with the parameters from table 5.4 and at $t = 20$ fm/c, the eigenvalues of $\mathcal{D}_s$ are computed and we check if they are all positive ($\geq 0$). If this is the case, the positivity is indeed preserved. The cumulated distribution of the eigenvalues of $\mathcal{D}_s$ are shown in figure 5.14 in the case with the $\mathcal{L}_4$ terms and in the case without the $\mathcal{L}_4$ terms.

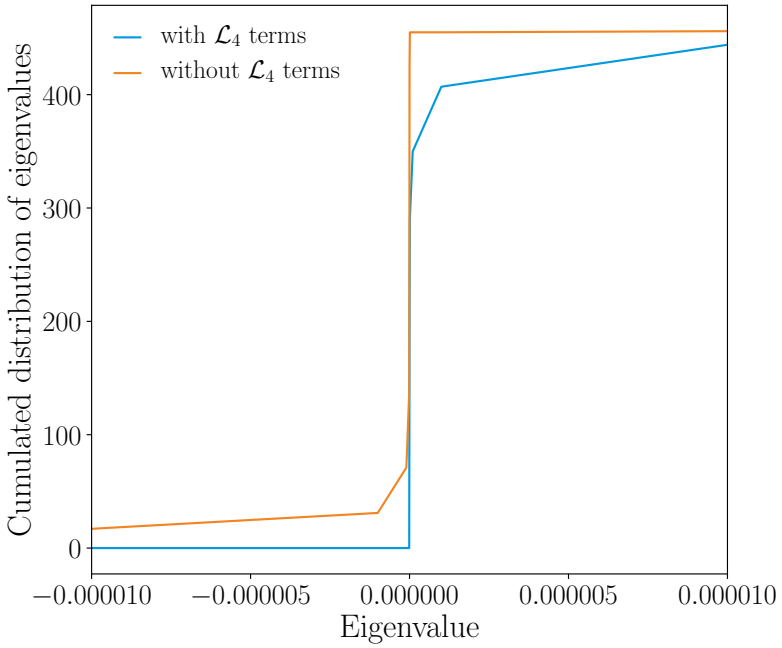


FIGURE 5.14 – Cumulated distribution of the eigenvalues of $\mathcal{D}_s$ at $t$ = 20 fm/c with (blue line) and without (orange line) the $\mathcal{L}_4$ terms.

We can see that with the $\mathcal{L}_4$ terms, all the eigenvalues are either positive or equal to zero, proving that positivity is indeed preserved numerically. However, if we remove the $\mathcal{L}_4$ terms, we see that eigenvalues of $\mathcal{D}_s$ can be negative, showing that the $\mathcal{L}_4$ are necessary to ensure positivity of the density matrix.

We will end the analysis of the numerical code by looking at its stability over time. To do so, we will resolve the equations until $t = 50$ fm/c and see if we can observe any behaviour compatible with the presence of any instability on projections.

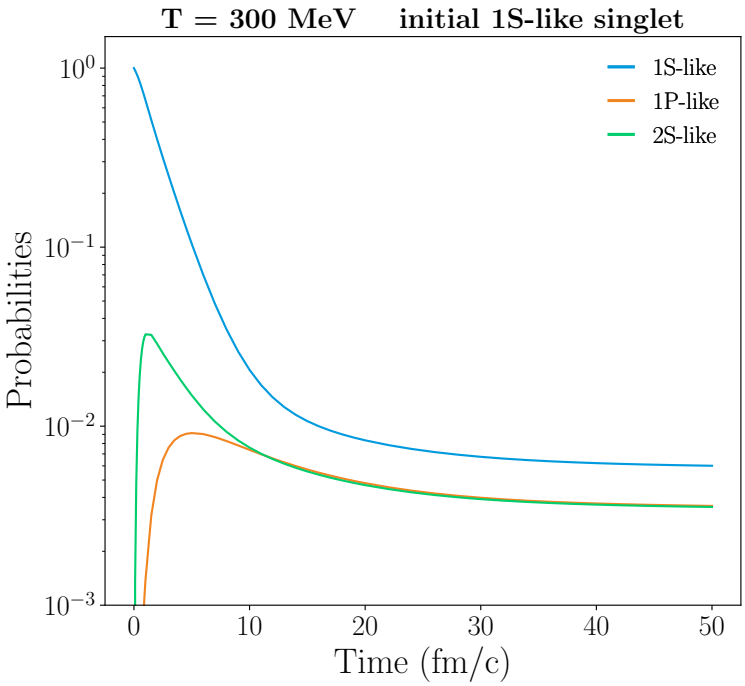


FIGURE 5.15 – Projections on vacuum eigenstates for T = 300 MeV.

As shown on figure 5.15, we do not observe any evidence for instability in the code, even after 50 fm/c, which demonstrate the stability of the code over time.

## 5.6 Conclusion

In this chapter, we presented the numerical implementation of the equations derived in the previous chapter, in the one-dimensional case. We introduced a novel one dimensional potential, parametrized to reproduce as best as possible the

features of a three dimensional potential obtained from Lattice QCD data while focusing on phenomenological features. The numerical scheme used was presented and the determination of the important parameters was done to minimize the numerical error on trace conservation as much as possible. Finally we proved that positivity was also preserved numerically. We thus have a robust numerical tool to finally study the dynamics of heavy quarkonium in the Quark-Gluon Plasma, which is the focus of the next chapter.

# Chapter 6

# Quarkonium dynamics in the Quark-Gluon Plasma

In this chapter, we proceed with the resolution of the equations presented in the chapter 4, using the methodology presented in the chapter 5. We focus on the $c\bar{c}$ system and, unless stated otherwise, we take the total pair momentum $p_{tot}$ equal to 0 GeV. We first consider a QGP medium at a fixed temperature. We start by analyzing how the color equilibrates for different temperatures. We then study the dynamics of the $c\bar{c}$ pair by analyzing the density matrix at different temperatures and for different initial states. An analysis of the legitimity of a semi-classical treatment, using the Wigner transform of the density matrix, is also presented. We finally focus on the projections on vacuum eigenstates again for different conditions and initial states. In a second part, we study a simple QGP scenario following a Björken-like temperature evolution and look at the projections on vacuum states over time. The complex potential used is the one-dimensional potential presented in the chapter 5, with the real part given by the equations (5.8) and (5.9) and the imaginary part given by the equation (5.10). As shown in the chapter 3, several works on quarkonium real-time dynamics exist, however, the point of this chapter is not the systematic comparison of the results presented with the ones obtained from other models.

## 6.1 Quarkonium dynamics at fixed temperature

We first consider the case of a static QGP medium with a fixed temperature during the whole evolution.

### 6.1.1 Color dynamics

The equations that are resolved couple the singlet and octet density operators through the $\mathcal{L}_{so}$ and $\mathcal{L}_{os}$ operators. It is interesting to study if and how color equilibrates over time. One can then access the color relaxation time. To do so, we consider two different initial states, prepared from a S-like state in the vacuum (T = 0 MeV), one in a singlet color state and the other in a octet color state and resolve the equations for a medium temperature of T = 300 MeV:

$$\begin{aligned} \mathcal{D}_s = |\Psi_S\rangle\langle\Psi_S| \quad \text{and} \quad \mathcal{D}_o = 0 \\ \text{OR} \quad \mathcal{D}_s = 0 \quad \text{and} \quad \mathcal{D}_o = |\Psi_S\rangle\langle\Psi_S| \,. \end{aligned} \tag{6.1}$$

We then compute the deviation of the trace of both $\mathcal{D}_s$ and $\mathcal{D}_o$ from the expected equilibrium value (given by $\left|\frac{1}{9} - \mathrm{Tr}\,\mathcal{D}\right|$, with $\mathcal{D}$ either $\mathcal{D}_s$ or $\mathcal{D}_o$) at each time, with the trace on $\mathcal{D}_o$ is divided by 8 to only consider one octet state:

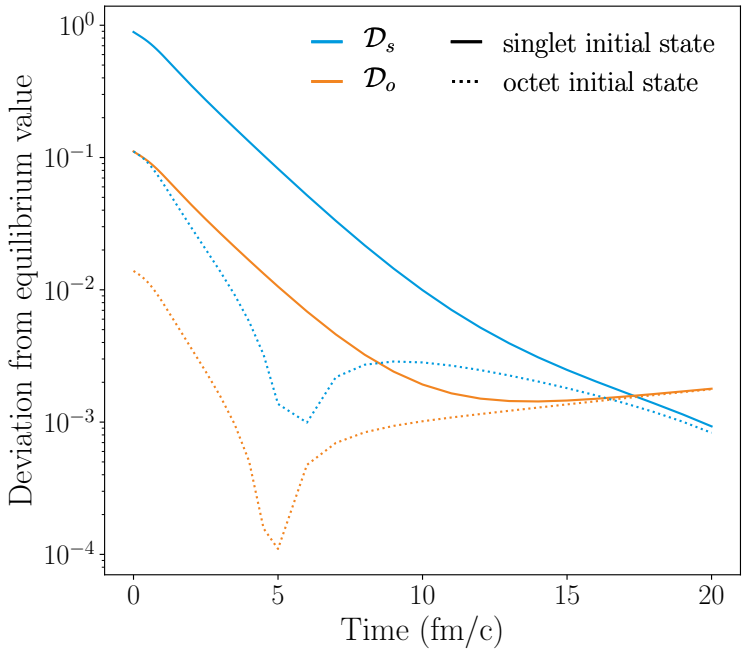


FIGURE 6.1 – Evolution over time of the deviation from the equilibrium value of the trace of $\mathcal{D}_s$ (blue curves) and $\mathcal{D}_o$ (orange curves) for an initial singlet state (solid curves) and octet state (dotted curves).

Figure 6.1 shows the progressive equilibration of the singlet color channel in the medium. We can however see that for the octet color component, we start to deviate from the equilibrium value after 5 fm/c in the case of an initial octet state and after around 12 fm/c in the case of an initial singlet state. This may be explained by a regeneration of an octet component that is not equilibrated induced by the discretization scheme that we use. We can also see that the relaxation time (shown as the slope of the cuves on figure 6.1 is not universal but depends on the initial state. We now only consider a color singlet initial state, still formed from a S-like vacuum state, and resolve the equations for T = 200, 300 and 400 MeV.

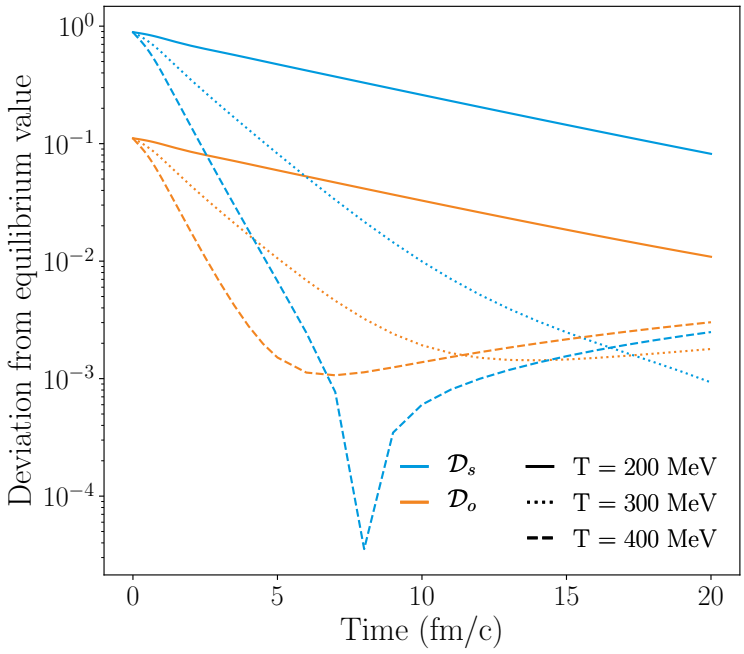


FIGURE 6.2 – Evolution over time of the deviation from the equilibrium value of the trace of $\mathcal{D}_s$ (blue curves) and $\mathcal{D}_o$ (orange curves) for an initial S-like singlet state, at T = 200 MeV (solid curves), 300 MeV (dotted curves) and 400 MeV (dashed curves).

We can observe on figure 6.2 that for every temperature, we have an exponential decrease of the deviation from the equilibrium value. For T = 400 MeV, this exponential decrease only lasts until around 7 fm/c. To study the typical time needed for equilibration further, one can fit the curves representing the evolution of the deviation from the equilibrium value of the trace of $\mathcal{D}_s$ by the following expression:

$$\left|\frac{1}{9} - \mathrm{Tr}\,\mathcal{D}_s(t)\right| \equiv Ae^{-t/\tau}, \tag{6.2}$$

with $A$ a global factor that is not of interest and $\tau$ the timescale we search. The values of $\tau$ for each temperatures are given in table 6.1 (The fit was only realized on the time range [0-7] fm/c as the curves do not all follow an exponential evolution after this time, which may be due to "bouncing" on the edges of the numerical grid).

| T (MeV) | $\tau$ (fm/c) |
|---|---|
| 200 | 7.77 |
| 300 | 2.13 |
| 400 | 1.19 |

TABLE 6.1 – Values of the timescale $\tau$ for T = 200, 300 and 400 MeV.

The relation between $\tau$ and T is clearly non trivial and an more precise analysis will be done in the near future to better characterize it.

We now consider a QED-like case, described by the equation on $\mathcal{D}_s$ with $\mathcal{D}_s = \mathcal{D}_o$, meaning that color is completely equilibrated and there are no color transitions. We initialize the density matrix as a 1S-like vacuum state (in a singlet color state for the QCD case) and project at each time the density matrix on the vacuum eigenstates, giving us the weights of the different states:

$$\begin{aligned} w_n^{QED} &= \left\langle \Psi_n^{QED} \middle| \mathcal{D} \middle| \Psi_n^{QED} \right\rangle \\ w_n^{QCD} &= \left\langle \Psi_n^{QCD} \middle| \mathcal{D}_s \middle| \Psi_n^{QCD} \right\rangle, \end{aligned} \tag{6.3}$$

and we resolve the equations for a medium temperature of 300 MeV.

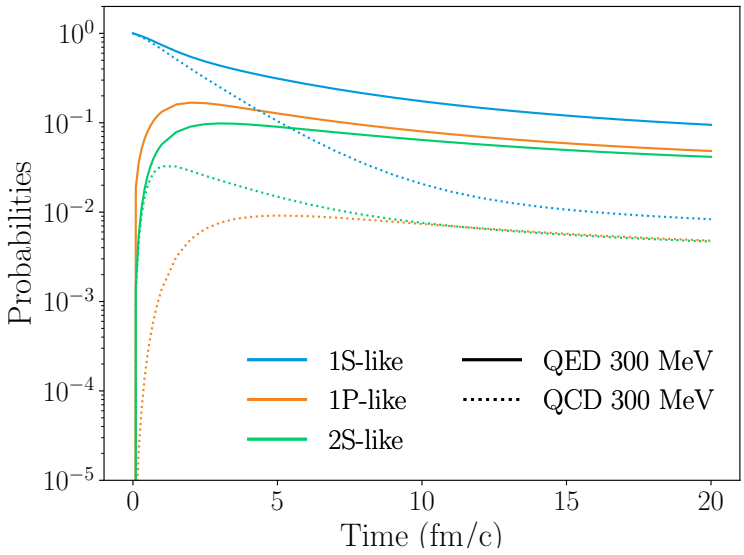


FIGURE 6.3 – Evolution over time of the weights of the first three vacuum eigenstates at T = 300 MeV in the QED-like case (solid curves) and in the QCD case (dotted curves)

Figure 6.3 shows the evolution of the weights in both cases. As expected, the survival probability of the initial 1S-like in the QCD case is much lower than in the QED-like case. This is explained by the transitions between color states that are present, which transfer a fraction of the norm in the octet sector. The same observation can be made for the 1P-like and 2S-like eigenstates. It is thus quite clear that color transitions are crucial to get a good understanding of the $c\bar{c}$ pair dynamics.

### 6.1.2 Dynamics of a $c\bar{c}$ pair

In this section, we investigate the dynamics of a $c\bar{c}$ pair by studying the singlet density matrix $\mathcal{D}_s$. We take as a reference a QGP medium with a temperature T = 300 MeV and the initial state is taken as the 1S-like vacuum eigenstate in a singlet color state.

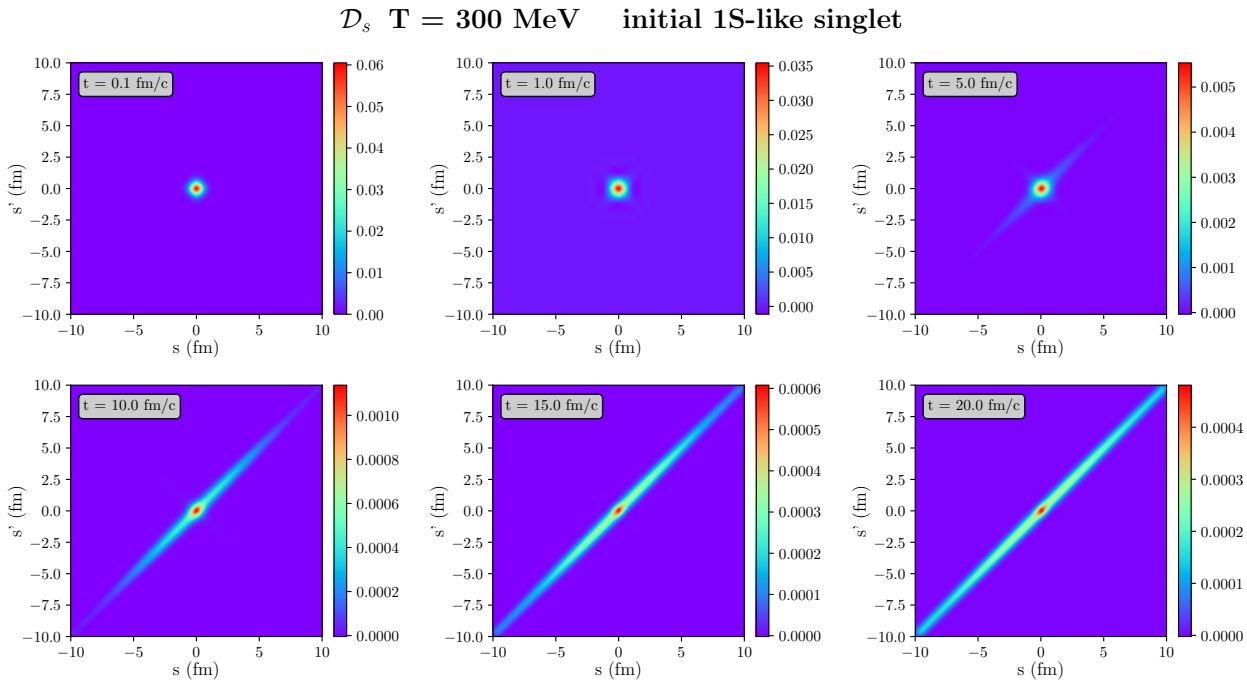


FIGURE 6.4 – Evolution of the singlet density matrix $\mathcal{D}_s$ over time. From top left panel to bottom right panel: 0.1, 1, 5, 10, 15 and 20 fm/c

Figure 6.4 shows the evolution of the singlet density matrix $\mathcal{D}_s$ over time. The initial 1S-like singlet state is progressively delocalized along the s = s′ axis and we also observe the progressive decoherence of the initial state, indicated by the narrowing of the density matrix distribution along the s = -s′ axis (see right side of figure 6.5). The singlet density matrix $\mathcal{D}_s$ at later times exhibits two different behaviours: a central core is present which is a remnant on the initial state and on the edges of the s = s′ axis, we observe a semi-classical like component.

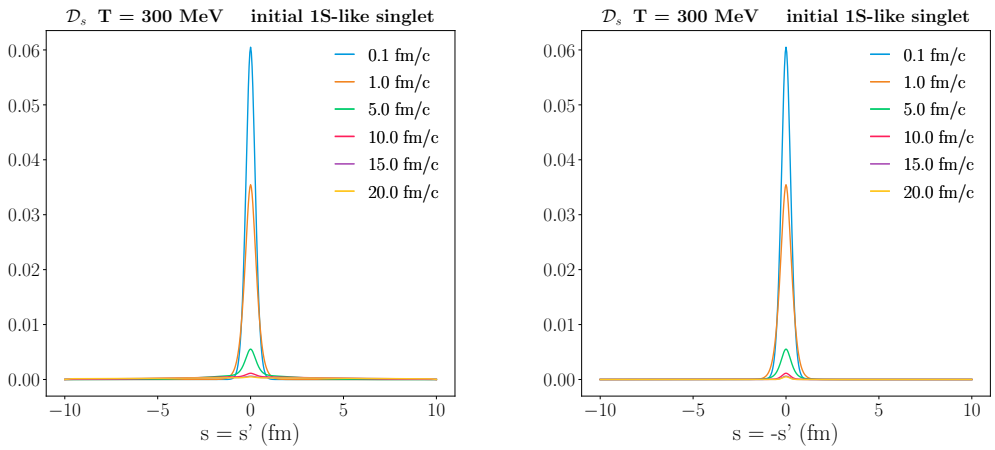


FIGURE 6.5 – *Left panel:* Evolution of the singlet density matrix $\mathcal{D}_s$ over time along the s= s′ axis. *Right panel :* Same along the s = -s′ axis

To analyse the semi-classical nature of $\mathcal{D}_s$, we compute its Wigner transform $f(r,p)$, defined as:

$$f(r,p) = \frac{1}{2\pi\hbar}\int e^{i\frac{py}{\hbar}}\mathcal{D}_s\Big(r+\frac{y}{2}, r-\frac{y}{2}\Big)dy, \tag{6.4}$$

with $r = \frac{s+s'}{2}$ and $y = s - s'$, with iso-$r$ lines corresponding to lines with $s = -s'$.

We compute in reality a discretized version of the Wigner transform, defined as:

$$f(k,p) = \frac{1}{2\pi\hbar}\sum_{l=-(2i_{max}-k)}^{2i_{max}-k} e^{i\frac{p\Delta s l}{\hbar}}\mathcal{D}_s^{\frac{k+l}{2},\frac{k-l}{2}}, \tag{6.5}$$

where $k = i + j$ and $l = i - j$ with $r + \frac{y}{2} = i\Delta s$ and $r - \frac{y}{2} = j\Delta s$.

If we observe the Wigner distributions obtained (see figure 6.6), three behaviours appear. The first distribution type is a gaussian distribution, the second one a non-gaussian distribution but still positive and finally Wigner distributions that are partially negative.

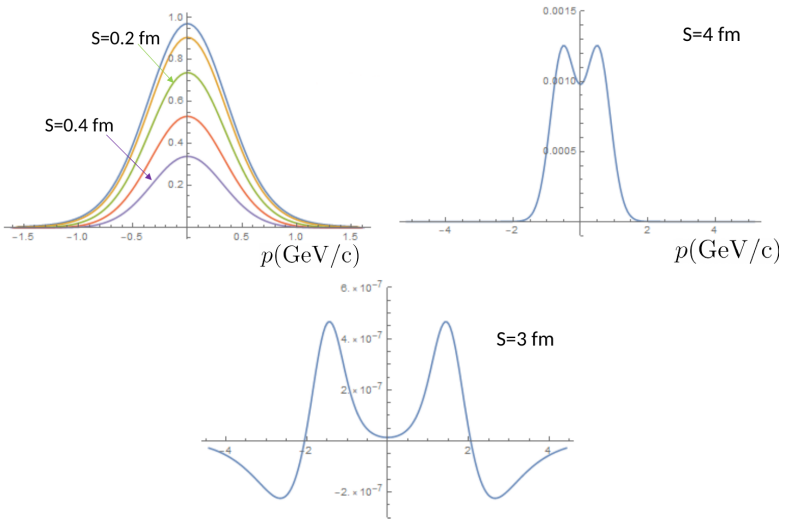


FIGURE 6.6 – Wigner transforms at different values of $\frac{s+s'}{2}$ and time. Three types of distributions appear: gaussian and positive Wigner distributions (top left panel), non-gaussian but still positive distributions (top right panel) and negative distributions (bottom panel).

We continue by fixing $r$ and compute the mean squared momentum $\sqrt{\langle p^2 \rangle}$, given by:

$$\sqrt{\langle p^2 \rangle}(r) = \frac{\sum_p p^2 W(r,p)}{\sum_p W(r,p)}, \tag{6.6}$$

with a sum on $p$ as we compute a discretized Wigner transform. We then proceed to compute $\sqrt{\langle p^2 \rangle}$ for values of $\frac{s+s'}{2}$ between 0 fm and 5 fm, with 0 fm corresponding to the anti-diagonal of $\mathcal{D}_s$ and 5 fm corresponding to half of the accessible range of $\frac{s+s'}{2}$, at different times.

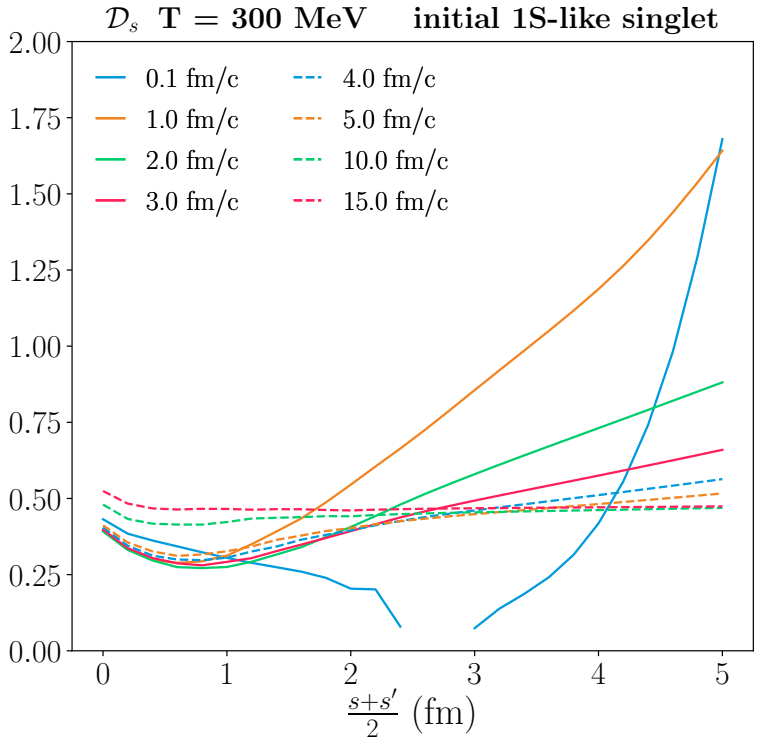


FIGURE 6.7 – Evolution of the mean squared momentum $\sqrt{\langle p^2 \rangle}$ over time at different values of $\frac{s+s'}{2}$.

We can see that at later times (dashed green and red curves on figure 6.7), $\sqrt{\langle p^2 \rangle}$ is converging towards a specific value (which should scale as the thermal wave number $\sqrt{\frac{MT}{2}}$ with $M$ the mass of the charm quark) for most of the range considered , indicating that the system reached thermalization. There exists a small range (∼0-1 fm) in $\frac{s+s'}{2}$, which corresponds to the central core observed in the two-dimensional representation of $\mathcal{D}_s$ where the value of $\sqrt{\langle p^2 \rangle}$ has not yet converged. This indicates that there may still be quantum effects due to the real part of the potential V binding the $c$ and $\bar{c}$ quarks of the pair. We can also note two regimes, a small distance regime (∼0-1.5 fm), corresponding to where the state is at the beginning of the evolution) and a long distance regime (∼3-5 fm) with different behaviours. At small distances, $\sqrt{\langle p^2 \rangle}$ is below the asymptotic value and increases with time while at larger distances, it is the opposite with an evolution "from above" and decreasing values. Finally, we can remark that at early times (0.1 fm/c), the value of $\langle p^2 \rangle$ becomes negative around 2.5 fm, meaning that the Wigner transform acquires negative part, as illustrated on figure 6.6. This may be due to quantum interference

effects, however one has to be careful as we are at very early times and we look at quite large distance, which may not have a clear physical sense.

We now consider a QGP medium with a temperature T = 200 MeV or T = 400 MeV. Figure 6.8 shows the evolution of the singlet density matrix for the three temperatures.

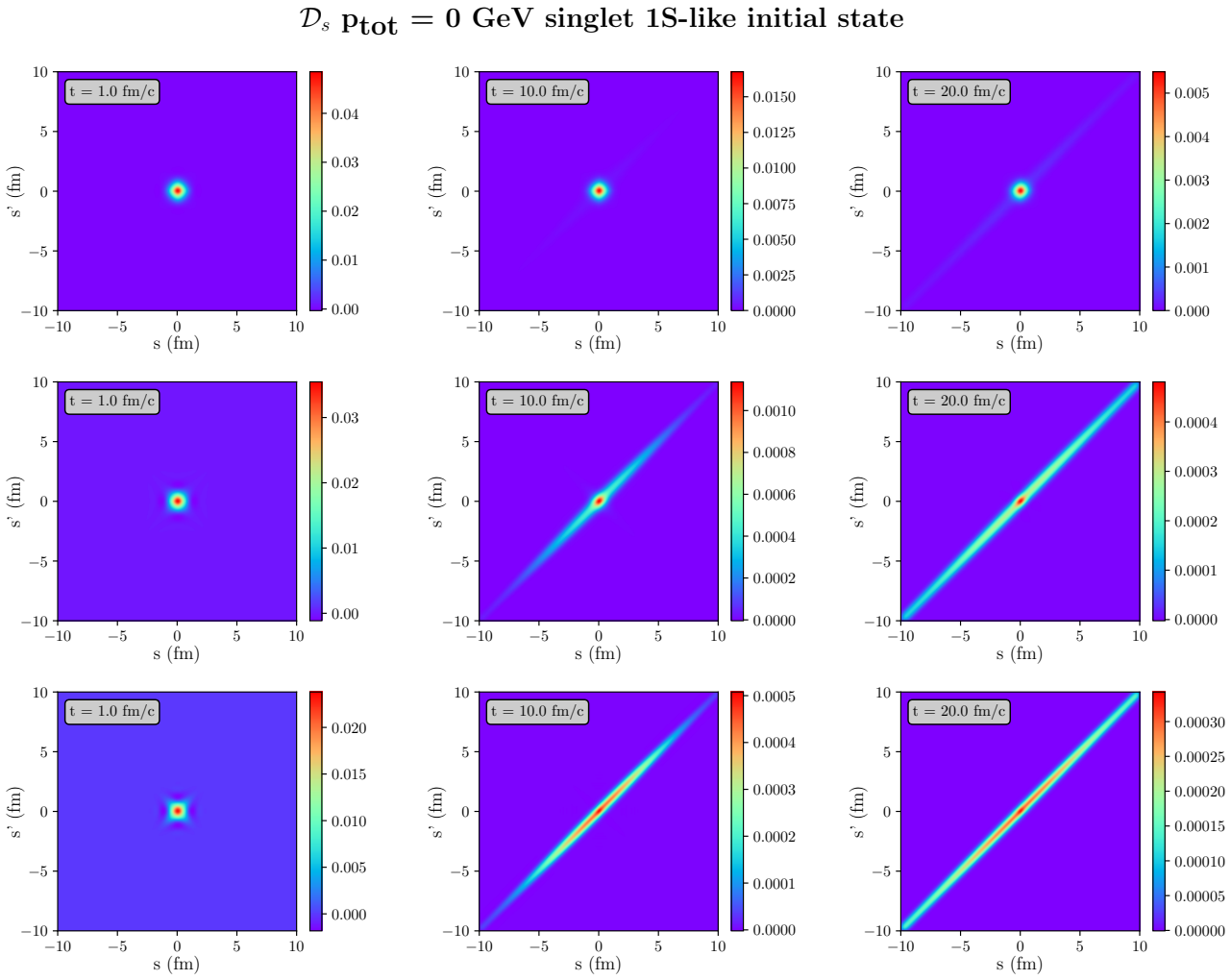


FIGURE 6.8 – Evolution of the singlet density matrix $\mathcal{D}_s$ over time. From left panel to right panel: 1, 10 and 20 fm/c. From top to bottom: medium temperature of 200 MeV, 300 MeV and 400 MeV

At T = 200 MeV (top panels of figure 6.8), the effects of the medium are not strong enough to delocalize the pair and the potential still binds the two quarks together for large times. At T = 400 MeV (bottom panels of figure 6.8), there are

more dynamical processes in the medium and the pair is delocalized quicker than at T = 300 MeV.

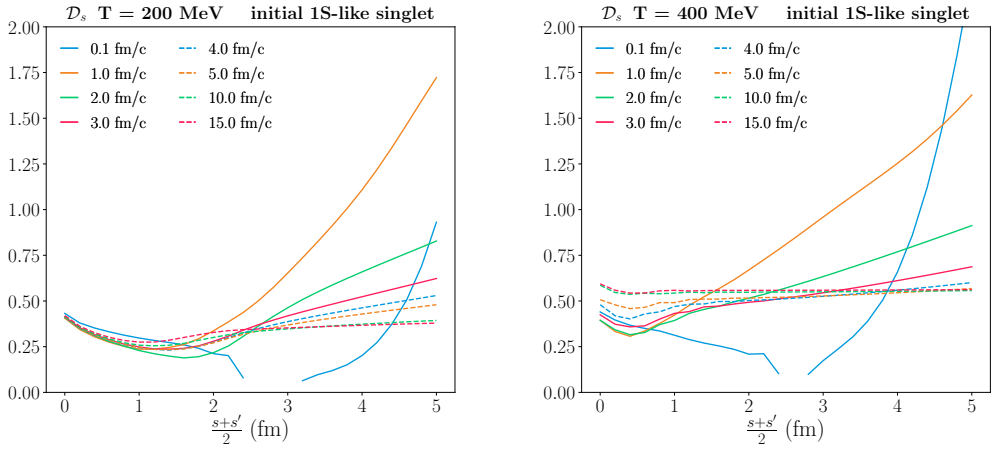


FIGURE 6.9 – *Left panel:* Evolution of the mean squared momentum $\sqrt{\langle p^2 \rangle}$ over time at different values of $\frac{s+s'}{2}$ for T = 200 MeV. *Right panel:* Same for T = 400 MeV.

We proceed to study the evolution of the mean squared momentum $\sqrt{\langle p^2 \rangle}$ for T = 200 MeV and T = 400 MeV. For both temperatures, we can observe (see figure 6.9) the small and large distance regimes, alongside the gap in $\frac{s+s'}{2}$ where the Wigner transform becomes negative. For T = 200 MeV, the small distance regime extends from 0 to 2.5 fm while for T = 400 MeV, it extends from 0 to 1 fm, which is consistent with the idea that the potential attraction zone is bigger at lower temperatures. The global behaviour of the small and large distance regimes is the same for all temperatures.

For a medium temperature T = 200 MeV, the system has not reached thermalization at t = 15 fm/c while the system reaches it faster for T = 400 MeV (already reached at t = 10 fm/c) than for T = 300 MeV. We can also note that the range in $\frac{s+s'}{2}$ where the value of $\sqrt{\langle p^2 \rangle}$ has not reached the asymptotic value is bigger ($\tilde{0}$-2.5 fm) for T = 200 MeV and smaller ($\tilde{0}$-0.5 fm) for T = 400 MeV than for T = 300 MeV. This matches with the observation done on the two-dimensional representation of $\mathcal{D}_s$ on the effect of the real part of the potential V.

The asymptotic value at large distance for T = 200 MeV is smaller than for T = 300

MeV, and the asymptotic value for T = 400 MeV is higher than for T = 300 MeV. On figure 6.10, we show the evolution of $\sqrt{\langle p^2 \rangle}$ for all temperatures at t = 15 fm/c. We observe that the asymptotic values do not scale with $\sqrt{\frac{MT}{2}}$, except for T = 200 MeV. A possible explanation is that this scaling depends on a balance between the $\mathcal{L}_2$ and $\mathcal{L}_3$ terms at large distance, however this balance may not be reached perfectly as our $\mathcal{L}_3$ term is slightly modified in the minimal set. This should be studied to understand the precise origin of this deviation.

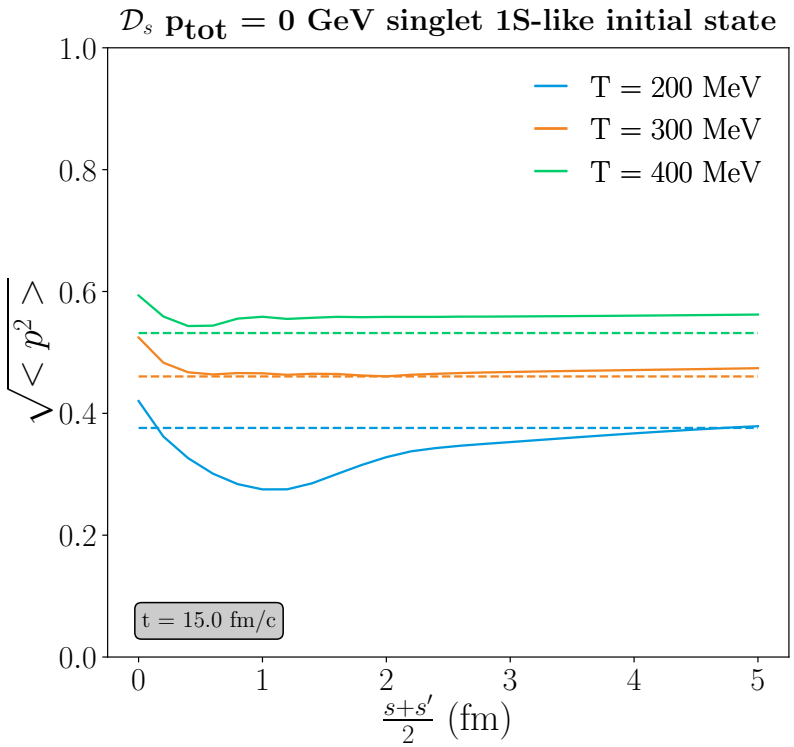


FIGURE 6.10 – Evolution of the mean squared momentum $\sqrt{\langle p^2 \rangle}$ for different values of $\frac{s+s'}{2}$ at t = 15 fm/c for a medium temperature T = 200, 300 and 400 MeV. For each temperature, the corresponding value of $\sqrt{\frac{MT}{2}}$ is shown by the dashed lines.

To study how the presence of a localized initial bound state influences the dynamics, we prepare the initial state as a P-like vacuum eigenstate in the octet color channel and study its ensuing evolution.

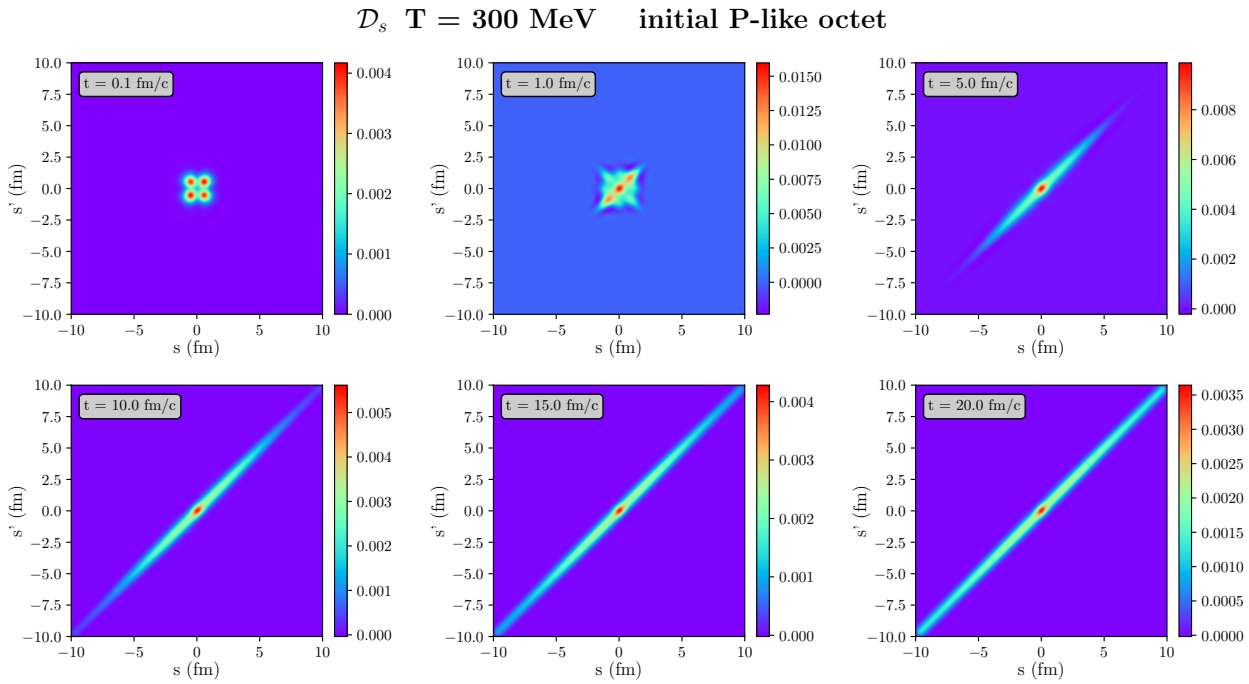


FIGURE 6.11 – Evolution of the singlet density matrix $\mathcal{D}_s$ over time. From top left panel to bottom right panel: 0.1, 1, 5, 10, 15 and 20 fm/c

Figure 6.11 shows that, starting from a P-like octet state, we first have a transition to a S-like state in the singlet channel (also visible on the left panel of figure 6.12). This can be seen better on figure 6.17. As time evolves, we observe the progressive delocalization along the s = s' axis. The final state is similar to the one obtained from an initial 1S-like state in the singlet color channel, with a slightly stronger central component, showing that the system reaches a steady state.

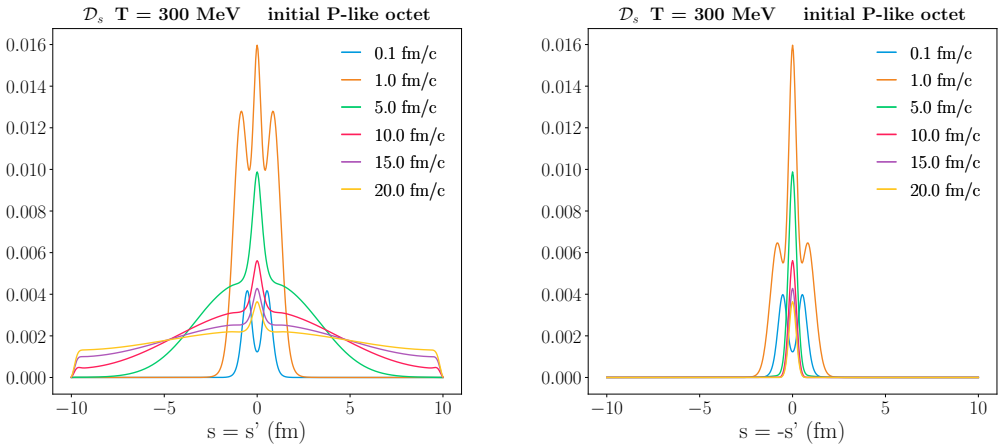


FIGURE 6.12 – *Left panel:* Evolution of the singlet density matrix $\mathcal{D}_s$ over time along the s= s′ axis. *Right panel :* Same along the s = -s′ axis

The evolution of the mean squared momentum for the initial octet P-like state is shown on figure 6.14. The mean squared momentum reaches the same asymptotic value as for an initial 1S-like singlet state, however the system reaches thermalization much quicker. We can also note that starting from 4 fm/c, the distribution of $\sqrt{\langle p^2 \rangle}$ is already rather flat. Another important feature is the different small distance behaviour. At very early times (0.1 fm/c), the Wigner transform is not positive for all values of $p$ at small distances (see top left panel of figure 6.13) as we just started to populate the singlet color channel.

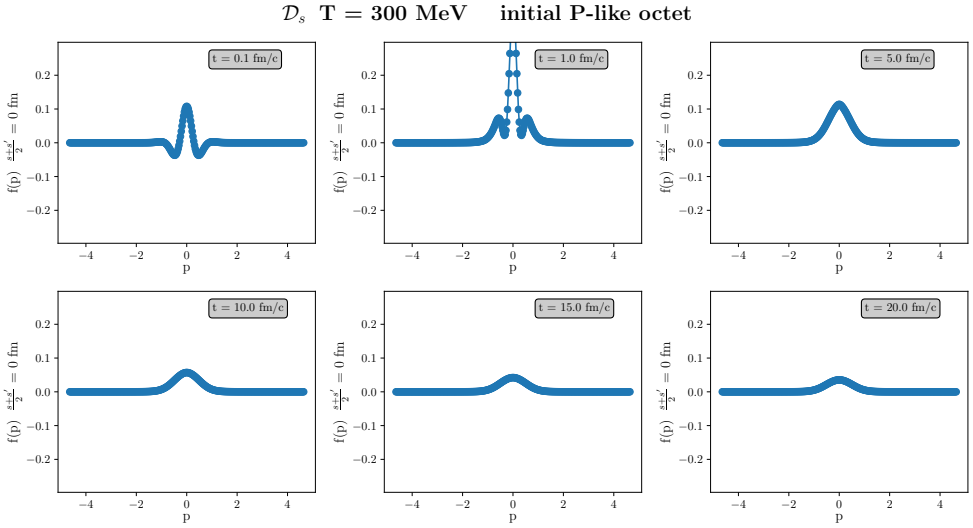


FIGURE 6.13 – Wigner distributions at $\frac{s+s'}{2}$ = 0 fm at different times.

However, even though the small distance regime is different from the singlet initial state case, there is still a small range in $\frac{s+s'}{2}$ from 0 to 0.5 fm where the mean squared momentum is not equal to the asymptotic value. Again, this shows the importance of the real part of the complex potential V.

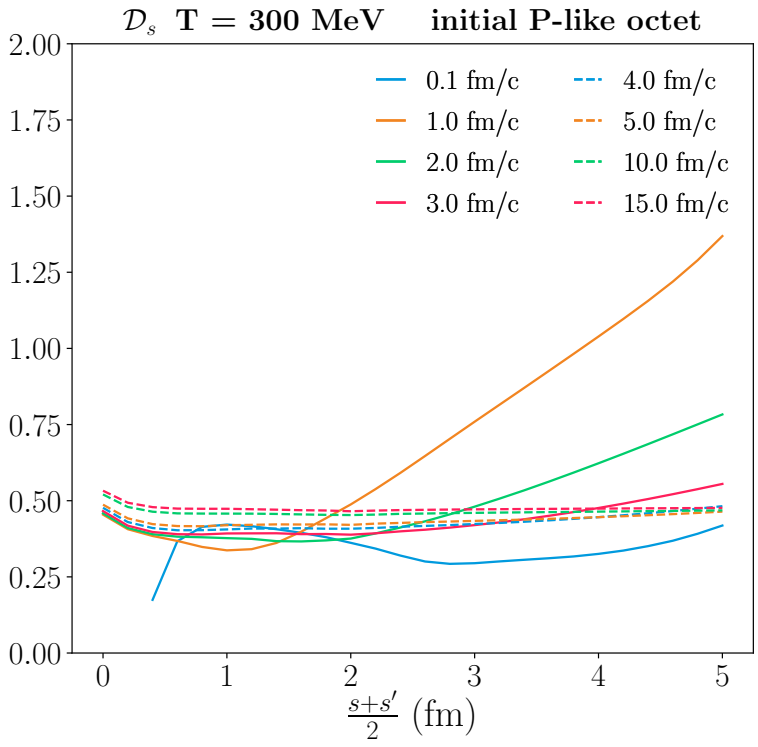


FIGURE 6.14 – Evolution of the mean squared momentum $\sqrt{\langle p^2 \rangle}$ over time at different values of $\frac{s+s'}{2}$.

### 6.1.3 Projections on vacuum states

It is also useful to look at the projections on vacuum eigenstates to learn more about the dynamics and the influence of the different parameters: the temperature, the choice of the initial state and the total pair momentum. As before, we start from an initial 1S-like singlet state for a medium temperature T = 200, 300 and 400 MeV. The reader should however be careful to only consider those projections as instantaneous projections that would result from a sudden freeze-out, as the eigenstates may not exist at the temperatures considered.

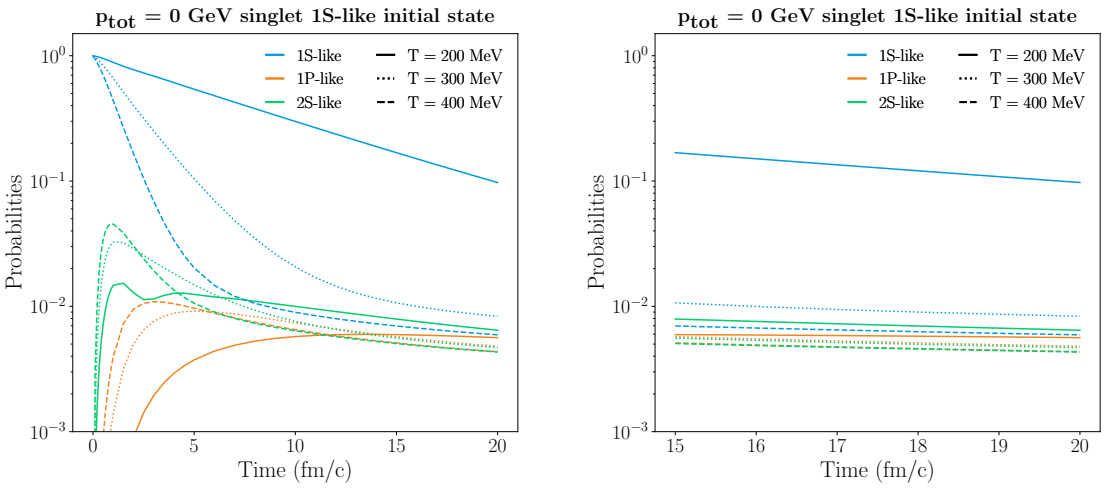


FIGURE 6.15 – *Left panel:* Evolution over time of the weights of the first three vacuum eigenstates with an initial 1S-like singlet state at T = 200 (solid curves), 300 (dotted curves) and 400 MeV (dashed curves). *Right panel:* Same but zoom on late time evolution.

One can observe on figure 6.15 the effect of temperature on the weights of vacuum eigenstates. The early-time evolution (up to $\sim$ 5 fm/c) is characterized by a transient phase corresponding to the re-equilibration of populations. The excited 1P-like and 2S-like states get populated at first due to transitions in the medium before decaying. The 2S-like immediately starts to get populated while the 1P-like state gets populated later. This is explained by the nature of the transitions involved. To populate the 1P-like state, one has to consider dipolar transitions, changing the parity of the state. Those transitions can also induce a transition from a singlet (an octet) to an octet (a singlet) color state but also from an octet to another octet state. One would first need to populate a P-like octet state and only then induce a second dipolar transition from an octet to another octet state to populate the 1P-like singlet state. In the case of the 2S-like state, the direct transition from a 1S-like is possible and due to the real part of the potential V, the 2S-like state can thus be populated earlier. As temperature increases the weight of the 1S-like state decrease, which is expected due to the stronger medium effects, inducing more transitions. We can also observe that the 2S-like state is more populated for T = 400 MeV but also decays quicker than for T = 300 MeV. We can also see that for T = 200 MeV, the behaviour of the populations is very different compared to their behaviour for the other temperatures.

The late-time evolution is the same for S-like states at T = 300 MeV and T = 400 MeV. By analyzing in more detail the late-time evolution (see right panel of figure 6.15), we can see that the gap between the 1S-like state and the 1P-like and 2S-like states becomes smaller as temperature increases. This is remniscent of the Maxwell-Boltzmann distribution, however, as we are not in the quantum optical regime, we do not expect the statistical equilibrium of the distributions.

We now fix the medium temperature to T = 300 MeV and modify the initial state to study its influence. We start by taking as initial states the 1P-like and 2S-like vacuum eigenstates in the singlet channel.

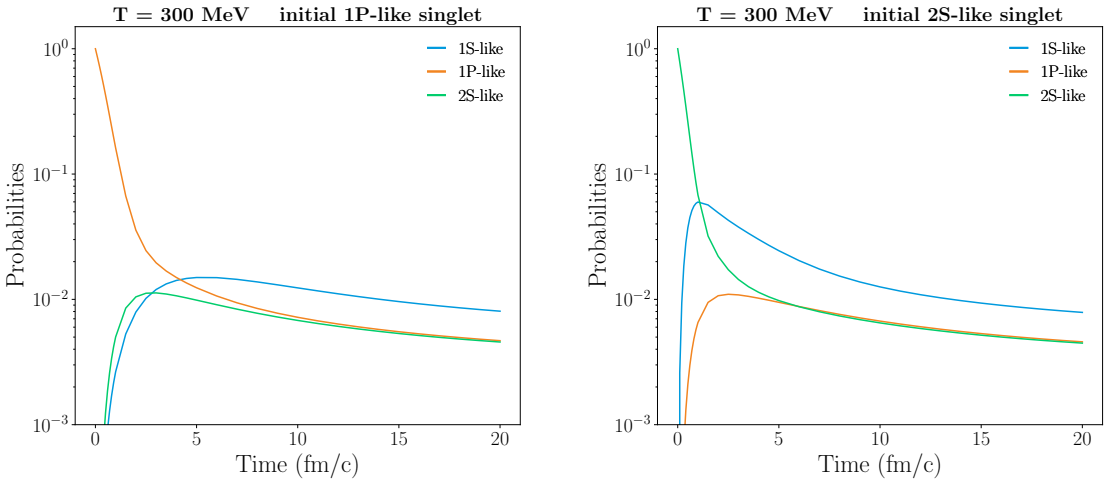


FIGURE 6.16 – *Left panel:*Evolution over time of the weights of the first three vacuum eigenstates at T = 300 MeV with an initial 1P-like singlet state. *Right panel:* Same with an initial 2S-like singlet state.

We can see on figure 6.16 that in both cases, we start by a transient phase where the populations are reordered. In the case of the 1P-like initial state, the 2S-like state is populated first while for the 2S-like initial state, it is the 1S-like state that is populated first as direct transitions between the 2S-like and 1S-like states are possible . The late time evolution in both cases is the same as for the initial 1S-like singlet state, which suggests the existence of a unique stationnary point.

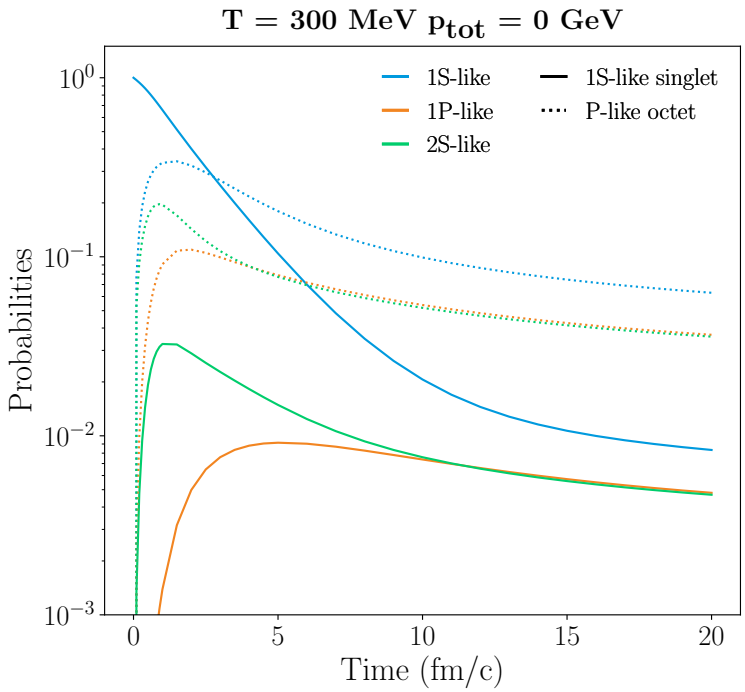


FIGURE 6.17 – Evolution over time of the weights of the first three vacuum eigenstates at T = 300 MeV with an initial 1S-like singlet state (solid lines) and an initial P-like octet state (dotted lines).

If we now take as initial state a P-like state in the octet channel as in section 6.1.2, we observe on figure 6.17 the formation of singlet bound states from an initial octet state at intermediate times (∼1-4 fm/c) due to color transitions. The S-like states are more populated at first since terms introducing transitions from octet to singlet color states also change parity. After the initial transient phase, the evolution is the same as for the other initial states. However, the weights of all three eigenstates are greater for an initial P-like octet state, which is expected as we have transitions from all the possible octet channels.

We showed in chapter 4 that the new $\mathcal{L}_4$ terms added a dependence on the total pair momentum $p_{tot}$. We now study the influence of those terms on the evolution of the populations of eigenstates.

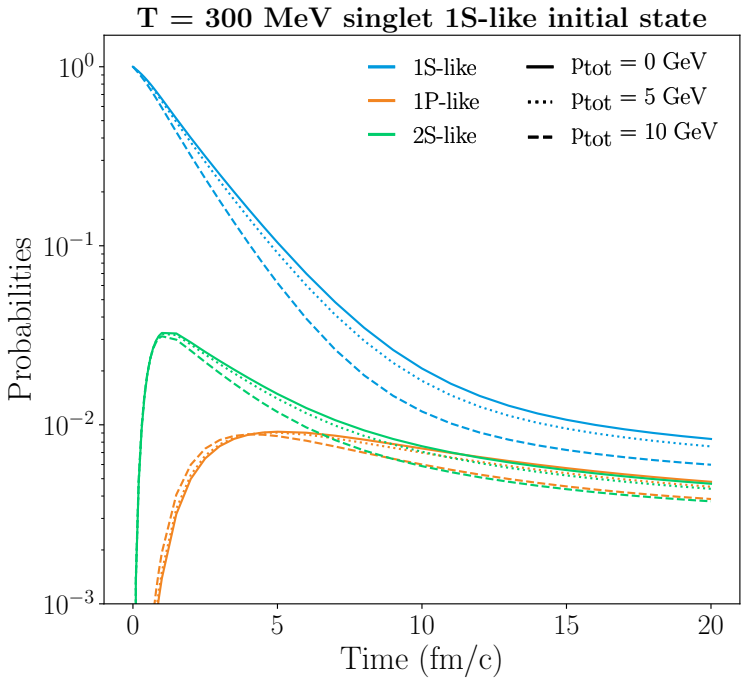


FIGURE 6.18 – Evolution over time of the weights of the first three vacuum eigenstates at T = 300 MeV with an initial 1S-like singlet state with a total pair momentum $p_{tot}$ = 0, 5 and 10 GeV.

We can see on figure 6.18 that the global evolution is the same for all 3 $p_{tot}$ considered. However, as $p_{tot}$ increases, the weights of the three eigenstates are smaller. The increase of the total pair momentum leads to an effective increase of the interactions between the $c\bar{c}$ pair and the QGP, leading to a decrease of the weights.

Finally, we study the effect of the $\mathcal{L}_4$ terms that are supposed to be subleading by comparing the projections on vacuum eigenstates with and without them. This is shown on figure 6.19.

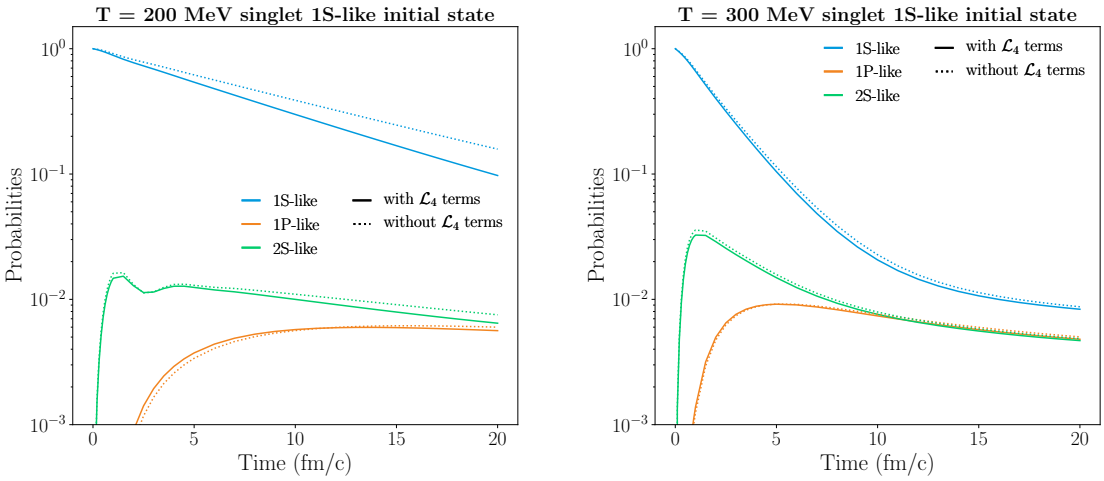


FIGURE 6.19 – *Left panel:*Evolution over time of the weights of the first three vacuum eigenstates for T = 200 MeV with (solid lines) and without (dashed lines) the $\mathcal{L}_4$ terms. *Right panel:* Same for T = 300 MeV.

We see that for T = 200 MeV, the effect of the $\mathcal{L}_4$ is quite important. This effect is much smaller for T = 300 MeV, showing that as temperature increases, the $\mathcal{L}_4$ terms are more and more subleading, as expected.

## 6.2 Quarkonium dynamics in an evolving medium

In the previous section, we considered a static medium with fixed temperature during the whole evolution, which is not realistic. We will now relax this last condition and consider a medium with a decreasing temperature over time. We consider a QGP medium with a temperature following a Björken-like temperature dependence[37]:

$$T(t) = T_0 \left( \frac{t_0}{t_0 + t} \right)^{1/3}, \tag{6.7}$$

with $T_0$ the initial temperature of the medium and $t_0$ a parameter, taken to be 1 fm/c. In this section, we consider a QGP medium with a starting temperature $T_0$ = 600 MeV and an initial 1S-like singlet state. As before, we stop the evolution at t = 20 fm/c, which corresponds to a final temperature T $\approx$ 217 MeV. We will first analyze the projections on vacuum states before looking at the density matrix itself.

### 6.2.1 Projections on vacuum states

As in section 6.1.3, we perform the instantaneous projection on vacuum eigenstates at several times. The evolution over time of the weights is given on figure 6.20

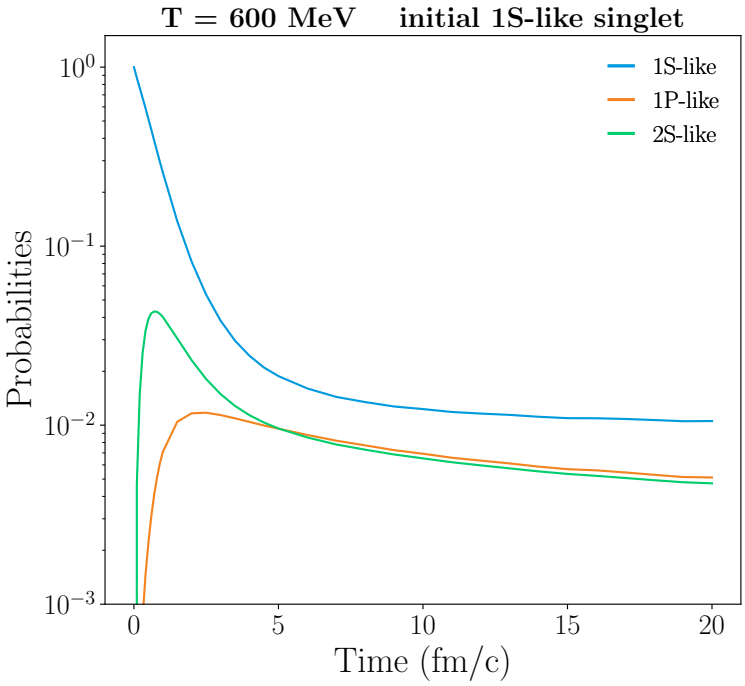


FIGURE 6.20 – Evolution over time of the weights of the first three vacuum eigenstates with an initial 1S-like singlet state with an initial medium temperature $T_0$ = 600 MeV.

We can observe the same features as for the fixed temperature case: A transient phase at early times followed by a phase corresponding to the decay of the eigenstates. As we start from a higher temperature (600 MeV), the transient phase is shorter and we reach a steady state where all 3 eigenstates decay in the same way. However, after around 13 fm/c, the 1S-like state starts to behave as it was repopulated. This also seems to happen to the excited states after 15 fm/c. This can be explained by the progressive cooling of the medium which leads to the dynamical binding of excited $c\bar{c}$ as well as $c\bar{c}$ from the continuum. It is then possible to observe an increase of the weight of the 1S-like state. If we compare with the results for a medium with fixed temperature T = 200 MeV (see left panel of figure 6.15), we

can see that this behaviour was not present in the fixed temperature case, which confirms that this is a physical effect.

### 6.2.2 $c\bar{c}$ dynamics

We proceed to analyze the evolution of the singlet density matrix $\mathcal{D}_s$ over time. This evolution is shown on figure 6.21. If we compare with figure 6.4, which represents the case of a medium with fixed temperature T = 300 MeV, the early time evolution is much faster in the present case, as the initial temperature is much higher. Starting from 10 fm/c the evolution is slower and we reach the same kind of final state. However, if we look at the values of $\mathcal{D}_s$ along the s = s' axis (see figure 6.22), we can see that they are slightly larger for the evolving temperature case, which is consistent with the observation we made in section 6.2.1.

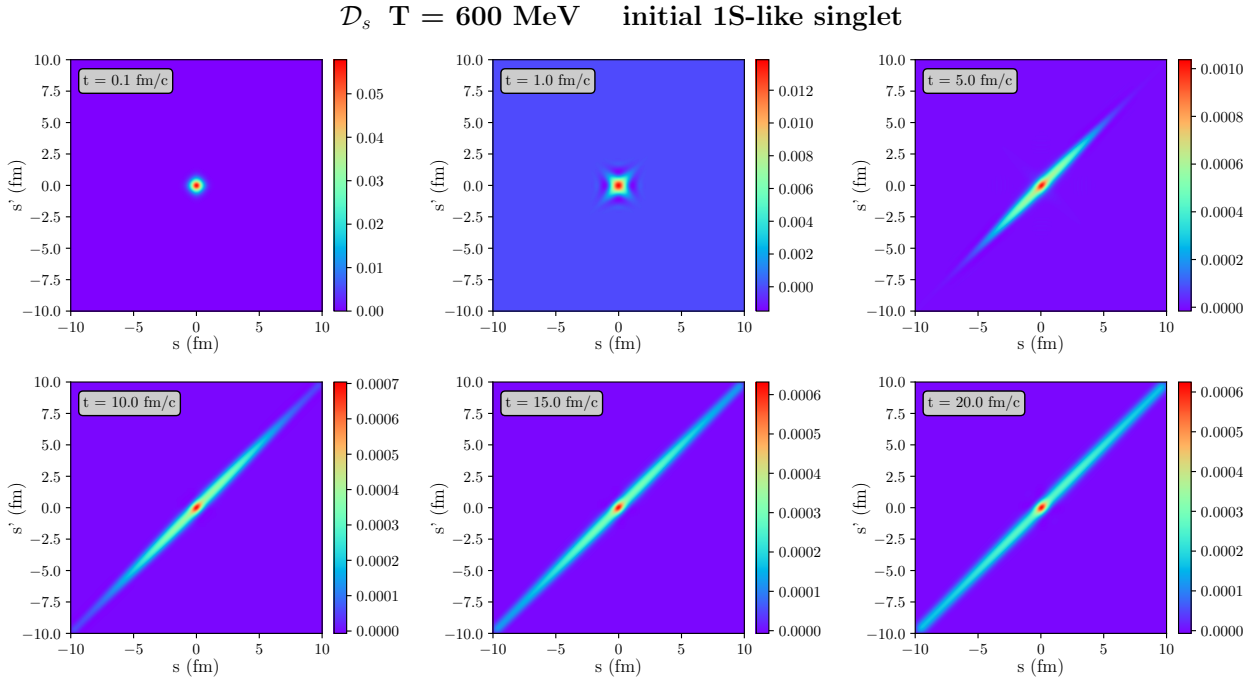


FIGURE 6.21 – Evolution of the singlet density matrix $\mathcal{D}_s$ over time with an initial temperature $T_0$ = 600 MeV. From top left panel to bottom right panel: 0.1, 1, 5, 10, 15 and 20 fm/c

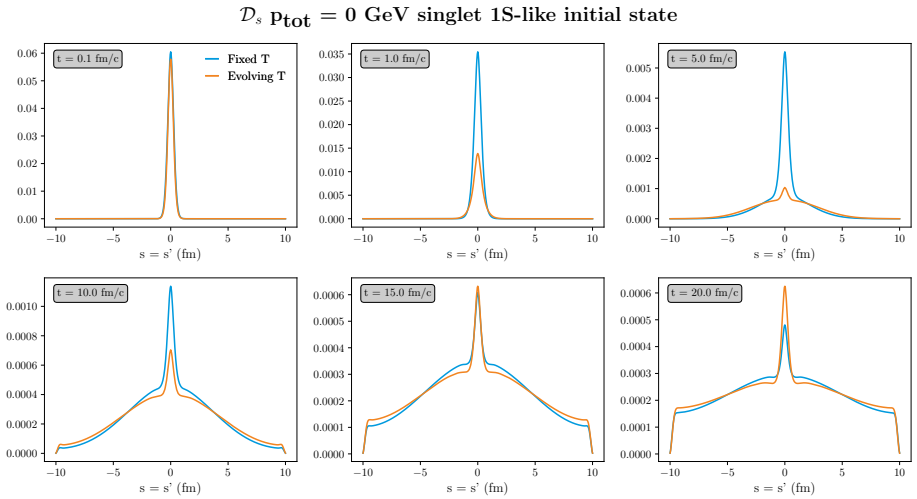


FIGURE 6.22 – Evolution of the singlet density matrix $\mathcal{D}_s$ along the s = s′ axis over time for a medium with initial temperature $T_0$ = 600 MeV and for a medium with fixed temperature T = 300 MeV. From top left panel to bottom right panel: 0.1, 1, 5, 10, 15 and 20 fm/c.

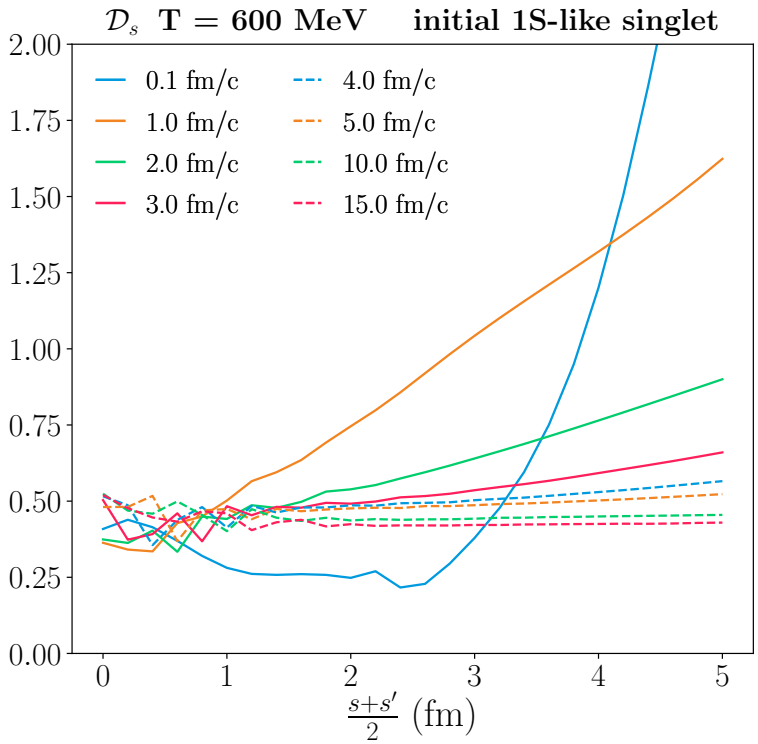


FIGURE 6.23 – Evolution of the mean squared momentum $\sqrt{\langle p^2 \rangle}$ over time at different values of $\frac{s+s'}{2}$ with an initial temperature $T_0$ = 600 MeV.

As in section 6.1.2, we now compute the Wigner transform of $\mathcal{D}_s$ and look the mean squared momentum $\sqrt{\langle p^2 \rangle}$ for different values of $\frac{s+s'}{2}$. As for the fixed temperature case, we observe the progressive appearance of an asymptotic value at large distance which decreases as time progresses due to the cooling of the medium. However, at small distances (0 to 1.5 fm), those asymptotic values are not reached, clearly showing that the system is not fully thermalized and the potential V still plays an important role.

## 6.3 Summary and conclusion

In this chapter, we have studied the dynamics of a single $c\bar{c}$ pair in a QGP medium in the case of both a fixed and a decreasing temperature. We showed the importance of the color degrees of freedom in the dynamics by analyzing how color equilibrates in the medium through the evolution of the trace of the density matrix in the singlet and octet color channels. The analysis of the projections on the vacuum eigenstates showed that for all initial conditions considered, the global evolution was separated into two phases: a transient phase of re-equilibration followed by a decay phase. We demonstrated that at higher temperatures, the final populations were much smaller, especially for the 1S-like state and that the total momentum of the pair was also impacting the final populations.

By looking at the singlet density matrix $\mathcal{D}_s$ itself, we observed the progressive decoherence induced by the medium on the initial state and its delocalization along the s = s' axis. Two components were identified: a central core, which was still under the effect of the real part of the potential V, and a semi-classical like component on the edges. To study further this last component and the feasability of a semi-classical treatment of the problem, we performed the Wigner transform of $\mathcal{D}_s$ and looked at the mean squared momentum $\sqrt{\langle p^2 \rangle}$ at different distances between the $c$ and $\bar{c}$ quarks. We could clearly observe that the system reaches thermalization, at a speed that depends on the temperature. However, we could also note that at small distances, the real part of the potential V still plays a role, even at late times. A fully semi-classical treatment may thus not be possible and a genuine quantum treatment of V may be needed. This work is a first step and the consequences of semi-classical approximations will be studied in the near future.

Finally, we extended this work to the case of a cooling QGP medium. We observed the repopulation at later times of the 1S-like state, due to the binding of excited $c\bar{c}$ pairs and $c\bar{c}$ pairs from the continuum due to the cooling of the medium. This physical effect was not observed in the fixed temperature case and shows the importance of having a realistic medium.

# Conclusion

In this thesis, we have investigated the real-time dynamics of a heavy charmonium in the Quark-Gluon Plasma. This work aimed at 1) describing the effects of the color screening and the collisions in the QGP on the $c\bar{c}$ pair and its dynamics, 2) obtaining a dynamical description of dissociation, recombination and transitions between bound states and 3) studying the feasability of a semi-classical treatment of a heavy quarkonium dynamics, which would allow the treatment of multiple quarkonia (crucial for charmonia phenomenology at high-energy colliders).

To do so, we extended the pioneering work of Blaizot & Escobedo in order to obtain well-defined quantum master equations, describing the dynamics of a single heavy quarkonium in the Quark-Gluon Plasma. Those equations take into account transitions between color states (allowing to treat dissociation and recombination, transitions between bound states and genuine dissipative effects from the medium. The equations were resolved in one dimension to reduce the heavy computational cost of such resolution, incorporating a novel potential tailored for quarkonium studies in one-dimension. We considered two different medium configurations 1) a QGP medium with fixed temperature during the entire evolution and 2) a cooling QGP medium, evolving according to a Björken profile. Starting from different initial states for the $c\bar{c}$ state, we first analyzed the evolution over time of the density matrix of the system and studied the performed a Wigner transform on it to see if the system can be treated semi-classically. In order to study the transition between bound states and the possible formation of a quarkonium state from a $c\bar{c}$ pair, we performed the instantaneous projection of the singlet density matrix on the vacuum eigenstates.

The resolution of the equations with different configurations showed that:

— Color degrees of freedom can not be neglected.

— The early stage of the evolution is characterized by a re-equilibration the populations of charmonium states, followed by a decay phase.

— For all initial conditions in a medium with fixed temperature, the system follows the same evolution at later times, indicating that it reaches a steady state (which is however not described by the Maxwell-Boltzmann distribution).

— The ground state can be repopulated as the medium cools down, which is not observed when the medium has a fixed temperature, proving the need of a realistic background.

— The system almost fully thermalizes, at a speed depending on the temperature of the medium.

— A small part of the system is still under the effect of the real potential V, even at late times and high temperatures.

— A fully semi-classical treatment may not be possible, and a genuine quantum treatment of the real potential may be required.

The work presented in this thesis naturally open several perspectives. The application of this work to the bottomonium system is straightforward and will be done. The resolution of the equations in three-dimensions, mandatory to provide reliable predictions, is a challenge that will require innovative numerical strategies as it requires humongous computational power. The treatment of the medium is often simplistic, and a more realistic description of the plasma is required. The use of event generators (such as EPOS) might be a good starting point at the numerical level, but assumptions at the theoretical level (medium in thermal equilibrium for example) should be relaxed. As temperature decreases, the assumptions for the quantum brownian regime are less and less justified, which calls for work on how to handle the transition between this regime and the quantum optical limit regime. Finally, the analysis of the use of semi-classical approximations will allow to determine if a semi-classical treatment of quarkonia dynamics is justified or not and in which regime. This is a truly important question as the treatment of multiple charmonia is crucial for phenomenology and the run 3 of the LHC is on the horizon.

# Appendix A

# Derivation of QCD terms

We first describe the global procedure to derive terms in the QED-like case, before showing how one can retrieve the QCD terms from the QED-like ones.

## A.1 Derivation procedure

We take the example of the $\mathcal{L}_1$ terms. Those terms were given by:

$$\mathcal{L}_1\mathcal{D} = -\frac{i}{2}\int_{\mathbf{x}\mathbf{x}'} V(\mathbf{x}-\mathbf{x}')\,[n_{\mathbf{x}}n_{\mathbf{x}'},\mathcal{D}], \tag{A.1}$$

with:

$$\langle \mathbf{r}_1\mathbf{r}_2|n_{\mathbf{x}}|\mathbf{r}_1'\mathbf{r}_2'\rangle = \delta(\mathbf{r}_1-\mathbf{r}_1')\delta(\mathbf{r}_2-\mathbf{r}_2')\,[\delta(\mathbf{x}-\mathbf{r}_1)-\delta(\mathbf{x}-\mathbf{r}_2)]. \tag{A.2}$$

We compute:

$$\langle \mathbf{r}_1\mathbf{r}_2|\mathcal{L}_1\mathcal{D}|\mathbf{r}_1'\mathbf{r}_2'\rangle = -\frac{i}{2}\int_{\mathbf{x}\mathbf{x}'} V(\mathbf{x}-\mathbf{x}')\,(\,\langle \mathbf{r}_1\mathbf{r}_2|n_{\mathbf{x}}n_{\mathbf{x}'}\mathcal{D}|\mathbf{r}_1'\mathbf{r}_2'\rangle - \langle \mathbf{r}_1\mathbf{r}_2|\mathcal{D}n_{\mathbf{x}}n_{\mathbf{x}'}|\mathbf{r}_1'\mathbf{r}_2'\rangle\,). \tag{A.3}$$

We will only demonstrate how to compute the first term, as the second one follows the same procedure and can be easily derived from the first one. We start by introducing completion relations:

$$\int_{\mathbf{x}\mathbf{x}'} V(\mathbf{x}-\mathbf{x}') \left\langle \mathbf{r}_1\mathbf{r}_2 \middle| n_{\mathbf{x}} n_{\mathbf{x}'} \mathcal{D} \middle| \mathbf{r}_1'\mathbf{r}_2' \right\rangle .$$
$$= \int_{\substack{\mathbf{x}\mathbf{x}' \\ \mathbf{a}\mathbf{a}' \\ \mathbf{b}\mathbf{b}'}} V(\mathbf{x}-\mathbf{x}') \left\langle \mathbf{r}_1\mathbf{r}_2 \middle| n_{\mathbf{x}} \middle| \mathbf{a}\mathbf{a}' \right\rangle \left\langle \mathbf{a}\mathbf{a}' \middle| n_{\mathbf{x}'} \middle| \mathbf{b}\mathbf{b}' \right\rangle \left\langle \mathbf{b}\mathbf{b}' \middle| \mathcal{D} \middle| \mathbf{r}_1'\mathbf{r}_2' \right\rangle . \tag{A.4}$$

Using equation (A.2), we get:

$$\int_{\substack{\mathbf{x}\mathbf{x}' \\ \mathbf{a}\mathbf{a}' \\ \mathbf{b}\mathbf{b}'}} V(\mathbf{x}-\mathbf{x}') \left\langle \mathbf{r}_1\mathbf{r}_2 \middle| n_{\mathbf{x}} \middle| \mathbf{a}\mathbf{a}' \right\rangle \left\langle \mathbf{a}\mathbf{a}' \middle| n_{\mathbf{x}'} \middle| \mathbf{b}\mathbf{b}' \right\rangle \left\langle \mathbf{b}\mathbf{b}' \middle| \mathcal{D} \middle| \mathbf{r}_1'\mathbf{r}_2' \right\rangle .$$
$$= \int_{\mathbf{x}\mathbf{x}'} V(\mathbf{x}-\mathbf{x}') [\delta(\mathbf{x}-\mathbf{r}_1) - \delta(\mathbf{x}-\mathbf{r}_2)] \left[\delta(\mathbf{x}'-\mathbf{r}_1) - \delta(\mathbf{x}'-\mathbf{r}_2)\right] \left\langle \mathbf{r}_1\mathbf{r}_2 \middle| \mathcal{D} \middle| \mathbf{r}_1'\mathbf{r}_2' \right\rangle . \tag{A.5}$$

Using the parity of V, we finally obtain:

$$\int_{\mathbf{x}\mathbf{x}'} V(\mathbf{x}-\mathbf{x}') \left\langle \mathbf{r}_1\mathbf{r}_2 \middle| n_{\mathbf{x}} n_{\mathbf{x}'} \mathcal{D} \middle| \mathbf{r}_1'\mathbf{r}_2' \right\rangle = 2[V(0) - V(\mathbf{r}_1-\mathbf{r}_2)] \left\langle \mathbf{r}_1\mathbf{r}_2 \middle| \mathcal{D} \middle| \mathbf{r}_1'\mathbf{r}_2' \right\rangle . \tag{A.6}$$

The second term of the right-hand side of equation (A.3) is obtained by doing the change of variables $(\mathbf{r}_1, \mathbf{r}_2) \leftrightarrow (\mathbf{r}_1', \mathbf{r}_2')$ in equation (A.6), which gives us:

$$\left\langle \mathbf{r}_1\mathbf{r}_2 \middle| \mathcal{L}_1 \mathcal{D} \middle| \mathbf{r}_1'\mathbf{r}_2' \right\rangle = \left[V(\mathbf{r}_1-\mathbf{r}_2) - V(\mathbf{r}_1'-\mathbf{r}_2')\right] \left\langle \mathbf{r}_1\mathbf{r}_2 \middle| \mathcal{D} \middle| \mathbf{r}_1'\mathbf{r}_2' \right\rangle . \tag{A.7}$$

The procedure is the same at every level, with the eventual need of performing integrations by parts.

There are 4 types of terms that we can encounter:

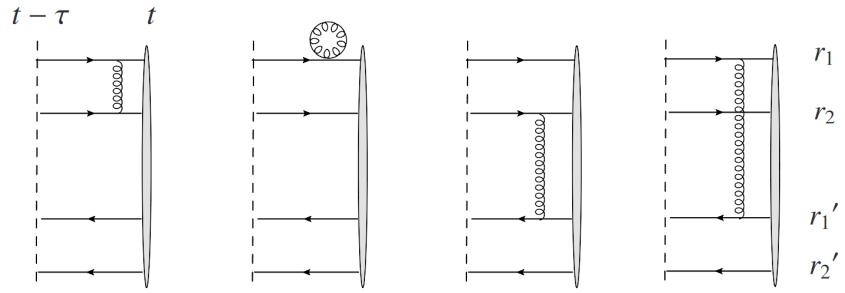


FIGURE A.1 – Diagrams representing the different types of terms we can encounter in the equations. [2]

The first and second diagrams correspond to interactions that do not mix the prime and non-prime variables. They are the $\mathcal{L}_a$ contributions. The second diagram correspond to self-interactions, described by terms of the form $W(\mathbf{r}_1 - \mathbf{r}_1)$ (and similar notations), they are the $\mathcal{L}_{QQ,a}$ terms. The first diagram correspond to interactions between the quark and antiquark, described by terms of the form $W(\mathbf{r}_1 - \mathbf{r}_2)$ (and similar notations), they are the $\mathcal{L}_{Q\bar{Q},a}$ terms.

The last two diagrams correspond to interactions mixing prime and non-prime variables, they correspond to the $\mathcal{L}_b$ contributions. Again, we can see interactions between a quark and "prime" quark (last diagram) and between a antiquark and "prime" quark (third diagram). Those correspond respectively to the $\mathcal{L}_{QQ,b}$ and $\mathcal{L}_{Q\bar{Q},b}$ terms and are described respectively by terms of the form $W(\mathbf{r}_1 - \mathbf{r}_1')$ and $W(\mathbf{r}_1 - \mathbf{r}_2')$ (and similar notations).

## A.2 QCD color factors and QCD equations

We now describe how to derive the terms in the QCD case. We focus on the terms at the $\mathcal{L}_2$ level only, but the procedure is the same at all levels. If we consider only a density matrix invariant under color transformations, we have:

$$\mathcal{D} = \mathcal{D}_0 \, \mathbb{1} \otimes \mathbb{1} + \mathcal{D}_8 \, t_a \otimes \bar{t}_a, \tag{A.8}$$

with $t_a$ the generators of SU(3). We can represent this in a diagrammatic form:

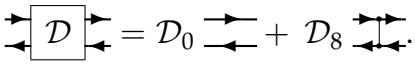

(A.9)

We use another basis in the equations and it is possible to perform a change of basis using the following identity:

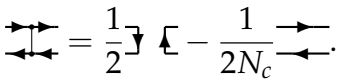

(A.10)

Using those relations and the following relations from Appendix D of [2]:

$$\mathcal{D}_s = \mathcal{D}_0 + C_F\mathcal{D}_8 \;\; ; \;\; \mathcal{D}_o = \mathcal{D}_0 - \frac{1}{2N_c}\mathcal{D}_8, \tag{A.11}$$

we get:

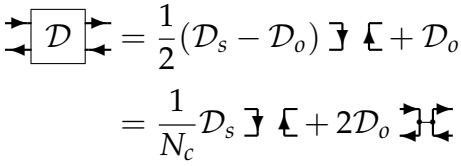

(A.12)

At the $\mathcal{L}_2$ level, there are two types of terms: terms of the form $nn\mathcal{D}$ and terms of the form $n\mathcal{D}n$. We can represent the $n$ operators in the following way:

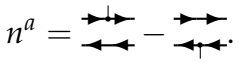

(A.13)

Using the diagrams, we can easily compute the color factors in front of each terms. To compute terms of the form $n^a n'^a \mathcal{D}$, we will use the following identity:

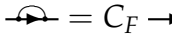

(A.14)

which gives us:

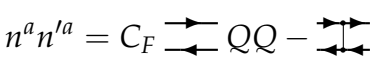

(A.15)

with $QQ$ and $Q\bar{Q}$ denoting the type of interaction. We recall that terms of the form $n^a n'^a \mathcal{D}$ correspond to $\mathcal{L}_a$ terms, therefore $QQ = \mathcal{L}_{QQ,a}$ and $Q\bar{Q} = -\mathcal{L}_{Q\bar{Q},a}$. Using the relation (A.10), we can derive the following one:

(A.16)

which allows us to compute:

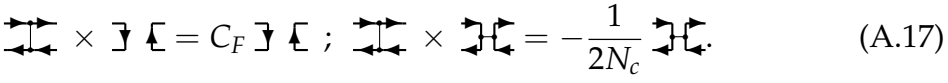

(A.17)

Using equations (A.12),(A.15) and (A.17), we finally obtain:

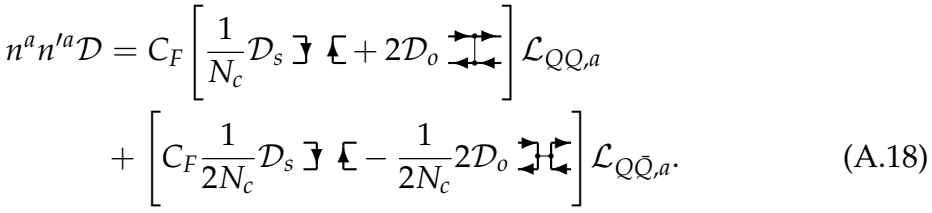

(A.18)

We then get the following contributions:

$$\begin{aligned}\mathcal{L}_{ss} &= C_F\left(\mathcal{L}_{QQ,a} + \mathcal{L}_{Q\bar{Q},a}\right)\\ \mathcal{L}_{oo} &= C_F\mathcal{L}_{QQ,a} - \frac{1}{2N_c}\mathcal{L}_{Q\bar{Q},a}.\end{aligned} \tag{A.19}$$

We now proceed with the $n^a \mathcal{D} n'^a$ terms, corresponding to the $\mathcal{L}_b$ contributions. We have:

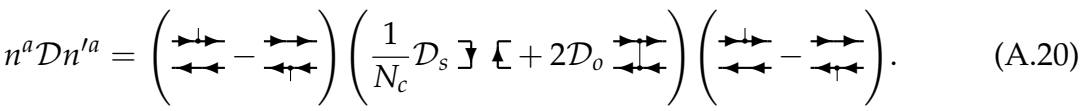

(A.20)

We start by computing the terms involving $\mathcal{D}_s$ and only consider the $QQ$ and $Q\bar{Q}$

contributions as the $\bar{Q}\bar{Q}$ and $\bar{Q}Q$ are the same. Those contributions are:

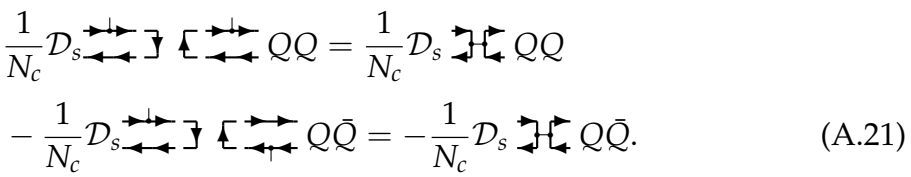

(A.21)

As for the $\mathcal{L}_a$ contribution, we have $QQ = \mathcal{L}_{QQ,b}$ and $Q\bar{Q} = -\mathcal{L}_{Q\bar{Q},b}$. If we regroup both terms from equation (A.21), we see that we obtain a transition from the singlet part of $\mathcal{D}$ to the octet part. Therefore we have the following operator:

$$\mathcal{L}_{os} = \frac{1}{2N_c}\Big(\mathcal{L}_{QQ,b} + \mathcal{L}_{Q\bar{Q},b}\Big). \tag{A.22}$$

Now let us proceed with the computation of the terms involving $\mathcal{D}_o$. They involve a double interaction that can be simplified using identity (A.10):

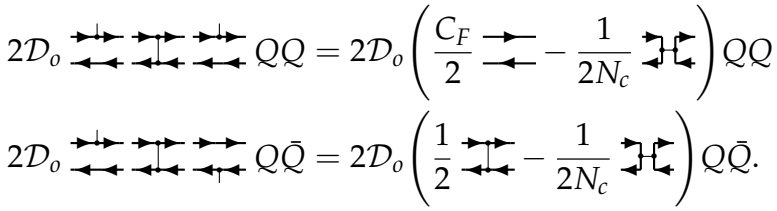

(A.23)

Again using identity (A.10), we can simplify the right-hand sides of equation (A.23):

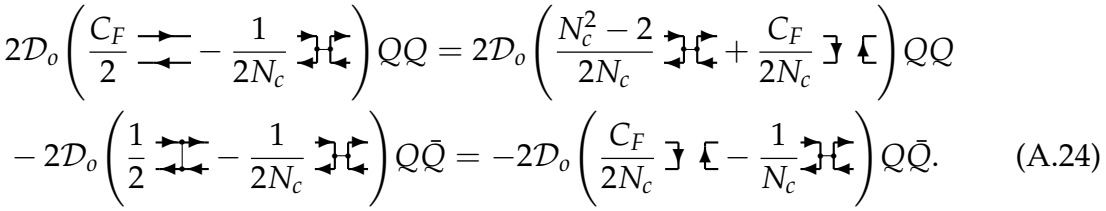

(A.24)

We observe a transition from the octet part of $\mathcal{D}$ to the singlet part with also an octet-octet transition. This gives us the following operators:

$$\begin{aligned}\mathcal{L}_{so} &= C_F\Big(\mathcal{L}_{QQ,b} + \mathcal{L}_{Q\bar{Q},b}\Big)\\ \mathcal{L}_{oo} &= \frac{N_c^2-2}{2N_c}\mathcal{L}_{QQ,b} - \frac{1}{N_c}\mathcal{L}_{Q\bar{Q},b}.\end{aligned} \tag{A.25}$$

Regrouping the contributions of equations (A.19), (A.22) and (A.25), we finally obtain the operators of the QCD equations:

$$\begin{aligned}\mathcal{L}_{ss} &= C_F\Big(\mathcal{L}_{QQ,a} + \mathcal{L}_{Q\bar{Q},a}\Big)\\ \mathcal{L}_{so} &= C_F\Big(\mathcal{L}_{QQ,b} + \mathcal{L}_{Q\bar{Q},b}\Big)\\ \mathcal{L}_{os} &= \frac{1}{2N_c}\Big(\mathcal{L}_{QQ,b} + \mathcal{L}_{Q\bar{Q},b}\Big)\\ \mathcal{L}_{oo} &= C_F\mathcal{L}_{QQ,a} - \frac{1}{2N_c}\mathcal{L}_{Q\bar{Q},a} + \frac{N_c^2-2}{2N_c}\mathcal{L}_{QQ,b} - \frac{1}{N_c}\mathcal{L}_{Q\bar{Q},b}.\end{aligned} \tag{A.26}$$

# Appendix B

# Résumé en français

Dans l'état actuel de nos connaissances, il est prédit que dans des conditions extrêmes de températures et/ou de densité, comme celles présentes au début de l'Univers, la matière nucléaire atteint un nouvel état, composé de quarks et gluons déconfinés (alors qu'ils sont confinés dans la matière hadronique usuelle), appelé Plasma de Quarks et de Gluons (PQG). Ces quarante dernières années, théoriciens et expérimentateurs ont étudiés intensivement l'existence et les propriétés de ce nouvel état de la matière nucléaire. La seule manière de produire sur Terre un PQG est de collisionner des ions lourds at des vitesses ultra-relativistes dans des accélérateurs comme le Relativistic Heavy Ion Collider (RHIC) ou le Large Hadron Collider (LHC). Une observable de choix pour l'étude du Plasma de Quarks et de Gluons est la suppression des quarkonia, qui correspond à une production plus faible de quarkonia (qui sont des particules composites composées d'un quark lourd et de son antiquark) en collisions d'ions lourds par rapport aux collisions proton-proton. Ce phénomène, prédit en 1986 par Matsui & Satz [1], a été étudié auprès des collisionneurs, où les expériences ont révélé que cette suppression était un processus très complex, nécessitant une compréhension théorique robuste. Ces dernières années, un effort significatif a été réalisé vers la description dynamique des quarkonia dans le PQG, à l'aide du formalisme des systèmes quantiques ouverts. Dans ce dernier, il est possible de décrire en temps-réel un système quantique (un quarkonium par exemple) en interaction avec un bain thermique (un PQG par exemple) en étudiant l'opérateur densité réduit du système. Cette thèse présente une approche basée sur les systèmes quantiques ouverts, visant à décrire la dynamique d'un quarkonium dans le Plasma de Quarks et de Gluons.

Le premier chapitre, intitulé "Modèle Standard et Plasma de Quarks et de Glu-

ons", décrit le cadre global dans lequel s'inscrit cette thèse. Il commence par présenter brièvement le Modèle Standard de la physique des particules avant de s'intéresser plus particulièrement à la théorie de la Chromodynamique Quantique (QCD), qui est la théorie décrivant l'interaction forte. Cette partie introduit les concepts de constante de couplage (ainsi que de son "running"), de confinement et de liberté asymptotique. La QCD sur réseau (Lattice QCD ou $\mathcal{L}$QCD) est également brièvement présentée. La première partie de ce chapitre est complétée par une introduction à la physique des quarkonia, ces derniers étant le sujet d'étude principal de cette thèse. La production de quarkonia, qui implique des aspects perturbatifs et non-perturbatifs de la QCD, est ensuite discutée, à travers la présentation de trois modèles permettant de décrire la production de paires quark-antiquark et leur hadronisation en quarkonia.

La seconde partie du chapitre est consacrée à la présentation du Plasma de Quarks et de Gluons, à travers tout d'abord l'étude du diagramme de phase de la matière nucléaire et des différentes transitions de phase entre matière hadronique et le PQG. Les collisions d'ions lourds, permettant de récréer cet état de la matière nucléaire, sont ensuite abordées. Les différentes étapes de ces collisions, de la collision entre les ions à proprement parler jusqu'aux hadrons finaux sont ensuite décrites en détail. Enfin, une dernière section présente les principales sondes du PQG, c'est-à-dire les principales observables expérimentales utilisées pour l'étude du PQG. Ces sondes, séparées en deux catégories: les sondes dites "molles" et les sondes dites "dures", sont le flot anisotropique, les photons et leptons thermiques, l'augmentation de la production d'étrangeté ou encore le phénomène dit de "jet quenching". Une dernière observable très importante, la suppression des quarkonia, est décrite dans le chapitre suivant.

Le second chapitre, intitulé "Phénoménologie de la suppression des quarkonia", donne tout d'abord une définition de la suppression des quarkonia, définie comme une réduction du nombre de quarkonia produits en collisions noyau-noyau par rapport à une collision proton-proton (une fois normalisé par le nombre de collisions proton-proton).

Dans un premier temps, les différents méchanismes influant sur la production de quarkonia sont présentés, en commençant par les effets nucléaires dits froids, qui sont des effets arrivant avant la production de la paire quark-antiquark. Les effets

dûs au milieu en lui-même sont ensuite développés. La présence de nombreuses charges de couleurs au sein du plasma entraîne un écrantage de l'interaction entre un quark un antiquark, qui peut conduire à la dissociation d'un quarkonium et donc à une production finale réduite. De plus, la présence de nombreux quarks légers et gluons peut entraîner des collisions entre un quarkonium et ces dernières, collisions pouvant également amener à la dissociation d'un état lié quarkonium. Ces effets sont généralement décrits par un potentiel complexe de partie réelle notée V et de partie imaginaire notée W, dépendant de la distance entre les deux quarks et de la température. Enfin, lorsque l'énergie dans le centre de masse de la collision initiale est grande (comme aux énergies du LHC), le nombre de quarks charm et anticharm produits est plus grand qu'à plus basse énergie, car les sections efficaces de production sont plus élevées. Le grand nombre de quarks et antiquarks charmés présents dans le milieu peut amener à un phénomène dit de recombinaison, où un quark charm et un antiquark charm se recombinent pour former un nouvel état lié charmonium. Ce phénomène contrebalance donc le phénomène de suppression. A noter que la recombinaison existe également pour les quarks bottom, mais est beaucoup plus faible.

Dans un second temps, un panorama des résultats expérimentaux du RHIC et du LHC sur la suppression des charmonia et bottomonia est présenté. Aux énergies du RHIC et du LHC, la suppression des bottomonia est plus forte pour les collisions les plus centrales et plus forte pour le $\Upsilon(2S)$ que pour le $\Upsilon(1S)$. Aucune dépendance n'est clairement observée par rapport à la rapidité ou l'impulsion transverse. Les données du RHIC sur la suppression des charmonia montrent quant à elles une suppression accrue pour les collisions les plus centrales ainsi qu'à rapidité avant. Aux énergies du LHC, des données de CMS ont montré n'ont pas montré de dépendance significative par rapport à la rapidité des collisions et une plus grande suppression pour les collisions les plus centrales. Des mesures de l'expérience ALICE ont également révélé une augmentation de la production de $J/\Psi$ à très basse impulsion transverse (0-2 GeV), indiquant que la recombinaison est importante à basse impulsion transverse. Une plus grande suppression du $\Psi(2S)$ par rapport au $J/\Psi$ a également été observée par CMS.

Pour terminer ce chapitre, une revue des principaux modèles théoriques utlisés pour décrire la suppression des quarkonia est faite. Le modèle de la suppression séquentielle, introduit par Matsui & Satz en 1986 [1], suppose que pour chaque état quarkonium, il existe une température de dissociation. Si au début de la phase de

PQG, la température du milieu est plus grande que la température de dissociation d'un état donné $T_\Phi^d$, ce dernier est supposé dissocié pour toujours alors que si la température est plus faible, l'état est supposé survivre. Les modèles de recombinaison statistique [108–114] supposent au contraire que toutes les paires quark-antiquark sont dissociées au début de la phase de QGP et qu'aucune corrélation n'existe entre le quark et l'antiquark d'une paire. Les quarks évoluent librement ensuite et ne s'hadronisent qu'à la fin de la phase de PQG de manière statistique. Les modèles de transport [127, 129–132] ont une vision plus dynamique de la dissociation et de la recombinaison. Ils décrivent généralement la distribution de quarkonia dans le milieu à partir d'équations de Boltzmann ou de Langevin relativistes. Enfin, le modèle des co-voyageurs [96–100] décrit la suppression des quarkonia causée par les interactions inélastique des quarkonia avec les hadrons "co-voyageurs" (avec une rapidité similaire à celle des quarkonia) ainsi que la recombinaison induite par le même méchanisme. Ces modèles sont de manière générale en bon accord avec les données expérimentales mais leurs hypothèses sont souvent discutables. Une autre voie théorique est de s'intéresser à la dynamique en temps réel des quarkonia dans le PQG, qui est un problème pouvant être traité dans le cadre du formalisme des systèmes quantique ouverts.

Le troisième chapitre, intitulé "Systèmes Quantiques Ouverts", présente ce formalisme ainsi qu'une revue des approches utilisant ce formalisme pour décrire la dynamique des quarkonia dans le plasma. Il commence par introduire le concept d'opérateur densité, qui décrit l'état d'un système (dans le cas qui nous intéresse, une paire quark-antiquark en interaction avec le PQG) et d'équation maîtresse quantique, qui décrit l'évolution d'un opérateur densité à travers le temps. Il est possible d'accéder à la dynamique de la paire (c'est la paire qui nous intéresse et non le système global) à travers l'opérateur densité réduit de la paire. L'équation maîtresse la plus générale décrivant la dynamique de cet opérateur densité réduit, appelée équation de Lindblad, est ensuite décrite en détail. Cette équation est très intéressante car elle préserve trois propriétés de l'opérateur densité réduit que sont sa positivité, son hermiticité ainsi que son unitarité. Une dérivation générale de l'équation de Lindblad est ensuite présentée. Cette dérivation fait appel à plusieurs approximations et exploite deux hiérarchies différentes entre les différentes échelles du temps du système global que sont le temps de corrélation de l'environnement $\tau_E$,

le temps intrinsèque du sous-système (la paire) $\tau_S$ et enfin le temps de relaxation du sous-système $\tau_R$. Suivant la hiérarchie utilisée dans la dérivation, deux limites peuvent être atteintes: la limite du mouvement brownien quantique dans le cas où $\tau_R \gg \tau_E$ et $\tau_S \gg \tau_E$ et la limite optique quantique dans le cas où $\tau_R \gg \tau_E$ et $\tau_R \gg \tau_S$.

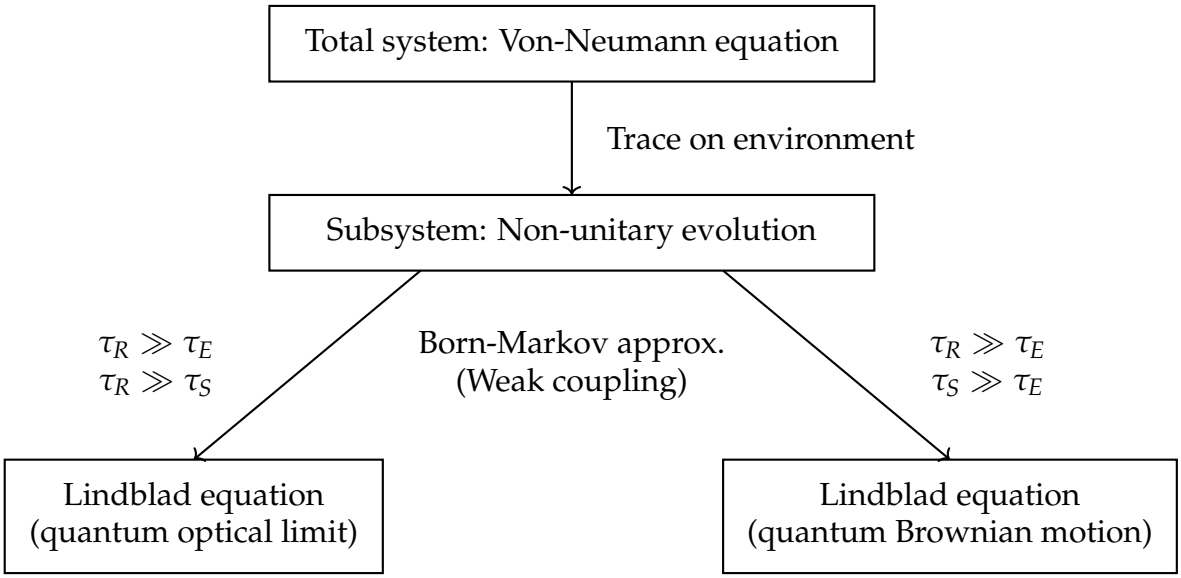


FIGURE B.1 – Principales étapes et hypothèses de la dérivation d'une équation de Lindblad

La deuxième partie de ce chapitre est consacrée à une revue des approches basées sur le formalisme des systèmes quantiques ouverts. Après avoir couvert les premières approches phénoménologiques [138, 139, 141, 142], les approches dérivées des premiers principes de la QCD sont abordées. Chacune de ces approches [2, 144, 156, 157, 163, 168] se basent sur une équation maîtresse quantique, dérivée dans l'une ou l'autre des limites précedemment citées, et utilisent des stratégies différentes pour résoudre ces équations. L'une d'entre elles, celle développée par Blaizot & Escobedo [2], est particulièrement intéressante car elle permet de traiter simultanément plusieurs paires quark-antiquark dans le PQG à l'aide d'une approche semi-classique, ce qui est encore un des problèmes majeurs du domaine. Cette question est cruciale car le traitement de nombreuses paires est indispensable pour pouvoir modéliser convenablement la recombinaison des charmonia. L'approche de Blaizot & Escobedo est résumée et ses hypothèses et limitations sont discutées. Notamment, les équations maîtresses dérivées dans leur approche ne conservent pas la positivité de l'opérateur densité décrivant la paire quark-antiquark. De plus la va-

lidité de leur approche semi-classique n'a pas été vérifiée directement en résolvant les équations directement et en comparant les résultats. L'approche développée dans cette thèse vise à combler ces lacunes en étendant les équations déjà existantes afin de préserver la positivité tout en résolvant directement ces équations, chose qui n'a jamais été faite et n'est pas triviale, afin 1) d'étudier la dynamique d'une paire quark-antiquark dans le PQG et 2) tester la validité d'une approche semi-classique.

Le quatrième chapitre, intitulé "Extension des équations de Blaizot & Escobedo et restoration de la positivité", présente le coeur des développements théoriques effectués durant cette thèse. Tout d'abord, une nouvelle dérivation des équations de Blaizot & Escobedo est présentée, basée sur une procédure proposée dans une annexe de leur article. Cette nouvelle dérivation introduit des termes d'ordre supérieur, supposés négligeables dans l'article original, doivent conduire à la conservation de la positivité de l'opérateur densité réduit. La dérivation des termes est d'abord réalisée dans un cas où les degrés de liberté de couleur sont ignorés puis l'extension au cas où ces degrés de libertés sont pris en compte est donnée. Les détails de cette extension sont donnés dans l'annexe A. Les équations obtenues sont de la forme:

$$\frac{\mathrm{d}\mathcal{D}_s}{\mathrm{d}t} = \mathcal{L}_{ss}\mathcal{D}_s + \mathcal{L}_{so}\mathcal{D}_o$$
$$\frac{\mathrm{d}\mathcal{D}_o}{\mathrm{d}t} = \mathcal{L}_{os}\mathcal{D}_s + \mathcal{L}_{oo}\mathcal{D}_o,$$

où $\mathcal{D}_s$ et $\mathcal{D}_o$ sont respectivement les opérateurs densités dans l'état de couleur singulet et octet et les opérateurs $\mathcal{L}_{ss}$,$\mathcal{L}_{so}$,$\mathcal{L}_{os}$ et $\mathcal{L}_{oo}$ représentent les transitions entre les différents états de couleur.

Avant de justifier la conservation de l'unitarité et de la positivité, une simplification est faite, qui consiste à effectuer la trace sur les degrés de liberté du centre de masse. Cette simplification est justifiée par le fait que la paire quark-antiquark est lourde et n'interagit que faiblement avec le milieu, le mouvement de son centre de masse varie donc peu. Cette simplification conduit à l'apparition de termes dépendant de l'impulsion totale de la paire, chose qui n'était pas présente dans les équations originales et qui vient des termes d'ordre supérieur.

La conservation de l'unitarité est ensuite explicitement prouvée, avec cepen-

dant une particularité. Dans le cas des équations de Blaizot & Escobedo, cette conservation était locale. Dans le cas des équations présentées dans cette thèse, cette conservation, bien qu'exacte, n'est plus complètement locale, ce qui a des conséquences sur la conservation de l'unitarité lorsque les équations sont résolues numériquement.

La conservation de la positivité est ensuite prouvée, d'abord dans le cas où les degrés de liberté de couleur sont négligés, puis dans le cas où ils sont pris en compte. Le rôle des termes d'ordre supérieur, introduits au début du chapitre, dans la conservation de la positivité est clairement mis en lumière. Il est également remarqué qu'il est possible de satisfaire cette propriété à partir d'un ensemble minimal de termes, à partir duquel on peut obtenir les termes manquants en redéfinissant la partie imaginaire W du potentiel complexe.

Cette observation est particulièrement intéressante et utile, car les équations obtenues au début du chapitres font intervenir des dérivées d'ordre 3 et 4 de cette partie imaginaire W. Ces dérivées sont en réalité divergentes, ce qui pose un problème majeur. Une stratégie est alors proposée, qui est dans un premier temps d' absorber ces termes problématiques en redéfinissant la partie imaginaire du potentiel, ce qui amène à ne garder que l'ensemble minimal de termes garantissant la conservation de la positivité. Plusieurs prescriptions sont possibles pour cette redéfinition, mais une en particulier permet d'éliminer complètement les divergences:

$$\tilde{W}(\mathbf{r}) \equiv -\int d^3\mathbf{q} \frac{\rho(\mathbf{q})}{\left(1+\frac{\hbar^2\|\mathbf{q}\|^2}{8MT}\right)^2}\left(e^{i\mathbf{q}\cdot\mathbf{r}}-1\right).$$

où $\mathbf{r}$ est la distance entre le quark et l'antiquark de la paire, $M$ la masse du quark considéré, $T$ la température du milieu et $\rho$ est la densité spectrale de la partie imaginaire du potentiel. Liberées de toute divergence et satisfaisant les propriétés d'une équation de Lindblad, ces équations peuvent maintenant être résolues numériquement.

Le cinquième chapitre, intitulé "Implémentation numérique", commence par présenter les équations maîtresses dans le cas unidimensionnel, qui seront ensuite résolues numériquement. Le choix d'une résolution en une dimension permet de réduire le coût de calcul tout en permettant d'explorer la dynamique d'une paire

quark-antiquark et d'étudier la validité d'un traitement semi-classique.

Un nouveau potentiel est ensuite présenté, développé spécifiquement pour une étude unidimensionnelle. Ce potentiel est basé sur un potentiel en trois dimensions [80], lui-même basé sur des résultats de QCD sur réseau. Le potentiel présenté vise à reproduire les largeurs de désintégrations des états propres charmonium et bottomonium ainsi que leurs masses, qui dépendent de la température. Deux paramétrisations des parties réelle et imaginaire du potentiel sont développées, chacune correspondant à un système (charmonia ou bottomonia). Ce potentiel est présenté en figure B.2 dans le cas des bottomonia.

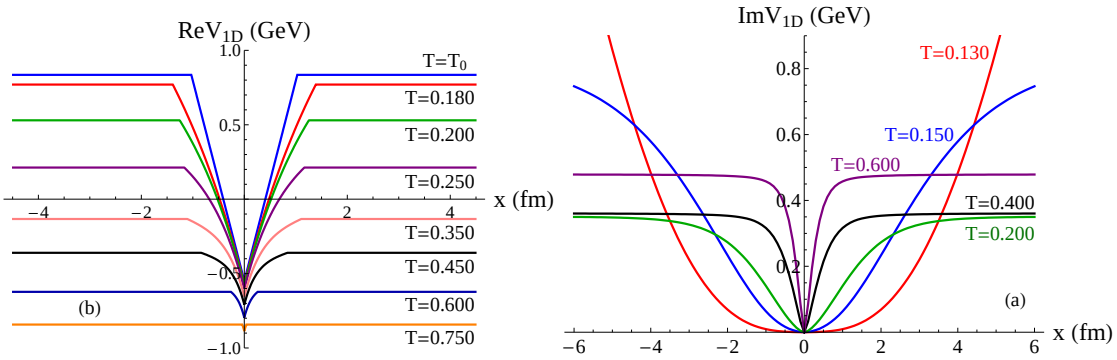


FIGURE B.2 – *Gauche:* Partie réelle du potentiel à une dimension pour les bottomonia. *Droite:* Partie imaginaire du potentiel à une dimension pour les bottomonia.

La méthode numérique utilisée est ensuite présentée en détail. Une méthode implicite, la méthode de Crank-Nicolson, a été retenue car le problème n'était pas traitable à l'aide de méthodes explicites comme la méthode de Runge-Kutta par exemple. Le test de la conservation de l'unitarité de l'opérateur densité est ensuite présenté. Une déviation est trouvée, qui est la conséquence de la conservation non locale de l'unitarité, comme montré dans le quatrième chapitre. Afin de déterminer les paramètres numériques (la taille de la grille sur laquelle le problème est discrétisé, le pas spatial et le pas temporel), le critère retenu est de minimiser la déviation obtenue. Les paramètres ainsi retenus sont une grille bi-dimensionnelle de taille 20 fm $\times$ 20 fm, avec un pas spatial de 0.04 fm et un pas temporel de 0.1 fm/c.

Pour terminer ce chapitre, la conservation de la positivité est prouvée en vérifiant que toutes les valeurs propres de l'opérateur densité restent positives ou nulles à la fin de l'évolution (fixée à 20 fm/c). Une rapide analyse de la stabilité de la

méthode numérique est ensuite présentée, montrant une stabilité jusqu'à 50 fm/c a minima (pour comparaison la limite de temps qui est utilisée dans le sixième chapitre est 20 fm/c).

Enfin, dans le sixième et dernier chapitre, intitulé "Dynamique des quarkonia dans le Plasma de Quarks et de Gluons", les équations maîtresses quantiques présentées au début du chapitre cinq sont résolues et appliquées au cas du système charmonium. Deux scénarios pour le milieu sont considérés: d'abord un PQG dont la température est constante dans le temps puis un PQG se refroidissant progressivement.

Une comparaison entre le cas où les degrés de liberté de couleur sont pris en compte et le cas où ils ne le sont pas est présentée. En s'intéressant à l'évolution des poids de chacun des trois premiers états propres du potentiel au cours du temps, l'importance des degrés de liberté de couleur apparaît nettement. La figure B.3 montre que sans les degrés de liberté de couleur, les poids sont clairement surestimés.

Le chapitre se poursuit avec l'analayse de l'évolution de l'opérateur densité singulet $\mathcal{D}_s$ au cours du temps, présenté en figure B.4. On observe clairement la délocalisation de l'état initial, un état singulet type 1S (au sens de la notation spectroscopique), le long de la diagonale $s = s'$, où $s$ est la distance relative entre le quark et l'antiquark et $s'$ la variable conjuguée. Deux composantes sont observables à 20 fm/c: un reliquat de l'état initial au centre ainsi qu'une composante compatible avec un comportement semi-classique aux bords de cette diagonale.

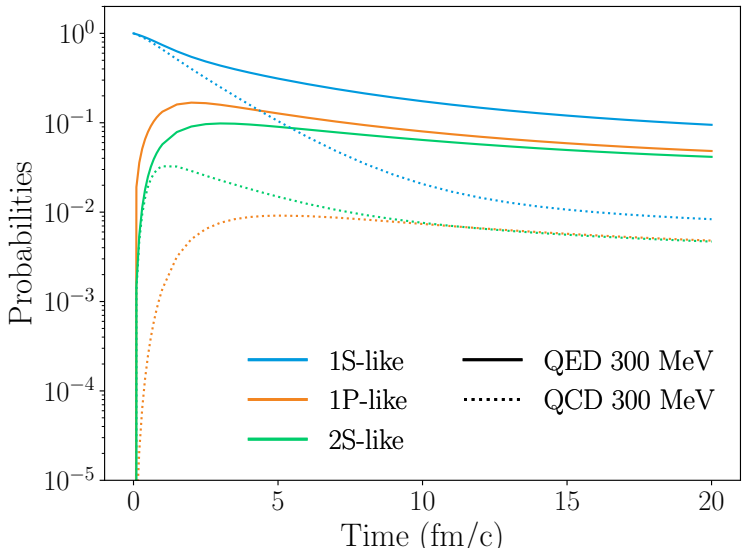


FIGURE B.3 – Evolution au cours du temps des poids des trois premiers états propres du vide pour T = 300 MeV dans le cas sans (lignes pleines) et avec degrés de liberté de couleur (lignes pointillées)

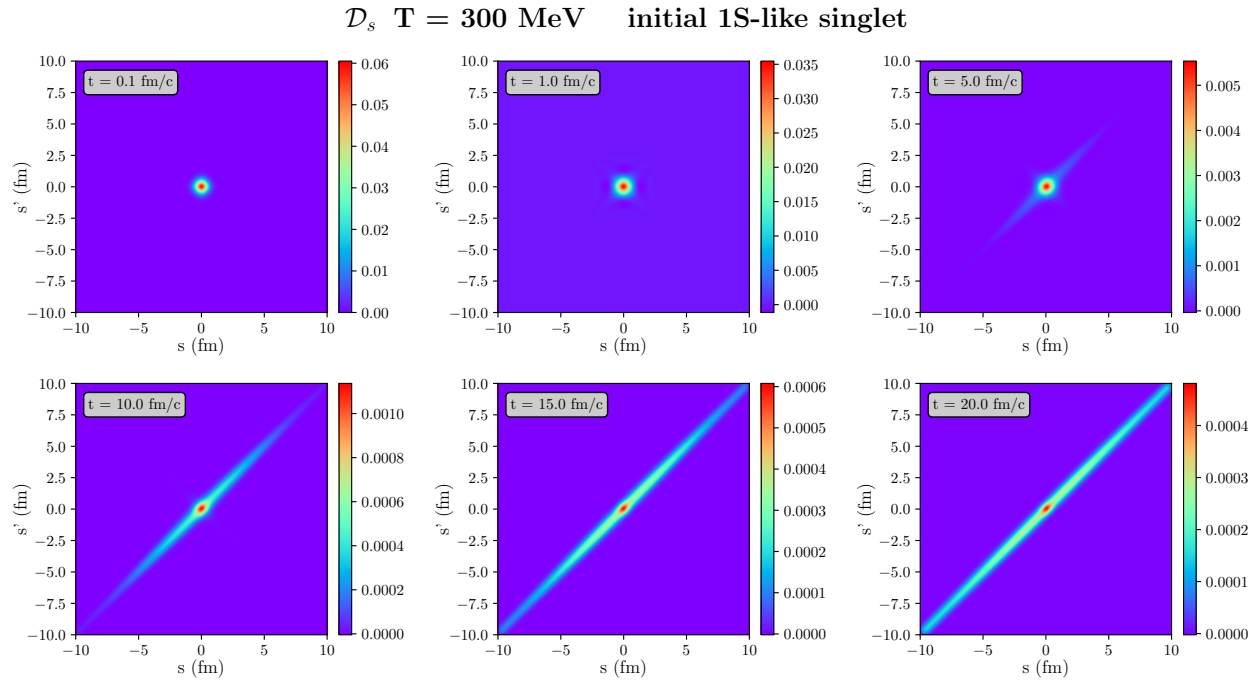


FIGURE B.4 – Evolution de l'opérateur densité singulet $\mathcal{D}_s$ au cours du temps. De haut en bas et de gauche à droite: 0.1, 1, 5, 10, 15 et 20 fm/c

Afin d'analyser la nature de cette dernière composante, la transformée de Wigner $f(r,p)$ de l'opérateur densité est calculée pour différentes valeurs de $r = \frac{s+s'}{2}$ à différents temps. Pour chacune des distributions obtenues, l'impulsion carrée moyenne $\sqrt{\langle p^2 \rangle}(r)$ est représentée sur la figure B.5.

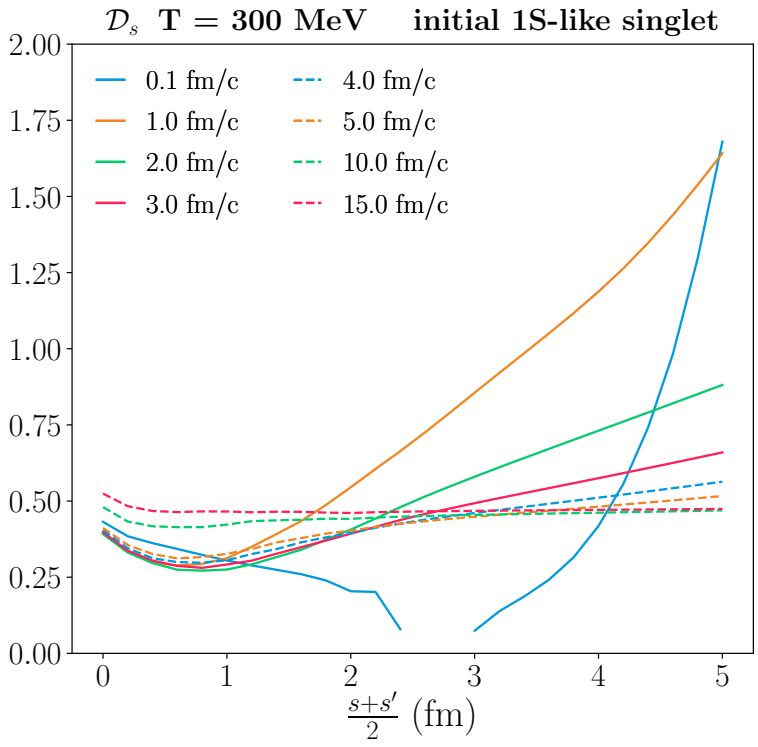


FIGURE B.5 – Evolution de l'impulsion carrée moyenne $\sqrt{\langle p^2 \rangle}$ au cours du temps pour différentes valeurs de $\frac{s+s'}{2}$.

La valeur de l'impulsion carrée moyenne converge vers une valeur spécifique à grand temps pour la majorité des valeurs de $\frac{s+s'}{2}$,ce qui semble indiquer que le système a atteint la thermalisation. Cependant, pour les très petites valeurs de $\frac{s+s'}{2}$ (entre 0 et 1 fm), cette valeur n'est pas atteinte. Cela peut indiquer que le potentiel V liant le quark et l'antiquark de la paire joue toujours un rôle.

Cette analyse est reproduite pour un état initial plus réaliste, où cette fois-ci un état octet (donc une paire non liée) type P est préparé. A nouveau l'évolution de l'opérateur densité singulet $\mathcal{D}_s$ au cours du temps est analysée, ainsi que la distribution de l'impulsion carrée moyenne au cours du temps et en fonction de $\frac{s+s'}{2}$. Les conclusions dans cette configuration sont les mêmes que pour la configuration

précédente, indiquant que le système atteint un état asymptotique commun à toutes les conditions initiales.

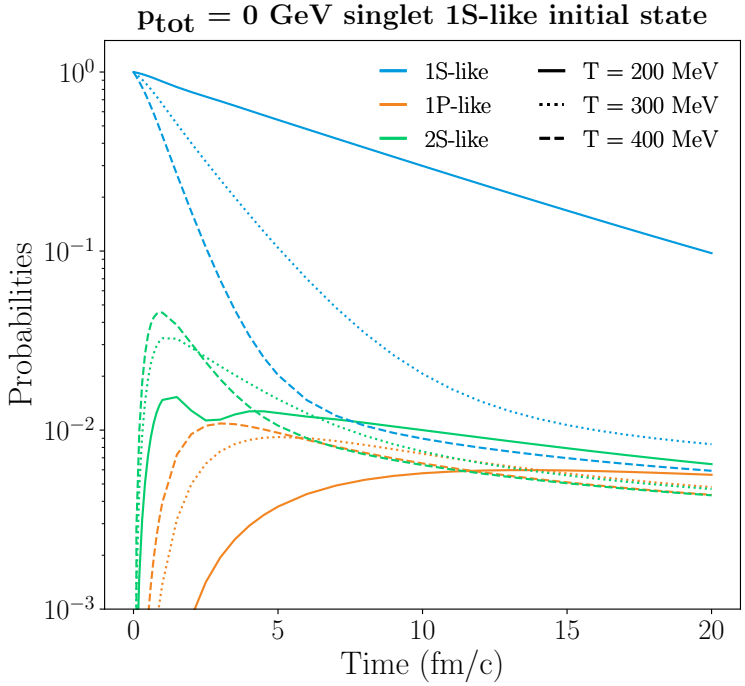


FIGURE B.6 – Evolution au cours du temps des poids des trois premiers états propres du vide pour un état initial singulet type 1S, pour une température T = 200 (lignes pleines), 300 (lignes pointillées) et 400 MeV (lignes discontinues)

L'évolution des poids des trois premiers états propres du vide est ensuite analysée, pour un PQG à une température T = 200,300 et 400 MeV et un état initial singulet type 1S. La figure B.6 présente cette évolution, caractérisée par une phase transitoire entre 0 et 5 fm/c, correspondant à un équilibrage des différentes populations et une phase de décroissance. Sous l'effet du milieu, les états excités sont peuplés avant de décroître. Plus la température du milieu est grande, moins le poids de l'état type 1S est grand à 20 fm/c, ce qui est attendu car les effets du milieu sont plus importants à haute température. La comparaison avec un état initial octet type P montre à nouveau que le même état asymptotique semble être atteint (voir figure B.7).

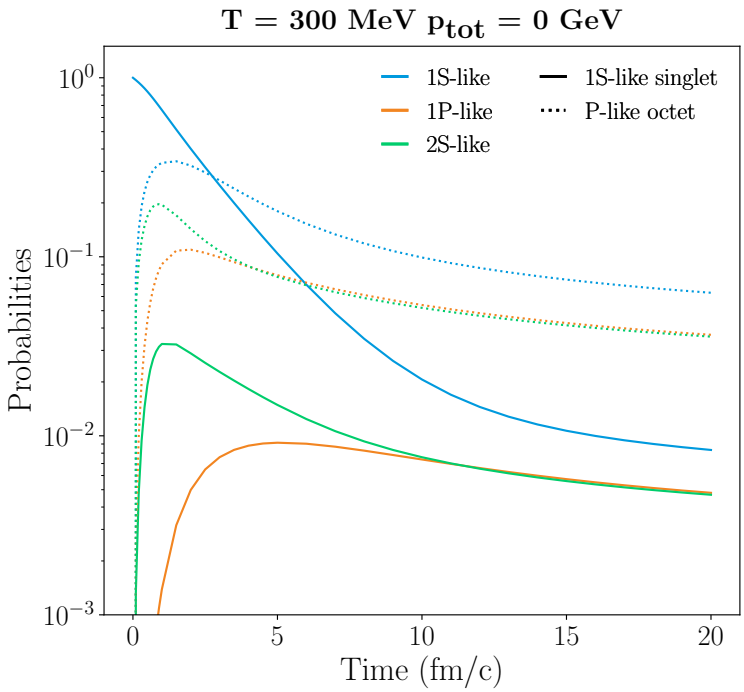


FIGURE B.7 – Evolution au cours du temps des poids des trois premiers états propres du vide pour une température T = 300 MeV pour un état initial singulet type 1S (lignes pleines) et un état initial octet type P (lignes pointillées).

Enfin, le cas d'un PQG se refroidissant au cours du temps est étudié. La figure B.8 permet d'observer un comportement additionnel sur l'évolution des populations d'états. A grand temps, le poids de l'état type 1S augmente, ce qui est dû au refroidissement progressif du milieu, qui permet une liaison plus facile de paires charm-anticharm. Cet effet n'était pas présent dans le cas où la température du PQG était fixe, illustrant la nécessité d'avoir une description réaliste du milieu. L'analyse de l'opérateur densité et de sa distribution de Wigner est la même que dans le cas à température fixe, avec une évolution cependant plus rapide, dûe à la température initiale plus élevée.

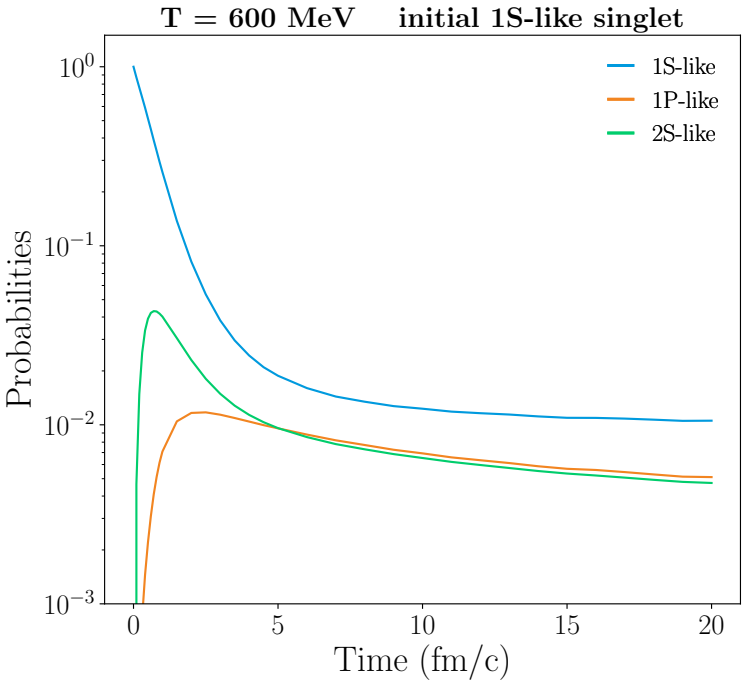


FIGURE B.8 – Evolution au cours du temps des poids des trois premiers états propres du vide pour une température initiale $T_0$ = 600 MeV pour un état initial singulet type 1S

Le manuscrit se conclut avec un récapitulatif des travaux réalisés durant cette thèse ainsi que des principaux résultats. L'analyse de la validité d'une approche semi-classique, entammée durant cette thèse, devra être poursuivie, car une telle approche permettrait d'accéder au traitement de multiples paires charm-anticharm. Des perspectives sont également discutées, notamment, l'importance d'avoir un formalisme permettant de traiter de nombreuses paires dans le milieu à l'aube du run3 du LHC est soulignée, ainsi que la nécessité d'avoir une description réaliste du milieu.

# Bibliography


[1] T. Matsui and H. Satz. "$J/\Psi$ suppression by quark-gluon plasma formation". *Phys. Lett. B* 178 (1986), 416–422.

[2] J.P. Blaizot and M. Escobedo. "Quantum and classical dynamics of heavy quarks in a quark-gluon plasma". *J. High Energ. Phys.* 2018.34 (2018). arXiv: 1711.10812v1.

[3] E. Rutherford. "The Scattering of $\alpha$ and $\beta$ rays by Matter and the Structure of the Atom". *Philosophical Magazine* 21 (1911), 669–688.

[4] J. Chadwick. "The Existance of a Neutron". *Proceedings of the Royal Society of London A :Mathematical, Physical and Engineering Sciences* 136 (1932), 692–708.

[5] M. Gell-Mann. "Symmetries of Baryons and Mesons." *Phys. Rev.* 125 (1962), 1067–1084.

[6] G. Zweig. "An SU(3) model for strong interaction symmetry and its breaking" (1964). Version 1.Technical Report CERN-TH-401, CERN, Geneva.

[7] A. Vauthier. "Mesure des corrélations photon-hadron auprès de lexpérience ALICE au LHC pour létude du plasma de quarks et de gluons". PhD thesis. Université Grenoble-Alpes, 2017.

[8] ALEPH Collaboration. "Determination of the number of light neutrino species". *Phys. Lett. B* 231 (1989), 519–529.

[9] O. W. Greenberg. "Spin and Unitary Spin Independence in a Paraquark Model of Baryons and Mesons". *Phys. Rev. Lett.* 13 (1964), 598–602.

[10] CMS Collaboration. "Observation of a new boson at a mass of 125 GeV with the CMS experiment at the LHC". *Phys. Lett. B* 716 (2012), 30–61. arXiv: 1207.7235v2.

[11] ATLAS Collaboration. "Observation of a new particle in the search for the Standard Model Higgs boson with the ATLAS detector at the LHC". *Phys. Lett. B* 716 (2012), 1–29. arXiv: 1207.7214v2.

[12] B. Pontecorvo. "Neutrino Experiments and the Problem of Conservation of Leptonic Charge". *Sov. Phys. JETP* 26 (1698), 984.

[13] B. Pontecorvo. "Mesonium and Antimesonium". *Sov. Phys. JETP* 6 (1658), 429.

[14] M.E. Peskin and D.V. Schroeder. *An introduction to quantum field theory*. Addison-Wesley Publishing Company, 1995.

[15] C. N. Yang and R. L. Mills. "Conservation of Isotopic Spin and Isotopic Gauge Invariance". *Phys. Rev.* 96 (1954), 191–195.

[16] F. Halzen and A. Martin. *Quarks and Leptons : An introductory course in modern particle physics*. John Wiley and Sons, 1984.

[17] G. Dissertori et al. *Quantum Chromodynamics : High Energy Experiments and Theory*. Clarendon Press, 2003.

[18] R. Keith Ellis et al. "QCD and collider physics". *Camb. Monogr. Part. Phys. Nucl. Phys. Cosmol.Phys. Rev. D* 8 (1996), 1–435.

[19] R. Katz. "A quantum approach to dynamical quarkonia suppression in high energy heavy ion collisions". PhD thesis. Ecole des Mines de Nantes, 2015.

[20] S. Bethke. "Experimental tests of asymptotic freedom". *Prog. Part. Nucl. Phys.* 58 (2007), 351–386. arXiv: hep-ex/0606035v2.

[21] B. Andersson, G. Gustafson, G. Ingelman, and T. Sjöstrand. "Parton fragmentation and string dynamics". *Phys. Rept* 97 (1983), 31–145.

[22] M. N. Chernodub. "Background magnetic field stabilizes QCD string against breaking" (2010). arXiv: 1001.0570.

[23] K. G. Wilson. "Confinement of quarks". *Phys. Rev. D* 10 (1974), 2445–2459.

[24] R. P. Feynman and A. R. Hibbs. *Quantum mechanics and path integrals*. McGraw-Hill, 1965.

[25] S. L. Olsen, T. Skwarnicki, and D. Zieminska. "Nonstandard heavy mesons and baryons: Experimental evidence". *Rev. Mod. Phys.* 90 (2018), 015003. arXiv: 1708.04012v1.

[26] H. Fritzsch. "Producing heavy quark flavors in hadronic collisions  A test of quantum chromodynamics". *Phys. Lett. B* 67 (1977), 217–221.

[27] F. Halzen. "CVC for gluons and hadroproduction of quark flavours". *Phys. Lett. B* 69 (1977), 105–108.

[28] J.F. Amundson, O.J.P. Éboli, E.M. Gregores, and F. Halzen. "Colorless states in perturbative QCD: Charmonium and rapidity gaps". *Phys. Lett. B* 372 (1996), 127–132. arXiv: 9512248v1.

[29] R. Baier and R. Rückl. "Hadronic collisions: A quarkonium factory". *Z. Phys. C - Particles and Fields* 19 (1983), 251–266.

[30] B. Guberina, J.H. Kühn, R.D. Peccei, and R. Rückl. "Rare decays of the Z0". *Nucl. Phys. B* 174 (1980), 317–334.

[31] E. Braaten and S. Fleming. "Color-Octet Fragmentation and the $\psi'$ Surplus at the Fermilab Tevatron". *Phys. Rev. Lett.* 74 (1995), 3327–3330.

[32] G. T. Bodwin, E. Braaten, and G. P. Lepage. "Rigorous QCD analysis of inclusive annihilation and production of heavy quarkonium". *Phys. Rev. D* 51 (1995), 1125–1171. Erratum: Phys. Rev. D 51, 1125 (1995).

[33] A. Andronic et al. "Heavy-flavour and quarkonium production in the LHC era: from protonproton to heavy-ion collisions". *Eur. Phys. J. C* 76 (2016), 107. arXiv: 1506.03981v2.

[34] M. G. Alford, A. Schmitt, K. Rajagopal, and T. Schäfer. "Color superconductivity in dense quark matter". *Rev. Mod. Phys.* 80 (2008), 1455–1515. arXiv: 0709.4635v2.

[35] E. V. Shuryak. "Quantum chromodynamics and the theory of superdense matter". *Phys. Rept.* 61 (1980), 71–158.

[36] A. Bazavov et al. "Chiral crossover in QCD at zero and non-zero chemical potentials". *Phys. Lett. B* 795 (2019), 15–21.

[37] J.D. Bjorken. "Highly relativistic nucleus-nucleus collisions: The central rapidity region". *Phys. Rev. D* 27 (1983), 140–151.

[38] M. L. Miller, K. Reygers, S. J. Sander, and P. Steinberg. "Glauber Modeling in High Energy Nuclear Collisions". *Ann.Rev.Nucl.Part.Sci* 57 (2007), 205–243. arXiv: nucl-ex/0701025v1.

[39] H-J. Drescher and Y. Nara. "Effects of fluctuations on the initial eccentricity from the color glass condensate in heavy ion collisions". *Phys. Rev. C* 75 (2007), 034905. arXiv: nucl-th/0611017v2.

[40] F. Gelis, E. Iancu, J. Jalilian-Marian, and R. Venugopalan. "The Color Glass Condensate". *Ann.Rev.Nucl.Part.Sci.* 60 (2010), 463–489. arXiv: 1002.0333v1.

[41] B. Schenke, P. Tribedy, and R. Venugopalan. "Fluctuating Glasma Initial Conditions and Flow in Heavy Ion Collisions". *Phys. Rev. Lett.* 108 (2012), 252301. arXiv: 1202.6646v2.

[42] S.A. Bass et al. "Microscopic models for ultrarelativistic heavy ion collisions". *Prog. Part. Nucl. Phys.* 41 (1998), 255–369. arXiv: nucl-th/9803035v2.

[43] K. Werner, I. Karpenko, M. Bleicher, T. Pierog, and S. Porteboeuf-Houssais. "Jets, bulk matter, and their interaction in heavy ion collisions at several TeV". *Phys. Rev. C* 85 (2012), 064907. arXiv: 1203.5704v2.

[44] C. Gale, S. Jeon, and B. Schenke. "Hydrodynamic Modeling of Heavy-Ion Collisions". *Int. J. of Mod. Phys. A* 28 (2013), 1340011. arXiv: 1301.5893v1.

[45] P. F. Kolb and U. Heinz. "Hydrodynamic description of ultrarelativistic heavy-ion collisions" (2003). arXiv: nucl-th/0305084v2.

[46] B. Hippolyte. "Production de hadrons légers et Plasma de Quarks et de Gluons au LHC" (2005).

[47] J. Rafelski and B. Müller. "Strangeness Production in the Quark-Gluon Plasma". *Phys. Rev. Lett.* 48 (1982), 1066–1069. Erratum: Phys. Rev. Lett. **56, 2334 (1986)**.

[48] P Koch, B Müller, and J Rafelski. "Strangeness in relativistic heavy ion collisions". *Phys. Rept.* 142 (1986), 167–262.

[49] J. Faivre. "Reconstruction et étude des baryons multi-étranges dans les collisions d'ions lourds ultra-relativistes à $\sqrt{s_{NN}}$ = 200 GeV avec l'expérience STAR au RHIC". PhD thesis. Université Louis Pasteur - Strasbourg I, 2004.

[50] NA57 Collaboration. "Results on hyperon production from the NA57 experiment". *Acta. Phys. Hung. A* 22 (2005), 113–120. arXiv: nucl-ex/0404030v1.

[51] K. Kajantie and H. I. Miettinen. "Muon pair production in very high energy nucleus- nucleus collisions". *Zeitschrift für Physik C Particles and Fields* 14(4) (1982), 357–362.

[52] NA54 Collaboration. "Recent results from Pb-Au collisions at 158 GeV/c per nucleon obtained with the CERES spectrometer". *Nucl. Phys. A* 661 (1999), 23–32. arXiv: nucl-ex/9910015v1.

[53] PHENIX Collaboration. "Enhanced Production of Direct Photons in Au + Au Collisions at $\sqrt{s_{NN}} = 200$ GeV and Implications for the Initial Temperature". *Phys. Rev. Lett.* 104 (2010), 132301. arXiv: 0804.4168v2.

[54] ATLAS Collaboration. "Observation of Long-Range Elliptic Azimuthal Anisotropies in $\sqrt{s} = 13$ and 2.76 TeV $pp$ Collisions with the ATLAS Detector". *Phys. Rev. Lett.* 116 (2016), 172301.

[55] PHENIX Collaboration. "Scaling Properties of Azimuthal Anisotropy in Au + Au and Cu + Cu Collisions at $\sqrt{s_{\mathrm{NN}}} = 200$ GeV". *Phys. Rev. Lett.* 98 (2007), 162301.

[56] CMS Collaboration. "First measurement of large area jet transverse momentum spectra in heavy-ion collisions". *J. High. Energ. Phys.* 2021.284 (2021). arXiv: arXiv:2102.13080v2.

[57] J. Faivre. "Étude du Plasma de Quarks et de Gluons au LHC : Mesure des corrélations photon-hadrons à laide du calorimètre de lexpérience ALICE". Habilitation à diriger des recherches, Université Grenoble-Alpes (2016).

[58] Y.L. Dokshitzer. "Calculation of the structure functions for deep inelastic scattering and $e^+$ $e^-$ annihilation by perturbation theory in quantum chromodynamics". *Sov. Phys. JETP* 46 (1977), 641–653.

[59] V.N. Gribov and L.N. Lipatov. "Deep inelastic $e - p$ scattering in perturbation theory". *Sov. J. Nucl. Phys.* 15 (1972), 438–450.

[60] G. Altarelli and G. Parisi. "Asymptotic freedom in parton language". *Nucl. Phys. B.* 126 (1977), 298–318.

[61] R. Vogt. "Cold nuclear matter effects on $J/\psi$ and Υ production at energies available at the CERN Large Hadron Collider (LHC)". *Phys. Rev. C* 81 (2010), 044903. arXiv: 1003.3497v1.

[62] I. Balitsky. "Operator expansion for high-energy scattering". *Nucl. Phys. B* 463 (1996), 99–157. arXiv: hep-ph/9509348v1.

[63] Y. V. Kovchegov. "Small-$x$ $F_2$ Structure Function of a Nucleus Including Multiple Pomeron Exchanges". *Phys. Rev. D* 60 (1999), 034008. arXiv: hep-ph/9901281v4.

[64] Y. V. Kovchegov. "Unitarization of the BFKL Pomeron on a Nucleus". *Phys. Rev. D* 61 (2000), 074018. arXiv: hep-ph/9905214v3.

[65] J. W. Cronin, H. J. Frisch, M. J. Shochet, J. P. Boymond, P. A. Piroué, and R. L. Sumner. "Production of hadrons at large transverse momentum at 200, 300, and 400 GeV". *Phys. Rev. D* 11 (1975), 3105–3123.

[66] C. Lourenço, R. Vogt, and H. K. Wöhri. "Energy dependence of $J/\psi$ absorption in proton-nucleus collisions". *J. High Energy Phys.* 02 (2009), 014. DOI: https://doi.org/10.1088/1126-6078/2009/02/014. arXiv: 0901.3054v1.

[67] K.J. Eskola, V.J. Kolhinen, and P.V. Ruuskanen. "Scale evolution of nuclear parton distributions". *Nucl. Phys. B* 535 (1998), 351–371. arXiv: hep-ph/9802350v1.

[68] K.J. Eskola, V.J. Kolhinen, and C.A. Salgado. "The scale dependent nuclear effects in parton distributions for practical applications". *Eur. Phys. J. C* 9 (1999), 61–68. arXiv: hep-ph/9807297v1.

[69] J. Pumplin, D. R. Stump, J. Huston, H.-L. Lai, P. Nadolsky, and W.-K. Tung. "New Generation of Parton Distributions with Uncertainties from Global QCD Analysis". *J. High Energy Phys.* 07 (2002), 012. arXiv: hep-ph/0201195v3.

[70] D. Stump, J. Huston, J. Pumplin, W.-K. Tung, H.-L. Lai, S. Kuhlmann, and J. F. Owens. "Inclusive jet production, parton distributions, and the search for new physics". *J. High Energy Phys.* 10 (2003), 046. arXiv: hep-ph/0303013v1.

[71] F. Arleo, S. Peigné, and T. Sami. "Revisiting scaling properties of medium-induced gluon radiation". *Phys. Rev. D* 83 (2011), 114036. arXiv: 1006.0818v2.

[72] F. Arleo and S. Peigné. "Heavy-quarkonium suppression in p-A collisions from parton energy loss in cold QCD matter". *J. High Energy Phys.* 2013 (2013), 122. arXiv: 1212.0434v2.

[73] F. Arleo, R. Kolevatov, S. Peigné, and M. Rustamova. "Centrality and $\mathbf{p}_{\mathrm{T}}$ dependence of $J/\Upsilon$ suppression in proton-nucleus collisions from parton energy loss". *J. High Energy Phys.* 2013 (2013), 155. arXiv: 1304.0901v1.

[74] F. Arleo, R. Kolevatov, and S. Peigné. "Coherent medium-induced gluon radiation in hard forward $1 \to 1$ partonic processes". *Phys. Rev. D* 93 (2016), 014006. arXiv: 1402.1671v2.

[75] S. Peigné and R. Kolevatov. "On the process-dependence of coherent medium-induced gluon radiation" (2014). arXiv: 1405.4241v1.

[76] F. Arleo and S. Peigné. "Quarkonium suppression in heavy-ion collisions from coherent energy loss in cold nuclear matter". *J. High Energy Phys.* 2014 (2014), 73. arXiv: 1407.5054v1.

[77] E. Eichten, K. Gottfried, T. Kinoshita, K. D. Lane, and T.-M Yan. "Charmonium: The model". *Phys. Rev. D* 17 (1978), 3090–3117. ;21 (1980) 313(E).

[78] A. Mócsy and P. Petreczky. "Can quarkonia survive deconfinement?" *Phys. Rev. D* 77 (2008), 014501. arXiv: 0705.2559v2.

[79] S. Necco and R. Sommer. "The $N_f = 0$ heavy quark potential from short to intermediate distances". *Nucl. Phys. B* 622 (2002), 328–346. arXiv: hep-lat/0108008v1.

[80] D. Lafferty and A. Rothkopf. "Improved Gauss law model and in-medium heavy quarkonium at finite density and velocity". *Phys. Rev. D* 101 (5 2020). arXiv: 1906.00035v4.

[81] G. Bhanot and M. E. Peskin. "Short-distance analysis for heavy-quark systems: (II). Applications". *Nucl. Phys. B* 156 (1979), 391–416.

[82] L. Grandchamp and R. Rapp. "Thermal versus direct $J/\Psi$ production in ultrarelativistic heavy-ion collisions". *Phys. Lett. B* 523 (2001), 60–66. arXiv: hep-ph/0103124v3.

[83] STAR Collaboration. "Y production in U + U collisions at $\sqrt{s_{NN}} = 193$ GeV measured with the STAR experiment". *Phys. Rev. C* 94 (2016), 064904. arXiv: 1608.06487v2.

[84] CMS Collaboration. "Suppression of Y(1S), Y(2S), and Y(3S) quarkonium states in PbPb collisions at $\sqrt{s_{NN}}$ =2.76TeV". *Phys. Lett. B* 770 (2017), 357–379. arXiv: 1611.01510v2.

[85] ALICE Collaboration. "Y production and nuclear modification at forward rapidity in PbPb collisions at $\sqrt{s_{NN}}$ =5.02TeV". *Phys. Lett. B* (2021), 136579. arXiv: 2011.05758v1.

[86] ALICE Collaboration. "Y suppression at forward rapidity in PbPb collisions at $\sqrt{s_{NN}}$ =5.02TeV". *Phys. Lett. B* 790 (2019), 89–101. arXiv: 1805.04387v2.

[87] PHENIX Collaboration. "$J/\psi$ suppression at forward rapidity in Au + Au collisions at $\sqrt{s_{NN}} = 200$ GeV". *Phys. Rev. C* 84 (2011), 054912. arXiv: 1103.6269v1.

[88] CMS Collaboration. "Measurement of prompt and nonprompt charmonium suppression in PbPb collisions at 5.02 TeV". *Eur. Phys. J. C* 78 (2018), 509. arXiv: 1712.08959v2.

[89] ALICE Collaboration. "Centrality and transverse momentum dependence of inclusive $J/\Psi$ production at midrapidity in PbPb collisions at $\sqrt{s_{NN}}$ =5.02 TeV". *Phys. Lett. B* 805 (2020), 135434. arXiv: 1910.14404v2.

[90] W. M. Alberico, A. Beraudo, A. De Pace, and A. Molinari. "Heavy quark bound states above $T_c$". *Phys. Rev. D* 72 (2005), 114011. arXiv: hep-ph/0507084v1.

[91] F. Riek and R. Rapp. "Quarkonia and heavy-quark relaxation times in the quark-gluon plasma". *Phys. Rev. C* 82 (2010), 035201. arXiv: 1005.0769v1.

[92] A. Jakovác, P. Petreczky, K. Petrov, and A. Velytsky. "Quarkonium correlators and spectral functions at zero and finite temperature". *Phys. Rev. D* 75 (2007), 014506. arXiv: hep-lat/0611017v1.

[93] G. Aarts, C. Allton, M.B. Oktay, M. Peardon, and J-I. Skullerud. "Charmonium at high temperature in two-flavor QCD". *Phys. Rev. D* 76 (2007), 094513. arXiv: 0705.2198v2.

[94] O. Kaczmarek Y. Burnier and A. Rothkopf. "Quarkonium at finite temperature: towards realistic phenomenology from first principles". *J. High Energy Phys.* 2015 (2015), 1–34. arXiv: 1509.07366v2.

[95] H. Satz. "The Quark-Gluon Plasma A Short Introduction". *Nuclear Physics A* 862-863 (2011), 4–12. arXiv: 1101.3937v1.

[96] A. Capella, A. Kaidalov, A. Kouider Akil, and C. Gerschel. "$J/\Psi$ and $\Psi'$ suppression in heavy ion collisions". *Phys. Lett. B* 393 (1997), 431–436. arXiv: hep-ph/9607265v1.

[97] N. Armesto and A. Capella. "A quantitative reanalysis of charmonium suppression in nuclear collisions". *Phys. Lett. B* 430 (1998), 23–31. arXiv: hep-ph/9705275v3.

[98] N. Armesto, A. Capella, and E. G. Ferreiro. "Charmonium suppression in lead-lead collisions: Is there a break in the $J/\psi$ cross section?" *Phys. Rev. C* 59 (1999), 395–404. arXiv: hep-ph/9807258v3.

[99] A. Capella, E. G. Ferreiro, and A. B. Kaidalov. "Nonsaturation of the $J/\Psi$ Suppression at Large Transverse Energy in the Comovers Approach". *Phys. Rev. Lett.* 85 (2000), 2080–2083. arXiv: hep-ph/0002300v1.

[100] A. Capella and E. G. Ferreiro. "$J/\psi$ suppression at $\sqrt{\mathbf{s}} = 200$ GeV in the comovers interaction model". *Eur. Phys. J. C* 42 (2005), 419–424. arXiv: hep-ph/0505032v1.

[101] A. Capella, L. Bravina, E. G. Ferreiro, A. B. Kaidalov, and E. Zabrodin. "Charmonium dissociation and recombination at RHIC and LHC". *Eur. Phys. J. C* 58 (2008), 437–444. arXiv: 0712.4331v1.

[102] E.G. Ferreiro. "Charmonium dissociation and recombination at LHC: Revisiting comovers". *Phys. Lett. B* 731 (2014), 57–63. arXiv: 1210.3209v2.

[103] E.G. Ferreiro. "Excited charmonium suppression in proton-nucleus collisions as a consequence of comovers" (2014). arXiv: 1411.0549v2.

[104] E. G. Ferreiro and J. P. Lansberg. "Is bottomonium suppression in proton-nucleus and nucleus-nucleus collisions at LHC energies due to the same effects?." *J. High Energy Phys.* 2018.94 (2018). arXiv: 1804.04474v1.

[105] CMS Collaboration. "Suppression of non-prompt $J/\Psi$, prompt $J/\Psi$, and $v(1S)$ in PbPb collisions at $\sqrt{s_{NN}}$ =2.76 TeV". *J. High Energy Phys.* 2012 (2012), 63. arXiv: 1201.5069v2.

[106] C. Mironov (for the CMS Collaboration). "Overview of results on heavy flavour and quarkonia from the CMS collaboration". *Nucl. Phys. A* 904-905 (2013), 194c–201c.

[107] R. Arnaldi (for the ALICE Collaboration). "$J/\Psi$ and $\Psi(2S)$ production in PbPb collisions with the ALICE Muon Spectrometer at the LHC". *Nuclear Physics A* 904-905 (2013), 595c–598c. arXiv: 1211.2578v1.

[108] P. Braun-Munzinger, J. Stachel, J.P. Wessels, and N.Xu. "Thermal equilibration and expansion in nucleus-nucleus collisions at the AGS". *Phys. Lett. B* 344 (1995), 43–48. arXiv: nucl-th/9410026v2.

[109] P. Braun-Munzinger, J. Stachel, J.P. Wessels, and N.Xu. "Thermal and hadrochemical equilibration in nucleus-nucleus collisions at the SPS". *Phys. Lett. B* 365 (1996), 1–6. arXiv: nucl-th/9508020v2.

[110] P. Braun-Munzinger, I. Heppe, and J. Stachel. "Chemical equilibration in Pb+Pb collisions at the SPS". *Phys. Lett. B* 465 (1999), 15–20. arXiv: nucl-th/9903010v2.

[111] P. Braun-Munzinger, D. Magestro, K. Redlich, and J. Stachel. "Hadron production in AuAu collisions at RHIC". *Phys. Lett. B* 518 (2001), 41–46. arXiv: hep-ph/0105229v2.

[112] P. Braun-Munzinger and J. Stachel. "(Non)thermal aspects of charmonium production and a new look at $J/\Psi$ suppression". *Phys. Lett. B* 490 (2000), 196–202. arXiv: nucl-th/0007059v2.

[113] P. Braun-Munzinger and J. Stachel. "On charm production near the phase boundary". *Nucl. Phys. A* 690 (2001), 119–126. arXiv: nucl-th/0012064v2.

[114] P.Braun-Munzinger and J. Stachel. *Charmonium from Statistical Hadronization of Heavy Quarks – a Probe for Deconfinement in the Quark-Gluon Plasma: Datasheet from Landolt-Börnstein - Group I Elementary Particles, Nuclei and Atoms ů Volume 23: "Relativistic Heavy Ion Physics"*. Ed. by R. Stock. arXiv: 0901.2500v1.

[115] ALICE Collaboration et al. "ALICE: Physics Performance Report, Volume II". *J. Phys. G* 32 (2006), 1295–2040.

[116] PHENIX Collaboration. "Centrality Dependence of Charm Production from a Measurement of Single Electrons in Au + Au Collisions at $\sqrt{s_{NN}} = 200$ GeV". *Phys. Rev. Lett.* 94 (2005), 082301. arXiv: nucl-ex/0409028v1.

[117] ALICE Collaboration. "$J/\Psi$ suppression at forward rapidity in PbPb collisions at $\sqrt{s_{NN}}$ =5.02 TeV". *Phys. Lett. B* 766 (2017), 212–224. arXiv: 1606.08197v2.

[118] A. Andronic, P. Braun-Munzinger, M.K. Köhler, K. Redlich, and J. Stachel. "Transverse momentum distributions of charmonium states with the statistical hadronization model". *Phys. Lett. B* 797 (2019), 134836. arXiv: 1901.09200v2.

[119] A. Andronic, P. Braun-Munzinger, K. Redlich, and J. Stachel. "Evidence for charmonium generation at the phase boundary in ultra-relativistic nuclear collisions". *Phys. Lett. B* 652 (2007), 259–261. arXiv: nucl-th/0701079v2.

[120] A. Andronic, P. Braun-Munzinger, K. Redlich, and J. Stachel. "Statistical hadronization of heavy quarks in ultra-relativistic nucleusnucleus collisions". *Nucl. Phys. A* 789 (2007), 334–356. arXiv: nucl-th/0611023v2.

[121] A. Andronic, P. Braun-Munzinger, K. Redlich, and J. Stachel. "Hadron yields in central nucleus-nucleus collisions, the statistical hadronization model and the QCD phase diagram" (2021). arXiv: 2101.05747v1.

[122] A. Andronic, P. Braun-Munzinger, M. K. Köhler, A. Mazeliauskas, K. Redlich, J. Stachel, and V. Vislavicius. "Energy dependence of $J/\psi$ absorption in proton-nucleus collisions". *J. High Energy Phys.* 2021 (2021), 035. arXiv: 2104.12754v2.

[123] STAR Collaboration. "$J/\psi$ production at low $p_T$ in Au + Au and Cu + Cu collisions at $\sqrt{s_{NN}} = 200$ GeV with the STAR detector". *Phys. Rev. C* 90 (2014), 024906. arXiv: 1310.3563v2.

[124] PHENIX Collaboration. "$J/\psi$ Production versus Centrality, Transverse Momentum, and Rapidity in Au + Au Collisions at $\sqrt{s_{NN}} = 200$ GeV". *Phys. Rev. Lett.* 98 (2007), 232301. arXiv: nucl-ex/0611020v1.

[125] ALICE Collaboration. "Centrality, rapidity and transverse momentum dependence of $J/\Psi$ suppression in PbPb collisions at $\sqrt{s_{NN}}$ =2.76 TeV". *Phys. Lett. B* 734 (2014), 314–327. arXiv: 1311.0214v4.

[126] S. Cao and S.A. Bass. "Thermalization of charm quarks in infinite and finite quark-gluon plasma matter". *Phys. Rev. C* 84 (2011), 064902. arXiv: 1108.5101v3.

[127] X. Zhao and R. Rapp. "Charmonium Production at High $\mathbf{p}_{\mathrm{T}}$ at RHIC" (2008). arXiv: 0806.1239v1.

[128] H. van Hees, M. He, and R. Rapp. "Pseudo-critical enhancement of thermal photons in relativistic heavy-ion collisions?" *Nucl. Phys. A* 933 (2015), 256–271. arXiv: 1404.2846v2.

[129] L. Yan, P. Zhuang, and N. Xu. "$J/\psi$ Production in Quark-Gluon Plasma". *Phys. Rev. Lett.* 97 (2006), 232301. arXiv: nucl-th/0608010v2.

[130] Y. Liu, Z. Qu, N. Xu, and P. Zhuang. "$J/\Psi$ transverse momentum distribution in high energy nuclear collisions". *Phys. Lett. B* 678 (2009), 72–76. arXiv: 0901.2757v2.

[131] X. Zhao and R. Rapp. "Medium modifications and production of charmonia at LHC". *Nucl. Phys. A* 859 (2011), 114–125. arXiv: 1102.2194v1.

[132] A. Emerick, X. Zhao, and R. Rapp. "Bottomonia in the Quark-Gluon Plasma and their Production at RHIC and LHC". *Eur. Phys. J. A* 48 (2012), 72. arXiv: 1111.6537v1.

[133] X. Du and R. Rapp. "Y(2S) Production at the LHC". *Journal of Physics: Conference Series* 779 (2017), 012042. arXiv: 1609.04868v1.

[134] X. Du, M. He, and R. Rapp. "Color screening and regeneration of bottomonia in high-energy heavy-ion collisions". *Phys. Rev. C* 96 (2017), 054901. arXiv: 1706.08670v2.

[135] V. Gorini, A. Kossakowski, and E.C.G. Sudarshan. "Completely positive dynamical semigroups of n-level systems". *Journal of Mathematical Physics* 17 (1976), 821–825.

[136] G. Lindblad. "On the generators of quantum dynamical semigroups". *Communications in Mathematical Physics* 48 (1976), 119–130.

[137] Y. Akamatsu. "Quarkonium in Quark-Gluon Plasma: Open Quantum System Approaches Re-examined" (2020). arXiv: 2009.10559v1.

[138] N. Borghini and C. Gombeaud. "Heavy quarkonia in a medium as a quantum dissipative system: Master-equation approach". *Eur. Phys. J. C* 72 (2012). arXiv: 1109.4271.

[139] C. Young and K. Dusling. "Quarkonium above deconfinement as an open quantum system". *Phys. Rev. C* 87 (2013). arXiv: :1001.0935.

[140] A.O. Caldeira and A.J. Leggett. "Path integral approach to quantum Brownian motion". *Physica A: Statistical Mechanics and its Applications* 121.3 (1983), 587–616.

[141] Y. Akamatsu and A. Rothkopf. "Stochastic potential and quantum decoherence of heavy quarkonium in the quark-gluon plasma". *Phys. Rev. D* 85 (2012). arXiv: 1110.1203.

[142] R. Katz and P.B. Gossiaux. "The SchrödingerLangevin equation with and without thermal fluctuations". *Annals of Physics* 368 (2016), 267–295. arXiv: 1504.08087v4.

[143] P.B. Gossiaux and R. Katz. "Upsilon suppression in the SchrödingerLangevin approach". *Nuclear Physics A* 956 (2016), 737–740. arXiv: 1601.01443v1.

[144] Y. Akamatsu. "Real-time quantum dynamics of heavy quark systems at high temperature". *Phys. Rev. D* 87 (2013). arXiv: arXiv:1209.5068.

[145] Y. Akamatsu. "Heavy quark master equations in the Lindblad form at high temperatures". *Phys. Rev. D* 91 (2015). arXiv: 1403.5783.

[146] R.P. Feynman and F.L. Vernon. "The theory of a general quantum system interacting with a linear dissipative system". *Annals of Physics* 24 (1963), 118–173.

[147] S. Kajimoto, Y. Akamatsu, M. Asakawa, and A. Rothkopf. "Quantum dynamical dissociation of quarkonia by wave function decoherence in quark-gluon plasma". *Nuclear Physics A* 982 (2019), 711–714. arXiv: 1705.03365v2.

[148] R. Sharma and A. Tiwari. "Quantum evolution of quarkonia with correlated and uncorrelated noise". *Phys. Rev. D* 101 (2020), 074004. arXiv: 1912.07036v1.

[149] Y. Akamatsu, M. Asakawa, S. Kajimoto, and A. Rothkopf. "Quantum dissipation of a heavy quark from a nonlinear stochastic Schrödinger equation". *J. High Energ. Phys.* 29 (2018). arXiv: 1805.00167v2.

[150] N. Gisin and I. C. Percival. "The quantum-state diffusion model applied to open systems". *Journal of Physics A: Mathematical and General* 25 (1992), 5677–5691.

[151] N. Gisin and I. C. Percival. "Quantum State Diffusion: from Foundations to Applications" (1997). arXiv: 9701024v1.

[152] T. Miura, Y. Akamatsu, M. Asakawa, and A. Rothkopf. "Quantum Brownian motion of a heavy quark pair in the quark-gluon plasma". *Phys. Rev. D* 101 (2020), 034011. arXiv: 1908.06293v2.

[153] O. Ålund, Y. Akamatsu, F.Laurén, T. Miura, J. Nordström, and A. Rothkopf. "Trace preserving quantum dynamics using a novel reparametrization-neutral summation-by-parts difference operator". *Journal of Computational Physics* 425 (2021), 109917. arXiv: 2004.04406v1.

[154] N. Brambilla, A. Pineda, J. Soto, and A. Vairo. "Potential NRQCD: an effective theory for heavy quarkonium". *Nuclear Physics B* 566.1 (2000), 275–310. arXiv: 9907240v2.

[155] N. Brambilla, A. Pineda, J. Soto, and A. Vairo. "Effective-field theories for heavy quarkonium". *Rev. Mod. Phys.* 77 (2005), 1423–1496. arXiv: 0410047v2.

[156] N. Brambilla, M.A. Escobedo, J. Soto, and A. Vairo. "Quarkonium suppression in heavy-ion collisions: An open quantum system approach". *Phys. Rev. D* 96 (2017), 034021. arXiv: 1612.07248v1.

[157] N. Brambilla, M.A. Escobedo, J. Soto, and A. Vairo. "Heavy quarkonium suppression in a fireball". *Phys. Rev. D* 97 (2018), 074009. arXiv: 1711.04515v2.

[158] N. Brambilla, M.A. Escobedo, M. Strickland, A. Vairo, P. Vander Griend, and J.H. Weber. "Bottomonium suppression in an open quantum system using the quantum trajectories method" (2020). arXiv: 2012.01240v1.

[159] J. Dalibard, Y. Castin, and K. Mølmer. "Wave-function approach to dissipative processes in quantum optics". *Phys. Rev. Lett.* 68 (1992), 580–583.

[160] N. Brambilla, M.A. Escobedo, A. Vairo, and P. Vander Griend. "Transport coefficients from in-medium quarkonium dynamics". *Phys. Rev. D* 100 (2019), 054025. arXiv: 1903.08063v2.

[161] H. Ba Omar, M.A. Escobedo, A. Islam, M. Strickland, S. Thapa, P. Vander Griend, and J. H. Weber. "QTRAJ 1.0: A Lindblad equation solver for heavy-quarkonium dynamics" (2021). arXiv: 2107.06147v1.

[162] N. Brambilla, M.A. Escobedo, M. Strickland, A. Vairo, P. Vander Griend, and J. H. Weber. "Bottomonium production in heavy-ion collisions using quantum trajectories: Differential observables and momentum anisotropy" (2021). arXiv: 2107.06222v1.

[163] X. Yao and T. Mehen. "Quarkonium in-medium transport equation derived from first principles". *Phys. Rev. D* 99 (2019), 096028. arXiv: 1811.07027v3.

[164] X. Yao and B. Müller. "Approach to equilibrium of quarkonium in quark-gluon plasma". *Phys. Rev. C* 97 (2018), 014908. arXiv: 1709.03529v4.

[165] X. Yao, W. Ke, Y. Xu, S. Bass, and B. Müller. "Quarkonium production in heavy ion collisions: coupled Boltzmann transport equations". *Nuclear Physics A* 982 (2019), 755–758. arXiv: 1807.06199v1.

[166] X. Yao, W. Ke, Y. Xu, S.A. Bass, and B. Müller. "Coupled Boltzmann transport equations of heavy quarks and quarkonia in quark-gluon plasma". *J. High Energ. Phys.* 2021 (46 2021). arXiv: 2004.06746v5.

[167] X. Yao. "Application of Effective Field Theory in Nuclear Physics". PhD thesis. Duke University, 2019. arXiv: 1911.08500v1.

[168] J.P. Blaizot, D. De Boni, P. Faccioli, and G. "Heavy quark bound states in a quarkgluon plasma: Dissociation and recombination". *Nuclear Physics A* 946 (2016), 49–88. arXiv: 1503.03857v1.

[169] D. De Boni. "Fate of in-medium heavy quarks via a Lindblad equation". *J. High Energ. Phys.* 2017 (2017). arXiv: 1705.03567v2.

[170] M. Le Bellac. *Thermal Field Theory*. Cambridge University Press, 1996.

[171] J.I. Kapusta and C. Gale. *Finite-Temperature Field Theory: Principles and Applications*. Cambridge University Press, 2006.

[172] A. Beraudo, J.P. Blaizot, and C. Ratti. "Real and imaginary-time $Q\bar{Q}$ correlators in a thermal medium". *Nuclear Physics A* 806 (2008), 312–338. arXiv: 0712.4394v1.

[173] M. Laine, O. Philipsen, P. Romatschke, and M. Tassler. "Real-time static potential in hot QCD". *J. High Energ. Phys.* 2007 (2007). arXiv: 0611300v2.

[174] R. Katz, S. Delorme, and P.B. Gossiaux. "One-dimensional imaginary potentials for quarkonia in a quark-gluon plasma" (2021). in preparation.

[175] G.M. Prosperi, M. Raciti, and C. Simolo. "On the running coupling constant in QCD". *Prog. Part. Nucl. Phys.* 58 (2007), 387–438. arXiv: 0607209.

[176] J. Crank and P. Nicolson. "A practical method for numerical evaluation of solutions of partial differential equations of the heat-conduction type". *Mathematical Proceedings of the Cambridge Philosophical Society* 43.1 (1947), 50–67.

[177] J.F. Wendt. *Computational Fluid Dynamics: An Introduction*. Springer, 2009.

DOCTORAT MATIERE BRETAGNE MOLECULES LOIRE ET MATERIAUX

IMT Atlantique
Bretagne-Pays de la Loire
École Mines-Télécom

Titre : Description théorique de la dynamique des quarkonia dans le plasma de quarks et de gluons au moyen d'une approche de type équation maîtresse quantique

**Mot clés :** Dynamique des quarkonia ; systèmes quantiques ouverts ; plasma de quarks et de gluons ; équation maîtresse quantique

**Résumé :** La Chromodynamique Quantique (QCD) prédit l'existence d'un état de la matière appelé Plasma de Quarks et de Gluons (PQG) dans des conditions extrêmes de température et de pression, qui peut être produit lors de collisions d'ions lourds. Une observable du PQG est la suppression des quarkonia (états liés de quark-antiquark lourds), qui est définie par une plus faible production de ces états en présence de PQG par rapport à la production en l'absence de plasma. Ces dernières années, un effort signicatif a été réalisé d'un point de vue théorique vers une description dynamique des quarkonia au sein du Plasma de Quarks et de Gluons, à l'aide du formalisme des systèmes quantiques ouverts. Cette thèse étudie la dynamique d'états quarkonium en résolvant une équation maîtresse quantique basée sur l'approche de Blaizot & Escobedo. Plus précisement, cette équation est résolue numériquement directement pour la première fois dans le cas d'un PQG statique et dans le cas d'un PQG se refroidissant. Les populations d'états quarkonium sont étudiées et la validité d'approximations semi-classiques amenant à des équations de Langevin est examinée.

Title: Theoretical description of quarkonium dynamics in the quark gluon plasma with a quantum master equation approach

**Keywords:** Quarkonia dynamics; open quantum systems; quark-gluon plasma; quantum master equation

**Abstract:** Quantum chromodynamics (QCD) predicts the existance of a state of matter called the Quark-Gluon Plasma (QGP) at extreme temperature and density, which can be produced in heavy ion collisions. One of the QGP observables is the so-called quarkonia (heavy quark-antiquark bound states) suppression which is defined by a smaller production of quarkonia states in presence of QGP compared to the production in absence of plasma. In recent years, a significant theoretical effort has been made towards a dynamical description of quarkonia inside the Quark-Gluon Plasma , using the open quantum systems formalism. This thesis investigates the dynamics of quarkonium states by resolving a quantum master equation based on the approach of Blaizot & Escobedo. More precisely, this equation is resolved numerically directly for the first-time in both a static and a cooling QGP. The populations of quarkonium states over time are studied and the validity of semi-classical approximations leading to Langevin equations is investigated.